Jorge Manuel Reis Magalhães

REMOTE SENSING OBSERVATIONS OF OCEANIC INTERNAL WAVES: MAIN GENERATION AND PROPAGATION MECHANISMS

Departamento de Geociências, Ambiente e Ordenamento do Território
Faculdade de Ciências da Universidade do Porto

Porto, Abril 2012

Jorge Manuel Reis Magalhães

REMOTE SENSING OBSERVATIONS OF OCEANIC INTERNAL WAVES: MAIN GENERATION AND PROPAGATION MECHANISMS

PhD thesis submitted to
Faculdade de Ciências da Universidade do Porto
(para a obtenção do grau de Doutor em Engenharia Geográfica)

Supervisores:
Prof. Dr. José Carlos Pinto Bastos Teixeira da Silva DGAOT-FCUP, CIIMAR
Prof. Dra. Maria Joana Afonso Pereira Fernandes DGAOT-FCUP, CIIMAR

Departamento de Geociências, Ambiente e Ordenamento do Território
Faculdade de Ciências da Universidade do Porto

Porto, Abril 2012

Abstract

The following thesis is mainly focused in the study of Internal Solitary Waves (ISWs) in the geophysical environment and uses satellite remote sensing as the primary data source. Data from satellite images are also often complemented with analysis of *in situ* data and modelling results. The investigations presented in this thesis can be essentially divided into four different regions of the world's oceans: Mozambique Channel (MC), Mascarene Ridge, Red Sea and west Iberian Coast (specially the Estremadura Promontory).

Satellite imagery from Synthetic Aperture Radars (SARs) of MC reveals sea surface signatures consistent with oceanic and atmospheric ISWs. The Sofala shelf region (near 20°S, 36°E) is identified as a strong and previously unknown source of Internal Tides (ITs) and oceanic ISWs. The generation and propagation mechanisms of the ISWs are investigated, and it is found that tidal currents and transports are the highest in this region (anywhere in MC) due to the particular nature of the bathymetry there. Two distinct types of ISWs are observed to travel offshore, away from the shelf-break, and possible generation mechanisms are discussed. Mode 2 solitary-like internal waves are identified in SAR and a possible generation mechanism is discussed in the light of recent laboratory and numerical results. A particular example of ISW refraction is documented where ISWs and eddy-like features are seen to interact. The influence of these rotating features in the refraction patterns is briefly discussed. On the other hand, it is also shown that large-scale Atmospheric Gravity Waves (AGWs) of solitary-like form are frequently observed over MC, and thus care must be taken when discriminating ISW signatures in SAR images.

The Mascarene Ridge in the western Indian Ocean is identified as a new ISW hotspot. SAR images show that large internal waves radiate both to the west and east of the Saya de Malha and Nazareth Banks (two major bathymetry features of the Mascarene Ridge). These ISWs appear in tidally generated packets and have crestlengths in excess of 350 km, amongst the longest yet recorded anywhere in the world's oceans. Travel-time graphics indicate that they are generated due to a splitting lee-wave that forms on the western side of the sill at the predicted time of maximum tidal flow to the west. Propagation speeds of the ISWs are well described by first mode linear waves interacting with background shear – taken from the westward flowing south Equatorial Current (a large part of which flows through the two banks mentioned above). This study also confirms the existence of mode 2 solitary-like internal waves that form on the western side of the sill and travel across it towards the east.

The Red Sea region is shown to be a major hotspot for the occurrence of AGWs and satellite imagery is used to reveal the spatial characteristics of these waves. The pre-conditions for wave generation and propagation in this region are investigated using statistical analyses combining satellite imagery and atmospheric data. Results from weakly nonlinear long wave theory are compared with the observed wave characteristics. Namely, the observed wavelengths are used to obtain predicted phase speeds, which are consistent with those observed. In addition, the Korteweg-de Vries theory is found to perform slightly better than the Benjamin-Davis-Acrivos-Ono model.

SAR images are used to identify the Estremadura Promontory (in the west Iberian Coast) as an oceanic hotspot for ISWs. The full two-dimensional structure and the main physical properties of these waves are revealed for the first time. The propagation of energy associated with the ISWs in the SAR images is evaluated, and refraction patterns are found to divert meridionally propagating waves to the east, where they eventually dissipate in the inner-shelf regions close to shore. The most likely generation locations are identified based on the P.G. Baines body force (Baines, 1982), and it is found that there is more energy coming from the south while the tidal forcing seems to be equally divided between both flanks of the promontory. It is suggested that the steeper slopes in the northern side are prone to generate internal hydraulic jumps and overturning that inhibit the disintegration of the IT into solitary waves – as suggested by Legg and Klymak (2008).

Keywords: Internal solitary waves, Atmospheric gravity waves, Synthetic aperture radar, Mozambique Channel, Mascarene Ridge, Red Sea, Portugal, Estremadura Promontory.

Resumo

A dissertação que se segue tem como principal objectivo o estudo de Ondas Internas Solitárias (OISs) dentro do contexto geofísico, utilizando imagens de satélite como principal fonte de dados, que podem depois ser complementadas com dados *in situ* e modelação numérica. Neste contexto, os resultados apresentados podem ser divididos em quatro regiões principais: Canal de Moçambique (CM), Crista das Mascarenhas, Mar Vermelho e costa oeste da Península Ibérica (mais concretamente o Promontório da Estremadura).

As imagens de satélite obtidas através de Radares de Abertura Sintética (SARs) do CM revelam a existência de assinaturas na superfície do mar consistentes com OISs oceânicas e atmosféricas. A plataforma continental na região de Sofala (localizada aproximadamente em 20°S, 36°E) é identificada como uma importante fonte de Ondas de Maré Interna (OMI) e OISs (previamente desconhecida na literatura). Os mecanismos de geração e de propagação das OISs são investigados, e verifica-se que as correntes e transportes de maré são os mais elevados nesta região (dentro do CM) devido à natureza peculiar da sua topografia. Observa-se que existem dois tipos distintos de OISs que viajam para a parte profunda do canal (afastando-se da plataforma continental), e os respectivos possíveis mecanismos de geração são discutidos. São também identificadas OISs de modo 2 em imagens SAR, e o mecanismo de geração responsável é discutido tendo em conta desenvolvimentos recentes obtidos em laboratório e através de modelação numérica. No CM podem também observar-se padrões de refracção associados à propagação de OISs, que são apresentados nesta tese através de um exemplo particular, onde se verifica a interacção entre estas ondas e vórtices oceânicos. A influência destas estruturas circulares nos padrões de refracção das OISs é brevemente discutida. Por fim, é igualmente demonstrado que OISs de larga-escala podem ser frequentemente observadas a propagarem-se na atmosfera sobre o CM, o que justifica uma discriminação atenta entre assinaturas de OISs oceânicas e atmosféricas em imagens de SAR.

A Crista das Mascarenhas, localizada no Oceano Índico ocidental é identificada como um novo *hotspot* de OISs. As imagens SAR desta região mostram a existência de grandes ondas internas que se propagam com uma componente zonal (para este e oeste) relativamente aos bancos da Saia de Malha e da Nazaré (duas grandes formações topográficas da Crista das Mascarenhas). Verifica-se que estas ondas aparecem em grupos separados por períodos da maré semi-diurna, e que possuem comprimentos de crista que podem exceder os 350 km, encontrando-se por isso entre as mais longas alguma vez já registadas. Gráficos relacionando tempos e distâncias indicam que as ondas são geradas devido a uma onda de sotavento de grandes proporções, que se forma no lado oeste do ponto central entre os dois bancos, no momento em que se prevê que as correntes de maré atinjam o máximo para oeste. As velocidades de propagação das OISs são consistentes com as de ondas lineares de modo 1 sob a influência de uma corrente adicional, resultante da Corrente Equatorial sul que flui para oeste – sendo que grande parte desta flui entre os dois bancos submarinos já mencionados. Este estudo também confirma a existência de OISs de modo 2 que se formam do lado oeste e atravessam os bancos na direcção oposta.

A região do Mar Vermelho é apresentada como um local importante para a geração de OISs que se propagam na atmosfera. Neste âmbito, são utilizadas imagens de satélite para revelar as principais características espaciais destas ondas. As condições para a geração e propagação de ondas nesta região também são investigadas através de análises estatísticas que combinam imagens de satélite e dados atmosféricos. Os resultados provenientes do uso de teoria fracamente não linear para ondas longas são comparados com as características observadas. Nomeadamente, os comprimentos de onda observados em satélite são utilizados para inferir as velocidades de fase calculadas através da teoria – que mostram ser consistentes com as velocidades observadas. Dentro dos dois modelos teóricos mais utilizados, observa-se que a teoria de Korteweg-de Vries apresenta resultados ligeiramente melhores que o modelo de Benjamin-Davis-Acrivos-Ono.

Através da utilização de imagens SAR, o Promontório da Estremadura (localizado na costa oeste da Península Ibérica) é identificado como um local privilegiado para a observação de OISs no oceano. Neste contexto, são reveladas pela primeira vez a estrutura espacial destas

ondas e as suas principais propriedades físicas. A propagação de energia associada às OISs é avaliada a partir das imagens de satélite, e observa-se que existem padrões de refracção associados à propagação das ondas que convergem progressivamente para este – onde eventualmente se dissipam nas regiões mais próximas da costa. Uma análise do forçamento barotrópico da maré (dado por P.G. Baines, 1982) é levada a cabo para identificar os locais mais prováveis para a geração destas ondas. Desta análise resulta também a percepção de que há mais energia proveniente da parte sul do promontório, enquanto o forçamento barotrópico parece igualmente dividido entre ambas as vertentes. Neste contexto, é demonstrado que esta aparente contradição está relacionada com os diferentes declives da topografia nos lados norte e sul do promontório. De facto, os declives mais acentuados da parte norte são propensos à geração de saltos hidráulicos e mistura vertical, que inibem a desintegração habitual das OMIs em OISs – tal como sugerido por Legg and Klymak (2008).

Palavras-chave: Ondas internas solitárias, Radar de abertura sintética (SAR), Canal de Moçambique, Crista das Mascarenhas, Mar Vermelho, Portugal, Promontório da Estremadura.

'The soul never *thinks without a picture*.'
Aristotle

Acknowledgments

How does one measure the weight of gratitude in the scales of human life? Under starry nights I wonder: sometimes, perhaps, it is just not possible. Great gestures go far too deep into the very foundations of our existence. Indeed, no ink could ever grasp and no paper could ever hold what only poetry can whisper. To those sparkling the sense of wonder, and whose names will remain in my own sweet melody: thank you.

First and foremost, a dedicated gratitude to my PhD supervisor that continually defies the pursuit of excellence in scientific knowledge, and is somehow able to steer steady courses in the heart of the ocean – even in otherwise stormy seas.

Also lecturing on life is my long time professor João Freitas: thank you for teaching us the ways of the world.

To the enchantment land high up in mountains and the wonderful people living there: thank you for setting right so many wrongs.

Thank you to all my friends. What a pleasant company to have in this longest journey.

Some souls just burn too bright. Thank you dear father, for teaching me what no one else dared to learn.

Thank you to you my dearest for so many adventures, most of which still to come …

Finally, the simplest thank you to my mother and brother. Indeed, you were right, it is worth it. This thesis is for you.

The author would like to thank the Portuguese Science and Technology Foundation (FCT) for a research grant (SFRH/BD/35898/2007). Some satellite images used here were kindly provided by Goddard Space Flight Center (NASA). The SAR images presented in this thesis were provided by the European Space Agency (ESA) under the project AOPT-2423 and by the German Aerospace Centre (DLR) under the project OCE0056. A proper acknowledgment is also in order to the Oceanography Centre (Lisbon) and the Faculty of Sciences of the University of Lisbon.

List of Research Articles

The following thesis includes several research articles that have been published (or are currently submitted and under review) throughout the author's PhD timeframe, and are a direct result of the work developed there. A reference list of these papers is given below.

- Magalhaes, J.M., da Silva, J.C.B., New, A.L., 2011. Internal solitary waves system in the Mozambique Channel. In: Vittorio Barale and Martin Gade (editors) Remote Sensing of the African Seas. Springer. Submitted.

- da Silva, J.C.B., New, A.L., Magalhaes, J.M., 2009. Internal solitary waves in the Mozambique Channel: Observations and interpretation. J. Geophys. Res. 114, C05001. doi:10.1029/2008JC005125.

- Matthieu, J.M., Mathur, M., Gostiaux, L., Gerkema, T., Magalhaes, J.M., da Silva, J.C.B., Dauxois, T., 2011. Soliton generation by internal tidal beams impinging on a pycnocline: laboratory experiments. J. Fluid Mech. Submitted.

- da Silva, J.C.B., New, A.L., Magalhaes, J.M., 2011. On the structure and propagation of internal solitary waves generated at the Mascarene Plateau in the Indian Ocean. Deep-Sea Res. 58, 229-240. doi: 10.1016/j.dsr.2010.12.003.

- Magalhaes, J.M., Araújo, I.B., da Silva, J.C.B., Grimshaw, R.H.J., David, K., Pineda, J., 2011. Atmospheric gravity waves in the Red Sea: a new hotspot. Nonlin. Processes Geophys. 18, 71-79. doi:10.5194/npg-18-71-2011.

- Magalhaes, J.M., da Silva, J.C.B., 2011. SAR observations of internal solitary waves generated at the Estremadura Promontory off the west Iberian Coast. Deep-Sea Res. I. Submitted.

These articles are included in chapters 2 to 7, each corresponding to one individual chapter, which are encompassed by an introduction in the beginning and some concluding remarks in the end. Further details of the copyright permissions (when necessary) are given within the corresponding chapters.

Contents

Chapter 1

General Introduction

Oscillating motions and wave-like phenomena surround us from the very tininess of the atom (e.g. electron diffraction) to the immeasurable universe (e.g. Doppler Effect). Indeed, waves are an intrinsic part of our world and a wide variety of these motions can be found ranging from the mighty ocean waves to the immaterial music. It was the dual nature of light itself (with particle and wave characteristics) that came together to inspire Louis Victor de Broglie (in 1924, in his PhD dissertation) to postulate that: "*perhaps all forms of matter have in fact wave-like properties*". History would prove him right.

In the most conceptual form it can be said that oscillatory motions appear whenever a system is brought out of balance, and some restoring force acts to bring it back to an equilibrium position. This induces an oscillating state that carries with it a given energy. This energy (imprisoned in the oscillating motion) can then propagate itself through matter, thus giving rise to a wave motion. However, in the physical world there are many different forms and types of waves, which can propagate throughout various media. It is the individual nature of the each restoring force that characterizes and distinguishes the different types of waves.

A particular case of wave motions are the Internal Waves (IWs), which owe their expression to the fact that they propagate within fluids, so that their maxima displacements are confined to the medium's interior. From a geophysical point of view, the restoring forces associated with IW motions can be twofold. Namely, either gravity or the earth's rotation (i.e. the Coriolis force) is at work. In the former case the nomenclature is usually termed internal gravity waves, while in the latter the waves are called inertial or gyroscopic – if both forces are present the waves can be termed internal inertial-gravity waves (see e.g. Gerkema and Zimmerman, 2008). Two distinct frequencies thus arise, each coupled with a different force: on the one hand there is the inertial frequency (or Coriolis parameter '*f*'), which is associated with the earth's rotation; and on the other hand there is the buoyancy (or Brunt-Väisälä) frequency, which is essentially related with gravity. These two frequencies are of the utmost importance since they determine the range for which IWs are allowed to exist in the geophysical world. It is also here, in the earth's oceans and atmosphere that IWs achieve some of their most striking characteristics. For instance, in geophysical fluid dynamics, and despite the role of *f*, it is mainly the basic vertical stratification in density (a consequence of gravity) that allows for these waves to exist. Due to the particular nature of these stratification distributions, the density differences are very small within both media when compared, for example, with the air-sea interface. This means that density gradients across typical waveguides for IWs and ocean surface waves can reach differences of several orders of magnitude. With Newton's second law, this can be translated into wave amplitudes, and hence explain why ocean waves reach as high as tens of meters while oceanic IWs can have amplitudes up to 100 m and more.

From an historical perspective IWs can be considered a relative recent field of study. Indeed, while general wave theory can be traced back for more than two hundred years (e.g. d'Alembert, 1747), the main developments in IW theory came only in past century (e.g. Krauss, 1966). In fact, one of the first measurements to ever be recorded in the oceans goes back just over a century when Hansen and Nansen (1909) first recognized the presence of these "*puzzling waves*", and realized their importance in determining the ocean's background state. From there, IW research has been increasing ever since. However, the number of

reports and observations of IWs in the ocean and in atmosphere has been increasing significantly only over the last few decades, owing mainly to the development of satellite technology and remote sensing techniques. These new measuring capabilities boosted the number of observations, which led to several studies that indicated that the phenomenon was in fact much more frequent than previously thought (see e.g. Jackson and Apel, 2002; Jackson, 2004; Jackson, 2007), and spurred new lines of research relating IWs and a wide variety of other fields of (multidisciplinary) study.

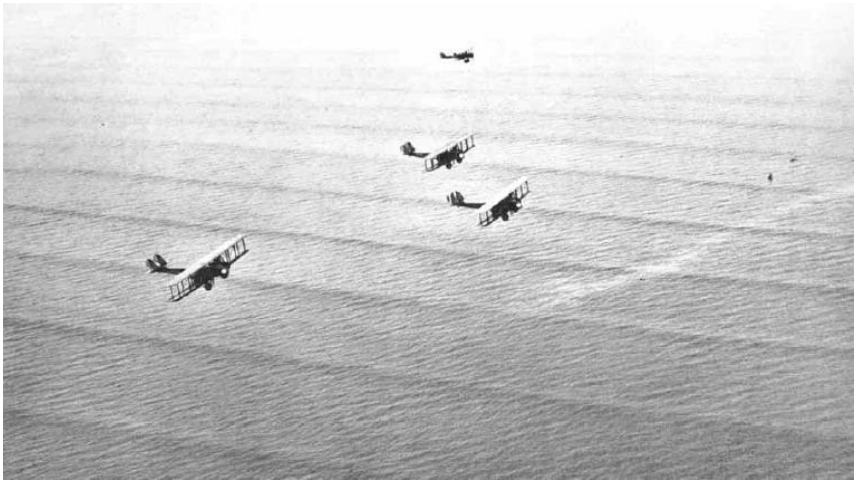

Figure 1. Aerial photography off the coast of Panama in 1933, showing military aircrafts flying in formation just above a packet of surface solitary waves. This image first appeared in 1933 in the National Geographic Society Magazine™ (volume 63), but it may also be found available online at: http://en.wikipedia.org/wiki/File:Periodic_waves_in_shallow_water.jpg

Within the entire IW spectra there is a very unique group of IWs that constitutes a special class of their own. These are usually termed Internal Solitary Waves (ISWs) and owe their name to the fact that they tend to occur on their own or in individual packets, and have often been identified with the soliton solutions of nonlinear wave theory. In these cases the waves propagate such that a delicate balance exists between nonlinear wave steepening and linear wave dispersion. This equilibrium allows for finite-amplitude waves of elevation, or depression (depending on the background state), to propagate for long distances without significant changes in form or shape. For further reference the author notes that the terms ISW (or solitary wave) and soliton are frequently found interchangeably in the literature. However, only the first term will be used when referring to the geophysical case to make it clear that it is the physical phenomena and not the theoretical concept that is being referred to.

ISWs are also ubiquitous phenomena whose manifestations are often remarkably impressive (see Figures 1 and 2 for examples of solitary waves propagating on the ocean surface and ISWs propagating in the atmosphere, respectively). The first observation of a solitary wave was documented in 1834 (see http://en.wikipedia.org/wiki/John_Scott_Russell for a historical note), in a narrow water canal linking Glasgow to Edinburgh, by a civil engineer named Scott Russell. According to Russell's description, a perturbation was generated when a barge came to an abrupt stop, which created a large solitary elevation in the water. Ridding on the back of his horse, he followed this peculiar wave as it "*rolled forward with great speed ... and without change of form or diminution of speed*". Later on, Russell recreated the phenomenon in laboratory experiments to derive the first empirical relationship in soliton wave theory. The mathematical description of solitary waves would only appear more than 30 years later (in the 1870s), when Boussinesq and Rayleigh independently provided a set of equations from which Russell's empirical relationship could be deduced (see Jeans, 1995). However, the proper wave equation for solitons came only at the end of the 19th century (1895), and was formulated by Korteweg-de Vries (KdV) assuming small amplitude

waves propagating in a shallow (frictionless and incompressible) fluid (see Jeans, 1995). Curiously, these special cases of nonlinear wave theory would then remain almost anomalously for many years to come. It was Zabusky and Kruskal (1965), who almost a century later revealed that these waves could retain their shapes and speeds after a collision – and thus coined the term 'soliton'. Finally, to amplify the KdV equation applicability, subsequent progress was made in the solitary wave field with the development of appropriate theories for deep (Benjamin, 1966; Ono, 1975) and intermediate waters (e.g. Joseph, 1977).

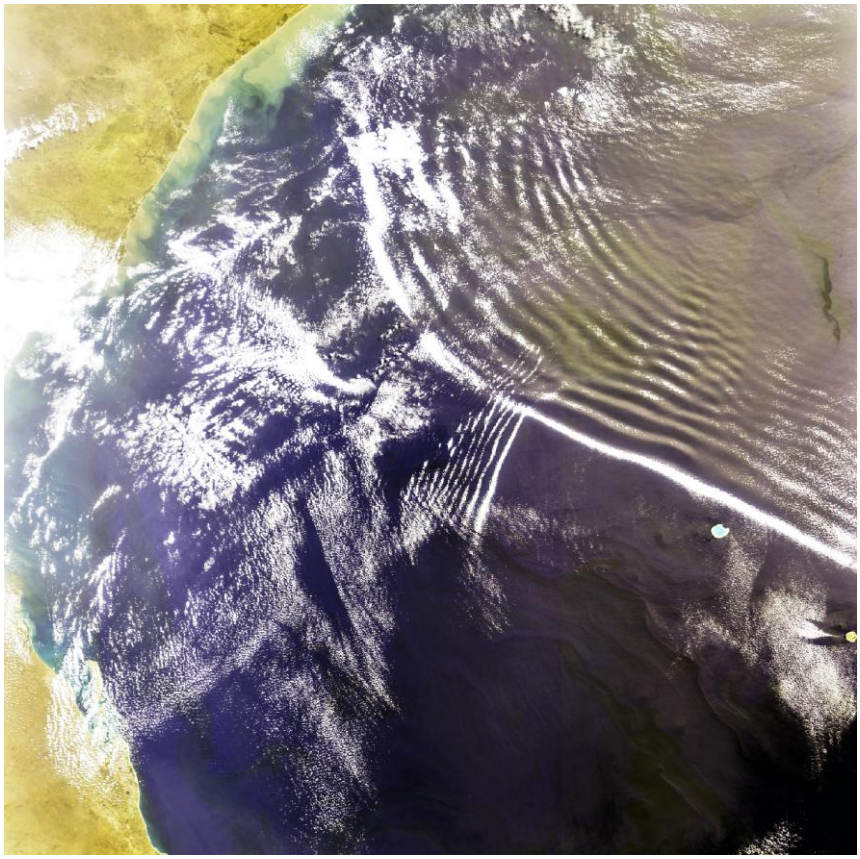

Figure 2. Envisat-MERIS RGB composite image dated 16 September 2004 and acquired at 07h15m UTC. The image covers an area of approximately 580×660 km^2 and shows a large-scale atmospheric ISW propagating southwest in the Mozambique Channel. The crestlength of the leading wave extends for more than 500 km.

The importance of ISWs (and all IWs in general) goes far beyond the classical academic framework and is something that has evolved in its own right. In fact, physical applications spread throughout the most various domains, and go all the way to quantum mechanics (Drazin, 1991). In the geophysical context, several useful applications have been claimed over the years as compelling motivations to study and investigate ISWs – both in the ocean and in the atmosphere. From an oceanic perspective, one of the first motivations to study ISWs may have been brought in via military interests, since these waves can be important to submarine navigation and detection systems (Garrett and Munk, 1979). In addition, they are also important in acoustical dynamics (Dushaw, 2006), and these effects need to be taken into account when considering underwater communications. The oil drilling industry has also been strongly supportive of field research, particularly in late 70's and early 80's, due to the costly disruption in drilling operations associated with large ISWs in the Andaman Sea (Osborne and Burch, 1980; see also Potter, 2001). Moreover, ISWs can often assume a highly nonlinear character, and like any other nonlinear wave; they too carry a net transport along their propagation paths. This has key implications in various fields, but particularly in coastal dynamics where sediment transports can be of great importance

(Bogucki et al., 1997; Cacchione et al., 2002; McPhee-Shaw, 2006; Quaresma et al., 2007). Also noteworthy, is their ability to carry energy and momentum, and it is here that some of the most interesting motivations can be found. In fact, ISWs can hold a sizeable amount of energy with the most energetic wave packets containing up to 10^{14} J (see e.g. Osborne and Burch, 1980) – enough energy to power an average light bulb for more than thirty thousand years… On the other hand, they are known to travel for great distances – like in the Mascarene Ridge (see Figure 3) where they depart from their point of origin for more than 400 km (da Silva et al., 2011). Consequently, some attention has also been devoted to understand the ultimate fate of ISWs, which are bounded to breaking and dissipation processes somewhere along their propagation paths. This means that some energy must be being transferred to vertical mixing inside the water column – mainly over continental shelves and coastal areas where ISWs are more frequently observed. This in turn has major implications for biological processes, especially because vertical mixing in shallow areas is determinant to bring cool and nutrient rich waters from bellow to the surface. In addition, the amount of mixing induced by oceanic IWs may extend further into the deep-ocean areas. Therefore, they may constitute and important part of the thermohaline circulation, which needs to be accurately accounted for in any realistic modeling of global long-term processes (such as climate change).

In the atmospheric domain, IWs of solitary-like form are usually termed Atmospheric Gravity Waves (AGWs). They can occur in a wide range of time and spatial scales, but are usually highly nonlinear, and are often identified to propagate in the lower troposphere, where they can form roll-cloud structures in packet-like configurations. Their origin can be attributed to various generation mechanisms, often involving convection, wind shear, gravity currents and air mass collisions. In summary, any atmospheric process leading to the displacement of density surfaces can be a potential source of AGWs, providing that suitable propagation conditions are previously met. From an applicability point of view, AGWs have been shown to constitute a serious hazard to aircrafts operating at low altitudes and small speeds (Christie and Muirhead, 1983; Bedard et al., 1986). Some large-scale AGWs may also have a significant role in establishing low-level circulation and determining the local vertical structure of wind, temperature and moisture. They can even modify and trigger convective motions and induce significant rain, (Reeder et al., 1995). Their ability to transfer energy and momentum, together with the fact that they can propagate for almost a 1000 km (e.g. in the Mozambique Channel, da Silva and Magalhaes, 2009), makes them an important topic of research, especially since their influence can also extend into weather forecast and climate models.

This ensemble of information, even if in the tip of the iceberg, was more than enough to capture this author's attention, and attract him to embark in this quest for knowledge and research venture. Indeed, the very foundations of the present work can be traced back to the graduating thesis, where IWs where to be studied for the first time. At that point in time an observational study of the Mozambique Channel (MC), regarding IW signatures in satellite images, was undertaken as part of a first approach to some unusual observations. This ideal scenario thus joined the research field of IWs with the measuring capabilities of satellite remote sensing, particularly with Synthetic Aperture Radars (SARs). In fact, it is well known that both oceanic and atmospheric IWs are capable of producing roughness patterns on the ocean surface and that they can generate recognizable signatures in radar images. Usually, AGWs have significantly different time and scales than oceanic IWs and discrimination of these features is simple. Occasionally however, large oceanic ISWs or small AGWs can easily be misinterpreted, and discrimination using SAR imagery alone can thus be difficult or sometimes impossible (Alpers and Huang, 2011). For this reason, SAR images over MC initially suggested the presence of oceanic IWs. It was not until later that cloud bands, observed in MODIS and MERIS imagery, revealed excessively large atmospheric wave trains which coincided with SAR observations. This introduced ambiguities in our initial interpretations of the satellite data, and eventually led to the discovery of an IW hotspot

where both oceanic ISWs and AGWs could be frequently observed. In turn, this would ultimately lead to two major studies – one devoted to the atmosphere and another focused in the ocean (da Silva and Magalhaes, 2009; da Silva et al., 2009, respectively).

During the final stages of studying the oceanic ISWs of MC, the author was given the chance to participate in a laboratory study dedicated to ISWs, which was held at the Grenoble Coriolis Platform (France) and coordinated by Dr. Theo Gerkema of the Royal Netherlands Institute of Sea Research (NIOZ). This set of experimental trials aimed to study, in a controlled environment, the influence of several parameters in a very unique generation mechanism for ISWs in the ocean – the so called 'local-generation' mechanism (New and Pingree, 1992; Gerkema, 2001; New and da Silva, 2002; da Silva et al., 2009). In this case the tidal currents are forced over rough topography (such as ridges, canyons or promontories), and tidal beams or rays are generated at critical bathymetry where baroclinic energy propagates at the same angle as the bottom slope. These rays then propagate towards the ocean floor, from which reflection occurs to re-emerge them upwards. As they reach for the surface they impinge on the thermocline from below, and create an interfacial disturbance there that can evolve into ISWs. The recreation of this mechanism for the first time in a laboratory scenario provided valued insights that further contributed to the understanding of this particular mechanism.

After the IWs in MC, it was the Mascarene Ridge that draw further attention. However, the study of IWs at this location had long begun its way. A research cruise had already been undertaken early on, during the year of 2002, as an observational campaign aboard the R.R.S. Charles Darwin (New, 2003; New et al., 2005, 2007). One of the primary aims of the cruise was to assess energy fluxes and mixing produced by IWs in the vicinity of the Mascarene Ridge (particularly in two large banks called Saya de Malha to the north and Nazareth to the south). Consequently, a significant amount of data was gathered at that time on several aspects of oceanographic importance. Inclusively, an important correction was made to the previous knowledge of the local bathymetry, which would eventually prove of great importance to our investigations. However, it was not until the end of 2008 that the first SAR images were available. For this reason, no satellite imagery was acquired during the field work onboard the R.R.S. Charles Darwin (1 June to 11 July, 2002) – at that time there was no satellite antenna covering this remote region of the Indian Ocean. Only later could SAR reveal ISWs signatures of considerable crestlength (see Figure 3) propagating to both sides of the 'suspected' generation site – to the east and to the west – for very long distances exceeding 400 km to both sides of the ridge. This immediately amplified the cruise objectives, and led to a more exhaustive investigation of the IW field in this study region. Some of the world's largest (in terms of crestlengths and propagation distances) oceanic ISWs were then discovered. Approximately during the same period, and still in eastern hemisphere, IW investigations were also being lured to the northeastern tip of Africa (near the Arabic Peninsula). Here, an amazing case study was collected, where large-scale ISWs literally engulfed the Red Sea area, as they propagated south along the sea's main axis (see Figure 4). Similar case studies were further revealed after a more thorough analysis. However, just like the MC, it was soon realized that this region was prone to the occurrence of both types of ISWs – oceanic and atmospheric. A study aimed to understand these waves' characteristics then took place, which eventually focused on the atmospheric IWs, due to their particular nature in size and frequency of occurrence (see also Magalhaes et al., 2011).

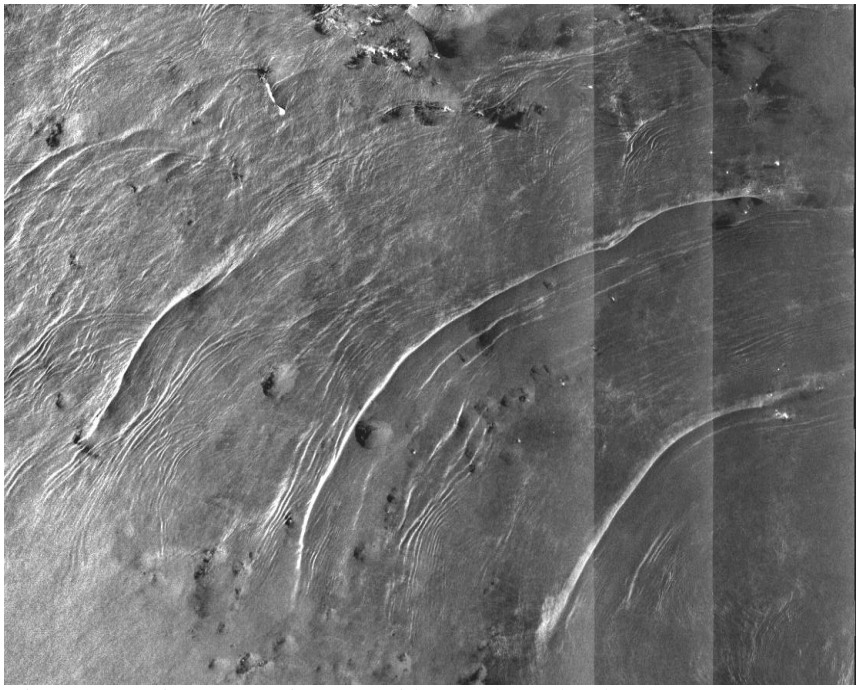

Figure 3. Envisat-ASAR image (Wide Swath mode) dated 11 February 2009 and acquired at 18h31m UTC. The image is approximately 400×400 km^2 and shows large-scale oceanic ISWs propagating from the Mascarene Ridge. The crestlengths of leading waves can exceed 350 km, and the propagation distances can be more than 400 km from their point of origin.

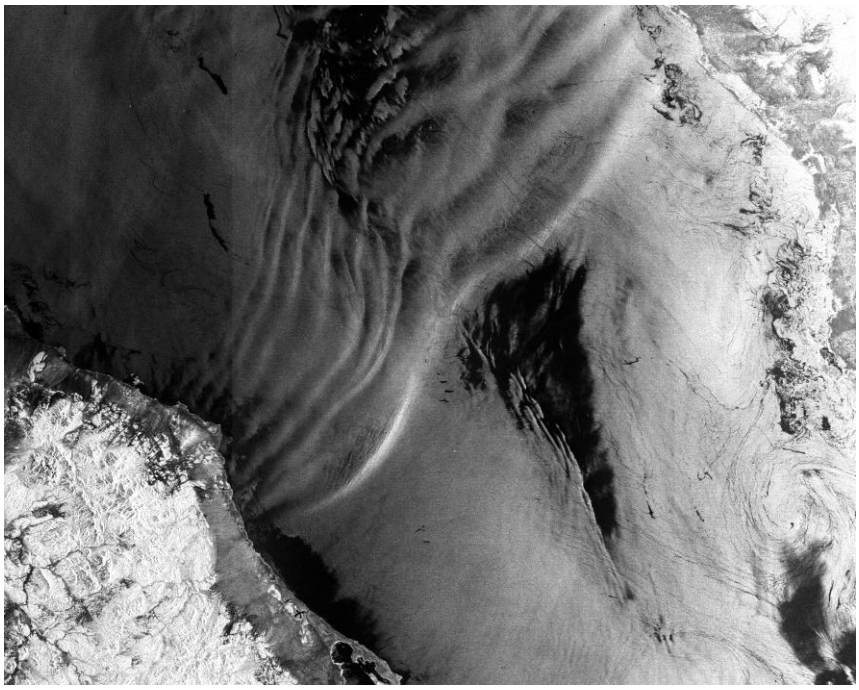

Figure 4. Envisat-ASAR (Wide Swath mode) image dated 11 May 2004 and acquired at 07h27m UTC. The image covers an area of approximately 400×400 km^2 and shows a large-scale AGW propagating southeast in the Red Sea region. The crestlength of the leading wave extends for at least 250 km – but may be larger since the sea surface signatures are limited to the Red Sea surface.

In between the submission and review processes of the research articles submitted on the Mascarene and Red Sea IWs (in 2010), the author had the chance to participate in an airborne field campaign held off the Portuguese Coast (titled A.NEW and performed under the transnational access projects made available by EUFAR), and he also attended an international course solely dedicated to IWs (during November 2010 at the Institut d'Etudes Scientifiques de Cargèse-Corsica, France). Both would reveal precious for this thesis's main work. On the one hand, a sizeable amount of images had been collected for the Portuguese Coast comprising a period of more than a decade. This large set of data clearly revealed that the Portuguese Coast was a unique study area where ISWs could be frequently observed. However, it also revealed that the majority of the observations were in fact concentrated around a major topographic feature – the Estremadura Promontory located to the west of Lisbon (in the west Iberian Peninsula). Despite that previous studies (Jeans and Sherwin, 2001a, 2001b; Sherwin et al., 2002; Small, 2002; da Silva et al., 2007; Quaresma et al., 2007) had already dealt with other regions off the Portuguese Coast, it was clear that this particular set of powerful waves had not been studied before – partially due to the particular nature of the observations that just seemed too puzzling. It was the preparation stages for the airborne campaign and the airborne mission itself that created awareness on two important subjects: first it became clear that the meridional barotropic tides were somehow degenerating into west-east propagating ISWs, thus forcing barotropic to baroclinic energy conversion in 90° turning patterns; secondly, the data collected in the very near coast areas revealed that the waves were reaching much closer to shore than previously realized (seen from the SAR data). On the other hand, the classes attended at the IW course also proved useful. After performing an energy analysis to the ISW field it was realized that there was a difference between the amount of wave energy propagating from the northern and southern flanks of the Estremadura Promontory, a fact somewhat unexpected if we considered the integrated barotropic forcing maps calculated based on methods developed by P.G. Baines (1982). The solution to this problem greatly benefited from the work developed by Legg and Klymak (2008). During the IW course at Cargèse there was a chance to discuss how barotropic energy may be converted to overturning in the presence of steep topography (rather than undergoing conversion to ISWs). In their investigations, Legg and Klymak (2008) provide a hypothesis based on numerical experiments that would offer a possible explanation to the observed north-south ISW energy budget. All the ingredients then combined, and the cornerstone of this work was completed with the aim of amplifying the knowledge of IWs off the Portuguese Coast, and in the western Iberian Coast.

The final stages of this PhD were spent in revisiting MC. This privileged location still had several observations that remained unexplained, and were left out of the first study. These included SAR signatures of oceanic ISWs consistent with a mode 2 vertical structure, propagating towards the coast near parallel 24°S, and refraction patterns with several IW packets undergoing a near 180° rotation. The first set of observations are exceptionally important, since mode 2 waves were recently predicted to be generated through 'local generation' (Grisouard et al., 2011; Mercier et al., 2012), and such case studies are scarce in the literature – especially those using remote sensing, which can uncover the waves' full two dimensional structure. The second set of observations came to unfold an apparent interaction between ISWs and eddy-like features, which propagate southwards along MC (see Swart et al., 2010). These rotating structures can apparently modify the local vertical structure of the ocean (dynamically and thermodynamically), thus influencing the ISWs usual propagation trajectories.

This short description summarizes the chain of events that represent the PhD's timeframe, together with the main developments and achievements. A detailed discussion of each individual subject is presented in the following chapters.

FRAMEWORK AND MAIN OBJECTIVES

This thesis is intended to provide a state of the art description of several IWs fields located in various study regions. This encompasses the aim to access the various generation and propagation mechanisms, as well as identifying the waves' main characteristics. This fundamental goal is not limited to the ocean, but is rather amplified by the need to better understand the separated dynamics of regions where IWs can coexist simultaneously in the ocean and in the atmosphere. These generic guidelines are supported by the following specific objectives:

1. Provide active contributions to the expansion and development of updated databases with IW observations using remote sensing data at a global scale;

2. Use remote sensing data to obtain synoptic insights into previously unknown hotspot regions for IW observations, both in the ocean and in the atmosphere;

3. Characterize the IW fields from the different study areas in terms of their main characteristics, and spatial and temporal distributions;

4. Attempt to identify and characterize the corresponding generation and propagation mechanisms, by combining knowledge learned from remote sensing data, *in situ* data, and modelling results (e.g. Baines body forcing, 1982);

5. Develop and incorporate new results and techniques into the already existing methodologies for IW investigations.

6. Ultimately, add to the state of the art research in IW fields, and determine their importance in a wider spectrum of geophysical applications.

OUTLINE

This thesis is divided into eight different chapters including a general introduction, six research articles already published or submitted to pear-review indexed journals, and a last section of concluding remarks. The different chapters are organized as follows:

- Chapter 1 consists of a general introduction that summarizes the most important concepts, definitions and properties related with IWs. It also provides a brief historical overview and delineates the main chain of events that render this thesis.

- Chapter 2 presents a summary of the research work developed in MC, which was recently submitted to become part of a book dedicated to remote sensing in the African continent (titled Remote Sensing of the African Seas, edited by Dr. Vittorio Barale from the European Commission's Joint Research Centre, and Dr. Martin Gade from the University of Hamburg). It includes all the investigations and main results for the ISWs propagating in MC, both in the ocean and in the atmosphere. It is to be presented in the foreground (despite being the last work written) since it represents the beginning of these investigations.

- Chapter 3 further extends Chapter 2 by providing the full research article published on the oceanic ISWs of MC. In this section the complete nature of

the observations are discussed, together with their main characteristics. The generation and propagation issues are also addressed in full detail.

- Chapter 4 follows with the research achievements born out of the laboratory experiments performed on ISWs and the 'local generation' mechanism. In this particular case, the author and his supervisor (Prof. José da Silva) had the opportunity to participate in the experimental trials, and bridge the insights gained on the 'local generation' mechanism from remote sensing with the outcomes of the experimental data. Later, the data were processed and analysed by the remaining authors, and our contribution was fundamentally in linking the mode 2 waves found in laboratory with geophysical observations made in satellite data.

- Chapter 5 turns to the Mascarene Ridge, to present the first detailed description of the full two-dimensional structure of some unusually large-scale oceanic ISWs observed in SAR. These waves are observed to propagate in two opposite directions from a sill point between two large banks (Saya de Malha and Nazareth). They are believed to be generated by a large amplitude lee-wave on the west side of the sill, which results from an increased flow upstream of the generation site. Among other characteristics, SAR imagery shows that they are among the biggest ever reported in the literature.

- Chapter 6 presents a research article dedicated to the AGWs observed in the Red Sea region, which aims to understand their dynamical properties in terms of propagation conditions. It also contains a weakly nonlinear wave analysis and discusses the miss-interpretation issues between ISWs radar signatures of oceanic and atmospheric nature.

- Chapter 7 concludes the collection of research articles with a paper dedicated to the IW field observed off the Estremadura Promontory (in the west Iberian Coast). This work includes a statistical analysis of the waves' characteristics and energy properties. It also discusses the likely generation locations, as well as their propagation characteristics.

- Finally, Chapter 8 concludes this thesis by presenting some concluding remarks, a summary of the main achievements, and some suggestions for future work.

Chapter 2

Internal solitary waves system in the Mozambique Channel

Magalhaes, J.M., da Silva, J.C.B., New, A.L., 2011. Internal solitary waves system in the Mozambique Channel. In: Vittorio Barale and Martin Gade (editors) Remote Sensing of the African Seas. Springer. Submitted.

Internal Solitary Waves System in the Mozambique Channel

J. M. Magalhaes[1,2], J. C. B. da Silva[1,2] and A. L. New[3]

[1] CIIMAR, Universidade do Porto, Rua dos Bragas 289, 4050-123 Porto, Portugal.
[2] Department of Geoscience, Environment and Spatial Planning (DGAOT), Rua do Campo Alegre 687, 4169-007 Porto, Portugal.
[3] James Rennell Division (254/21) for Ocean Circulation and Climate, National Oceanography Centre, Southampton, European Way, Southampton SO14 3ZH, UK.

Abstract

Synthetic aperture radar (SAR) satellite imagery (from Envisat and ERS) of the Mozambique Channel (MC) reveals sea surface signatures of oceanic internal solitary waves (ISWs). P.G. Baines (1982) predicted this region to be a major hotspot for the generation of internal tides (ITs) in the ocean. New results now show that the Sofala shelf (located near 20°S, 36°E) is indeed a strong and previously unknown source for the generation of ITs and ISWs. The hotspot area is localized between 20 and 21°S, where the barotropic tidal forcing and tidal transports are highest in the area, due to the particular nature of the bathymetry there. Two distinct types of ISWs are observed to travel offshore, away from the shelf-break, and possible generation mechanisms are discussed. Mode 2 ISWs propagating in the MC are also observed in SAR imagery and we suggest that these may be generated by a tidal beam impinging the thermocline from below, in a similar process to some of the Mode 1 ISWs generated off the Sofala shelf. ISW refraction patterns, often identified in SAR imagery in the MC are presented, and a particular example is shown where ISWs and eddy-like features are seen to interact. The influence of these rotating features in the refraction patterns is briefly discussed. Finally, it is shown that large-scale atmospheric gravity waves of solitary-like form are also frequently observed in the region, and thus care must be taken when discriminating oceanic and atmospheric ISW signatures in SAR images for a correct interpretation to be made.

1.1 Introduction

Internal waves (IWs) are an important element in several processes within geophysical fluid dynamics. They are ubiquitous features in the oceans and atmosphere that can exist in a wide variety of time and space scales, and owe their existence to the vertical density stratification that characterizes both mediums.

In the ocean, tidal flow over irregular bottom topography can force vertical motions at the tidal frequency and generate internal waves of tidal period that propagate along the thermocline and are often referred to as internal tides (ITs). These can then steepen and generate internal waves of shorter period that are usually termed ISWs. The term 'solitary' is used since they tend to occur in individual packets (usually trapped in the troughs of the IT), and have often been identified with the soliton solutions of nonlinear wave theory. In the atmosphere, these short-scale waves that are usually highly nonlinear, can also be identified to propagate in the lower troposphere (typically around altitudes of 3 to 5 km), and are often accompanied by roll-cloud structures that resemble the packet-like structure of their oceanic counter-part. Their origin can be attributed to various generation mechanisms, often involving convection, wind-shear, gravity currents and different air mass collisions. In summary, any atmospheric process leading to the displacement of density surfaces can be a potential source of IWs, providing that suitable propagation conditions are previously met.

During the last few decades remote sensing has played a key role, in providing the scientific community with an increasing number of IW observations (both of oceanic and atmospheric nature). Imaging sensors such as SARs, and visible and near-infrared spectrometers have proved to be particularly useful in proving new and valuable insights into these waves' physical characteristics. These new measuring capabilities that boosted the number of observations led to several studies that indicated that the phenomenon is in fact much more frequent than previously thought (Jackson and Apel, 2002; Jackson, 2004; Jackson, 2007; da Silva and Magalhaes 2009; Magalhaes et al. 2011). SAR in particular has proved very useful in revealing the two dimensional structure of IWs, as well as their spatial and temporal distributions. It is well known that both oceanic and atmospheric internal waves are capable of producing roughness patterns on the ocean surface. Therefore they can generate recognizable signatures in radar images. The oceanic roughness patterns are a result of either hydrodynamic modulation of Bragg waves by surface current gradients or wave damping due to surface films (Alpers, 1985; da Silva et al., 1998). In contrast, the atmospheric internal wave signatures are a consequence of wind stress variability introduced by the disturbed wind velocity field associated with wave propagation (Alpers and Stilke, 1996). SAR imagery has also been playing a key role in indentifying and characterizing several IW hotspots as well as in providing valuable insights into the generation mechanisms (*e.g.* New and da Silva, 2002; Zhao et al., 2004; Vlasenko and Alpers, 2005; Nash and Moum, 2005; Azevedo et al., 2006; da Silva et al., 2007; da Silva and Helfrich, 2008; da Silva and Magalhaes, 2009; da Silva et al., 2009; da Silva et al., 2011; Magalhaes et al., 2011).

IWs can play an important role in several dynamic aspects and in a wide variety of geophysical processes. A more special case of these waves are the solitary waves of finite amplitude and permanent form, which owe their existence to a delicate balance between linear wave dispersion and nonlinear wave steepening. These are usually found in rank-order packets (a consequence of their speed being an increasing function of

amplitude) and they have been observed to travel for considerable amounts of distance without significant changes in form. In turn this is a clear indication that these waves can in fact be responsible for transferring considerable amounts of energy throughout large distances, which is one of the main reasons why they are so important in the dynamics of the coastal oceans and in the lower troposphere.

On the one hand, ISWs in the ocean have been proved to significantly contribute to ocean mixing, either during breaking processes in their final stages of propagation, or due to their highly turbulent character as they propagate along the pycnocline (Pinkel, 2000; Moum et al., 2003; Haren et al., 2005; Lamb and Farmer, 2011). In fact, recent studies have shown that IWs contribute considerably to shelf dynamics in terms of vertical heat fluxes and ocean-shelf mass transports (Shroyer et al., 2010a, 2010b). Mixing due to IWs has also been shown to be important from a biological point of view. Several studies have shown that the dissipation of ISWs may constitute the primary mixing mechanism, and that it may be sufficient to induce strong upward fluxes of nutrients across the thermocline and produce bursts of primary production (Sandstrom and Elliott, 1984; Pingree et al., 1986). Da Silva et al. (2002) also suggested that enhanced primary production could simply occur due to the increase and decrease in available light experienced by phytoplankton during up and downward advection induced by IWs.

On the other hand atmospheric gravity waves (AGWs) have been shown to constitute a serious hazard to aircrafts operating at low altitudes and small speeds (Christie and Muirhead, 1983; Bedard et al., 1986). Some large-scale AGWs may also have a significant role in establishing low-level circulation and determining the vertical structure of wind, temperature and moisture. They can even modify and trigger convective motions and induce significant rain, (Reeder et al., 1995). Their ability to transfer energy and momentum (together with the fact that they propagate for several hundreds of km) makes them an important topic for research, especially since their influence can also extend into weather forecast and climate models.

Furthermore, ISWs can sometimes occur in regions where both mediums (ocean and atmosphere) can support simultaneously propagation. In these cases care should be taken to avoid miss-interpretation. It is also important to recognize that atmospheric internal waves may not always be associated with cloud structures since the ascending branches of the waves may not find the necessary conditions (high moisture in the atmosphere) for condensation to occur (Crook, 1986). In these cases there are no guaranteed methods to discriminate between oceanic and atmospheric wave SAR signatures. However, recent research based on solitary wave and radar imaging theory has provided useful criteria (sometimes with resort to other information on the ocean and atmosphere) to help in the distinguishing process (Alpers and Huang, 2011).

The MC (sometimes referred to as the Strait of Madagascar) is a relative narrow passage centred at 20°S between the African continent (Mozambique) and the island of Madagascar (see Figure 1.1). It extends approximately from the northeast to the southwest for more than 1500 km. The width of the channel is approximately 400 km in the narrowest passages, while at 20°S it reaches a maximum width of about 1000 km. The continental shelves on both sides are generally narrow, and are confined by super critical continental slopes. However, near 20°S the shelf extends further into the ocean for more than 100 km (in the Sofala Bank region, see Figure 1.1 for location) and it is there that the tidal currents are the largest in the MC.

This region is a privileged site for the occurrence of IWs both in the ocean and in the atmosphere. The existence of oceanic IWs is in accord with the study presented by Baines (1982), which estimated tidal energy fluxes from several shelf regions of the world's oceans, and showed that the MC was among the 12 most energetic regions for IT generation. Here, the (semidiurnal) barotropic tidal ranges are over 7 m, and the barotropic currents typically exceed 0.50 ms^{-1} at spring-tides, with significant spring-neap variability. The shelf slope is also supercritical with respect to the M_2 tide, allowing the existence of critical regions for IT generation at the shelf break. Also noteworthy is the fact that the flow in the MC is influenced by large, southward propagating eddies, which feed their waters into the Agulhas Current system, and therefore constitute a major contribution to the overall flow within the channel.

1.2 Oceanic ISWs

1.2.1 Introduction

Tidal energy generated at the shelf-break may radiate away either horizontally in the form of interfacial ITs that propagate along the thermocline, or as internal tidal beams that propagate into the deep stratified ocean below. Therefore, large interfacial ITs may form in the thermocline directly above the shelf break and evolve (through nonlinear processes) to higher-frequency ISWs packets. Another possibility is that the IT energy, which propagates downward into the deep ocean, may give rise to a second generation mechanism known as "local generation" (New and Pingree, 1992; Gerkema, 2001; New and da Silva, 2002; Akylas et al., 2007; da Silva et al., 2007; Grisouard et al., 2011; Mercier et al., 2012). Here, a beam (or ray) of internal tidal energy is generated at "critical" slope regions of the shelf-break where the bottom topographic slope matches the slope of the ray paths, and propagates at an angle (θ) to the horizontal into the deep ocean interior (see equation (1.2.1) where σ is the tidal frequency, f the Coriolis parameter and N the buoyancy frequency). These rays reflect from the seafloor (Pingree and New, 1989, 1991), and interact with the thermocline from below, causing large IT oscillations there, and "locally" generating ISWs (far from the shelf break where the beam is initially generated). We will show clear evidence (based on remote sensing SAR imagery and modelling results) that both generation mechanisms are taking place in the MC, which means that there are waves being formed directly at the shelf-break, and remotely through local generation.

$$\theta = \pm\left(\frac{\sigma^2 - f^2}{N^2 - \sigma^2}\right)^{1/2} \tag{1.2.1}$$

We note that this hypothesis was originally proposed to be the case in the northern Bay of Biscay, where it was studied for the first time, and where SAR imagery helped to clearly distinguish a bimodal distribution of ISWs. This distribution results from the direct generation mechanism near the shelf-break and from the local generation processes taking place some 150 km into the ocean (New and da Silva, 2002). Nonetheless, the widespread occurrence of the local generation hypothesis in other regions of the world ocean has been recently put forward with the contribution of *in situ* and satellite data. In fact, several other studies have emerged since which have also identified locally generated waves. Namely, the southern Bay of Biscay (Azevedo et al., 2006), the Estremadura Promontory (da Silva et al., 2007), and more recently the MC (da Silva et al., 2009), has also been found as a major hotspot region for the local generation mechanism.

1.2.2 SAR evidence of ISWs

Figure 1.2 is a subset of the Envisat ASAR image from 4 December 2009 (centred at 36.26°E, 20.33°S – see Figure 1.1 for location) and corresponds to an area of approximately 77×77 km^2. Several individual solitary waves can be identified as belonging to a packet resulting from direct generation over the shelf. The ISW sea surface signatures that can be identified in the centre of the image are consistent with mode 1 waves of depression. At least 3 individual solitons are already formed in the northeast end of the packet, but their coherence is lost towards the other end. This together with the short wavelengths is an indication that these waves have been recently

formed. Another example of ISWs propagating farther off the Sofala Bank is given in Figure 1.3. This image shows a subset of an Envisat ASAR image (WS mode) dated 7 April 2003 (centred at 36.6°E, 21.3°S – see Figure 1.1 for location), which corresponds to an area of approximately 76×156 km^2. It is a typical example of the local generation mechanism with waves being generated locally and farther off-shelf than the ones shown in the previous example. Three well-developed waves can be clearly distinguished propagating towards the southeast with larger crestlengths compared with those in Figure 1.2 (the first of which with more than 100 km). It can also be seen that these individual waves are organized in a rank-ordered fashion, and that there are brighter bands preceding darker ones in the direction of propagation (a typical feature of mode 1 waves of depression).

Several other examples of ISW signatures have been found in similar images acquired over the MC. A composite map of these examples has been assembled (to be presented in the next section) where it will be clearly seen that (similarly to the Bay of Biscay) there are two distinct concentrations of ISW signatures. These local maxima are consistent with simultaneous generation near the shelf-edge and farther offshore, owing to the local generation mechanism.

1.2.3 Tidal forcing

We now examine the generation issue more closely in order to investigate the most likely locations for the generation of these IWs. To do so the methodology that is usually presented in the literature consists of two main approaches. On the one hand, the Baines (1982) barotropic tidal forcing is often used to search and identify hotspot regions of ISWs within a given study area. It has proved to be a valuable indicator in several other independent studies, particularly to study the possibility of the local generation mechanism. For instance, Azevedo et al. (2006) and da Silva et al. (2007) have used this method to investigate the local generation mechanism in the southern Bay of Biscay (near Cape Finisterre), and in the southern slopes of the Estremadura Promontory (off the west Iberian shelf). In addition, there have been other authors that also used this technique over the last decade, as a valuable indicator of where large ITs may be generated (Colosi et al., 2001, Merrifield and Holloway, 2002; Niwa and Hibiya, 2004). On the other hand, ray-tracing techniques are used to see if the location where ISWs first appear is consistent with the local generation mechanism (i.e. if the first ISW packets appear a few km ahead of the expected impact of an IT beam with the pycnocline). ITs in a continuously stratified ocean can be described by beams or rays that follow characteristic pathways (along which their energy can propagate – see equation (1.2.1)). In other words, this means that when the bottom slopes match the local value of θ (called a critical region) the generation of ITs is more pronounced, particularly if the barotropic currents are strong. In such cases, the direction of the forcing barotropic flow is then coincident with the motion plane for free internal waves, resulting in resonant conditions and enhanced generation of the ITs and ISWs.

The barotropic forcing term (following Baines, 1982) for ITs, resulting from the interaction of bottom topography and tidal flow, can be defined as

$$F = zN^2(z)\int \vec{Q}\, dt.\vec{\nabla}(1/h) \tag{1.2.2}$$

where z is the vertical coordinate (positive upwards), Q is the barotropic mass flux vector $Q=(uh,vh)$ with u and v being the zonal and meridional components of the barotropic velocity, and h is the ocean depth. This means that F can be analytically integrated provided that Q is previously known. For the following calculations, the components of the barotropic velocity vector were taken from the 1/8° resolution OTIS model (Oregon state university Tidal Inversion Software, developed by Egbert and Erofeeva, 2002). The model included the M_2 and S_2 tidal constituents of the barotropic tide since these are the most important in this study region (da Silva et al., 2009). The bathymetry data is part of the one minute global bathymetry from Smith and Sandwell (1997), and N (assumed to be spatially constant) is the same used in da Silva et al. (2009) for the October stratification (see their Figure 2a).

Figure 1.4 shows the tidal ellipses for a complete semi-diurnal tidal cycle corresponding to the image in Figure 1.2 (4 December 2009). These current ellipses, that are needed to calculate Q, were derived using least-squares fits to the data in each grid point. Note that the original outputs do not form perfectly closed ellipses due to the slowly varying nature of the tide. It can be seen that the barotropic tidal currents achieve their biggest values over the continental shelf (in the Sofala Bank region), after crossing the 200 m depth contour. It can also be seen that these are approximately aligned with the bathymetry gradient. This indicates that there will be a strong tidal forcing owing to strong tidal currents passing directly over steep slopes. The magnitudes of these currents (see reference ellipse on the right) can reach relatively large values, some close to $1 ms^{-1}$ farther inside the inner-shelf. However, there is a rapid decrease in the tidal currents towards the open ocean areas that starts immediately after crossing the shelf-break (with an average depth of 50 m). We note in passage that these values over the Sofala Bank are in fact the biggest anywhere within the MC and are among the biggest anywhere in the world.

Figure 1.5 shows the overall maximum of the depth-integrated body force within a complete semi-diurnal tidal cycle for the Sofala Bank area (for the tidal currents computed for 4 December 2009, and shown in Figure 1.4). Together with this 2D body force a composite map of ISWs observations is also shown for ease of interpretation. The dataset used in the composite map contains a total of 6 images acquired from 2003 to 2006, during the southern spring and summer (a complete description may be found in da Silva et al., 2009 – see their Table 1). Note that the present body force map shown in Figure 1.5 was computed for a different day of the ISWs represented in the composite map, but results would remain fairly the same for any other choice of dates. A closer inspection of the body force in Figure 1.5 shows that there are localized regions of maximum forcing coincident with steep slopes and focused along a narrow line (with depths approximately between 100 and 500 m) that is generally along the edge of the continental shelf. The tidal forcing is actually very weak everywhere else (in general) so that the body force values decay rapidly to zero in the shallower areas above 100 m, and in the deep ocean basin that extend farther away into the MC.

The black profile shown in Figure 1.5 that extends approximately perpendicular to the shelf edge from the northwest to the southeast is representative of a section for IT ray-paths (see the inset shown in the lower right corner). The red star marks the position of critical bathymetry along that same profile for the M_2 tidal constituent and using the October stratification used earlier (the same used to calculate F – see Figure 2a in da Silva et al., 2009). The black square is the corresponding reemergence at the thermocline. It can be seen that there are internal tidal beams originating from critical

topography coincident with elevated regions of F that initially slope downward into the ocean interior. The IT beam then reflects upward from the seafloor between 1100 and 1300 m, and reemerges later at the thermocline at about 90 km offshore. Considering the relative positions of the ISWs signatures and the geometry of the IT beam reflection, a region of low activity can be identified near the shelf-break that lies behind the reemergence of IT energy. This region is then followed by another elevated area of ISW activity that closely coincides with the surfacing positions of the IT rays. Similarly to the case in the Bay of Biscay, this suggests that there is a region of elevated forcing near the shelf edge that is simultaneously generating ISWs directly above, and IT rays that are propagating to the deeper ocean, reflecting from the sea floor, and locally generating ISWs some 90 km farther offshore.

1.3 Mode 2 ISWs

1.3.1 Introduction

Cases of satellite observations and *in situ* measurements of mode 2 oceanic ISWs are seldom, and they are hardly ever found in the literature. In fact, despite that they have long been predicted in theory, it was not until recently that they were seen to exist in nature using *in situ* and satellite image data (Farmer and Smith, 1980; Konyaev et al., 1995; Vázquez et al., 2006; Shroyer et al., 2011; da Silva et al., 2011). SAR observations now suggest that mode 2 IWs can be more frequent than previously acknowledged. In this section it will be shown that mode 2 IWs can also be generated in the Mozambique Channel by IT beams with semi-diurnal frequency.

Sea surface signatures of mode 1 and mode 2 ISWs can be unambiguously identified in SAR images provided the waves propagate in relatively deep water (when the lower layer is significantly deeper than mixed layer depth). If interfacial waves (in a two layer system) travelling along the pycnocline are waves of depression (which is often the case in deep waters), then mode 1 ISWs will be revealed in SAR images by bright bands preceding darker ones in their direction of travel (see Alpers, 1985). However, mode 2 ISWs will have exactly the opposite contrast in the SAR, since their radar signature consists of dark bands preceding bright bands in their direction of propagation (see Figure 1.6). This is because surface velocity fields induced by travelling ISWs of different modes can create different convergence and divergence patterns, which then modulate the surface roughness and thus the intensity of the radar backscatter signal. In particular, a mode 2 ISW travelling along the thermocline will generate a divergence pattern at the surface, followed by a convergence pattern in the propagation direction (see Figure 1.6). It is this dynamical feature, which is reversed with respect to mode 1 ISWs that produce the characteristic dark bands ahead of the bright bands in the direction of travel.

Research on mode 2 ISWs generated by IW rays hitting a pycnocline have been recently presented using numerical models and laboratory experiments (Grisouard et al., 2011 and Mercier et al., 2011, respectively). These studies were focused on the local generation mechanism (see Section 1.2), and have also addressed the generation of higher mode waves by IW rays. Grisouard et al. (2011) used a (nonlinear and non-hydrostatic) numerical model and concluded that higher mode ISWs (particularly mode 2) may also be generated by an IW beam hitting a pycnocline at an angle. In their studies, high mode waves are favoured by a strongly stratified pycnocline or, equivalently, by short-wavelength IT beams. Laboratory measurements of ISWs generated by an internal wave beam were presented by Mercier et al. (2011), and are in agreement with the results of Grisouard et al. (2011). Following these numerical and laboratory studies, we will now show satellite observations of mode 2 ISWs, which are consistent with local generation by an IW beam impinging on the ocean pycnoclyne from below.

1.3.2 SAR observations of mode 2 ISWs

Figure 1.7 shows a typical example of a SAR image where two wave trains can be seen to propagate towards the shore (approximately in the west-northwest direction and approximately perpendicular to the local isobaths) in the southern end of the

Mozambique Channel (near parallel 24°S). The left panel shows an ERS-2 SAR image dated 24 September 2001 (acquired at 7:39 UTC), which is centred approximately at 23.75°S and 35.75°E. Note that land and coast lines are also marked in gray areas outlined by a black contour, respectively, and that bathymetry levels for 100 m, 200 m, 500 m and 1000 m are also shown. The black filled circle on the image indicates the predicted position where an IT beam would impinge on the thermocline from below (assumed at an average depth of 50m), and the dashed line indicates its trajectory coming from deeper bathymetry to the east (passing through the centre and taken perpendicular to the wave crests). The right hand side of Figure 1.7 shows a vertical section which is aligned and partially coincident with the black dashed line on the left, together with a simulated IT beam of semi-diurnal frequency based on local stratification. The arrow indicates the direction of energy propagation and the inset shows the geographic location of the observation (the star in the inset denotes the geographic location of the image centre).

The SAR image shown in Figure 1.7 reveals that the ISWs in the deeper wave packet are characterized by the usual rank-ordered bright and dark bands of radar intensity, which decrease in amplitude from the front to the rear. However, while these signatures look like many other typical SAR signatures of ISWs, it can be seen that in this case the contrast pattern is reversed in relation to the general pattern. Here, dark bands precede bright bands in the propagation direction, indicating that these radar signatures are consistent with mode 2 internal waves (see schematics shown in Figure 1.6 for mode 2 ISWs). Another important characteristic of this image is that it shows the ISWs to appear close to (but in front of) the surfacing position of predicted IT rays of semi-diurnal frequency (with M_2 tidal constituent), generated at the critical slopes farther east. This strongly suggests that these mode 2 ISWs are generated locally after the impact of an IT beam in the pycnocline from below. We note that this is in agreement with the numerical and laboratory studies done by Grisouard et al. (2011) and Mercier et al. (2011), respectively, since they too predicted the possibility of ISWs with higher mode structures being “locally generated”.

1.3.3 Comparison of average propagation speeds with theory

To reinforce the hypothesis that the observed ISWs in Figure 1.7 are of mode 2, we will also estimate an average phase speed from the SAR image, and compare it with a theoretical model. To do so the Taylor–Goldstein (TG) model is used, which is solved numerically to investigate the propagation speeds of the lowest IT modes (see e.g. Kundu and Cohen, 2004). For the MC case, we have assumed a semi-diurnal frequency for the IT with a M_2 tidal constituent (with $\sigma = 1.4 \times 10^{-4}$ rad.s^{-1}), and a mean density profile typical for the southern winter stratification (namely October, see Figure 2a of da Silva et al, 2009). Based on Figure 1.7, we also considered an average ocean depth of 300 m to the west of the ISWs along their apparent propagation path (region between the two consecutive packets that are observed in the SAR). Additionally, we assumed that the two packets in Figure 1.7 were generated at the same phase of the tide and at the same position – that is near the impact point of the internal tide beams with the pycnocline. Under those assumptions, and considering that the two ISW packets in the SAR are separated along their apparent propagation path by an average distance of 13 km (see black arrow on top of left panel in Figure 1.7), the estimated phase speed of the mode 2 ISWs in the SAR is 0.3 m/s. On the other hand, the TG model assuming an

average depth of 300 m predicts linear phase speeds of 0.4 and 1.0 m/s for mode 2 and mode 1 linear IWs of tidal frequency, respectively. This further suggests that the waves in Figure 1.7 are indeed mode 2 waves, since both signatures (discussed in section 1.3.2) and phase speeds are concordant with a mode 2 vertical structure.

1.4 Eddy-like structures and IW refraction

Da Silva et al. (2009) reported that on some occasions ISWs in the MC (off the Sofala Bank – see Figure 1.1 for location) were observed farther to the south than the average pattern. In their study, the seasonal variability of currents during the southern winter was the plausible explanation for this ISWs propagation anomaly. To justify this seasonal variability they referred to the work done by Maltrud et al. (1998), who believed that the Mozambique Current (which flows southward along the western slopes of the basin) was much stronger during the austral winter. Based on the knowledge of the Mozambique Current available at that time, da Silva et al. (2009) then proposed that the increased southward flow in the southern winter months could explain why some ISWs were refracted (or advected) towards more southerly pathways at that time of year. However, more recent research (Ridderinkhof et al., 2010; Ullgren et al., 2011) indicates that the MC currents are in fact highly variable, which is mainly due to the presence of eddy-like features that originate in the Indian Ocean and travel southwards throughout the MC. In this section we will show an example of ISWs propagating through eddy-like structures (which are observed in altimetry data) and undergoing dramatic refraction patterns.

Figure 1.8 shows a map of ISWs based on our interpretation of an Envisat-ASAR image (WS mode), acquired on 4 December 2009 at 20:07 UTC, that is centred approximately at 21.0°S and 36.3°E. For clearance two types of wave packets (discussed earlier in Section 1.2) where marked with 'SG' for shelf-generation and 'LG' for local generation), until they reach 21.5 °S. This is because further south of 21.5 °S along their trajectory, the interpretation of the sea surface signatures starts to become ambiguous, mainly due to dissipation, interactions with currents and winds, and interaction among different ISW packets. We note that, this interpretation is further reinforced if the average propagation speeds of the several packets are taken into account. Indeed, according to Silva et al. (2009) the average phase speeds of these waves were found to be around 1.5 ms^{-1}, and the same values can also be found for the sequences SG1, SG2, and SG3, and LG1 and LG2 based on distances measured in the SAR. The map in Figure 1.8 also displays Sea Surface Height (SSH) anomalies taken from altimetry data (SSALTO DUACS data products available online at http://www.aviso.oceanobs.com), where different colours and dashed quasi-circular lines are used to indicate the presence of eddy-like features observed at approximately the same time as the SAR image (4 December 2009 at 00:00 UTC, the closest product available in time). The blue and red curves refer to negative and positive SSH anomalies, respectively, and a green line has been drawn for reference indicating the boundary between them (an apparent reference level). There are tangential surface currents associated to these SSH anomalies, whose rotation directions are indicated by arrows in Figure 1.8. These currents can be rather large in the MC (as large as 0.5 m/s according to Swart et al., 2010, and thus of the order of the ISWs propagation speeds) and their influence can extend in diameter for some 200 km. In terms of vertical sections the SSH anomalies are associated with isopycnical deformations, which are in general in the opposite way to the surface displacements. From Figure 1.8 it is clear that the eddy-like features associated to the SSH anomalies interfere with the propagation of the ISWs, apparently causing an overall refraction pattern. This will be briefly discussed in the next paragraph.

In the southern hemisphere eddies with an anti-clockwise rotation are warm eddies, whose SSH anomalies are positive at the surface but are characterized by bowl-like (or bulge) downward displacements of their isopycnicals at depth (isopycnicals can be displaced some 100m downwards or more at the core of a warm eddy near the pycnocline). On the other hand, cold eddies spin in the clockwise direction, which are characterized by negative SSH anomalies, and have their isopycnicals displaced upwards near the core. This means that the eddy-like features identified in Figure 1.8 are those of a cold eddy just off the Sofala Bank (in blue), and a warm eddy somewhat farther south and offshore (in red). It can be seen that the ISW crests showed in Figure 1.8 are clearly interacting with the eddy structures that were measured in the SSH data. First the cold eddy closer to the shelf and afterwards the warm eddy farther offshore (and southwards of the cold eddy) are located directly along the ISWs path. Note that the sequence of ISW crests shown in Figure 1.8 also exhibits what appears to be a clockwise rotation pattern. In fact, the packets labelled SG1, SG2, LG1, SG3 and LG2 (forming a chronological sequence) progressively propagate more to the south and less to the east, until they reverse the component of east-west propagation velocity and return back on to the shore, undergoing a near 135° clockwise rotation. In this interpretation we considered that the ISW crest sequence mentioned above is progressively older in time, with respect to their generation sites and propagation paths. We believe that the pattern of ISWs rotating clockwise in their direction of propagation is essentially caused by interaction with the near-surface currents produced by eddies. However, refraction may also be caused (at least to some extent) by different stratifications and mixed layer depths resulting from the relative positions of eddies along the ISWs propagation pathways. The latter effect has been explained successfully by Sherwin et al. (2002) off the northern Portuguese shelf (in the west Iberian Coast), where refraction of ISWs occurs basically due to an offshore downward tilt of the isopycnicals. In the Iberian case, similarly to the MC, ISWs were first found to propagate in an off-shelf direction and then refract back onto the coast some 50 km north of their generation site (roughly the same distance that ISWs need in the MC to refract back to shore).

1.5 AGWs in the MC and oceanic ISW look-alikes

In the previous sections we have clearly shown that the MC is a hotspot for oceanic IWs, which adds to the idea that these features represent ubiquitous phenomena in the world ocean. However, the MC is also a region where atmospheric IWs are frequently observed, being amongst the largest (in terms of spatial scales and crestlengths) observed anywhere in word (da Silva and Magalhaes, 2009).

A particular case of large-scale AGWs propagating in the MC can be found in Figure 1.9, where we present a RGB image from Envisat-MERIS dated 16 September 2004, acquired at 07:15 UTC. The image covers an area of about 580×660 km^2 in the southwest part of the MC, and it is centred near 20.4°S and 38.0°E. A large-scale AGW can be seen travelling southwest towards the south end of the MC, in the centre of the image (labeled L). The crestlength of the leading wave, in this case, extends for more than 500 km and its crest-to-crest spatial scale is approximately 10 km on average. It is interesting to note that several of these individual waves are made visible by characteristic cloud bands, which have considerable lateral extensions and uniform cross-sections.

Satellite imagery (mainly SAR, visible and near infrared) exhibiting these large-scale AGWs are a regular occurrence in the MC, particularly between July and October when they are more frequently observed. Satellite data such as MODIS, MERIS and ENVISAT ASAR in Wide Swath (WS) mode has been used to characterize the horizontal structure of these AGWs, which have mean dispersive wavelengths between 3.5 and 8.5 km, mean crestlengths of 443 km, and propagation speeds that can exceed 10 ms^{-1}. Two preferential pathways were found to dominate the AGWs, which propagate mainly to northeast (form the south end of the MC) and to southwest (coming from Madagascar). It was also found that high pressure systems born in the Polar Regions (known as Moving Polar Highs, MPHs), which are associated with air subsidence in the MC, can play a major influence on the propagation of these waves. This is because MPHs change the atmosphere's stability, which enables its vertical structure to form suitable waveguides necessary for AGWs to propagate, and can even trigger their generation (see da Silva and Magalhaes, 2009 for a detailed study).

The sea surface signatures of the AGWs in the MC can usually be distinguished from their oceanic counter parts (discussed in Sections 1.2 to 1.4) due to their large dimensions (wavelength and crestlength). However, in many cases, other smaller-scale AGWs can also be found to propagate across the MC, including those areas where oceanic ISWs are frequently present (e.g. see composite map in Figure 1.5). A good example is the MERIS image in Figure 1.9 where a small-scale AGW (labeled S, and smaller than the largest packet labeled L) is seen to travel southeast, in an almost perpendicular direction to the larger-scale AGW (labeled L) that is travelling southwest. In fact, this observation is very similar to the oceanic ISWs presented in Section 1.2 since it has the same main characteristics (namely, spatial scales, crests orientation, propagation direction and geographic location).

Care should be taken when interpreting sea surface manifestations of internal waves in SAR (as mentioned in Section 1). SAR images cannot detect the presence of cloud structures, which would clearly indicate the atmospheric nature of AGWs. On the other hand, clouds may not form at all in the presence of large amplitude AGWs, since the ascending branches of the waves may not meet the necessary moisture for condensation to occur. In fact, Figure 1.9 shows that some of the solitary waves in the trailing edge of the large packet (labeled L) are only partially recognizable as clouds – the remaining segments are merely seen as sea surface patterns of banded roughness on

a smoother background. In such cases, alternative methodologies should be taken under consideration to discriminate between oceanic and atmospheric internal waves. A detailed discussion of these issues can be found in the work presented by Alpers and Huang (2011), where lists of discriminating criteria were presented based on soliton and SAR theory, and further complemented by additional information on the ocean and atmosphere.

1.6 Summary

This chapter describes remote sensing data from SARs and image spectrometers to clearly show that the MC is a hotspot for observing ISWs in the ocean and in the atmosphere. Oceanic ISWs have been found to be generated directly off the shelf by steepening of an interfacial tidal wave and through a different generation mechanism by which the impact of a tidal beam from below the thermocline generates ISWs, known as local generation of ISWs. Both mechanisms are associated with an elevated region of body forcing near the Sofala Bank, which results from strong barotropic tidal currents interacting with critical slopes. SAR imagery has also revealed that the MC is a preferential region for observing other IW phenomena such as mode 2 ISWs and refraction patterns. The data suggests that the mode 2 ISWs have also been generated by tidal beams, similarly to some of the mode 1 waves observed in the SAR. This confirms some conclusions drawn from other independent studies using modeling and laboratory experiments (Grisouard et al., 2011 and Mercier at al., 2011, respectively) about the origin of mode 2 solitary-like waves by tidal beams. The refraction patterns in SAR revealed that it is likely that ISWs in the MC frequently interact with oceanic features such as eddy-like structures, which propagate year-round through the MC and affect the local vertical structure of the ocean. Large-scale AGWs are also a ubiquitous feature in the MC, especially from July to October, and care should be taken to avoid miss-interpretations in SAR with oceanic ISWs.

1.7 References

Akylas, T.R., Grimshaw, R.H.J., Clark, S.R., Tabaei, A., 2007. Reflecting tidal wave beams and local generation of solitary waves in the ocean thermocline. J. Fluid Mech. 593, 297-313. doi:10.1017/S0022112007008786.

Alpers, W., 1985. Theory of radar imaging of internal waves. Nature (London) 314, 245-247. doi:10.1038/413245a0.

Alpers, W., Stilke, G., 1996. Observations of a nonlinear wave disturbance in marine atmosphere by synthetic aperture radar aboard the ERS 1 satellite. J. Geophys. Res. 101, 6512-6525.

Alpers, W., Huang, W., 2011. On the Discrimination of Radar Signatures of Atmospheric Gravity Waves and Oceanic Internal Waves on Synthetic Aperture Radar Images of the Sea Surface. IEEE Transactions on Geoscince and Remote Sensing 49 (3), 1114-1126.

Azevedo, A., da Silva, J.C.B., New, A.L., 2006. On the generation and propagation of internal waves in the southern Bay of Biscay. Deep-Sea Res. I 53, 927941. doi:10.1016/j.dsr.2006.01.013.

Baines, P.G., 1982. On internal tides generation models. Deep-Sea Res. Part A 29, 307-338. doi:10.1016/0198-0149(82)90098-X.

Bedard, A.J., Canavero, F., Einaudi, F., 1986. Atmospheric gravity waves and aircraft turbulence encounters. J. Atmos. Sci. 43 (23), 2838-2844.

Colosi, J.A., Beardsley, R.C., Lynch, J.F., Gawarkiewicz, G., Chiu, C.-S., Scotti, A., 2001. Observations of nonlinear internal waves on the outer New England continental shelf during the summer Shelfbreak Primer study. J. Geophys. Res. 106 (C5), 9587-9601. doi:10.1029/2000JC900124.

Christie, D.R., Muirhead, K.J., 1983. Solitary waves: a hazard to aircraft operating at low altitudes. Aust. Met. Mag. 31, 97–109.

Crook, A.N., 1986. The effect of ambient stratification and moisture on the motion of atmospheric undular bores. J. Atmos. Sci. 43(2),171-181.

da Silva, J.C.B., Magalhaes, J.M., 2009. Satellites observations of large atmospheric gravity waves in the Mozambique Channel. Int. J. Rem. Sens. 30 (5), 1161–1182.

da Silva, J.C.B., Ermakov, S.A., Robinson, I.S., Jeans, D.R.G., Kijashko, S.V., 1998. Role of surface films in ERS SAR signatures of internal waves on the shelf. 1. Short-period of internal waves. J. Geophys. Res. 103 (C4), 8009-8031. doi:10.1029/97JC02725.

da Silva, J.C.B., New, A.L., Srokosz, M., Smyth, T., 2002. On the observability of internal tidal waves in remotely-sensed ocean color data. Geophys. Res. Lett. 29 (12), 1569-1572. doi:10.1029/2001GL013888.

da Silva, J.C.B., New, A.L., Azevedo, A., 2007. On the role of SAR for observing "Local Generation" of internal solitary waves off the Iberian Peninsula. Can. J. Remote Sensing 33, 388-403. doi:10.5589/m07-041.

da Silva, J.C.B., Helfrich, K.R., 2008. Synthetic Aperture Radar observations of resonantly generated internal solitary waves at Race Point Channel (Cape Cod). J. Geophys. Res. 113, C11016. doi:10.1029/2008JC005004.

da Silva, J.C.B., New, A.L., Magalhaes, J.M., 2009. Internal solitary waves in the Mozambique Channel: observations and interpretation. J. Geophys. Res. 114, C05001. doi:10.1029/2008JC005125.

da Silva, J.C.B., New, A.L., Magalhaes, J.M., 2011. On the structure and propagation of internal solitary waves generated at the Mascarene Plateau in the Indian Ocean. Deep-Sea Res. I 58, 229-240. doi:10.1016/j.dsr.2010.12.003.

Egbert, G.D., Erofeeva, S.Y., 2002. Efficient inverse modeling of barotropic ocean tides. J. Oceanic Atmos. Technol. 19, 183-204. doi:10.1175/1520-0426(2002)019<0183:EIMOBO>2.0.CO;2.

Farmer, D.M., Smith, J.D., 1980. Tidal interaction of stratified flow with a sill in Knight Inlet. Deep-Sea Res. 27A, 239-254.

Gerkema, T., 2001. Internal and interfacial tides: beam scattering and local generation of solitary waves. J. Mar. Res. 59, 227-255. doi:10.1357/002224001762882646.

Grisouard, N., Staquet, C., Gerkema, T., 2011. Generation of internal solitary waves in a pycnocline by an internal wave beam: a numerical study. J. Fluid Mech. 676, 491-513. doi:10.1017/jfm.2011.61.

van Haren, H., Groenewegen, R., Laan, M., Koster, B., 2005. High sampling rate thermistor string observations at the slope of Great Meteor Seamount. Ocean Sci. 1, 17-28. doi:10.5194/os-1-17-2005.

Jackson, C.R., 2004. An atlas of internal solitary-like waves and their properties. Second edition. Available online at: www.internalwaveatlas.com (accessed 07 January 2010).

Jackson, C.R., 2007. Internal wave detection using the moderate resolution imaging spectroradiometer (MODIS). J. Geophys. Res. 112, C11012. doi:10.1029/2007JC004220.

Jackson, C.R., Apel, J.R., 2002. An atlas of internal solitary-like waves and their properties. First edition. Available online at: www.internalwaveatlas.com (accessed 07 January 2010).

Konyaev, K.V., Sabinin, K.D., Serebryany, A.N., 1995. Large-amplitude internal waves at the Mascarene ridge in the Indian Ocean. Deep Sea Res. Part I, 42, 2075-2091. doi:10.1016/0967-0637(95)00067-4.

Lamb, K.G., Farmer, D., 2011. Instabilities in an Internal Solitary-like Wave on the Oregon Shelf. J. Phys. Oceanogr. 41, 67-87. doi:10.1175/2010JPO4308.1.

Magalhaes, J.M., Araújo, I.B., da Silva, J.C.B., Grimshaw, R.H.J., Davis, K., Pineda. J., 2011. Atmospheric gravity waves in the Red Sea: a new hotspot. Nonlin. Processes Geophys. 18, 71-79. doi:10.5194/npg-18-71-2011.

Maltrud, M.E., Smith, R.D., Semtner, A.J., Malone R.C., 1998. Global eddy-resolving ocean simulations driven by 1985–1995 atmospheric winds. J. Geophys. Res. 103, 30,825–30,853. doi:10.1029/1998JC900013.

Mercier, M.J., Mathur, M., Gostiaux, L., Gerkema, T., Magalhaes, J.M., da Silva, J.C.B., Dauxois, T., 2012. Soliton generation by internal tidal beams impinging on a pycnocline : laboratory experiments. J. Fluid Mech., accepted.

Merrifield, M.A., Holloway, P.E., 2002. Model estimates of M2 internal tide energetics at the Hawaiian Ridge. J. Geophys. Res. 107 (C8), 3179. doi:10.1029/2001JC00996.

Moum, J.N., Farmer, D.M., Smyth, W.D., Armi, L., Vagle, S., 2003. Structure and generation of turbulence at interfaces strained by internal solitary waves propagating shoreward over the continental shelf. J. Phys. Oceanogr. 33, 2093-2112. doi:10.1175/1520-0485(2003)033<2093:SAGOTA>2.0.CO;2.

Nash, J.D., Moum, J.N., 2005. River plumes as a source of large-amplitude internal waves in the coastal ocean. Nature 437, 400-403. doi:10.1038/nature03936.

New, A.L., Pingree, R.D., 1992. Local generation of internal soliton packets in the central Bay of Biscay. Deep-Sea Res. Part A 39, 1521-1534. doi:10.1016/0198-0149(92)90045-U.

New A.L., da Silva, J.C.B., 2002. Remote-sensing evidence for the local generation of internal soliton packets in the central Bay of Biscay. Deep-Sea Res. I 49, 915-934. doi:10.1016/S0967-0637(01)00082-6.

Niwa, Y., Hibiya, T., 2004. Three-dimensional numerical simulation of M2 internal tides in the East China Sea. J. Geophys. Res. 109 (C4), C04027. doi:10.1029/2003JC001923.

Pingree, R.D., New, A.L., 1989. Downward propagation of internal tidal energy into the Bay of Biscay. Deep Sea Res. Part A, 36, 735-758. doi:10.1016/0198-0149(89)90148-9.

Pingree, R.D., New, A.L., 1991. Abyssal penetration and bottom reflection of internal tidal energy in the Bay of Biscay. J. Phys. Oceanogr. 21, 28-39. doi:10.1175/1520-0485(1991)021<0028:APABRO>2.0.CO;2.

Pingree, R.D., Mardell, G.T., New, A.L., 1986. Propagation of internal tides from the upper slopes of the Bay of Biscay. Nature 312, 154-158. doi:10.1038/321154a.

Pinkel, R., 2000. Internal solitary waves in the warm pool of the western equatorial pacific. J. Phys. Oceanogr. 30, 2906-2926. doi:10.1175/1520-0485(2001)031<2906:ISWITW>2.0.CO;2.

Reeder, M.J., Christie, D.R., Smith, R.K., Grimshaw, R.H.J., 1995. Interacting Morning Glories over Northern Australia. Bull. Amer. Met. Soc. 76, 1165-1171.

Ridderinkhof, H., van der Werf, P.M., Ullgren, J.E., van Aken, H.M., van Leeuwen, P.J., de Ruijter, W.P.M., 2010 Seasonal and interannual variability in the Mozambique

Channel from moored current observations. J. Geophys. Res. 115, C06010. doi:10.1029/2009JC005619.

Sandstrom, H., Elliott, J.A., 1984. Internal tide and solitons on the Scotian Shelf: a nutrient pump at work. J. Geophys. Res. 89 (C4), 6415-6426. doi:10.1029/JC089iC04p06415.

Sherwin, T.J., Vlasenko, V.I., Stashchuk, N., Jeans, D.R.G., Jones, B., 2002. Along-slope generation as an explanation for some unusually large internal tides. Deep-Sea Res. I 49, 1787-1799. doi:10.1016/S0967-0637(02)00096-1.

Shroyer E.L., Moum, J.N., Nash, J.D., 2010a. Vertical heat flux and lateral mass transport in nonlinear internal waves. Geophys. Res. Lett. 37, L08601. doi:10.1029/2010GL042715.

Shroyer, E.L., Moum, J.N., Nash, J.D., 2010b. Energy transformations and dissipation of nonlinear internal waves over New Jersey's continental shelf. Nonlinear Processes Geophys. 17, 345-360. doi:10.5194/npg-17-345-2010.

Shroyer, E.L., Moum, J.N., Nash, J.D., 2011. Nonlinear internal waves over New Jersey's continental shelf. J. Geophys. Res. 116, C03022. doi:10.1029/2010JC006332.

Smith, W.H.F., Sandwell, D.T., 1997. Global sea floor topography from satellite altimetry and ship depth soundings. Science 277 (5334), 1956-1962. doi:10.1126/science.277.5334.1956.

Swart, N. C., Lutjeharms, J.R.E., Ridderinkhof, H., de Ruijter, W.P.M., 2010. Observed characteristics of Mozambique Channel eddies. J. Geophys. Res. 115, C09006. doi:10.1029/2009JC005875.

Ullgren, J., van Aken, H., Ridderinkhof, H., 2010. Unique measurements of ocean currents east of Africa. NIOZ Annual Report 2010, 21-22.

Vázquez, A., Stashchuk, N., Vlasenko, V., Bruno, M., Izquierdo, A., Gallacher, P.C., 2006. Evidence of multimodal structure of the baroclinic tide in the Strait of Gibraltar. Geophys. Res. Lett. 33, L17605. doi:10.1029/2006GL026806.

Vlasenko, V., Alpers, W., 2005. Generation of secondary internal waves by the interaction of an internal solitary wave with an underwater bank. J. Geophys. Res. 110, C02019. doi:10.1029/2004JC002467.

Zhao, Z., Klemas, V., Zheng, Q., Yan, X.-H., 2004. Remote sensing evidence for the baroclinic tide origin of internal solitary waves in the northeastern South China Sea. Geophys. Res. Lett. 31, L06302. doi:10.1029/2003GL019077.

Figures

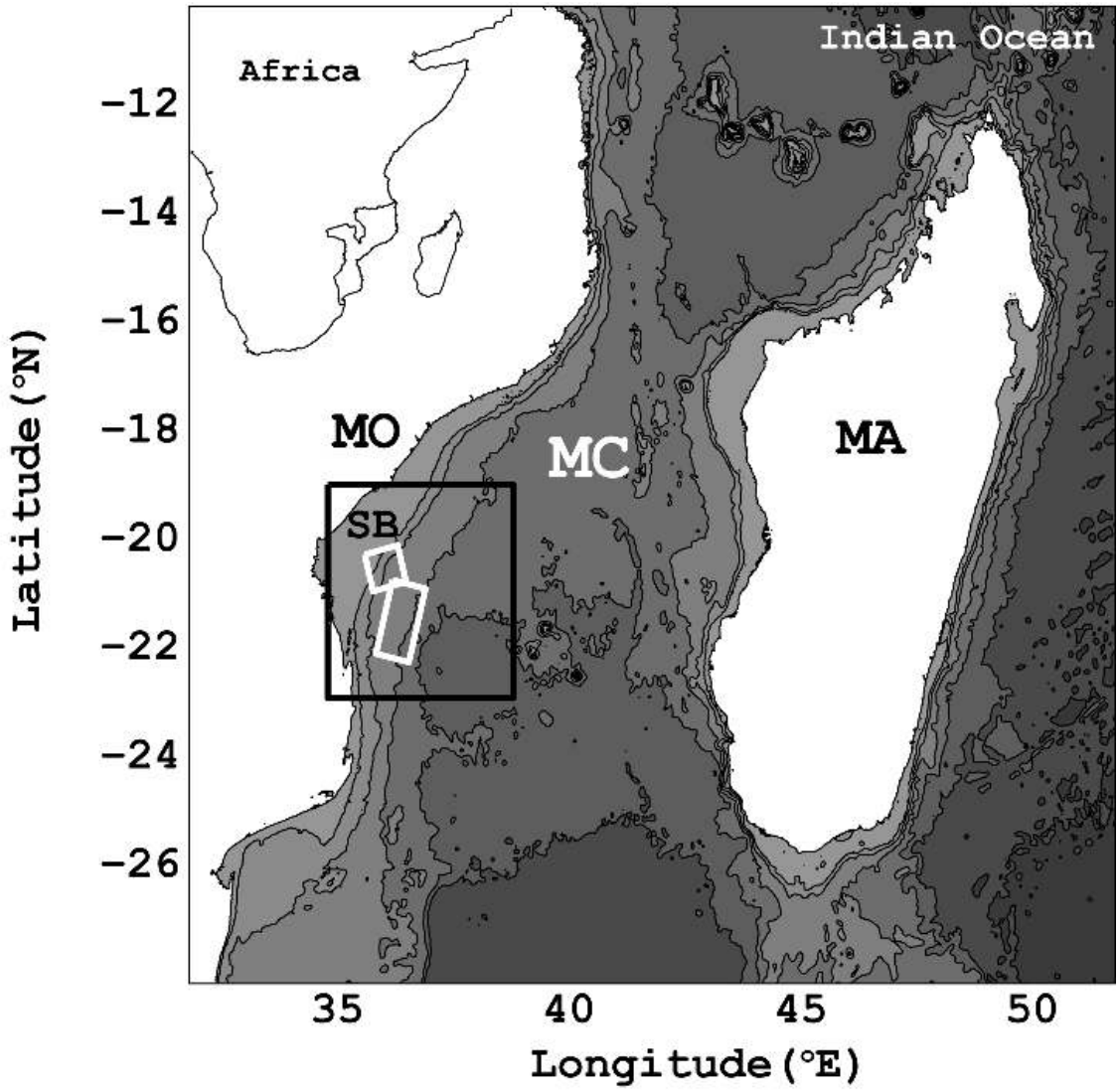

Fig. 1.1 Detailed bathymetry and location of the Mozambique Channel (labelled MC) in the southwest Indian Ocean. The labels MO and MA stand for Mozambique and Madagascar, respectively, and a reference location for the Sofala Bank is labelled SB. The inset in the top-right corner shows the locations of Mozambique and Madagascar in relation to the African continent. White areas represent land and black contours with grey areas mark isobaths for 200, 1000, 2000, 3000 and 4000 m. The white rectangular frames delineate the area surveyed in the SAR images shown in Figures 1.2 and 1.3.The black rectangular frame is shown for reference and outlines the detailed area in Figures 1.4 and 1.5.

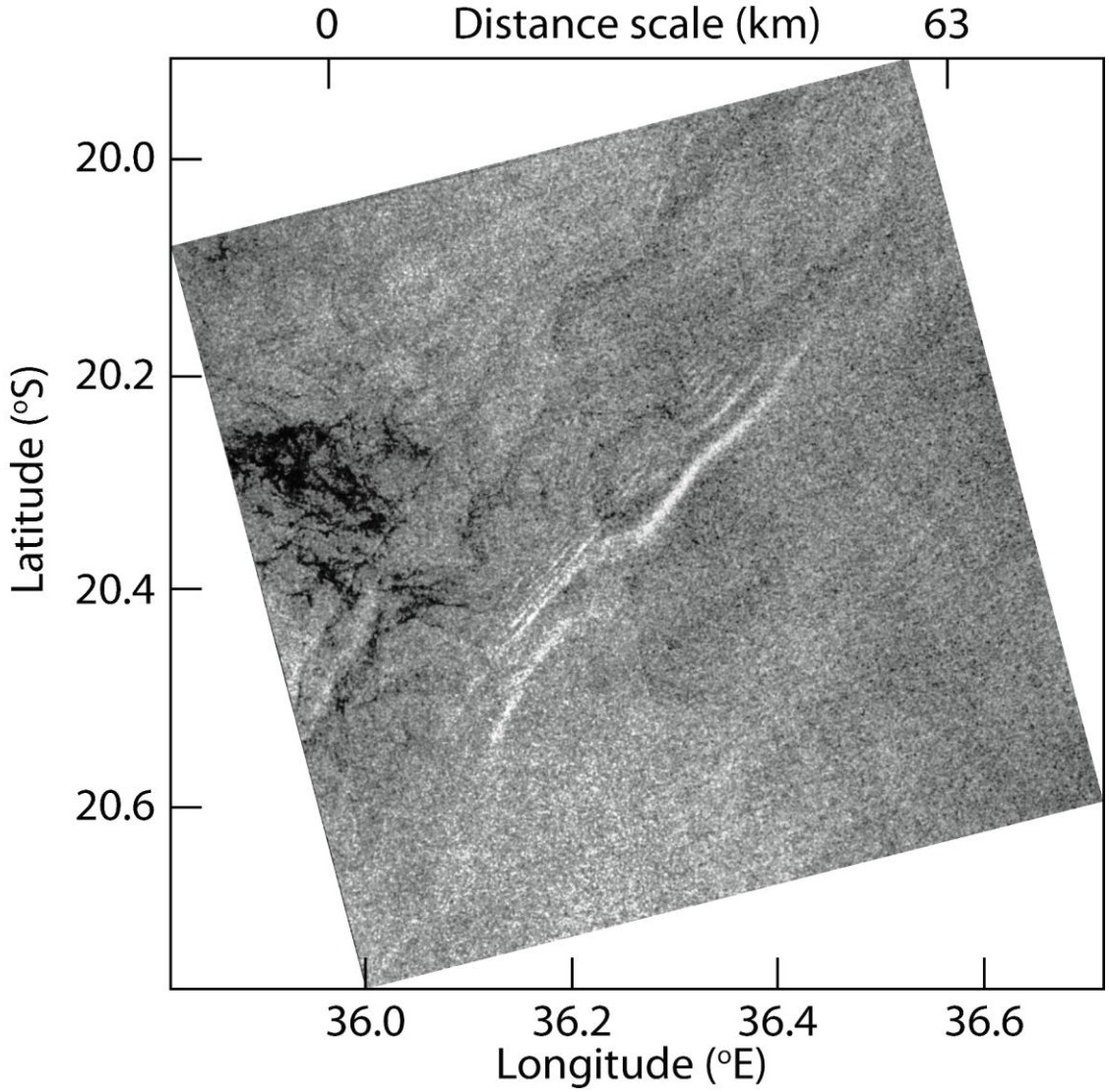

Fig. 1.2 Subset of an Envisat-ASAR image (WS mode) showing a case of an ISW packet generated directly over the shelf. The image is dated 4 December 2009 and was acquired at 20h07m UTC. It is centred approximately at 36.26°E, 20.33°S, with an area of about 77x77 km^2 to the east of Mozambique, which is outlined in Figure 1.1 by the white square line.

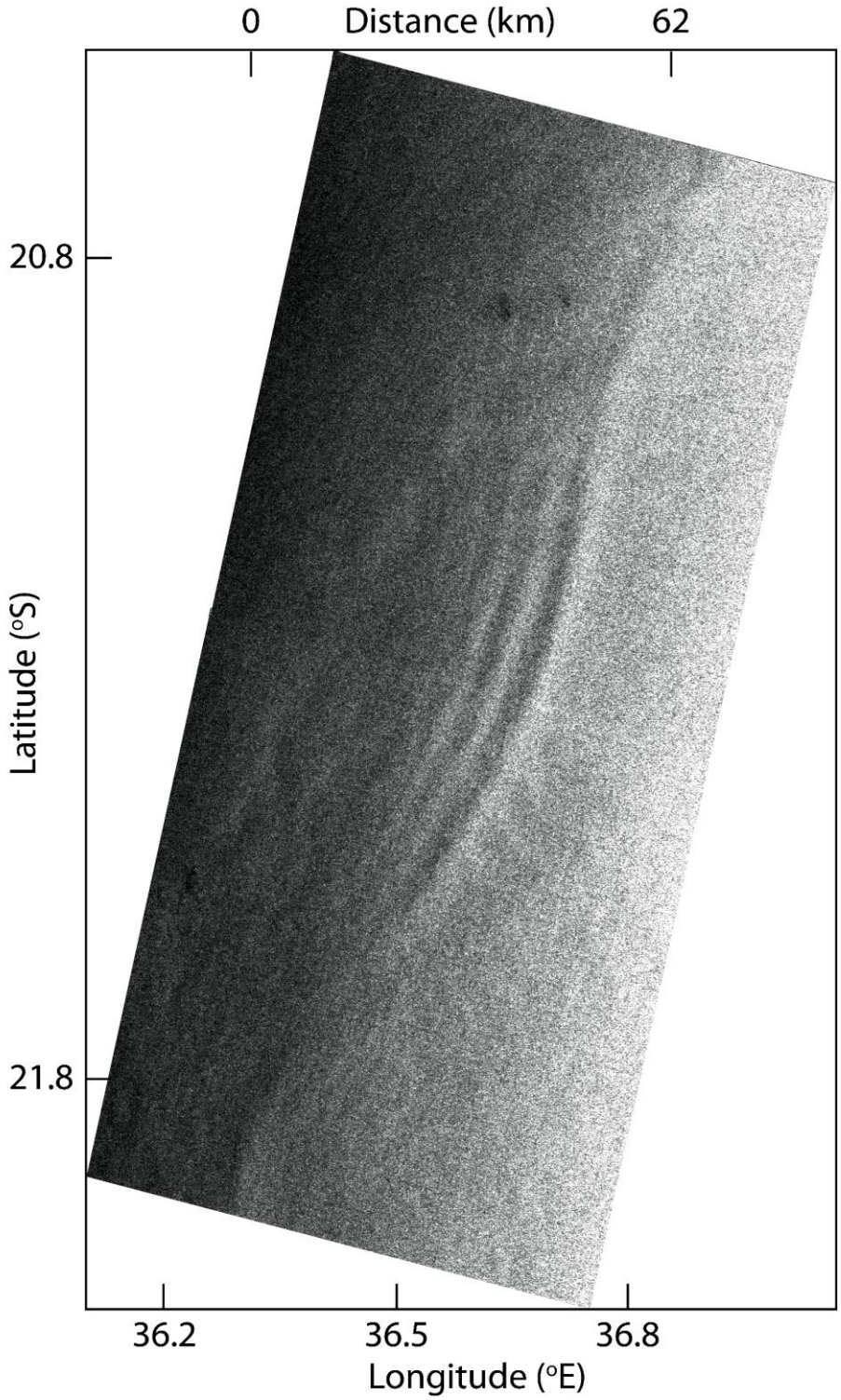

Fig. 1.3 Subset of an Envisat-ASAR image (WS mode) showing a typical case of locally generated ISWs. The image is dated 7 April 2003 and was acquired at 07h09m UTC. It is centred approximately at 36.6°E, 21.3°S, with an area of about 76x156 km^2 to the east of Mozambique, which is outlined in Figure 1.1 by the white rectangle.

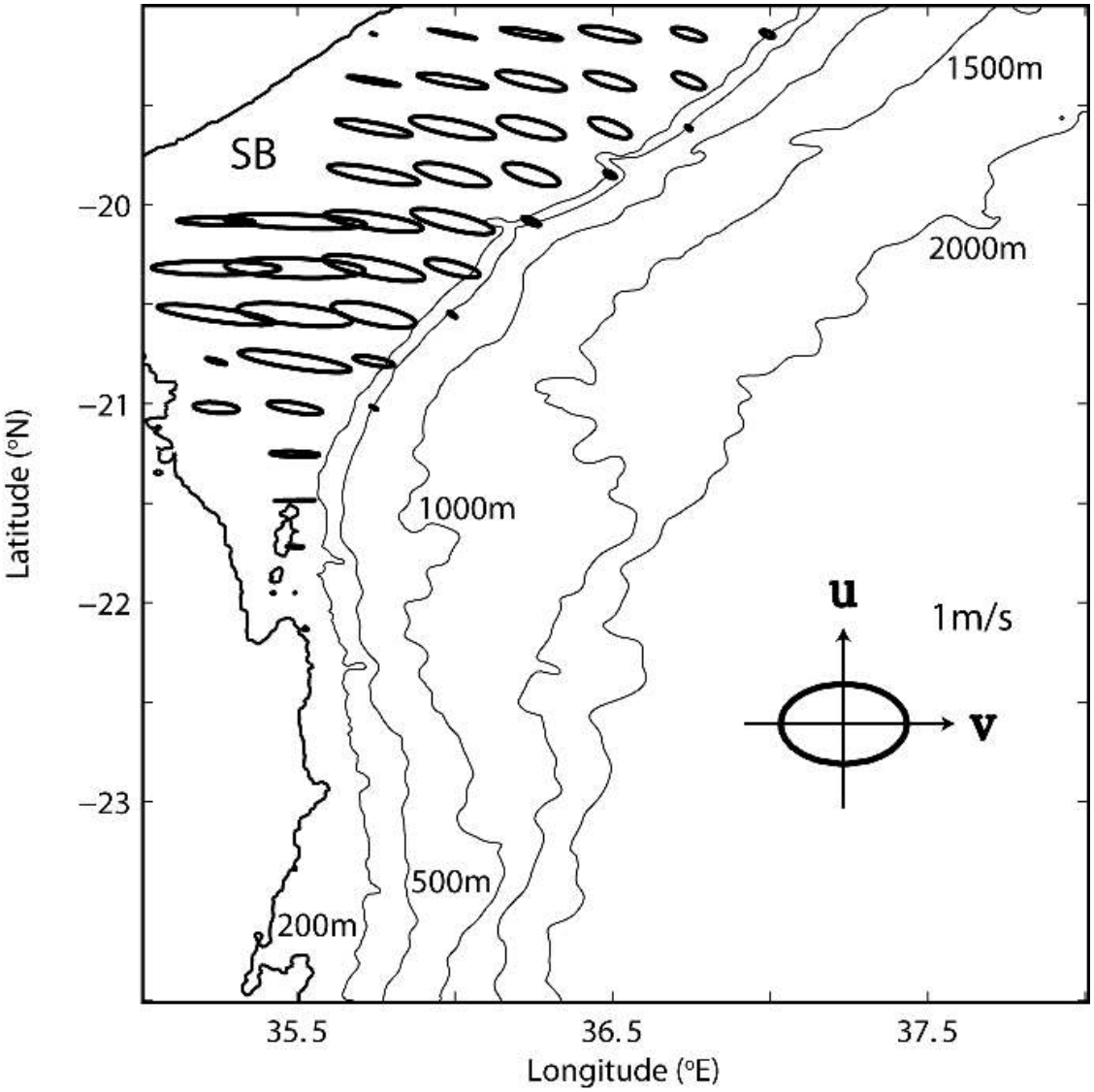

Fig. 1.4 Detailed bathymetry of the area outlined by the black rectangle in Figure 1.1 together with ellipse tidal currents for the date of the image in Figure 1.2 (4 December 2009). A reference ellipse is shown on the right-hand side (with both axes representing a speed of 1 ms^{-1}). For clarity ellipses with axes below 0.05 ms^{-1} are not represented. Depth contours are also shown in meters (starting at 200m, 500m, 1000m, 1500m and 2000m). A reference location for the Sofala Bank is labelled SB.

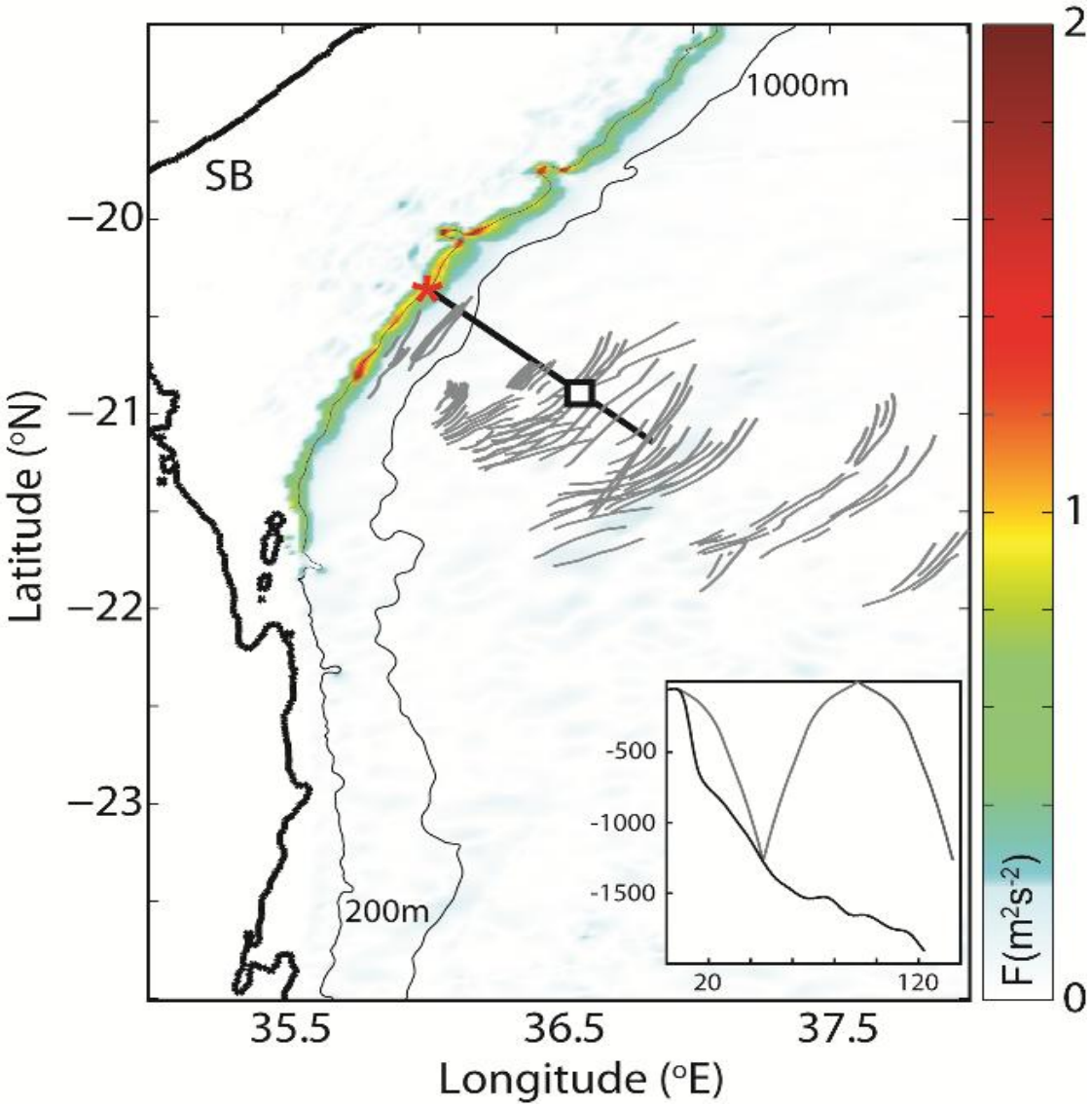

Fig. 1.5 Maxima of Baines (1982) depth-integrated body force (F) over a complete tidal cycle, calculated using Equation (1.2.2) for 4 December 2009 (same date as Figure 1.2 and 1.4). The area shown corresponds to the black rectangle in Figure 1.1. A reference location for the Sofala Bank is labelled SB. The coastline is marked by a black contour and the thin lines are the 200 m and 1000 m isobaths. A composite map of ISW observations (six in total, see text for details) propagating in the MC is also shown in grey thick lines. The inset on the bottom-right corner is a vertical section corresponding to the black profile, which goes from the region of maximum F towards the southeast along the ISWs propagation path. The vertical and horizontal axes are depth in meters and distance in km (measured from the northwest end). The vertical section shows a ray-tracing diagram for the M_2 tidal constituent and assuming stratification typical for the summer in the MC. The red star in the map represents the critical bathymetry from where IT beams are generated, and the black square is the corresponding reemergence at the thermocline (see text for more details).

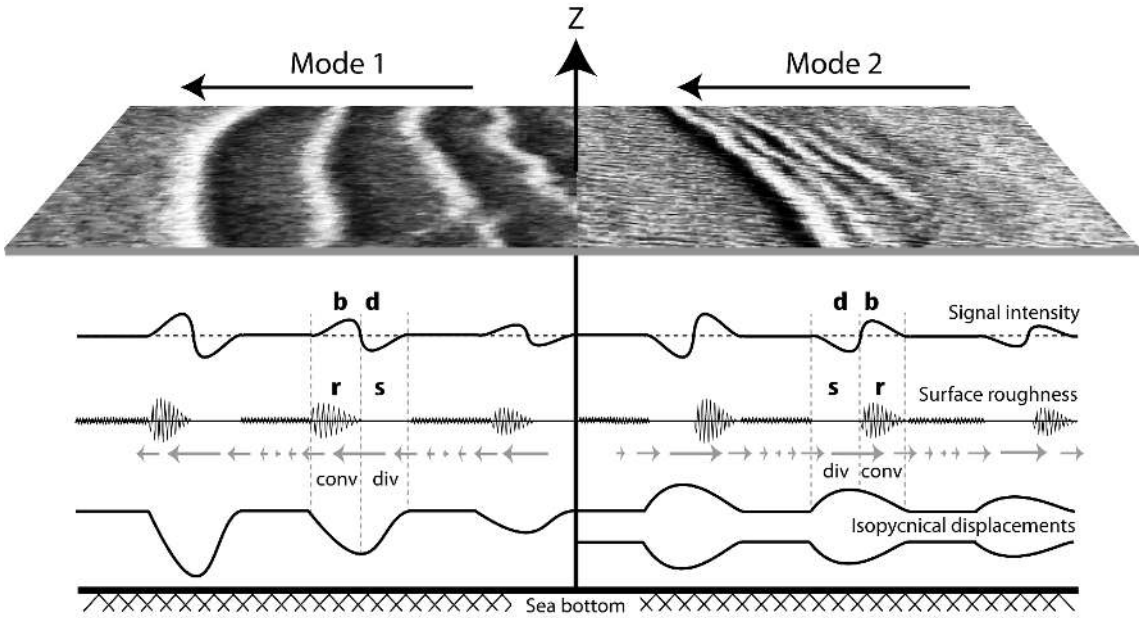

Fig. 1.6 Examples of SAR images with sea surface signatures of mode 1 and 2 internal solitary waves are shown at the top (left and right, respectively). The ISWs are assumed to be moving from right to left. From top to bottom the horizontal profiles represent the following features: SAR intensity profile along the ISWs, with bright enhanced backscatter (b) preceding dark reduced backscatter (d) in the direction of propagation of mode 1 waves; surface roughness representation indicating how rough (r) and smooth (s) the surface is along an ISW wave packet; surface current variability induced by ISWs (note indication of convergence and divergence fields near the surface); isopycnical displacements produced by ISW propagation. Note how the SAR signatures, surface roughness, current fields and convergence and divergence patterns are all reversed between mode 1 (on the left) and mode 2 (on the right) ISWs.

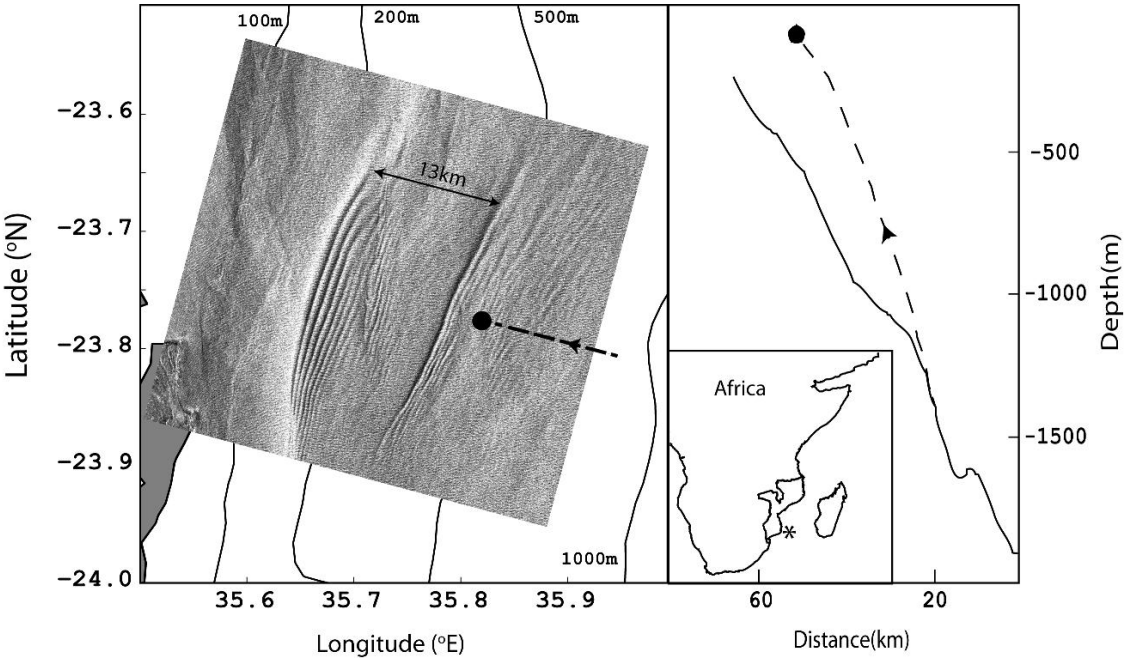

Fig. 1.7 ERS2-SAR image dated 24 September 2001 and acquired at 7:39 UTC, showing two packets of ISWs consistent with a mode 2 vertical structure (separated by approximately 13 km – see black arrow on top). Isobaths for depths of 100, 200, 500, and 1000 m are also shown. On the right hand side a vertical section corresponding to the dashed profile on the left (perpendicular to the ISW crests) is shown with a simulated ray trajectory (dashed line) coming from critical bathymetry and based on local stratification (the arrows indicate the direction of energy propagation). The black circle on both panels indicates the predicted position where an internal tide beam impinges on the thermocline from below. The inset shows the geographic location of the observation in the Mozambique Channel.

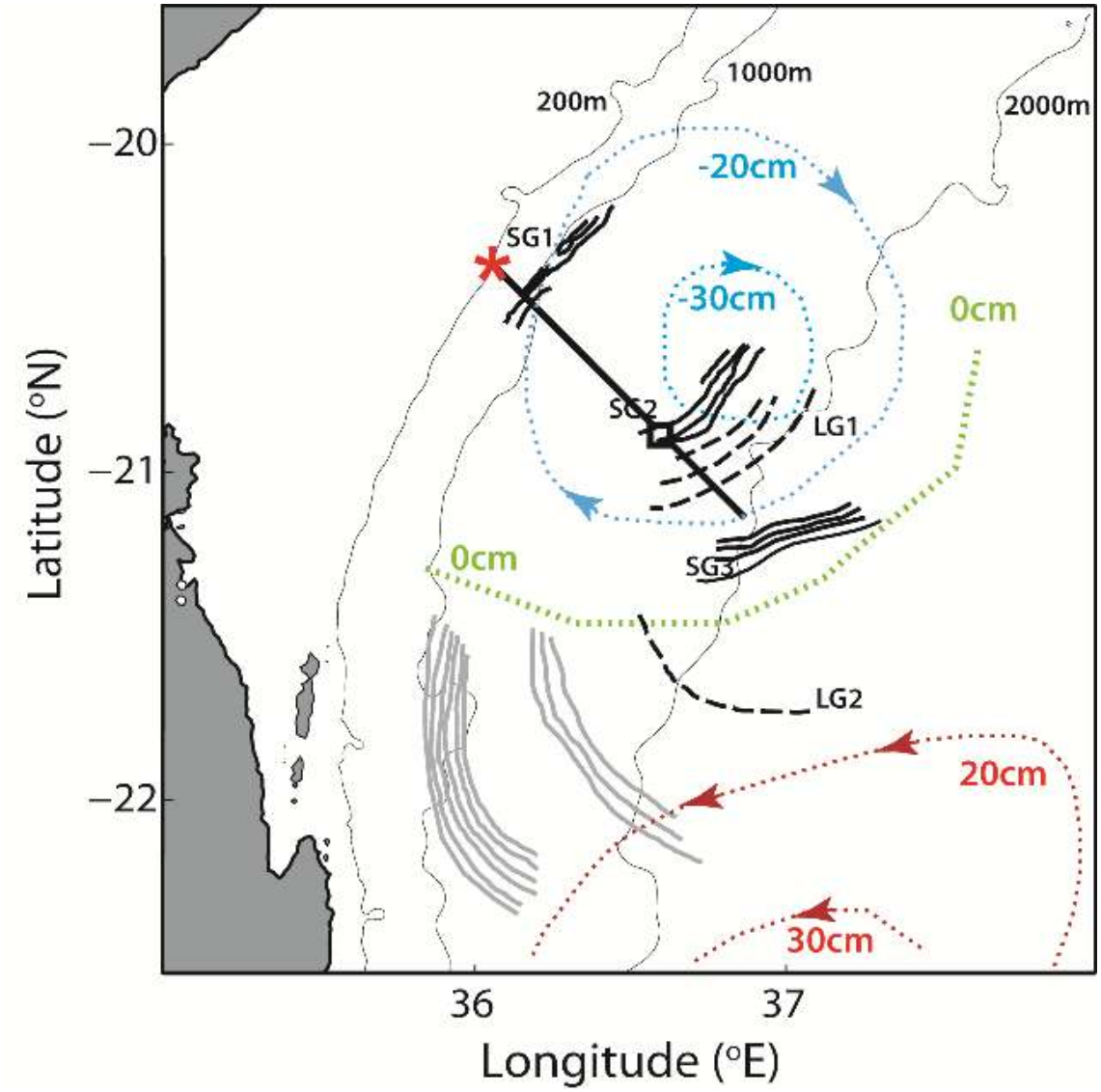

Fig. 1.8 Location map for ISWs observed to propagate in an Envisat-ASAR image (WS mode) over the Mozambique Channel, dated 4 December 2009 and acquired at 20h07m UTC. Land is shown in grey areas and isobaths for 200, 1000, and 2000m are marked in thin black lines. ISWs interpreted to be generated directly over the shelf (SG) are in solid black lines, while locally generates waves (LG) are in dashed black lines. Each group is numbered chronologically from their generation to later stages of development. ISWs that could not be discriminated (for their generation mechanism) are marked in grey (see text for details). The red star, black square and black profile are the same as in Figure 1.5, and are shown here for a reference location of critical bathymetry and the re-emergence of IT rays at the thermocline. The blue and red dashed lines mark the locations of eddy-like features detected in altimetry data, and whose rotation is indicated by arrows. The green line represents a reference level of neutral sea surface height.

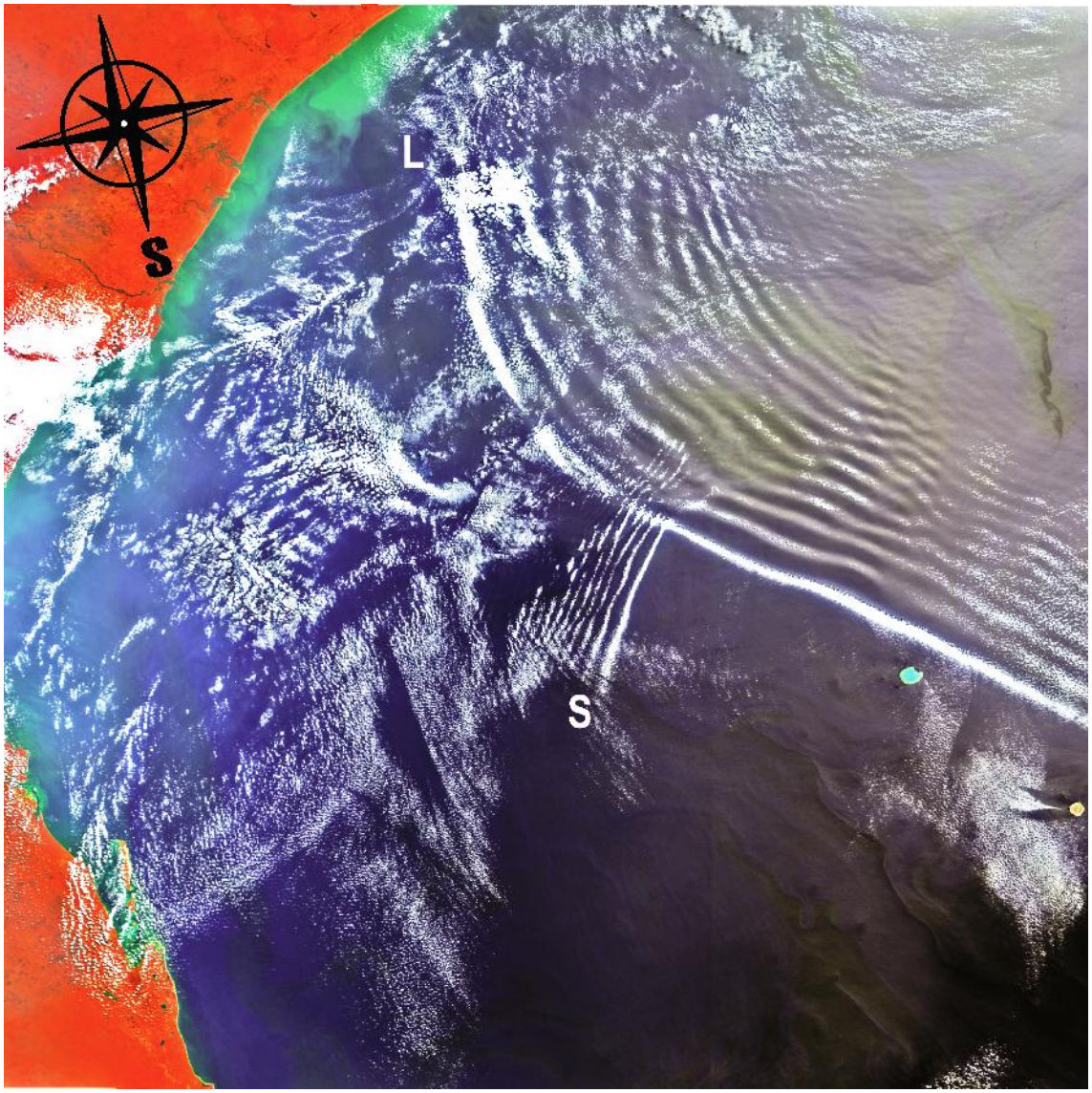

Fig. 1.9 Envisat-MERIS image dated 16 September 2004 acquired at 07h15m UTC. The image covers an area of about 580×660 km^2 and it is centred near 20.4°S and 38.0°E. The black compass overlaid on the top-right corner indicates north, and the back circle has been drawn to have approximately 70 km in diameter (for a scale reference). Two waves can be seen to propagate in the southwest part of the Mozambique Channel, one large-scale AGW (L) going southwest and a smaller AGW (S) going southeast.

Chapter 3

Internal solitary waves in the Mozambique Channel: Observations and interpretation

JOURNAL OF GEOPHYSICAL RESEARCH, VOL. 114, C05001, doi:10.1029/2008JC005125, 2009

Internal solitary waves in the Mozambique Channel: Observations and interpretation

J. C. B. da Silva,[1] A. L. New,[2] and J. M. Magalhaes[1]

Received 15 September 2008; revised 11 February 2009; accepted 19 February 2009; published 1 May 2009.

[1] This paper presents new results showing that the Sofala shelf in the Mozambique Channel (20°S, 36°E) is a previously unknown "hot spot" for the generation of internal tides and internal waves. We investigate available Envisat advanced synthetic aperture radar imagery of the region, which is capable of showing the surface signatures of the internal waves. This is complemented by modeling of the ray pathways of internal tidal energy propagation, and of the P. G. Baines (1982) barotropic body force, which drives the generation of internal tides near the shelf break. The hot spot region is localized between 20° and 21°S because of the particular nature of the bathymetry there. Farther north and south, the forcing is reduced and insufficient to generate internal solitary waves in the synthetic aperture radar images. The analysis reveals two distinct types of internal wave trains that are observed traveling oceanward away from the shelf break, and we suggest that these result from direct generation at the shelf break and from "local" generation at about 80 km from the shelf break, respectively, because of the surfacing of internal tidal rays at the thermocline. Finally, we have investigated seasonal differences in the wave patterns, which penetrate more extensively into the channel during the southern summer and appear slightly farther to the south during the southern winter. We also conclude that the local generation process is more likely to occur during the winter when the stratification is reduced.

Citation: da Silva, J. C. B., A. L. New, and J. M. Magalhaes (2009), Internal solitary waves in the Mozambique Channel: Observations and interpretation, *J. Geophys. Res.*, *114*, C05001, doi:10.1029/2008JC005125.

1. Introduction

[2] Internal waves are now viewed as an important mixing mechanism in the world's ocean, not only for the role they play in deep-ocean mixing [*Garrett and St. Laurent*, 2002], but also for mixing at the base of the mixed layer and in the seasonal thermocline [*Moum et al.*, 2003]. In the former case, internal waves may be generated by tidal flow, mean flow, or eddies, interacting with deep ocean topography. While uncertainties still exist over the relative importance of the various mechanisms involved, the breaking of these internal waves may mix the water masses up to middepth in some ocean basins (e.g., in the Indian Ocean [*New et al.*, 2007]). On the other hand, mixing near the surface affects the properties of those water masses which define the exchanges of heat and freshwater between the atmosphere and ocean. The importance of such mixing in the seasonal thermocline has been strikingly illustrated by *Moum et al.* [2003], who observed Kelvin-Helmholtz billows leading to turbulence in internal solitary waves (ISWs) over the Oregon continental shelf. In their study it was also shown that ISWs may be continually triggering instabilities as they propagate over the shelf, well before approaching a breaking point in the nearshore. Therefore, a significant proportion of the ISW's energy may be lost as it propagates on shore over the shelf. Furthermore, observations of upper ocean ISWs in deep water in the Western Equatorial Pacific also indicate they may be highly turbulent [*Pinkel*, 2000], and *Pingree et al.* [1986] showed that mixing from internal tides and waves is important for biological productivity over the Celtic shelf break in the Bay of Biscay. These facts point to the significant role that internal waves may play in near-surface mixing, and it is therefore important to gain knowledge of which areas of the world's oceans have high levels of internal wave activity, and of the mechanisms by which they are formed. Satellite synthetic aperture radars (SARs) are very efficient sensors to explore regions not yet surveyed in detail for the presence of such ISWs, and this paper contributes to the knowledge of where and how ISWs are generated in the Mozambique Channel of the Indian Ocean.

[3] The interaction of the barotropic tide with steep shelf break topography may often result in the generation of large internal waves of tidal period, known as internal (baroclinic) tides (ITs). Internal tidal energy generated at the shelf break may radiate away either horizontally in the form of interfacial ITs on the thermocline, or as "rays" into the stratified continuum below. Consequently, large "interfacial" ITs may form in the thermocline directly above the shelf break, and these, through nonlinear evolution, lead to the genera-

[1] Institute of Oceanography and Department of Geographic Engineering, Geophysics and Energy, University of Lisbon, Lisbon, Portugal.
[2] Ocean Modelling and Forecasting Group, National Oceanography Centre, Southampton, Southampton, UK.

0148-0227/09/2008JC005125$09.00

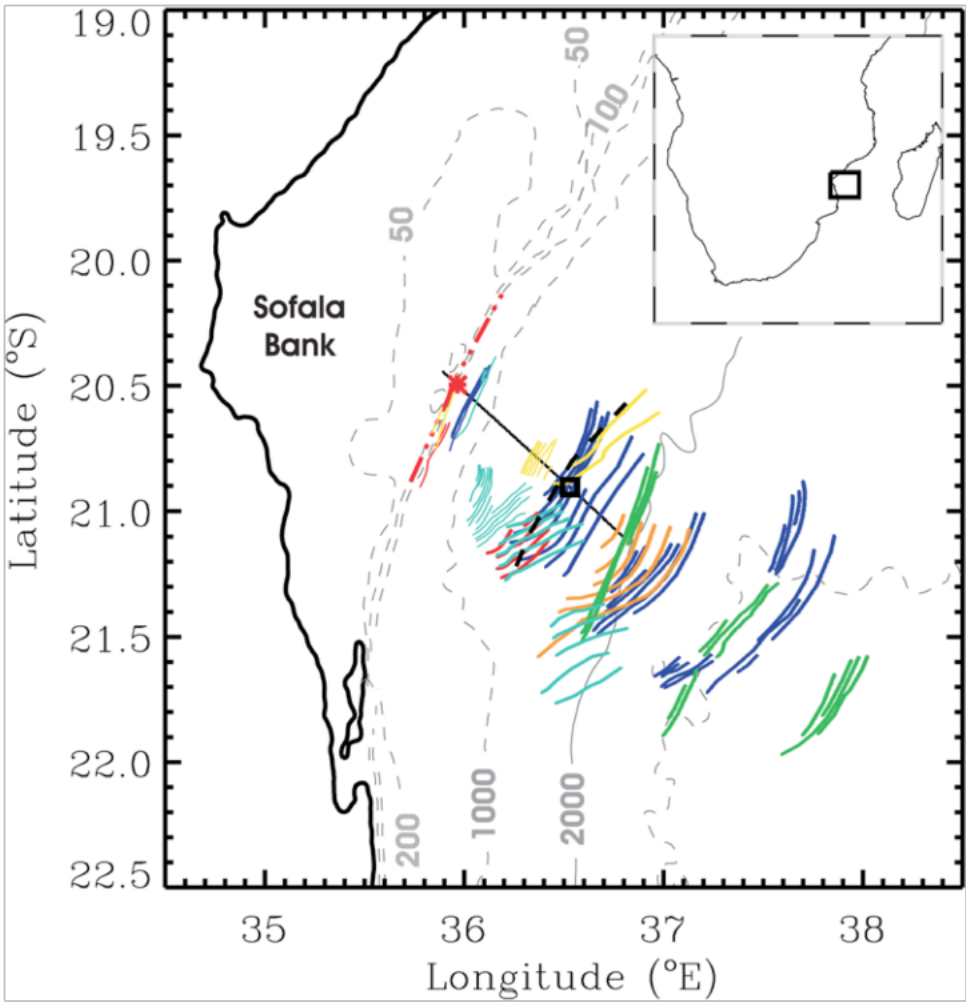

Figure 1. Composite map of ISW observations based on Envisat ASAR observations from 26 September 2003 acquired at 7:04 (orange), 23 April 2004 acquired at 7:04 (green), 10 August 2005 acquired at 7:07 (light blue), 13 August 2005 acquired at 7:12 (red), 17 February 2006 acquired at 7:03 (dark blue), and 20 February 2006 acquired at 7:09 (yellow). All times refer to UTC. The straight continuous black line shows the section for the internal tidal raypaths in Figures 2b and 2c (also P1 in Figure 4a). The red star marks the position of critical topography for the M_2 (October) ray, and the black square its reemergence at the thermocline. The red dash-dotted line represents the approximate position of critical topography, and the black dashed line represents the location of reemergence at the thermocline, for all such rays (see text for details). Contours mark isobaths in meters, and the inset shows the study region in relation to the African continent and Madagascar.

tion of packets of higher-frequency ISWs that can be observed either in situ or in SAR images. On the other hand, the IT energy which propagates downward into the deep ocean may give rise to a second generation mechanism known as "local generation" [*New and Pingree*, 1990, 1992, 2000; *Gerkema*, 2001; *New and da Silva*, 2002; *Zhao et al.*, 2004; *Akylas et al.*, 2007; *da Silva et al.*, 2007]. Here, a beam or ray of internal tidal energy is generated at "critical" slope regions of the shelf break where the bottom topographic slope matches the slope of the raypaths, and propagates at an angle to the vertical into the deep ocean interior (see equation (1)). These rays reflect from the seafloor [*Pingree and New*, 1989, 1991], and interact with the thermocline from below [*New and Pingree*, 1990], causing large IT oscillations there, and "locally" generating ISWs (i.e., far from the generating shelf break). For the northern Bay of Biscay, this results in a bimodal distribution of ISW packets, resulting from the "direct" generation mechanism near the shelf break and from "local" generation some 150 km into the ocean [*New and Pingree*, 1992; *New and da Silva*, 2002]. The local generation mechanism has also been found to be operative in the southern Bay of Biscay by *Azevedo et al.* [2006], and at the Mascarene Ridge in the Indian Ocean (a region not far from the Mozambique Channel, and with similar bottom slopes) by *Konyaev et al.* [1995]. It has also been studied theoretically by *Gerkema* [2001] and by *Akylas et al.* [2007].

[4] The northernmost part of the Mozambique Channel (MC) has been studied by *Manders et al.* [2004], who showed the existence of ITs (but not ISWs) in the narrowest

Table 1. Maximum Depth-Integrated Body Force Values for All Case Studies Shown Together With the Corresponding Tidal Ranges, the Nearest Spring-Neap Tidal Ranges, the Number of Locally Generated Large Waves in a Packet, and the Soliton Width

Date	Maximum Body Forcing (m^2 s^{-2})	Tidal Range (m)	Spring/Neap Tidal Range (m)	Number of Locally Generated Large Waves	Soliton Width (km)[a]
26 Sep 2003	6.62	6.1	6.6–1.0	6	2.6
10 Aug 2005	5.27	4.8	4.9–2.1	5	2.1
13 Aug 2005	1.80	3.4	4.9–2.1	4	2.5
17 Feb 2006	7.36	5.3	5.6–1.2	3	1.4
23 Apr 2004	6.78	4.7	5.6–1.0	0	–
20 Feb 2006	3.14	3.8	5.6–1.2	2	1.5

[a]Soliton width is shown for the first wave in each packet.

passage between Mozambique and Madagascar near 15°–17°S. However, to our knowledge, there has so far been no evidence of the existence of ISWs anywhere within the MC, nor of internal tidal activity in the central and southern parts of the MC. In this paper we report recently acquired SAR images of the MC which show for the first time that the Sofala Bank (see Figure 1) is a "hot spot" for internal tidal and solitary wave activity. This is in accord with the study of *Baines* [1982], which estimated energy fluxes from several shelf regions of the world's oceans, and showed that the MC was among the 12 most energetic regions for IT generation. Here, the (semidiurnal) barotropic tidal ranges are over 7 m, and the barotropic currents typically exceed 50 cm/s at spring tides, with significant spring-neap variability (see Table 1). The shelf slope is also steeper than the raypaths (see section 2 and Figures 2b and 2c), allowing the existence of critical regions for IT generation. In the present study we show evidence that both the above generation mechanisms are operative in the MC, with waves being formed directly at the shelf break, and remotely through local generation.

[5] The paper is organized as follows. We begin by describing the new satellite SAR observations of the short-period ISW trains in the MC in section 2, together with a preliminary interpretation of their patterns in terms of IT ray propagation pathways. This is followed by an examination of the depth-integrated body force of *Baines* [1982] in section 3, together with an analysis of cross-slope transports. This is able to explain why the ISWs occur in the observed locations, rather than farther north or farther south, and confirms the Sofala shelf as a hot spot region for the ITs and ISWs. The paper then concludes, in section 4, with a more detailed examination and discussion of the SAR observations, the effects of seasonal variations, and the likely generation mechanisms for the ISWs.

2. SAR Observations and Interpretation

[6] It is well known that ISWs propagating on the near surface thermocline (or pycnocline) are capable of producing sea surface roughness patterns that are observable by satellite-borne SARs when the wind speed is not excessively strong [*Alpers*, 1985; *da Silva et al.*, 1998]. Here we investigate available Envisat advanced synthetic aperture radar (ASAR) imagery of the MC region (19°–22.5°S, 34.5°–38.5°E). The ESA EOLI-SA image catalog was used to analyze quick looks, and images were then requested when strong signatures of ISWs were visible. Figure 1 is a composite map derived from six satellite SAR overpasses corresponding to the strongest ISW signatures identified in the Envisat images. The images selected were those dated 26 September 2003, 23 April 2004, 10 and 13 August 2005, and 17 and 20 February 2006, and these are identified by different colors in Figure 1. They all correspond to the Wide Swath WS image mode, which is optimum for observing local generation of ISWs [see *da Silva et al.*, 2007] because of its extensive coverage (400 km × 400 km) and high spatial resolution (75 m). Although there were additional observations of ISWs in the MC in other satellite data sets (ERS SAR and MODIS), we have not included these because of their smaller swath widths. All the images shown cover the entire area in Figure 1 except for the yellow and red waves (the cutoff for which is at the southern edge of the wave packets shown).

[7] Detailed inspection of the SAR signatures (in the manner of *Thompson and Gasparovic* [1986]) reveals that the ISW packets shown (having crests approximately parallel to the shelf break) all propagate offshore in the general direction of ESE or SE. The overall pattern of the ISW trains is similar to the patterns previously observed in other regions, such as the Bay of Biscay [*New and da Silva*, 2002; *Azevedo et al.*, 2006; *da Silva et al.*, 2007]. In the northern Bay of Biscay there are enhanced levels of activity close to the shelf break, then an off-shelf region with a reduced number of ISW observations, followed by an increase of activity from about 120–150 km from the shelf break (this latter activity being due to local generation). Similarly, in the MC off the Sofala Bank (Figure 1), we observe short-wavelength ISW trains near the shelf break (e.g., the 200 m contour), then a decrease in the off-shelf direction, followed by an increase in activity at about 80 km away from the shelf break. This off-shelf region of ISW activity is about 100 km wide, and extends to the SE for some 200 km farther offshore toward the center of the Channel.

[8] We also note in passing that no ISW packets were seen on the shelf, whereas at first sight, one would expect waves to be visible both oceanward and shelfward of the shelf break. For instance, *Lamb* [1994] modeled internal wave generation over Georges Bank and showed that these could propagate both off-bank and onto the bank. However, the stratification used by Lamb had a strong sharp thermocline (with a maximum N = 0.027 s^{-1}). In the present case, the waters on the Sofala Shelf are essentially well mixed because of the strong tides there (N below 0.003 s^{-1}), and so cannot support the propagation of internal waves (for which stratification is required).

[9] To begin to explain these patterns in more detail, we now turn to theoretical considerations. Internal tides in a

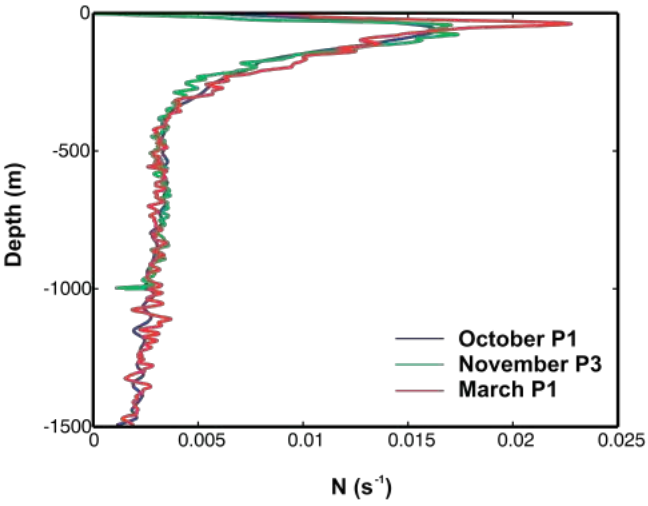

Figure 2a. Mean stratifications for the study area are shown for October and November (blue and green representative of spring season) and March (red representative of summer season). Stratifications for October and November were computed using sections in the approximate cross-slope direction near P1 and P3, respectively (see Figure 4a). March stratification was calculated with a zonal section near P1 (see Figure 4a).

continuously stratified ocean can be described by beams or rays that follow characteristic pathways (along which their energy can propagate) with a slope c to the horizontal given by

$$c = \pm\left(\frac{\sigma^2 - f^2}{N^2 - \sigma^2}\right)^{1/2} \quad (1)$$

where N is the local Brunt-Väisälä frequency, σ is the semidiurnal frequency, and f the Coriolis parameter. When the seafloor slope matches the local value of c (a critical region) generation of ITs is pronounced, particularly if the barotropic currents are strong. In such cases, the direction of the forcing barotropic flow is then coincident with the motion plane for free internal waves, resulting in resonant conditions and enhanced generation of the ITs.

[10] Figure 2a shows average profiles of the Brunt-Väisälä frequency for different seasons and locations in the MC. The dark blue profile represents an average stratification for October 2007 based on 10 CTD stations from close to profile P1 in Figure 4a (also shown in Figure 1) and covering water depths between 326 and 2192 m (with a mean latitude of 20.25°S). The red profile is based on 9 CTD stations from the RV Pelagia (cruise 64PE156) in March 2000 and represents an average stratification of the summer season from a zonal section at 20°S (water depths between 270 and 2500 m) close to P1. This latter is very similar to the stratification presented by *Manders et al.* [2004] for the same month (March) but farther north (at 16.5°S). We have also evaluated an average stratification for November 2007 (the green curve in Figure 2a) in a region close to section labeled P3 in Figure 4a. The stations used have an average latitude of 17.75°S, and cover water depths between 300 and 2200 m. The Brunt-Väisälä frequency profiles are quite similar for both P1 and P3 regions at this time of year, taken as representative of spring stratification. Figure 2a therefore provides a good description of the variability of the stratification within the MC, both spatially and seasonally.

[11] In Figures 2b and 2c we present internal tide raypaths computed using the stratifications for March and October, respectively, both for the M_2 and S_2 tidal frequencies (respectively 1.4052×10^{-4} rad/s and 1.4544×10^{-4} rad/s).

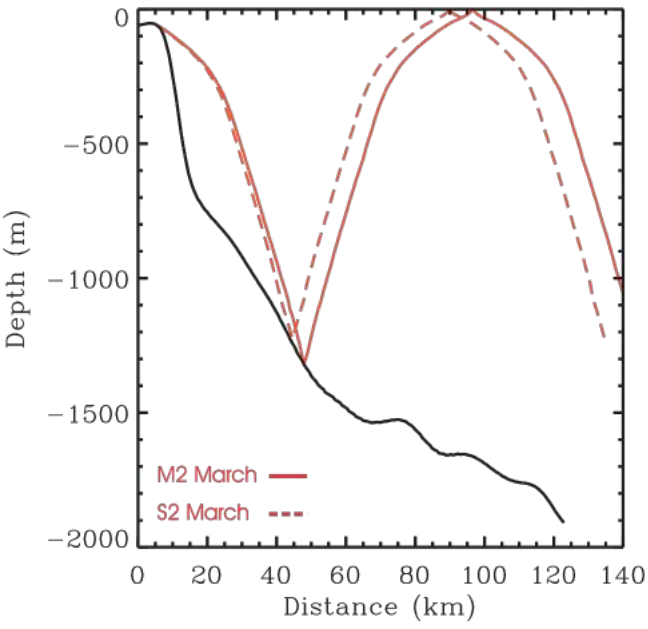

Figure 2b. Internal tidal ray-tracing diagrams for the M_2 (solid line) and S_2 (dashed line) tidal constituents assuming the average summer stratification in Figure 2a. The location of the vertical section is the straight continuous black line in Figure 1 (also profile P1 in Figure 4a; see text for details).

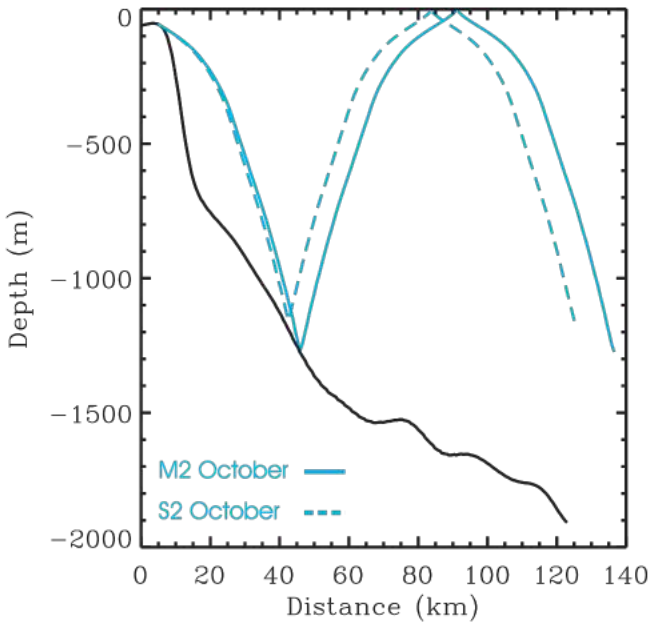

Figure 2c. Same as Figure 2b but assuming the average spring (October) stratification in Figure 2a.

The raypaths are computed along the section in Figure 1 shown by the black line oriented almost perpendicularly to the 200 m isobath (that is also coincident with profile P1 in Figure 4a). The rays emanate from the critical region of the shelf break, initially slope downward into the deep ocean, reflect upward from the seafloor at a depth of 1100–1300 m (some 35–45 km seaward from the shelf break), and reemerge at the surface at about 75–90 km from the break. From one season to another, there is a spatial (horizontal) difference of about 5–7 km between the positions of the rays when they reach the surface after bottom reflection.

[12] A similar difference arises between the ray positions for the M_2 and S_2 frequencies for a given season. It is important to acknowledge that the divergence of the raypaths for the M_2 and S_2 frequencies will mean that baroclinic spring tides at any location will not necessarily occur at the same time as barotropic spring tides. As shown by *Gerkema* [2002], the time of occurrence of baroclinic spring tides depends spatially on the local phase difference of the M_2 and S_2 (lunar and solar semidiurnal) tides. These phases in turn depend on the pathways which the two rays follow. The divergence of the two rays will therefore lead to possible differences in the timing of baroclinic spring tides (i.e., the forcing by the upward beam when it strikes the thermocline in the local generation process will not necessarily be a maximum at the same time as barotropic spring tides at the shelf break). However, we comment that we were only able to find examples of waves in the SAR images within a few days of barotropic spring tides (see Table 1), so this effect appears to be small in the present case.

[13] The red star and black square in Figure 1 show the positions where the ray in Figure 2c (for October stratification and the M_2 frequency) is generated (the critical position) and where it subsequently intersects the thermocline (at 60 m depth), respectively. Measured at the surface, a distance of about 80–85 km off the Sofala Bank region is typical for this ray bounce geometry. This is shown in Figure 1 by the red discontinuous (dash-dotted) curve and the black dashed curve. These represent the approximate positions of the critical topography along the shelf break and the intersections of the reemerging IT rays with the thermocline in the oceanward direction, respectively, and have been drawn from the analysis of several rays similar to that shown in Figure 2c.

[14] It is clear in Figure 1 that the ISW packets close to shelf break are generally composed of just a few waves of relatively small wavelength (0.5–1.5 km) when compared to (some of) the wave trains observed farther offshore (wavelengths in excess of 5 km). There is a region of relatively low ISW activity between the shelf break and the reemergence at the surface of the IT rays. This is followed by a marked increase in ISW activity at about 80 km from the shelf break which coincides closely with the surfacing positions of the IT rays. Consequently, it would seem that at least some of these wave packets could potentially result from local generation. Typically, multiple ISW packets are observed in any particular image, except for those on 26 September 2003, marked orange in Figure 1 (and in some recent images where only a single soliton was observed, in summer, that are discussed in section 4). In these individual images (e.g., the dark blue waves), the ISW packets are separated by typical distances of 60–70 km. Assuming this is the distance the packets travel between tidal cycles implies a phase speed of 1.35–1.55 m/s. This is consistent with phase speeds inferred from the local stratification (two-layer model), and so confirms that the packets do indeed have a tidal origin, and are generated on succeeding tidal cycles (as is typically the case in other areas).

[15] In addition, in the off-shelf region of ISWs in Figure 1, there are ISW packets with both large and small wavelengths at the same time, and closely located to one another. For instance, in the ISW packets colored light blue, dark blue and yellow (dated 10 August 2005, 17 February 2006, and 20 February 2006, respectively), there are such wave groups near and oceanward of the ray surfacing position. The packets of longer waves occur ahead of (farther to the SE) the shorter waves. The occurrence of seemingly different types of ISWs also indicates the possibility that these packets could result from different generation mechanisms (i.e., from the shelf break, and locally), and this is discussed in section 4.

[16] We note that the ISWs which occur during the southern summer generally penetrate farther into the Channel than those occurring during the winter. On the other hand, those occurring during the winter are generally found farther to the south than those occurring in the summer. Possible reasons for these differences are discussed in section 4.

3. Body Force Modeling

[17] We now examine why the ISWs are seen in the observed locations through an investigation of the barotropic body forcing term for the ITs. This has been found to be a useful indicator of where hot spot generation regions of ISWs may occur in several other independent studies [*Sherwin et al.*, 2002; *Merrifield and Holloway*, 2002; *Niwa and Hibiya*, 2004; *Azevedo et al.*, 2006; *da Silva et al.*, 2007].

[18] Following *Baines* [1982], the barotropic forcing term, or "body force," for internal tides resulting from shelf break interactions, can be found as

$$F = zN^2(z) \int Q dt \cdot \nabla\left(\frac{1}{h}\right) \tag{2}$$

where z is the upward vertical direction, $N(z)$ is the local Brunt-Väisälä frequency, Q is the barotropic mass flux vector $Q = (Q_x, Q_y) = (u_1 h, v_1 h)$, u_1 and v_1 are the zonal and meridional components of the barotropic velocity, and h is the ocean depth. The body force F can thus be analytically integrated provided the mass flux vector Q is known. In the present work, the components of the barotropic velocity vector were obtained from the 1/4° resolution (global) tidal model OTIS (Oregon State University Tidal Inversion Software), developed by *Egbert and Erofeeva* [2002]. We first calculated the components of the barotropic mass flux vector (Q_x and Q_y) for a complete tidal cycle (on any particular day) on an interpolated grid with resolution of 1/8°. The model included the M_2 and S_2 constituents of the barotropic tide, as these are the most important for determining the conditions at spring tides for the study region. The model was run for all the dates of the SAR

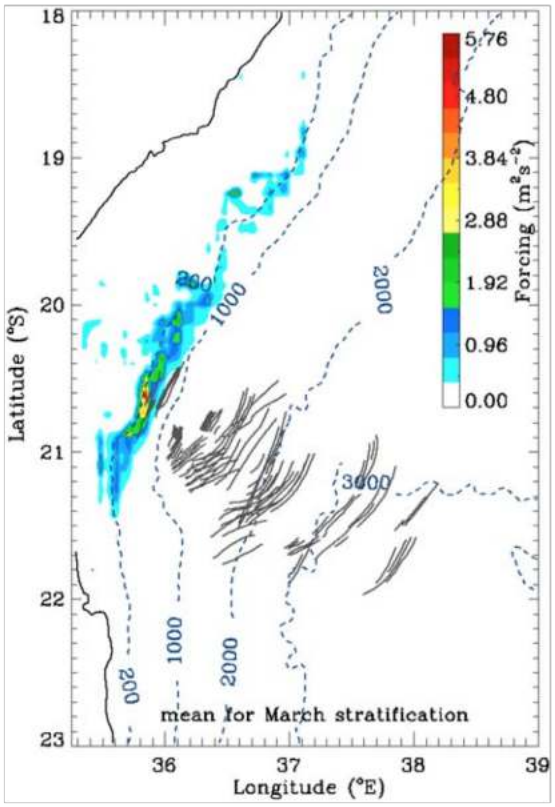

Figure 3a. Map of the average of the maximum depth-integrated barotropic body force for the three summer case studies (23 April 2004, 17 February 2006, and 20 February 2006). Also marked are all the ISW trains from Figure 1 (dark thin curves). Note the region of strong forcing near the shelf break off Sofala Bank between 20° and 21°S. Contours mark isobaths in meters.

images with strong internal wave events and shown in Figure 1. The Brunt-Väisälä frequency N was assumed to be spatially constant over the study region (given the small spatial variability discussed in section 2), and we accounted for seasonal differences by using the most appropriate profile for the date of each SAR image (from March or October on the P1 section in Figure 2a).

[19] Figures 3a and 3b show the depth-integrated body force for the region of the Sofala Bank (18°–23°S; 35.25°–39°E). For each of the days when there was a satellite overpass, one of these maps was created of the tidal maximum (vertically) integrated forcing for each point of the model domain. Figure 3a is the average of the three maps corresponding to the individual SAR images of the summer season (taking the average stratification of March). Similarly, Figure 3b is the average of the three maps corresponding to the individual SAR images of the spring season (taking the average stratification of October). It can be clearly seen that there is a region of elevated and coherent values of strong forcing along the shelf break and close to the 200 m contour, from approximately (20°S, 36.4°E) to (21.3°S, 35.6°E), in both Figures 3a and 3b. In fact, both body force maps are qualitatively similar, the differences being essentially in the maximum values of integrated body force which are higher for the summer season, as one would expect since N is also higher (see equation (2)). This region has an average maximum forcing of 5.76 m^2s^{-2} and 4.56 m^2s^{-2} for the summer and spring season, respectively (the values for the individual maps corresponding to the days of the individual images are given in Table 1). This is significantly higher than the body force previously calculated for the southern Bay of Biscay and the southern Iberian regions [*Azevedo et al.*, 2006; *da Silva et al.*, 2007]. The Mozambique Channel, and in particular the region off the Sofala shelf, is therefore identified as an efficient generator of baroclinic tides. Moreover, the observed ISW wave trains (overlaid in Figures 3a and 3b) appear directly oceanward of the region of maximum body force, in a direction consistent with their propagation direction.

[20] Since tidal elevations of the barotropic tide are large throughout the MC and in fact increase to the north of Sofala Bank, being higher at the narrowest part of the MC (see map of lunar semidiurnal tidal component M_2 based on TOPEX/POSEIDON Altimetry data available at http://svs.gsfc.nasa.gov/stories/topex/tides.html), we now extend some of the analysis farther north, to cover the region studied by *Manders et al.* [2004], near 16.5°S. Figure 4a presents a body force map, computed in the same manner as described above for a larger region (16°–23°S; 35.25°–41°E), and representing the conditions for 26 September

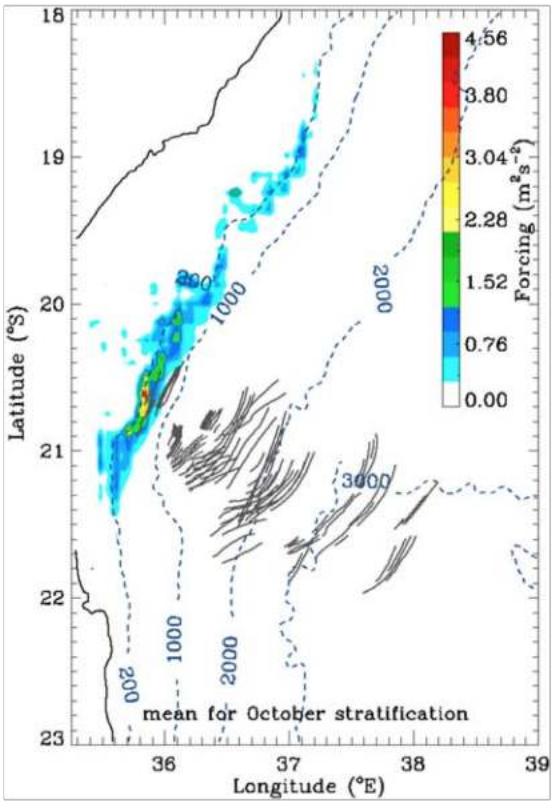

Figure 3b. Same as Figure 3a but for the three winter case studies (26 September 2003, 10 August 2005, and 13 August 2005). Also marked are all the ISW trains from Figure 1 (dark thin curves). Note the region of strong forcing near the shelf break off Sofala Bank between 20° and 21°S. Contours mark isobaths in meters.

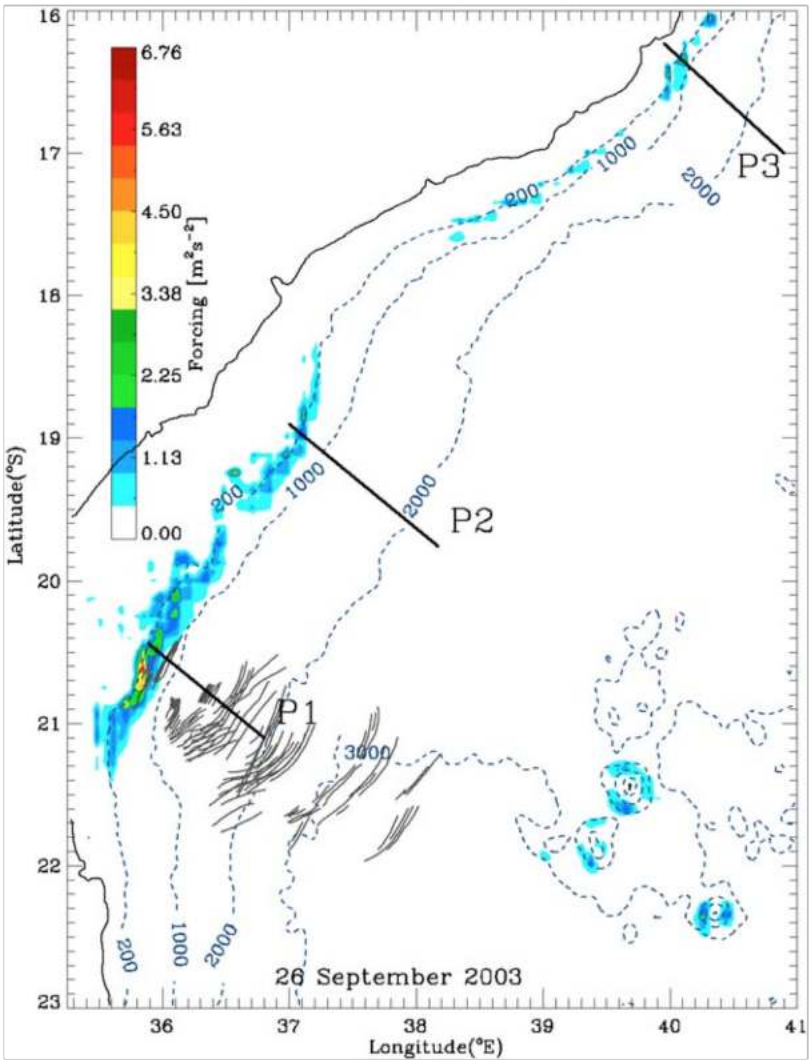

Figure 4a. Extended map of the maximum depth-integrated barotropic body force for 26 September 2003 (16°–23°S; 35.25°–41°E) is shown together with all the ISW trains from Figure 1 (dark thin curves). Three profiles labeled P1, P2, and P3 (solid black lines) are also marked in the approximate cross-slope direction. Contours mark isobaths in meters.

2003 (orange waves in Figure 1). This case has the maximum forcing of all examples in winter, when conditions might be most favorable for local generation. One can see from Figure 4a that the body force values progressively decrease and become less coherent in space to the north. Since there is very little difference in stratification at various positions along the shelf slope, this is instead likely to be due to differences in the topography. To better understand this we also show the cross-slope transports in Figure 4b, computed for three cross-slope sections along the western margin of the MC (P1, P2 and P3). The importance of the cross-slope mass fluxes in determining the energy fluxes in the internal waves which radiate away from the shelf slope bathymetry has been pointed out by *Morozov* [1995]. It can be seen that cross-slope transports are large ($Q = 50\ m^2s^{-1}$) and comparable to other regions where ISWs are observed [*Gerkema et al.*, 2004] for profile P1 (Sofala) but rather small farther north for profiles P2 and P3 (see Figures 4a and 4b). Indeed, for steep (supercritical) slopes, such as those off the Sofala Bank, the internal tidal energy flux (equivalent to the integrated conversion rate C_{int} of *Gerkema et al.* [2004]) is actually proportional to the square of the mass (or volume) flux Q, which further enhances the contrast between P1 on the one hand, and P2/3 on the other. This further emphasizes the high efficiency of the Sofala Bank in generating internal tides, as compared to the region previously studied by *Manders et al.* [2004].

[21] Now, the body force [see *Azevedo et al.*, 2006] is related to the product of the topographic slope and the transport crossing this topography. There is not much difference in the topographic slope offshore from the shelf break at depths greater than 100 m (see Figure 1). However, the cross-slope transport is very large for the section P1 passing through the region of the body force maximum, and is much smaller at locations (P2 and P3) farther along the shelf slope. In turn, we anticipate that this cross-slope transport is so large here because of the detailed nature of the topography. In particular, there are two raised banks, less than 50 m depth, at 20.6° and 20.4°S. The barotropic tide is forced around and between these two banks, and

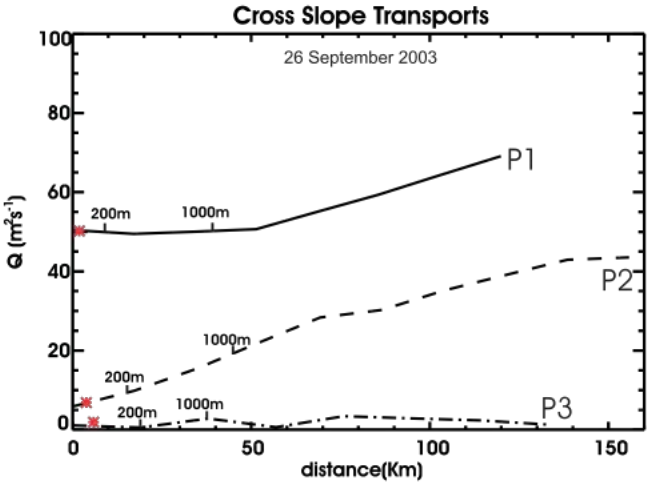

Figure 4b. Cross-slope transports for the three profiles shown in Figure 4a (P1, P2, and P3). The red stars mark the positions of critical topography for each corresponding profile. The 200 and 1000 m depths are also marked by vertical black ticks for each profile. Distances taken in the offshelf direction along the marked profiles in Figure 4a.

moreover is allowed to flow without hindrance onto the broad shelf area farther to the east, being further encouraged to do so by the area deeper than 50 m directly behind these banks. This is similar to the situation on the Hawaiian island chain in which the topographic forcing is much enhanced at the saddle points between the islands, giving rise to regions of large internal tidal energy fluxes there [e.g., *Merrifield and Holloway*, 2002]. Thus we believe that the special form of the shelf break topography near 20.5°S gives rise to the strongest cross-slope transports, and so to the strongest body force, and hence to the preferred generation of the ISWs from this location. Farther north as the shelf becomes progressively narrower, it becomes increasingly hard for the barotropic tide to flow across the shelf slope and into such a reduced shelf area. The tidal ellipses become preferentially aligned in the along-slope direction. Thus in the region covered by *Manders et al.* [2004], the generation of ITs is weaker and no ISWs were observed by these authors in this location (and neither in the SAR images used in our study).

[22] We therefore conclude that the ISWs observed in the SAR images do indeed result from the forcing because of the interaction of the barotropic tides with the shelf break topography, and are found directly oceanward of the region of maximum forcing, as would be expected. This shows that the body force is indeed a good indicator of where the waves are most likely to be observed, and supports our choice in using it. It also appears that the body force must reach a certain value before the waves will appear, as no waves are seen farther along the shelf slope where the body force is weaker.

4. Discussion

[23] We now discuss in more detail the SAR signatures of the ISWs and make suggestions as to possible generation mechanisms. Figure 5 is an extract of the Envisat ASAR image from 17 February 2006 (waves marked in dark blue in Figure 1) corresponding to an area of approximately 155 × 95 km. Several individual wave packets can be identified. Starting from the left, there is an ISW packet (A) of relatively short wavelengths near the shelf break. This contains at least 8 well-developed waves with typical wavelengths of about 1 km. Some 67 km farther to the ESE, in the general propagation direction of the ISW trains, we observe another wave train labeled B. The wavelengths in packet B are considerably larger (2 to 3 km) than for packet A, and there are at least 20 waves with typical along-crest distances of 100 km. Farther offshore (in the direction of ISW propagation), another wave packet (C) is found 63 km away from B. The interpacket separations between packets A and B, and B and C, are typical of internal tide wavelengths, and correspond to an average phase speed of approximately 1.4–1.5 m/s (the long wave speed for a

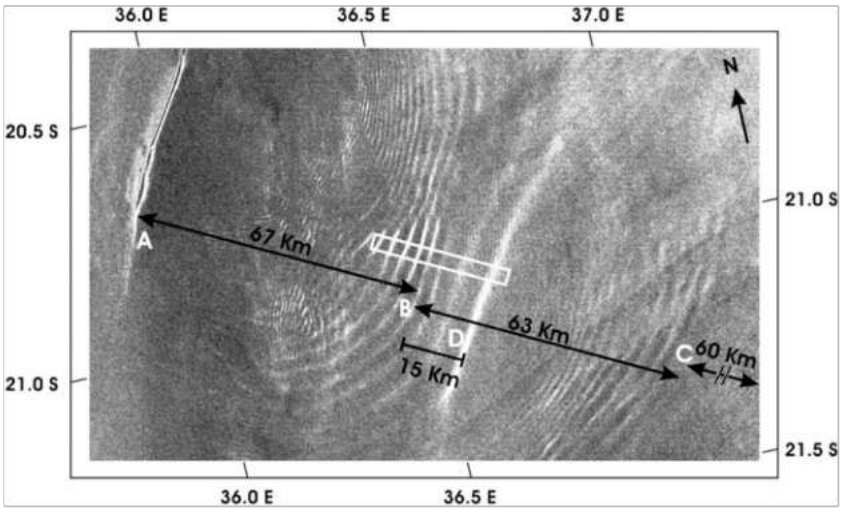

Figure 5. Extract of an Envisat ASAR image (WS mode) from 17 February 2006 acquired at 7:03 UTC (wave trains corresponding to the dark blue lines in Figure 1). Four ISW trains can be identified and are labeled as packets A, B, C, and D (see text for details).The separations between the various packets are shown in kilometers.

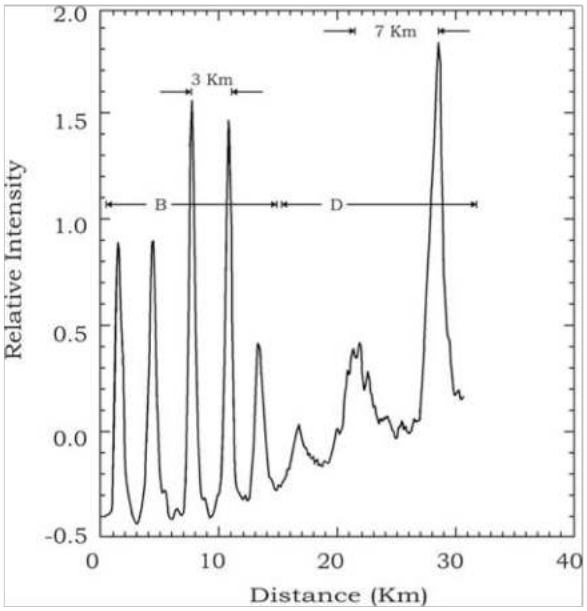

Figure 6. Envisat ASAR image intensity profile corresponding to wave packet D and the first five waves of packet B from 17 February 2006 (taken from the white rectangle in Figure 5). The waves in packet D have wavelengths of 7–3 km, whereas those in packet B are shorter than 3 km.

two layer model using appropriate parameters for the study region is close to this, being approximately 1.4 m/s).

[24] However, in between packets B and C we note the presence of another large-scale wave packet, labeled D in Figure 5. The wavelengths of packet D (distance between wave crests) are considerably larger (7–3 km) than those for packets B and C, possibly indicating a different generation mechanism. The discrepancy between the wavelengths in packets D and B is further illustrated in Figure 6 which provides a SAR image intensity profile across packets D and B in the region denoted by the white rectangle in Figure 5. We interpret packet D as containing the leading three longest waves on the right-hand side of Figure 6, which is followed by packet B. Packet D is therefore approximately 15 km in length overall, and contains waves with separations rank ordered as 7, 5 and 3 km. Furthermore, the intensity profile in Figure 6, taken as the relative variation compared to the unperturbed mean backscatter (see *da Silva et al.* [1998] for more details) decreases from the front to the rear of Packet D (from 1.8 to about 0.05 units for the crest values), but then rises again (to 1.5 units) for Packet B. These intensity variations are related to the amplitudes of the underlying ISWs (i.e., to the displacements of the isopycnals), although their interrelationship is not straightforward because of other factors (such as the wind speed and direction, and the presence of surface films). Nevertheless, because of the nonmonotonic variation of the SAR image intensity and taking into account the disparity between the wavelengths from packets D and B, we suggest that these are two individual wave packets which are likely to have different generation mechanisms.

[25] We therefore propose that packet B was formed a (semidiurnal) tidal cycle before packet A at the shelf break, and propagated from its origin for a tidal wavelength (67 km) to reach the observed position. We also interpret packet C as the predecessor of packet B since this is located a further 63 km offshore. At an additional 60 km offshore in the same direction (toward the ESE) there is another packet (not shown in Figure 5, but indicated, and also shown in dark blue in Figure 1) that therefore also appears to be part of the same family (i.e., with the same generation site and mechanism). We note that the above mentioned wave packets are approximately equally spaced (67, 63, 60 km apart), although their interpacket separation decreases oceanward. Also, the wave crest separation within packet C seems to be slightly larger than in the packet farther offshore (see dark blue waves in Figure 1). This latter aspect seems at first contrary to what should be expected from nonlinear theory of solitary wave propagation, as the individual waves should spread apart along their offshore propagation direction into deeper waters. However, analysis of MODIS Ocean Color level 3 images and Sea Surface Height Anomalies of TOPEX/POSEIDON (not shown) revealed the presence of a large anticyclonic eddy in the locality of these wave packets which would impose an adverse current against wave packets C and that farther offshore (the eddy being centered at 38°E, 23°S and with an northern edge near 21°S). It is likely that this would act (through internal wave-current interaction) to reduce the wavelengths of the individual waves in the most offshore wave packet, as well as reducing the interpacket spacings between packets B and C, and between packets C and that farther offshore. Similar effects on ISWs have been observed by *Sabinin and Serebryanyi* [2007]. Overall, we therefore interpret these wave packets (A, B, C and that farther offshore) as resulting from direct generation at the shelf break on successive tidal cycles.

[26] However, it seems unreasonable to include packet D in the same grouping. For if we supposed that packet D was actually the leading edge of the first wave group oceanward from the shelf break (instead of packet B), this would lead to interpacket spacings of 82, 48, and 60 km. These would not form a regular series and so we discount this possibility. We thus hypothesize that packet D is an independent wave packet, with a different generation mechanism. The location of packet D is consistent with the local generation hypothesis, in that it is found just to the oceanward side of the emerging IT wave beam in Figure 1. The emerging IT wave beam, after reflecting from the seafloor, impinges on the thermocline from below at 20.9°S, 36.54°E, some 20 km from the leading wave in packet D. This geometry is similar to those previously observed in the Bay of Biscay and off the Iberian shelf, in which the locally generated ISW trains are first observed 20–30 km away (in the direction of ray propagation) from the position of the ray intersection with the thermocline. (This gives time for the ISWs to form from the large IT displacements of the thermocline there.)

[27] Furthermore, in Figure 7 we show another example of a SAR image (that from 20 February 2006) with two distinct ISW packets, labeled E and F (these are also shown in yellow in Figure 1). Packet E, the wave train farther offshore, has two clear large-scale wave crests that show as bright bands on a dark background (this type of SAR signature is typical of very low wind speeds, as has been explained by *da Silva et al.* [2000]). Shelfward of packet E

Figure 7. Extract at full resolution of an Envisat ASAR image (WS mode) from 20 February 2006 (yellow waves in Figure 1) showing two distinct wave packets (E and F). The image size is 38 km × 38 km and its center is at (20.72°S, 36.48°E).

we see another wave packet labeled F. This is characterized by much shorter waves (with an average wavelength of 1.5 km as compared with 5 km for packet E). As can be seen both here and in Figure 1, packets E and F are propagating in rather different directions (packet E toward 140° T and packet F toward 120° T) and have the appearance of being completely separate wave trains. Moreover, packet E is oceanward of the surfacing of the IT ray (see Figure 1), similarly to packet D in Figure 5. Since packet F is shelfward of the IT ray surfacing position while packet E is oceanward of this position we suggest that packet E also results from the local generation mechanism, while packet F is generated at the shelf break.

[28] Several of the other SAR images also show evidence for local generation. For instance, the images from 10 and 13 August 2005 (light blue and red in Figure 1, respectively) also show large wavelength ISW packets that are consistent (in terms of their location) with local generation. In particular, on 10 August, two sets of ISWs are again apparent near to the ray surfacing position, with the packet of longer waves leading the packet of shorter waves. This again suggests that waves generated both through the local generation process, and from the shelf break, are apparent in this image. In addition, on 26 September 2003, the only ISW packet observed (the orange waves in Figure 1) are of long wavelength (matching the wavelengths of the other packets identified as being locally generated), and there are no other wave packets closer to the shelf break (as would be expected if the waves were generated tidally at the shelf break). Consequently, it seems that only local generation may be occurring on this occasion.

[29] Table 1 now summarizes properties of the waves identified as having been locally generated. For each of the six SAR images discussed, Table 1 presents the maximum depth-integrated body force, the tidal range on the day in question (high-low water difference at the coastline in Beira, 20°S), the spring-neap tidal range for the time period spanning the observation date, the number of solitons identified as locally generated, and their "widths" defined from the SAR transects (this latter quantity being the width over which the SAR backscatter rises significantly above the background value). (This latter quantity is not the same as the wavelengths previously referred to, and refers to the average width of the leading soliton in the packet in question.) The locally generated waves generally have larger wavelengths and are wider than those emanating from the shelf break. Their widths vary between 1.4 and 2.6 km. Table 1 also shows that we were only able to find examples of waves in the SAR images within a few days of barotropic spring tides at the shelf break (i.e., the tidal range on the day in question is always close to the range of the neighboring spring tide). Although *Gerkema* [2002] showed that baroclinic spring tides may have an appreciable phase shift from the time of barotropic spring tides, this appears to be a relatively small effect here, as discussed earlier.

[30] We now discuss the effects of the seasonal variation of the stratification on the ISWs. First, we note that there are appreciable differences between the wave packets in the southern summer (February–April, being farther north and extending farther into the channel) and those in the southern winter (August–September, being farther south and extending less far into the channel). We have investigated the seasonal variation in stratification in Figure 2a and shown that the main difference between the seasons is that the stratification is stronger during the southern summer within the seasonal thermocline (depths shallower than 100 m). This means both that the raypaths penetrate more extensively into the channel at this time of year, and that the body force (thought to generate the waves, and proportional to N^2) is stronger. However, the surfacing positions of the rays are only different by about 5 km, and so unlikely to explain the deeper penetration of the waves into the channel (by 50–100 km). Furthermore, a simple two-layer calculation shows that the long wave phase speed is about the same (1.4 m s^{-1}) at both times of year (the weaker thermocline in October being compensated by a deeper upper layer), so that seasonal differences in the wave speeds must also be discounted from any explanation of deeper penetration into the channel during the southern summer.

[31] However, we have shown that the average of the maximum depth-integrated body force is 5.76 m^2s^{-2} in March but only 4.56 m^2s^{-2} in October. We feel that this stronger body force offers a more plausible explanation of why the waves penetrate farther into the channel at this time of year (i.e., during the southern summer when the body force is stronger, and the waves would be expected to be more energetic). Another possible factor for the more extensive penetration of the waves into the channel in the southern summer is that the thermocline at this time of year may sustain any generated interfacial waves better than the thermocline in the winter. The rate at which wave energy would leak from the thermocline into the deeper ocean (causing dissipation of the waves on the thermocline) has been termed "radiation damping" and investigated theoretically by *Akylas et al.* [2007]. Given that the long

wave speeds (c_0) are similar for both the present stratifications (as mentioned above), but that the upper layer depth (h) is larger in October (see Figure 2a), then the parameter μ of *Akylas et al.* [2007] will be larger in October (i.e., in the winter/spring), with more rapid dissipation of the waves being expected [see *Akylas et al.*, 2007, equations 2.3 and 2.18].

[32] Turning now to the issue of why the waves are farther to the south in the southern winter, we consider the seasonal variation of the currents in the region. While *Schott and McCreary* [2001] indicate that there seems to be insufficient observational evidence to make reliable statements about variations in the currents in this region, *Maltrud et al.* [1998] offer insights from a high-resolution modeling study with the POP model. This shows that the Mozambique Current (which flows southward along the western slopes of the basin) is much stronger during July–September (often 10–15 Sv southward) than during March–May (typically 0–5 Sv southward). We believe that the increased southward flow in the southern winter months would be likely to refract (advect) the waves toward a more southerly pathway at this time of year, as observed.

[33] We next consider the effect of seasonal variations in the stratification on the local generation process. In an idealized modeling study, *Gerkema* [2001] showed that this would only occur for thermoclines of ''intermediate'' strength, for which the reduced gravity parameter g' (for a two-layer stratification) lay between 0.002 and 0.02. We have estimated this parameter for the present study area as g' = 0.035 for October and g' = 0.042 for March. While these values are somewhat higher than Gerkema's theoretical intermediate range, they are significantly lower than other ocean basins (e.g., 0.08 in the Sulu Sea), and than Gerkema's strong thermocline case (g' = 0.4). Hence while we believe (from the examples presented here) that local generation is possible for both these values of g', it may be that the winter stratification with the lower value of g' is more conducive to local generation. This may also be inferred from the separate modeling study of *Akylas et al.* [2007], who investigated local generation when a beam of tidal energy is incident on the thermocline from below. For a tidal beam of fixed amplitude (C = 1), we may compare Akylas et al.'s Figure 6a, for a strong thermocline (with normalized density jump $\Delta = 4 \times 10^{-3}$ across the thermocline, and only few locally generated solitons), Figure 4b (intermediate thermocline, $\Delta = 1.5 \times 10^{-3}$, many solitons), and Figure 6b (weak thermocline, $\Delta = 0.04 \times 10^{-3}$, fewer solitons again). For the present case, our value of Δ is 4.2×10^{-3} in the summer and 3.5×10^{-3} in the winter, thus indicating that our winter examples would be expected to show more locally generated solitons.

[34] This conclusion is indeed borne out by the observations, as shown in Table 1. Our images during the winter typically have 4–6 locally generated solitons, whereas those in the summer have less than (or equal to) 3. We have also identified three additional Envisat SAR images (dated 20 May 2007, 22 February 2008, and 24 February 2008, not shown), which show only one large (in terms of width) solitary wave off the Sofala Bank, at distances consistent with local generation. These images correspond to the summer season, when the thermocline strength is enhanced. This supports our conclusion that local generation is more likely in the winter months.

[35] Finally, diurnal tides can propagate as free waves in the region north of 30°S, and so could be potentially important in the Mozambique Channel. However, *Egbert and Ray* [2003] computed (from T/P data) tidal dissipation rates and vertically integrated kinetic energy global maps for diurnal and semidiurnal constituents. Their results (Figures 1 and 2a–2c) suggest that, in the Mozambique Channel, barotropic to baroclinic conversion (i.e., the generation of internal tides from surface tides) is much stronger for semidiurnal tides (M_2) than for diurnal tides (K_1). In addition, ray tracing diagrams show that diurnal frequency IT beams would reemerge at the surface at about 230 km from the shelf break, much too far to play a part in explaining the occurrence of the observed ISWs from about 80–90 km from the shelf break. We thus conclude that, in the Mozambique Channel, diurnal tides are not expected to play an important role in the generation of internal tides and ISWs.

[36] In conclusion, we have identified the Mozambique Channel, and in particular the Sofala Shelf between 20° and 21°S, as a hot spot for the generation of internal waves and internal tides which travel oceanward away from the shelf break. This results from a strong barotropic tidal forcing and large cross-slope transports, coupled with shelf break topography that is sufficiently steep for critical regions to occur from which deep oceanward internal tidal rays may emanate. The hot spot region is localized between 20° and 21°S because of the particular nature of the bathymetry there. Farther north and south, the forcing is reduced and insufficient to generate ISWs. We have suggested that the internal solitary wave packets result from both direct generation at the shelf break and from local generation at about 80 km oceanward from the break because of the surfacing of internal tidal rays at the thermocline. Finally, we have investigated seasonal differences in the wave patterns, which penetrate more extensively into the channel during the southern summer, and appear slightly farther to the south during the southern winter. We also conclude that the local generation process is more likely to occur during the winter when the stratification is reduced.

[37] **Acknowledgments.** The SAR image data presented here were provided by the European Space Agency (ESA) under project AOPT-2423. The work was undertaken as part of the SPOTIWAVE-II, hot spots of internal wave activity off Iberia revealed by multisensor remote sensing satellite observations (project codes POCI/MAR/57836/2004 and POCTI/CTA/41130/2001), and AMAZING (project code PDCTE/CTA/49953/2003) projects, funded by the Portuguese Science and Technology Foundation (FCT). We thank both the reviewers for their helpful comments, which we feel have helped to improve the paper significantly.

References

Akylas, T. R., R. H. J. Grimshaw, S. R. Clarke, and A. Tabaei (2007), Reflecting tidal wave beams and local generation of solitary waves in the ocean thermocline, *J. Fluid Mech.*, *593*, 297–313, doi:10.1017/S0022112007008786.

Alpers, W. (1985), Theory of radar imaging of internal waves, *Nature*, *314*, 245–247, doi:10.1038/314245a0.

Azevedo, A., J. C. B. da Silva, and A. L. New (2006), On the generation and propagation of internal solitary waves in the southern Bay of Biscay, *Deep Sea Res., Part I*, *53*, 927–941, doi:10.1016/j.dsr.2006.01.013.

Baines, P. G. (1982), On internal tide generation models, *Deep Sea Res., Part A*, *29*, 307–338, doi:10.1016/0198-0149(82)90098-X.

da Silva, J. C. B., S. A. Ermakov, I. S. Robinson, D. R. G. Jeans, and S. V. Kijashko (1998), Role of surface films in ERS SAR signatures of internal

waves on the shelf: 1. Short-period internal waves, *J. Geophys. Res.*, *103*, 8009–8031, doi:10.1029/97JC02725.

da Silva, J. C. B., S. A. Ermakov, and I. S. Robinson (2000), Role of surface films in ERS SAR signatures of internal waves on the shelf: 3. Mode transitions, *J. Geophys. Res.*, *105*, 24,089–24,104, doi:10.1029/2000JC900053.

da Silva, J. C. B., A. L. New, and A. Azevedo (2007), On the role of SAR for observing local generation of internal solitary waves off the Iberian Peninsula, *Can. J. Remote Sens.*, *33*, 388–403.

Egbert, G. D., and S. Y. Erofeeva (2002), Efficient inverse modeling of barotropic ocean tides, *J. Oceanic Atmos. Technol.*, *19*, 183–204, doi:10.1175/1520-0426(2002)019<0183:EIMOBO>2.0.CO;2.

Egbert, G. D., and R. D. Ray (2003), Semi-diurnal and diurnal tidal dissipation from TOPEX/POSEIDON altimetry, *Geophys. Res. Lett.*, *30*(17), 1907, doi:10.1029/2003GL017676.

Garrett, C., and L. St. Laurent (2002), Aspects of deep ocean mixing, *J. Oceanogr.*, *58*, 11–24, doi:10.1023/A:1015816515476.

Gerkema, T. (2001), Internal and interfacial tides: Beam scattering and local generation of solitary waves, *J. Mar. Res.*, *59*, 227–255, doi:10.1357/002224001762882646.

Gerkema, T. (2002), Application of an internal tide generation model to baroclinic spring-neap cycles, *J. Geophys. Res.*, *107*(C9), 3124, doi:10.1029/2001JC001177.

Gerkema, T., F.-P. A. Lam, and L. R. M. Maas (2004), Internal tides in the Bay of Biscay: Conversion rates and seasonal effects, *Deep Sea Res., Part II*, *51*, 2995–3008, doi:10.1016/j.dsr2.2004.09.012.

Konyaev, K. V., K. D. Sabinin, and A. N. Serebryany (1995), Large-amplitude internal waves at the Mascarene ridge in the Indian Ocean, *Deep Sea Res., Part I*, *42*, 2075–2091, doi:10.1016/0967-0637(95)00067-4.

Lamb, K. G. (1994), Numerical experiments of internal wave generation by strong tidal flow across a finite amplitude bank edge, *J. Geophys. Res.*, *99*, 843–864, doi:10.1029/93JC02514.

Maltrud, M. E., R. D. Smith, A. J. Semtner, and R. C. Malone (1998), Global eddy-resolving ocean simulations driven by 1985–1995 atmospheric winds, *J. Geophys. Res.*, *103*, 30,825–30,853, doi:10.1029/1998JC900013.

Manders, A. M. M., L. R. M. Maas, and T. Gerkema (2004), Observations of internal tides in the Mozambique Channel, *J. Geophys. Res.*, *109*, C12034, doi:10.1029/2003JC002187.

Merrifield, M. A., and P. E. Holloway (2002), Model estimates of M2 internal tide energetics at the Hawaiian Ridge, *J. Geophys. Res.*, *107*(C8), 3179, doi:10.1029/2001JC000996.

Morozov, E. G. (1995), Semidiurnal internal wave global field, *Deep Sea Res., Part I*, *42*, 135–148, doi:10.1016/0967-0637(95)92886-C.

Moum, J. N., D. M. Farmer, W. D. Smyth, L. Armi, and S. Vagle (2003), Structure and generation of turbulence at interfaces strained by internal solitary waves propagating shoreward over the continental shelf, *J. Phys. Oceanogr.*, *33*, 2093–2112, doi:10.1175/1520-0485(2003)033<2093:SAGOTA>2.0.CO;2.

New, A. L., and J. C. B. da Silva (2002), Remote-sensing evidence for the local generation of internal soliton packets in the central Bay of Biscay, *Deep Sea Res., Part I*, *49*, 915–934, doi:10.1016/S0967-0637(01)00082-6.

New, A. L., and R. D. Pingree (1990), Large-amplitude internal soliton packets in the central Bay of Biscay, *Deep Sea Res., Part A*, *37*, 513–524, doi:10.1016/0198-0149(90)90022-N.

New, A. L., and R. D. Pingree (1992), Local generation of internal soliton packets in the central Bay of Biscay, *Deep Sea Res., Part A*, *39*, 1521–1534, doi:10.1016/0198-0149(92)90045-U.

New, A. L., and R. D. Pingree (2000), An intercomparison of internal solitary waves in the Bay of Biscay and resulting from Korteweg-de Vries-type theory, *Prog. Oceanogr.*, *45*, 1–38, doi:10.1016/S0079-6611(99)00049-X.

New, A. L., S. G. Alderson, D. A. Smeed, and K. L. Stansfield (2007), On the circulation of water masses across the Mascarene Plateau in the south Indian Ocean, *Deep Sea Res., Part I*, *54*, 42–74, doi:10.1016/j.dsr.2006.08.016.

Niwa, Y., and T. Hibiya (2004), Three-dimensional numerical simulation of M2 internal tides in the East China Sea, *J. Geophys. Res.*, *109*, C04027, doi:10.1029/2003JC001923.

Pingree, R. D., and A. L. New (1989), Downward propagation of internal tidal energy into the Bay of Biscay, *Deep Sea Res., Part A*, *36*, 735–758, doi:10.1016/0198-0149(89)90148-9.

Pingree, R. D., and A. L. New (1991), Abyssal penetration and bottom reflection of internal tidal energy in the Bay of Biscay, *J. Phys. Oceanogr.*, *21*, 28–39, doi:10.1175/1520-0485(1991)021<0028:APABRO>2.0.CO;2.

Pingree, R. D., G. T. Mardell, and A. L. New (1986), Propagation of internal tides from the upper slopes of the Bay of Biscay, *Nature*, *321*, 154–158, doi:10.1038/321154a0.

Pinkel, R. (2000), Internal solitary waves in the warm pool of the western equatorial Pacific, *J. Phys. Oceanogr.*, *30*, 2906–2926, doi:10.1175/1520-0485(2001)031<2906:ISWITW>2.0.CO;2.

Sabinin, K. D., and A. N. Serebryanyi (2007), "Hot Spots" in the field of internal waves in the ocean, *Acoust. Phys.*, *53*, 357–380, doi:10.1134/S1063771007030128.

Schott, F. A., and J. P. McCreary (2001), The monsoon circulation of the Indian Ocean, *Prog. Oceanogr.*, *51*, 1–123, doi:10.1016/S0079-6611(01)00083-0.

Sherwin, T. J., V. I. Vlasenko, N. Stashchuk, D. R. G. Jeans, and B. Jones (2002), Along-slope generation as an explanation for some unusually large internal tides, *Deep Sea Res., Part I*, *49*, 1787–1799, doi:10.1016/S0967-0637(02)00096-1.

Thompson, D. R., and R. F. Gasparovic (1986), Intensity modulation in SAR images of internal waves, *Nature*, *320*, 345–348, doi:10.1038/320345a0.

Zhao, Z., V. Klemas, Q. Zheng, and X. Yan (2004), Remote sensing evidence for the baroclinic tide origin of internal solitary waves in the northeastern South China Sea, *Geophys. Res. Lett.*, *31*, L06302, doi:10.1029/2003GL019077.

J. C. B. da Silva and J. M. Magalhaes, Institute of Oceanography, University of Lisbon, Rua Ernesto de Vasconcelos, Campo Grande, 1749-016 Lisbon, Portugal. (jdasilva@fc.ul.pt; jmagalhaes@fc.ul.pt)

A. L. New, Ocean Modelling and Forecasting Group, National Oceanography Centre, Southampton, European Way, Southampton SO14 3ZH, UK. (anw@noc.soton.ac.uk)

Chapter 4

Soliton generation by internal tidal beams impinging on a pycnocline: laboratory experiments

Matthieu, J.M., Mathur, M., Gostiaux, L., Gerkema, T., Magalhaes, J.M., da Silva, J.C.B., Dauxois, T., 2011. Soliton generation by internal tidal beams impinging on a pycnocline: laboratory experiments. J. Fluid Mech. Submitted.

Soliton generation by internal tidal beams impinging on a pycnocline : laboratory experiments

MATTHIEU J. MERCIER[1,6]†, MANIKANDAN MATHUR[2,3,1], LOUIS GOSTIAUX[2], THEO GERKEMA[4], JORGE M. MAGALHÃES[5], JOSÉ C. B. DA SILVA[5] AND THIERRY DAUXOIS[6]

[1]Department of Mechanical Engineering, Massachusetts Institute of Technology, 77 Massachusetts Avenue, Cambridge, MA 02139, USA.

[2] Laboratoire des Ecoulements Geophysiques et Industriels (LEGI), UMR 5519 CNRS-UJF-INPG, 21 rue des Martyrs, 38000 Grenoble, France.

[3] Laboratoire de Météorologie Dynamique, École Polytechnique, 91128 Palaiseau, France.

[4] Royal Netherlands Institute for Sea Research (NIOZ), P.O. Box 59, 1790 AB Den Burg, Texel, The Netherlands.

[5] CIMAR/CIIMAR, Centro Interdisciplinar de Investigacão Marinha e Ambiental and Departamento de Geociências, Ambiente e Ordenamento do Território, Universidade do Porto, Rua do Campo Alegre, 687, 4169-007 Porto, Portugal.

[6] Laboratoire de Physique de l'École Normale Supérieure de Lyon, Université de Lyon, CNRS, 46 Allée d'Italie, F-69364 Lyon cedex 07, France.

(Received 4 August 2011)

Several observations of internal solitary waves in the deep ocean using Synthetic Aperture Radar (SAR) imagery have been reported in the last two decades, as a result of tidal wave beams (generated at a bottom topography site) impinging on the seasonal thermocline near the ocean surface. This mechanism of "local generation" has recently

† Email address for correspondence: mmercier@mit.edu

been investigated both theoretically and numerically, but a direct correspondence with the ocean observations still remains elusive. In this paper, we present the first laboratory experiments that show the generation of internal solitary waves by the impingement of a quasi two-dimensional internal wave beam on a thermocline-like feature (referred to as the pycnocline in the rest of the paper). Nonlinear processes involved are of two kinds. First, we observe the generation of a mean flow and higher harmonics in our experiments, and their characteristics are presented in detail using Particle Image Velocimetry measurements. Then, the appearance of internal solitary waves is characterized using a bulge-like feature in the power spectra of the pycnocline displacements measured using ultrasonic probes. Finally, the relevance of our results for understanding ocean observations is discussed.

1. Introduction

Internal solitary waves (ISWs) are among the most noticeable kinds of internal waves in the ocean; their surface manifestation may be visible even from spacecraft (see, for example, Jackson 2007). They often appear in groups, and the groups themselves usually appear regularly, every tidal period. This points to a tidal origin; barotropic tidal flow over topography creates internal tides, which, while propagating away from their source, may steepen and split up into ISWs. This is the common picture, in which the internal tide is regarded as a horizontally propagating, interfacial wave. In the early nineties, New & Pingree (1990, 1992) showed the first evidence of a very different generation mechanism of ISWs. The origin is still tidal, but the mechanism involves an internal tidal beam, generated over the continental slope, which first propagates downward, then reflects from the ocean floor, and finally, as its energy goes upward, impinges on the seasonal thermocline; here it creates a depression, which, while propagating away, steepens and evolves into ISWs. This interpretation has been corroborated by Synthetic Aperture Radar (SAR) imagery, showing a great increase of ISWs in the central Bay of Biscay, just beyond the area where the beam is expected to approach the surface (New & Da Silva 2002; Da Silva *et al.* 2007). Recently, the same mechanism has been proposed to explain ISWs off Portugal (Da Silva *et al.* 2007) and in the Mozambique Channel (Da Silva *et al.* 2009).

In this paper we present results on laboratory experiments – carried out at the LEGI Coriolis Platform in Grenoble in 2008 – that were set up to create ISWs by this very mechanism, i.e. by an internal wave beam impinging on a pycnocline. At the beginning of the generation process lies the internal 'tidal' beam, generated here with a recently designed wavemaker (Gostiaux *et al.* 2007; Mercier *et al.* 2010), which creates a well-defined monochromatic unidirectional beam. We varied the stratification (i.e. the strength, depth

and thickness of the pycnocline), and for each stratification we carried out experiments with different forcing frequencies, thus changing the angle the beam makes with the vertical.

In the set-up of the experiments, we were guided by theoretical studies on the subject. The process starts at the wavemaker, from which the internal-wave beam originates. So as long as it propagates through the layer of uniform stratification, no significant changes are expected to occur. The point is that any beam depending on just one of the characteristic coordinates, propagating in a uniformly stratified Boussinesq fluid, satisfies not only the linear but also the nonlinear equations of motion (Tabaei & Akylas 2003). It is only when the other characteristic coordinate comes into play as well, that nonlinear effects arise; at the junction of the beams, higher harmonics are then created (Tabaei *et al.* 2005; Jiang & Marcus 2009). This situation occurs when beams cross or reflect from boundaries.

In our set-up (and in the ocean, too), the first deformation of the beam is expected to happen when it leaves the layer of near-constant stratification, i.e. when it encounters the pycnocline. This strong inhomogeneity of the medium causes the beam to reflect partially from and within the pycnocline, a linear process that 'scatters' the beam. As a result, energy stays behind in the pycnocline; it has been shown in theoretical studies that this forms the basis from which ISWs may later evolve (Gerkema 2001; Akylas *et al.* 2007). At the same time, the partial reflections within the pycnocline, as well as the full reflection from the upper surface, create junctions of crossing beams, and hence form a source of nonlinear generation of higher harmonics. In our laboratory experiments, we thus focused on these two features: first, the evolution of the pycnocline after the impact of the beam, and second, higher harmonics. In a way, they are contrasting phenomena: ISWs in the pycnocline are the nonlinear result of a depression that steepened, the

depression itself originating from an essentially linear process (internal reflections in the pycnocline). On the other hand, higher harmonics, propagating as isolated beams into the constantly stratified lower layer, behave as linear waves but find their origin in a nonlinear process at the junction of the main beam and its reflected counterpart. This distinction in behaviour has consequences for the tools by which they may be analyzed; in particular, the application of harmonic analysis is well-suited to extract the essentially linear higher harmonic beams from the measurements, but cannot expect to yield anything clear on the genuinely nonlinear ISWs. The same is true for wave spectra. We discuss this further below.

The linear regime of the problem we address, an internal wave beam impinging a continuously stratified pycnocline in a finite-depth tank, was studied in Mathur & Peacock (2009). Their experimental results on wave beam ducting, a scenario where the incident energy tends to remain trapped in the pycnocline even after multiple reflections within the pycnocline, were in excellent agreement with the viscous theory. This linear process, as discussed in Gerkema (2001) and Akylas *et al.* (2007), serves as a precursor to the formation of solitons.

Previous experimental and theoretical studies have identified the key parameters governing the response of the pycnocline to the incident beam. Delisi & Orlanski (1975) derived a parameter β which (apart from a factor of two) is the ratio of the phase speed for interfacial waves, $C_{if} = \omega/k_{if}$, and the horizontal phase speed of the incident beam, $C_b = \omega/k_b$ (Here ω denotes the wave frequency, k_{if} the wavenumber of the interfacial wave and k_b the dominant wavenumber of the beam.). The interfacial waves were (implicitly) assumed to be purely interfacial and short, and hence must obey the dispersion relation $\omega^2 = g'k_{if}/2$ (with reduced gravity g'), so that their phase speed becomes $C_{if} = g'/2\omega$. The ratio thus becomes $C_{if}/C_b = g'k_b/2\omega^2$, which equals $\beta/2$ in the

definition of Delisi & Orlanski (1975). (We reproduce the argument in some detail here, because the analysis by Delisi & Orlanski (1975) contains a few unclarities; notably, some of their assumptions are implicit, and they confound k_{if} with k_b. An alternative exegesis of their result was put forward by Thorpe (1998).) Their experimental results show that the response of the pycnocline is largest when $|\beta| \approx 1$. In a different setting, in which the interfacial waves were assumed to be long rather than short, a similar criterion was identified in terms of a parameter γ, defined as the ratio of the phase speed of interfacial waves and that of the first mode of the uniformly stratified lower layer (Gerkema 2001). We amplify on this below. Finally, Akylas *et al.* (2007), in a setting closer to that of Delisi & Orlanski (1975) – their lower uniformly stratified layer being infinitely deep –, recovered the same key parameter β (which they call α). In either setting, the parameter g' plays a key role, and we study its influence by examining different shapes and strengths of the pycnocline.

Recently, in a configuration similar to the present setup, Grisouard *et al.* (2011) reproduced the local generation of ISWs with nonlinear, nonhydrostatic numerical simulations and showed that higher mode ISWs (namely mode-2 and 3) may also be generated by this mechanism. In their studies, high mode waves (such as mode-2) are favoured by a strongly stratified pycnocline or, equivalently, by a beam with short wavelength.

The paper is organized as follows. In section 2, a description of the experimental set-up and the measurement techniques is given. An analysis of the results from Particle Image Velocimetry is given in Section 3, where we focus on the mean flow and harmonics. Results from the ultrasonic probes are presented in Section 4; they provide a quantitative view of the pycnocline displacements and the ISWs. Finally, we end with a discussion of our results and conclusions in section 5.

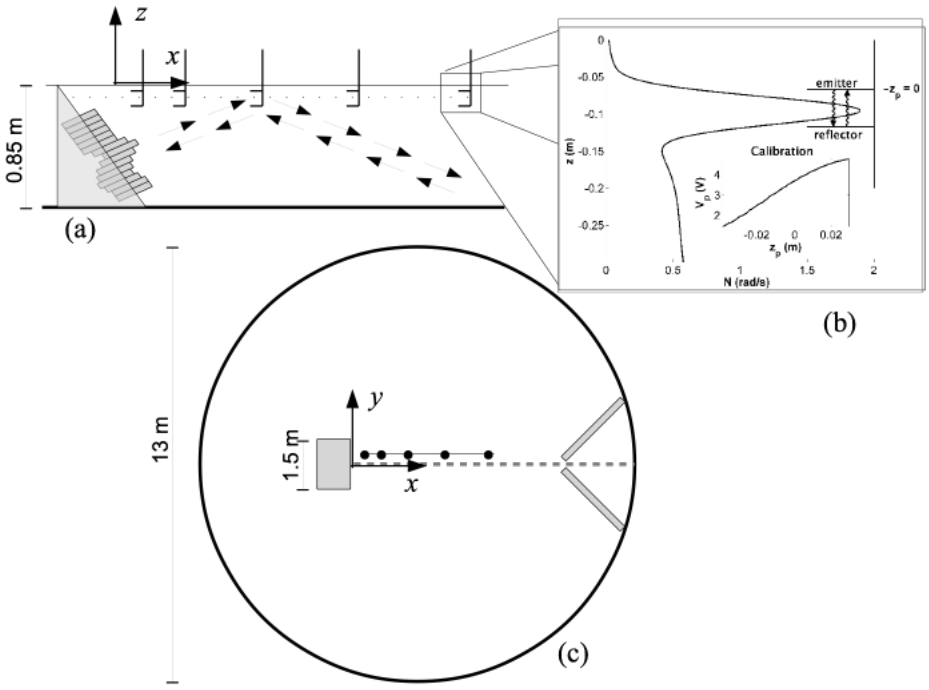

FIGURE 1. Schematic of the experimental setup, (a) side view and (c) top view. (b) Zoom on the ultrasonic probe and its relative positioning with respect to the stratification. Note that the emitter and the reflector encompass the pycnocline. A typical calibration curve obtained by traversing the probe in quiescent medium is shown in the inset.

2. Description of the experimental set-up

The experiments were carried out at the Coriolis Platform of LEGI, Grenoble (see Figure. 1 for a schematic of the experimental setup). This facility is a 13 m diameter rotating basin that can be filled with salty water; during the process of filling, the salinity can be changed, so that a vertically stratified layer is formed. The platform can serve as a turntable, but the experiments discussed here were done without rotation.

2.1. *Experimental parameters*

A vertically stratified layer of height 80 cm was created by filling the tank from below with water whose salinity was gradually increased; this resulted in a layer whose density

ρ increased from 1010 kg/m^3 at the top to 1040 kg/m^3 at the bottom. Thus, a layer of uniform stratification was formed with $N_0 = 0.58$ rad/s, where N_0 is the Brunt-Väisälä frequency. The first experiments were carried out with this layer alone, which did not stay uniformly stratified in subsequent days. As a result, the stratification in the lowest part of the tank became slightly weaker with time.

Then, a thin layer (viz. 4 cm) of fresh water ($\rho \approx 1000$ kg/m^3) was added from above on top of the uniformly stratified layer. This served as the upper mixed layer, while the sharp transition of density between the two layers ensured the presence of a pycnocline. The pycnocline tended to lose its sharpness rather quickly, especially during the experiments, and so new fresh layers were added after experiments, or sometimes the upper part of the water column was removed before adding fresh water. In this way, a whole range of different pycnoclines (in terms of peak value, thickness, and depth) was created, serving as varying background conditions during which the experiments were carried out (see Figure 9 (a)).

In the basin, an internal-wave beam directed upwards was generated by a wavemaker similar to the one developed by Gostiaux *et al.* (2007), to which we refer for a detailed description. Briefly, the device consists of 24 stacked PVC sheets, shifted with respect to each other so as to form a wave pattern similar to the Thomas-Stevenson wave beam described in Mercier *et al.* (2010). The plates are connected via two eccentric camshafts, which, when subject to rotation, results in downward (phase) propagation of the wave pattern. Placed in a stratified fluid with an angle of 30° with respect to the vertical, as depicted in Figure. 1 (a), this wave motion is imparted to the fluid, thus producing a unidirectional internal wave beam at a single frequency. Measured along the wavemaker, the width of the generated beam is of the order of 33 cm. The device had a finite width

Name	N_0 (rad/s)	γ	T (s)	k_η (rad/m)	λ_x (cm)	C_x (cm/s)
EXP03	0.58	0	21.6	31.7	39.5	1.83
EXP08	0.58	0.11	21.6	31.7	39.5	1.83
EXP16	0.58	0.19	21.6	31.7	39.5	1.83
EXP19	0.58	0.24	21.6	31.7	39.5	1.83
EXP21	0.58	0.17	41.8	32.8	73.8	1.77
EXP22	0.58	0.17	21.6	31.7	39.5	1.83
EXP25	0.58	0.17	16.9	32.2	30.4	1.80

TABLE 1. Name of the experiment; N_0, the near-uniform stratification in the lower layer; γ, a measure of the strength of the pycnocline (as explained below); the forcing period T; the dominant wavenumber of the initial beam k_η; the horizontal wavelength of the initial beam, $\lambda_x = 2\pi/k_\eta \sin\theta$, where θ is the angle of the beam with the horizontal; and finally, the corresponding horizontal phase speed, $C_x = \lambda_x/T$.

of 1.5 m along the y-direction, resulting in three-dimensional effects close to the edges. The periods of oscillation in various experiments are listed in Table 1.

Quantitative measurements of the velocity field and the pycnocline displacements were made using Particle Image Velocimetry and ultrasonic probes, respectively.

2.2. *Particle Imagery Velocimetry (PIV)*

Velocity fields have been obtained through PIV measurements done in the (xOz) plane as shown in Figure 1 (c) (grey dashed line). Two CCD 12-bit cameras of resolution 1024 x 1024 record images of particles at 3 Hz using a 6 W continuous laser. Although the spatial resolution obtained is good, smaller than 1 mm/pix, it is only possible to visualize the linearly stratified region due to the strong optical distortions caused by the presence of the pycnocline.

Furthermore, the seeding of particles in the homogeneous surface layer is insufficient

since the particles used here rather match the density range of the stratified layer. Some information can be extracted from floating particles at the free surface, as we will see in section 3.1, which allow us to extrapolate the velocity field from the the top of the linearly stratified region up to the free surface.

Experimental data are processed using open source CIVx algorithms by Fincham & Delerce (2000) and the free Matlab toolbox UVMAT developed at LEGI. Some overlap between the fields of view of the two cameras allow for a horizontal merging of the velocity fields, leading to visualization windows of 1.6 x 0.8 m.

2.3. *Ultrasonic probes*

The ultrasonic probes designed at LEGI (Michallet & Barthlemy 1997) consisted of a sound emitter (which also acts as a receiver) and a reflector that were 0.05m apart. Ten such probes were positioned at $x = 0.18$, 0.39, 0.62, 0.89, 1.20, 1.254, 1.59, 2.09, 2.80 and 4.0 m from the wave generator, respectively (see Figure 1 (a)). Each probe was mounted vertically on a plane that was slightly off-centered (so as to not interfere with the PIV measurements), at a height that ensured that the emitter was in the mixed layer and the reflector in the lower constant stratification layer. The voltage output from the probe is proportional to the time taken for the sound to traverse its path from the emitter to the reflector and back to the emitter/receiver. This traverse time is directly proportional to the relative distance between the emitter and the pycnocline, if the pycnocline is infinitesimally sharp. In realistic scenarios, like the stratification in our experiments, where the pycnocline is of finite thickness, the output from the ultrasonic probe is a measure of the average (over z) displacement of the pycnocline at the specific x location of the probe.

To calibrate each ultrasonic probe, it is moved (using a linear traverse mechanism) up and down by known distances in a quiescent setting where there is no flow (and hence

no pycnocline displacements). The output voltage is continuously recorded as a function of the position of the probe. This allows us to get a voltage V_p vs. relative position of the pycnocline z_p relation for the probe (see Figure 1 (b)), and the procedure is done for every probe. Converting the output voltage from experiments to equivalent pycnocline displacements involves interpolation on the respective calibration curves.

It is important to note that the values thus found are a measure of the mean vertical displacements between the emitter and receiver. A mode trapped in the pycnocline will have maximum vertical excursions at a certain depth, while the excursions decline rapidly above and below. The acoustic probes, then, will not yield this maximum excursion, but a lower value, because it also registers over parts in which the amplitude is declining.

3. Mean flow and harmonics

Using PIV, we visualize what happens when the incident wave beam encounters the pycnocline and subsequently reflects from it. To demonstrate the significance of the presence of a pycnocline, we first present a qualitative comparison between settings without and with a pycnocline, see Fig. 2. The effect of the pycnocline, as seen in the unfiltered PIV data presented in the lower panel of Fig. 2, is twofold. First, it shifts the beam slightly to the right because the beam propagates at a shallower angle with respect to the horizontal in the layer of strong stratification (as indicated by the dashed line which represents the theoretical path of energy propagation). Second, the reflected beam is broadened, and therefore less intense, when it emerges from the pycnocline. This is caused by (multiple) internal reflections: the beam reflects not only from the upper free surface but also from and within the pycnocline itself (see, e.g., Gerkema (2001); Mathur & Peacock (2009)).

As mentioned in the introduction, two kinds of nonlinear phenomena are expected to take place during reflection at the pycnocline: the nonlinear evolution of the pycnocline displacements excited by the incoming beam, and the generation of higher harmonics at the junction between the incident and reflected beams (The latter occurs even if no pycnocline is present, namely upon reflection from the surface.). As noted earlier, the upper most part of the water column produces no visible signal with PIV in the experiments with a pycnocline. Therefore, we resort to the acoustic probes for visualizing and analyzing the response at the pycnocline, the subject of section 4. In this section, we focus on the features extracted from the PIV data, notably the principal beam and its harmonics.

The harmonics cannot be properly interpreted unless we take into account another phenomenon that we found in our experiments: the occurrence of a mean flow in the upper layer. We therefore proceed to discuss this phenomenon first.

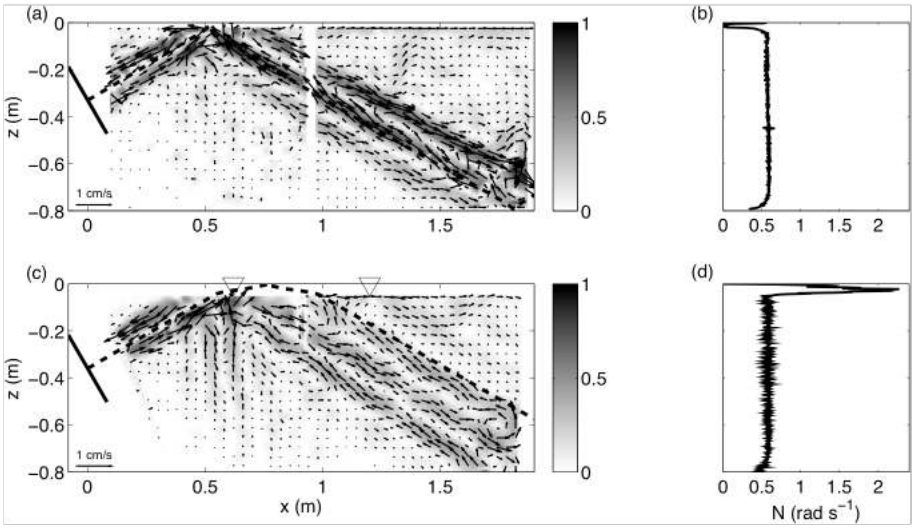

FIGURE 2. Comparison between experiments without (upper panels, EXP03) and with a pycnocline (lower panels, EXP08). The stratification profiles are shown in (b) and (d), and the corresponding experiments with a forcing period of 21.6 s in (a) and (c), respectively. Grey tones indicate the amplitude of the velocity field (in cm s^{-1}), defined as $\sqrt{u^2 + w^2}$, at $t = 240$ s after the start-up of the forcing; the arrows indicate the corresponding instantaneous velocity vectors. The position of the wavemaker is indicated by the solid line on the left. The dashed lines represent the theoretical direction of internal-wave energy propagation, starting from the center of the wavemaker. Insufficient overlap between the two cameras, around $x = 0.9$ m, leads to a gap in the velocity field in (a). The two inverted triangles in (c) indicate the positions of the ultrasonic probes at $x = 0.62$ m and $x = 1.20$ m.

3.1. *Mean flow*

Apart from extracting the higher harmonics from the PIV data, harmonic analysis also reveals the presence of a mean flow. The mean flow for EXP08, in which the cameras were placed close to the wavemaker, is shown in Figure 3. It is found to originate from the area of reflection of the forced beam at the pycnocline, and spread further in the direction of wave propagation, but remains restricted to the upper layer. The horizontal mean velocity displayed here is obtained by averaging over 12 forcing periods, starting at $t = 360$ s after the start-up of the forcing.

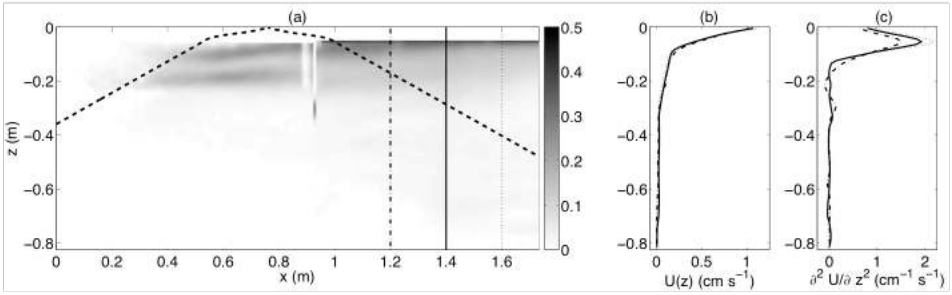

FIGURE 3. (a) Mean horizontal velocity in cm s^{-1} and vertical profiles of (b) the horizontal velocity and (c) its second derivative extracted at $x = 1.2$ m (dashed-dotted line), 1.4 m (continuous line) and 1.6 m (dotted line) from the wavemaker, for EXP08. The horizontal velocity at the free surface is estimated from PIV images and used to interpolate cubically the missing values in the pycnocline. The thick dashed line represents the theoretical direction of internal-wave energy propagation, starting from the center of the wavemaker. Insufficient overlap between the two cameras, around $x = 0.9$ m, leads to a gap in the velocity field.

A complete description of the mean-flow field is not directly available as the PIV data lacks information in the upper few centimeters (typically 5 cm, with the exact value depending on the experiment). This is partially remedied by determining, from the raw PIV images, the strength of the mean flow at the free surface ($z = 0$) by following the particles trapped there by capillary effects. This allows us to establish the profile of the mean flow over the entire vertical, without having to extrapolate; we only interpolate (cubically) over the interval where data is lacking, typically $z \in [-5; 0[$ cm. Fig. 3 (a) and (b) illustrate such profiles. The second vertical derivative of the mean horizontal velocity, plotted in Fig. 3 (c), is an important quantity as it features in equation (3.1), determining the vertical modal structure. A noticeable characteristic of the mean flow is that its amplitude varies with x, being maximum where it originates (at the area of reflection of the forced beam at the pycnocline) and then decaying slightly as you go away from the wavemaker (see the three extracted profiles in Fig. 3). This evolution must be a signature of a three-dimensional structure of the flow; the amplitudes of the wave field

at the forcing and higher harmonic frequencies, however, did not exhibit a similar decay in x. Hence, for the present purposes we assume the flow to be quasi-two-dimensional.

Interestingly, the mean flow is also present in the case without a pycnocline (EXP03, not shown). So, it is the reflection from the surface, rather than the passage through the pycnocline, which lies at the origin of the mean flow. Furthermore, we verified that the mean flow is not present at the beginning of the experiment and is noticeable only after the beam impinges on the pycnocline and surface.

In none of the experiments is an appreciable mean flow found near the bottom of the tank, even though there, too, beam reflection takes place. The first reflected beam (from the pycnocline/free surface) is weaker than the incident forced beam when it arrives near the bottom, but not considerably weaker (see Figure 2). The contrast between the presence of a mean flow near the surface and its absence near the bottom is presumably due to the different nature of the boundaries, a free surface versus a solid boundary (i.e., free-slip versus no-slip). Furthermore, nonlinear effects are stronger at the pycnocline and may result in a net deposit of momentum. These explanations, however, must remain hypotheses since our experiments do not allow us to draw any firm conclusions. Other experiments dedicated to this mean flow are needed to better understand its cause and its possibly three dimensional structure, as well as its dependence on various parameters (impinging beam angle/profile, strength of the pycnocline etc.). As discussed in the following sections, incorporating the effects of the mean flow plays a crucial role in the interpretation of the higher harmonics and other nonlinear waves in our experiments.

3.2. *Higher harmonics*

Here, we present a harmonic analysis of the PIV data from three experiments that were carried out on the same day (i.e. with the same density profile), but at different forcing frequencies: $\omega_f = 0.15$ rad/s (EXP21), $\omega_f = 0.29$ rad/s (EXP22), $\omega_f = 0.37$ rad/s

(EXP25). These three experiments had the cameras placed further away from the wavemaker than in EXP08, and hence provide a more complete view of the region after reflection from the pycnocline.

In EXP25, presented in Figure 4, the principal beam at the forcing frequency reflects from the pycnocline and surface, and broadens due to internal reflections; the dominant wavenumber in the reflected beam, $k_x^{(r)} \simeq 10.7$ rad/m is much smaller than the corresponding value in the incident wave beam, $k_x^{(i)} = 20.7$ rad/m. The reflected beam at the forcing frequency, which radiates away from the pycnocline into the lower layer, is in stark contrast with the higher harmonics $2\omega_f$ (and $3\omega_f$, not shown in the figure), which are trapped in the upper part of the water column and propagate purely horizontally with a well-defined horizontal periodicity. For the $2\omega_f$-signal, we find a horizontal wavelength of 22 cm. The fact that the harmonics are trapped is readily understood from linear internal-wave theory, since their frequencies $2\omega_f, 3\omega_f$ etc. exceed the buoyancy frequency of the lower layer (N_0); hence the harmonics cannot propagate into it and are constrained to the pycnocline.

The experimentally measured horizontal wavelength of the trapped higher harmonics may be compared with the theoretical estimates from the eigenvalue problem for the vertical modal structure

$$W'' + \Big[\frac{N^2}{(U-c)^2} - \frac{U''}{U-c} - k^2\Big]W = 0\,, \tag{3.1}$$

with the vertical velocity $w(x,z,t) = \Re[W(z)\exp[i(kx-\omega t)]]$, and the boundary condition $W = 0$ at the surface and bottom (LeBlond & Mysak 1978, Eq. 41.8). Here, $c = \omega/k$ is the horizontal phase speed, $U(z)$ is the background mean flow profile, $U''(z)$ its second derivative and $N(z)$ the buoyancy frequency profile. We note that this equation is different from the one in terms of the vertical isopycnal displacement, η (In the literature,

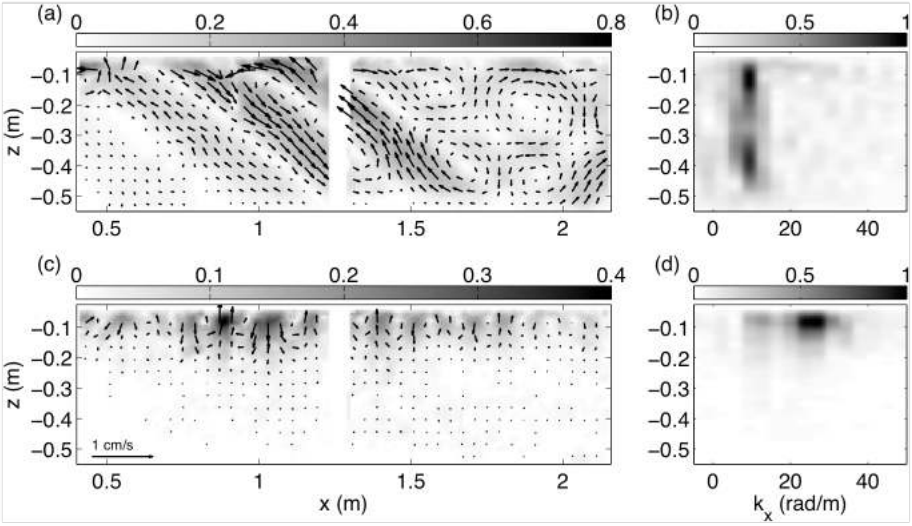

FIGURE 4. EXP25, harmonic analysis for the forcing frequency ω_f (upper panels), and the first harmonic $2\omega_f$ (lower panels). Panels (a) and (c) display the velocity vector fields with grey tones indicating the amplitude of the velocity field (in cm s^{-1}). The arrow indicating the scale of the velocity vectors in (c) is also valid for (a). Panels (b) and (d) show the spectra of the horizontal wavenumber and its vertical variation (for each, amplitudes are normalized to one).

the two forms are sometimes confounded.). The relation between the two follows from $w = \eta_t + U\eta_x$, so that $W = ik(U-c)\phi$, where $\eta = \Re\{\phi(z)\exp[i(kx-\omega t)]\}$.

For $\omega = 2\omega_f$, and observed $N(z)$ and $U(z)$, we solve (3.1) to obtain the modes W_n and corresponding wavenumbers k_n or wavelengths $\lambda_n = 2\pi/k_n$. For EXP25, we find $\lambda_1 = 49$, $\lambda_2 = 20$ and $\lambda_3 = 15$ cm, using the background mean flow profile measured at $x = 1.15$m. The observed horizontal wavelength of the signal at $\omega = 2\omega_f$ is the closest to that of the theoretical 2^{nd} mode (i.e., 22 cm). This is confirmed by the excellent agreement between the experimental and theoretical profiles of W_2 and U_2, as shown in Figure 5, at least so far as the comparison can be made (as mentioned earlier, PIV data is not available in the upper few cm). Exactly why the first harmonic (i.e., $2\omega_f$) manifests itself as a second mode, and not as some other mode, is not clear. We also note that the horizontal phase speed of the incident internal wave beam (1.8 cm s^{-1}) is not particularly

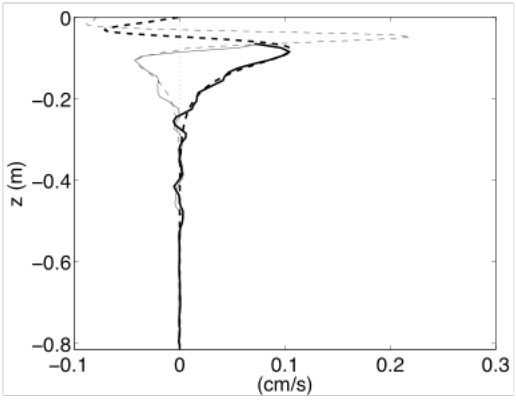

FIGURE 5. EXP25, Comparison between the mode-2 shape (dashed lines) for $\omega = 2\omega_f$, as calculated from (3.1), and the observed vertical profile (solid lines) of the velocity field filtered at $\omega = 2\omega_f$ at $x = 1.15$ m (*cf.* panel (c) in Fig. 4). The thin and the thick lines represent the horizontal and vertical velocities, respectively.

close to the measured mode-2 phase speed for $\omega = 2\omega_f$ ($c_2 = 2\omega_f/k_2 = 2.3$ cm s^{-1}). Furthermore, the theoretically calculated horizontal phase speeds of mode-2 and mode-3 for $\omega = 2\omega_f$ ($c_2 = 2\omega_f/k_2 = 2.3$ cm s^{-1}, $c_3 = 2\omega_f/k_3 = 1.7$ cm s^{-1}) suggest that a phase speed matching mechanism such as the one discussed by Grisouard *et al.* (2011), who examined the local generation of internal solitary waves with a numerical model, is not in play here.

The importance of the shear flow to the modal propagation of the higher harmonics can be illustrated by solving the modes from (3.1) with $U = 0$; then, for $\omega = 2\omega_f$, we find much smaller horizontal wavelengths: $\lambda_1 = 41$, $\lambda_2 = 13$ and $\lambda_3 = 8$ cm, none of which matches the observed wavelength.

For EXP22, we again find that the measured horizontal wavelength (35 cm) of the harmonic $2\omega_f$ is the closest to the corresponding theoretical wavelength of mode-2 ($\lambda_1 = 73$, $\lambda_2 = 27$ and $\lambda_3 = 18$ cm). We note however that the wavelengths are in this case sensitively dependent on the frequencies $\omega = 2\omega_f$ and N_0, because they are very close. (For example, with $\omega = 0.5$ rad/s we find for the second mode $\lambda_2 = 73$ cm, whereas with

$\omega = 0.6$ rad/s, we find 24.5 cm.) Thus the quantitative agreement between experiment and theory could be better or worse for even small changes in ω or N_0. As it was the case for EXP25, the vertical structure of the first harmonic signal ($2\omega_f$) agrees well with the theoretically computed mode-2 shape, except in the deep parts of the lower layer. In the lower layer, where the measured background shear flow is negligible, equation (3.1) predicts a linear variation of W with z for $\omega = 2\omega_f \approx N_0$ (since the equations boils down to $W'' \sim 0$); however, we observe a more rapid decay of the signal in the lower layer, the cause of which remains unclear.

In the case of EXP21, for which $3\omega_f < N_0$, the first two harmonics are not trapped but are allowed to propagate into the lower layer; hence they radiate from the pycnocline as beams and cannot be identified with any one mode, as shown in Fig. 6. However, a different simple regularity appears from Fig. 6. For each harmonic (n), the beam pattern is clearly periodic (see panels on the left); the horizontal wavenumber associated with this periodicity ($k^{(n)}$, say) obeys the simple rule $k^{(n)} = nk^{(1)}$ (see dashed lines in panels on the right of Fig. 6). This implies that the horizontal phase speeds are the same for all harmonic beams.

Finally, it is evident from Fig. 4 and Fig. 6 that the amplitude of the harmonics at $n\omega_f$ is weaker than the one at $(n-1)\omega_f$ (for $n > 1$), and that these higher harmonics originate from the region of interaction between the incident wave beam and the pycnocline. These observations confirm that the higher harmonics are a result of weakly nonlinear interactions between the incoming and reflected beams. A detailed study of the influence of the amplitude of the incoming beam on the amplitude of the generated harmonics is recommended for future research.

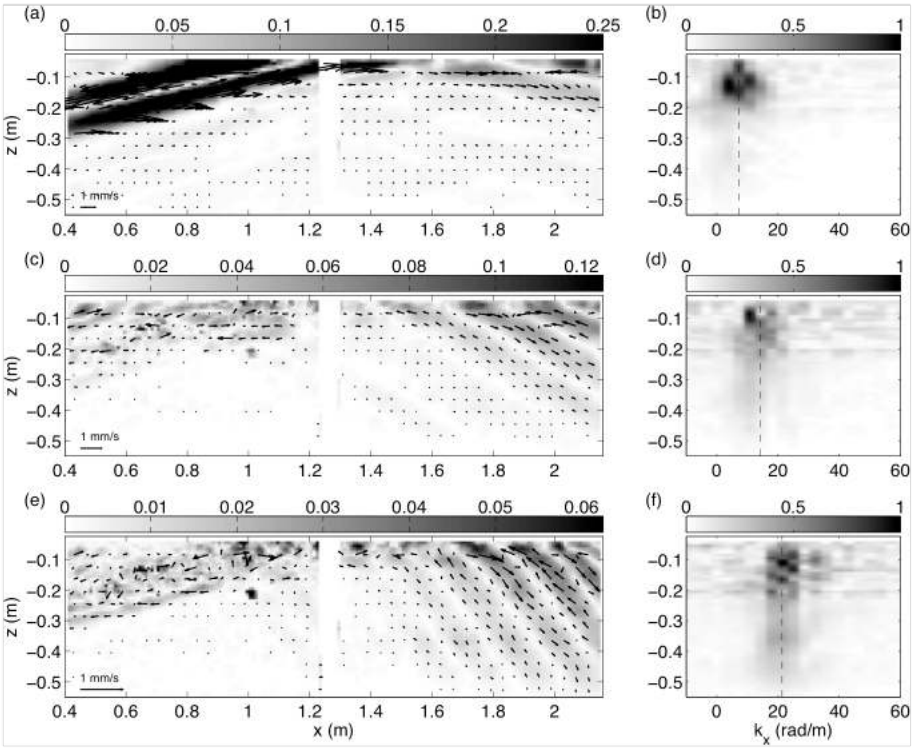

FIGURE 6. EXP21, harmonics analysis as in Fig. 4 for the frequency $n\omega_f$, with $n = 1, 2, 3$. Left panels display the velocity vector fields with grey tones indicating the amplitude of the velocity field (in cm s^{-1}). Right panels show the spectra of the horizontal wavenumber and its vertical variation (for each, amplitudes are normalized to one). The dashed lines in (b), (d) and (f) represent, for harmonic $\omega = n\omega_f$, the value $k^{(n)} = nk^{(1)}$ with $k^{(1)} = 7.1$ rad/m.

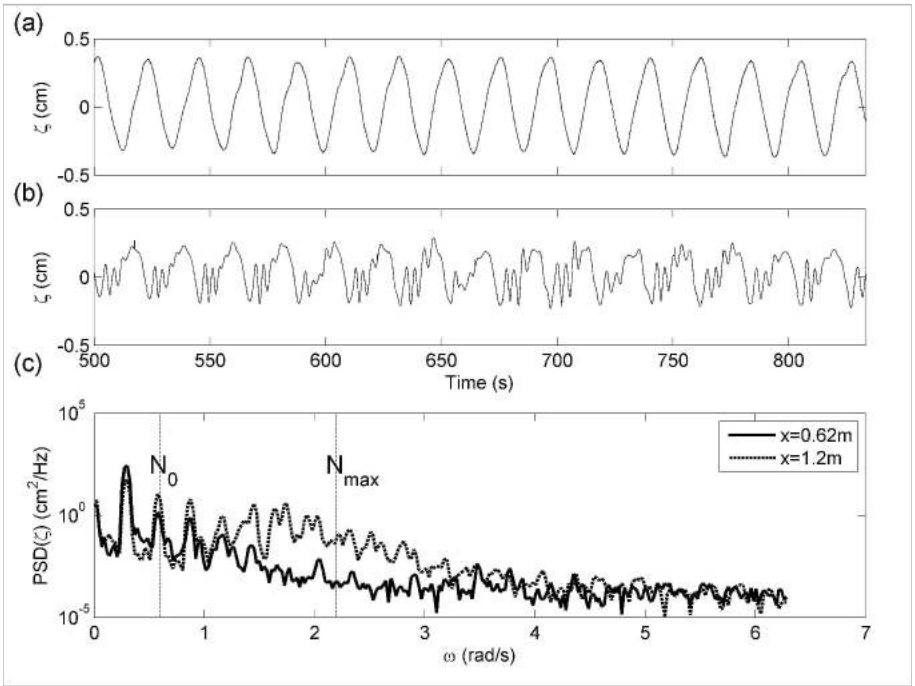

FIGURE 7. Steady state pycnocline displacements at (a) $x = 0.62$ and (b) $x = 1.2$m in the $\gamma = 0.11$ experiment (EXP08). (c) Corresponding Fourier spectra.

4. Evolution of the pycnocline

In this section, we discuss the evolution of the pycnocline, as measured by the acoustic probes. As mentioned in Section 2.3, ten acoustic probes were positioned at various positions in the range 0 to 4 m from the wave generator. The proximity of two probes located at $x = 1.20$ & 1.254 m, respectively, allows us to determine the horizontal phase speed of the signal, for its structure remains similar between the two, so that specific peaks can be identified in both. In every experiment, the acoustic probe measurements were initiated well before the wave generator was started, allowing us to visualize the transients before a steady state was achieved.

In figures 7 (a) & (b), we plot the pycnocline displacements ζ (i.e., vertical averages over the thickness of the pycnocline, as described in section 2.3) at $x = 0.62$ m and $x = 1.2$ m, respectively. In a qualitative way, the results from the probes indicate the

formation of ISWs in the pycnocline: the wave pattern is nearly sinusoidal at the region of impact, steepens as it propagates away, and at some point its steep front splits up into higher-frequency peaks, which are, at least initially, ordered in amplitude (the larger ones being ahead). Furthermore, as shown in figure 7 (c), the power spectrum of the time series at $x = 1.2$ m has a distinct bulge around the frequencies in the neighborhood of $\omega = N_{max}$, a feature we discuss in detail later in the current section. In a quantitative sense, however, it is not obvious that nonlinear effects are at work; after all, the amplitude of the peaks is small (a few mm) compared to the depth of the pycnocline (a few cm).

We note, however, that the actual peak amplitudes of interfacial displacements are presumably larger than the measured outputs from the ultrasonic probes as the probes measure the *mean* amplitudes over the layer between the transmitter and the receiver. This effect is particularly pronounced for the high-frequency waves that are trapped in the pycnocline, for their amplitude diminishes rapidly outside of the pycnocline. We also note that the waves shape and amplitudes we find are similar to those observed in earlier experiments on internal solitons in a two-layer system (Horn *et al.* (2001)).

4.1. *Interpretation of spectra*

The generation of higher harmonics due to nonlinear interaction at the junction of two beams was discussed in Section 3.2. Being relatively weak, their behavior must be close to linear as they propagate away from their source. This means that they can be properly identified in spectra, as seen in Fig. 7 (c) and Fig. 11, which after all amounts to treating the signal as if it were linear. For ISWs it is less clear how they might manifest themselves in spectra. Being genuinely nonlinear waves, they are not associated with any particular harmonic; neither can they be described by a superposition of harmonics. Still, technically, one can calculate the spectrum of a signal containing ISWs. As a test case, we use results from a set of KdV-type equations for interfacial waves, which include

forcing terms due to barotropic tidal flow over topography (Gerkema 1996). In one model calculation, we switched off the nonlinear terms while still including terms representing barotropic advection of the internal-wave field. In this case, then, the internal-wave field is linear but contains higher harmonics due to the barotropic advection terms. In another calculation, the nonlinear terms were included, giving rise to internal solitons; in this case, there are higher harmonics as well as ISWs, and so this is qualitatively the situation we supposedly have in our laboratory experiments.

If we now calculate the spectra for the results of both model runs, we find important and qualitative differences (see Fig. 8). For the quasi-linear case, peaks at higher harmonics are found, and, as expected, they get lower and lower for higher frequencies. In the nonlinear case, the same qualitative behaviour is found at the lowest frequencies, but then a bulge appears, which is not associated with any one harmonic, but more wide-spread, involving a group of harmonics. This is easily understood from the fact that solitons are not associated with harmonics *per se*, but have nonetheless certain time scales within the range of some of the harmonics. Harmonics in the neighbourhood of these time scales show marked peaks in the spectrum. This does not mean that the solitons are formed by a superposition of higher harmonics (after all, the signal is nonlinear), but are the result of applying a linear technique (harmonic analysis) to a nonlinear signal. In any case, the presence of a bulge helps to distinguish the physically distinct cases of pure higher harmonics on the one hand, and solitons on the other.

Such a bulge appears in our experiments too, as is illustrated in figure 7 (c). This confirms the direct visual impression from the probe results shown in figure 7 (b), in which groups of peaked waves are clearly visible. We proceed, in the next section, to investigate the effect of the pycnocline properties (depth, vertical extent, strength etc.)

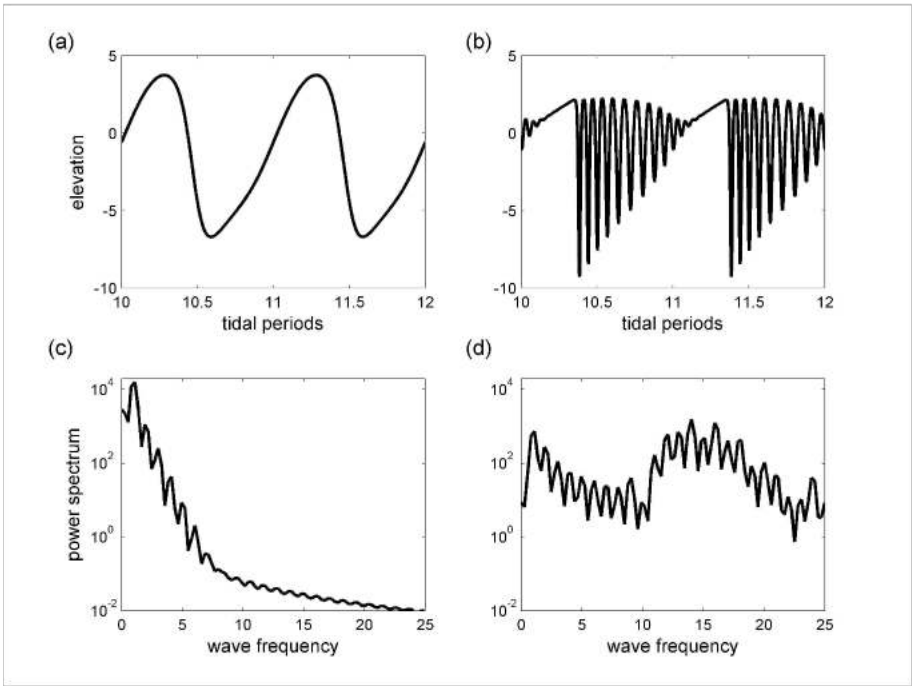

FIGURE 8. Examples from a nonlinear nonhydrostatic KdV type model for interfacial tidally generated waves. Panel (a) shows the wave profile over two tidal periods, created from the quasi-linear version of the model, where higher harmonics are generated by barotropic advection of the baroclinic field; these harmonics manifest themselves as peaks in the corresponding power spectrum, shown in (c). In (b), genuinely nonlinear effects of the baroclinic field itself are included, giving rise to solitons; the corresponding spectrum in (d) is now markedly different, showing a bulge enveloping higher frequencies.

on the bulge and hence propose a way to capture all the properties into one parameter, the magnitude of which determines the appearance of solitons.

4.2. *Effect of the pycnocline strength*

By removing the upper layer, and refilling it with fresh water, we varied the depth, the amplitude, and the width of the peak of the pycnocline (see Figure 9 (a) for the various stratification profiles that were set up during the course of all our experiments). In this section, we present results from three experiments with the same forcing frequency (such

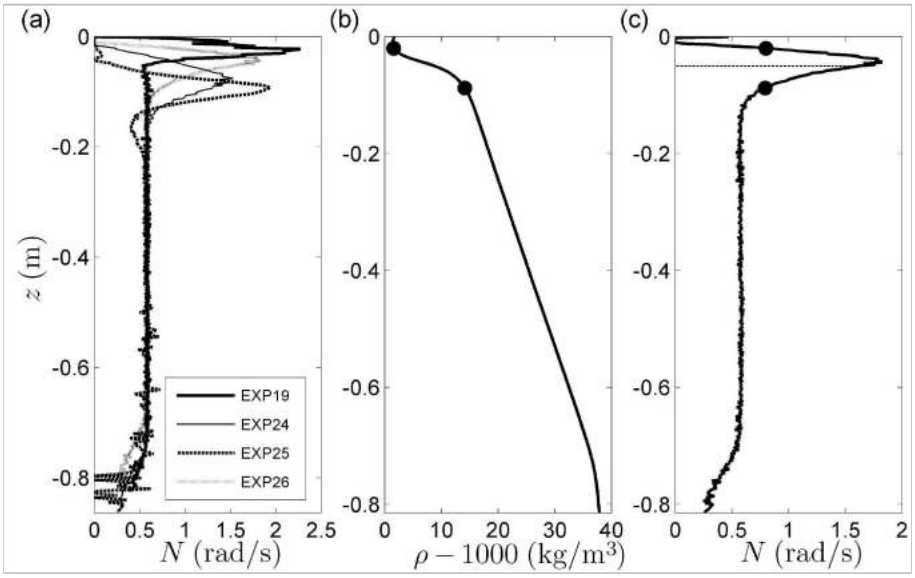

FIGURE 9. (a) Different profiles of stratification with which experiments were carried out. (b) & (c) Determination of γ from the profile for experiments EXP21 to 26. The top and base of the pycnocline, indicated by black dots, are determined using the density profile shown in (b). The depth of the weighted center of the pycnocline, i.e. d, is indicated by the horizontal dotted line in (c).

that the incident internal wave beam propagates at 30° with respect to the horizontal) but with different pycnocline properties.

A key parameter for the response of the pycnocline, due to an impinging internal-wave beam, was identified by Gerkema (2001) using linear theory. In that study, a "2c-layer" stratification was adopted, consisting of an upper mixed layer of thickness d, an interfacial pycnocline of strength g', beneath which lies a layer of constant buoyancy frequency, N_c. The total water depth being H, the parameter in question is defined by

$$\gamma = \frac{(g'd)^{1/2}}{N_c H}\,. \tag{4.1}$$

In the numerator of equation 4.1, we recognize the phase speed of long interfacial waves in a 2-layer system, while the expression in the denominator is a measure of the phase speed of vertical modes in a constantly stratified layer of depth H. These modes add up

to form beams, so the parameter γ reflects the ratio of the phase speeds associated with the interface (i.e. pycnocline) and the uniformly stratified lower layer. It was found that for γ either very small or very large, there is no significant transfer of energy from beams to interfacial waves. Such a transfer occurs only for intermediate values, characterized by $\gamma \approx 0.1$. This would therefore be expected to serve as a necessary condition for having locally generated ISWs which emerge from the initial interfacial perturbation as it propagates and steepens. It is, however, not a sufficient condition, for the forcing frequency, which does not feature in (4.1), must also affect the evolution into ISWs.

In the present situation we have a more complicated profile of stratification, but the parameters in (4.1) are still meaningful if interpreted in the following way. First, we look at the density profile to identify the base and top of the pycnocline; an example is shown in figures 9 (b) & (c). As explained in Gerkema (2001), the parameter g' equals the area enclosed by the pycnocline in the N^2 versus z graph; so, $g' = \int dz\, N^2$, where the integral is taken between the previously identified base and top of the pycnocline. The parameter d corresponds to the depth of the pycnocline, but this depth is of course not uniquely defined here. To take the depth of the peak would not always make sense because it may not be representative of where the bulk of the pycnocline lies. Therefore, we calculated a 'weighted depth', as $d = \int dz\, zN^2/(\int dz\, N^2)$, where the boundaries of the integrals are again the base and top of the pycnocline. The depth d thus found is illustrated in Figure 9 (c). Finally, the parameter H is simply the total water depth, and N_c is taken equal to the mean of N from the bottom to the base of the pycnocline. We have thus obtained all the parameters needed to calculate γ, which is listed for different profiles in Figure 9 (a) and also in Table 1.

In figures 10 (a)-(c), the pycnocline displacements at $x = 1.59$ m from three different experiments (all corresponding to $\omega_f = 0.29$ rad/s) with $\gamma = 0.11, 0.17, 0.19$, respectively,

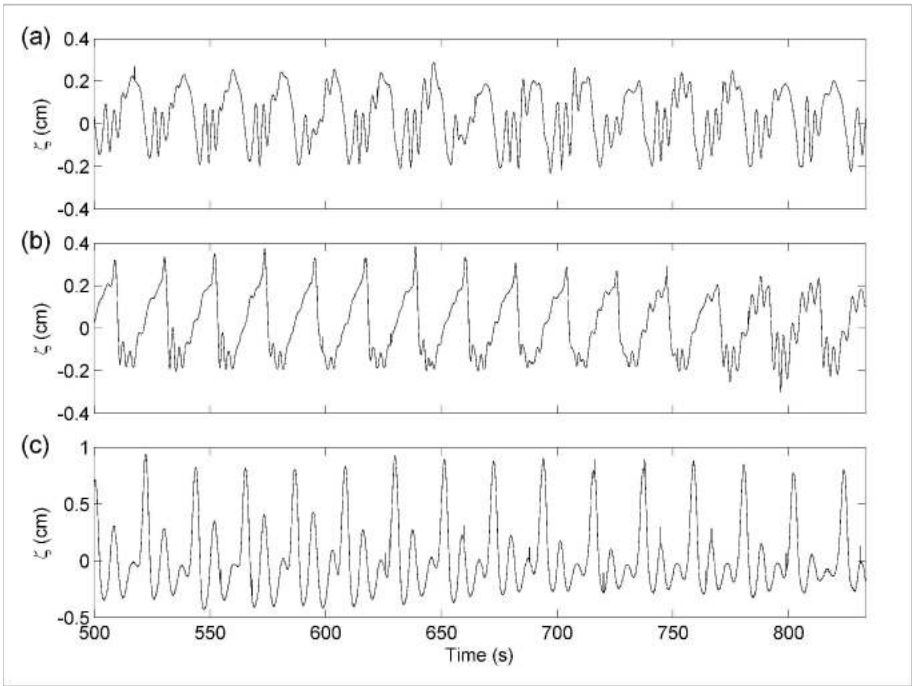

FIGURE 10. Steady-state pycnocline displacements at $x = 1.59$ m in (a) EXP08 ($\gamma = 0.11$), (b) EXP22 ($\gamma = 0.17$) and (c) EXP16 ($\gamma = 0.19$).

are presented. As is evident from the figures, groups of peaked waves are most clearly visible for EXP08. The corresponding power spectra, presented in figures 11 (a)-(c), show that the bulge at frequencies larger than the forcing frequency is most pronounced for EXP08, confirming that the bulges in the power spectra are indeed directly correlated with the appearance of solitons. The bulge is relatively weaker in EXP22, and is the weakest in EXP16, for which the higher harmonics dominate solitary-wave-like features. Finally, the solitons being most evident for $\gamma = 0.11$ is consistent with the theoretical criterion of $\gamma \approx 0.1$ given by Gerkema (2001) for optimal excitation of solitons in the pycnocline, and also with oceanic observations. Indeed, recent studies of the stratification in the Mozambique Channel (where local generation of ISWs was proposed by Da Silva *et al.* (2009)) give $\gamma = 0.08$, a value very close to the observed optimum stratification for soliton generation in our experiments.

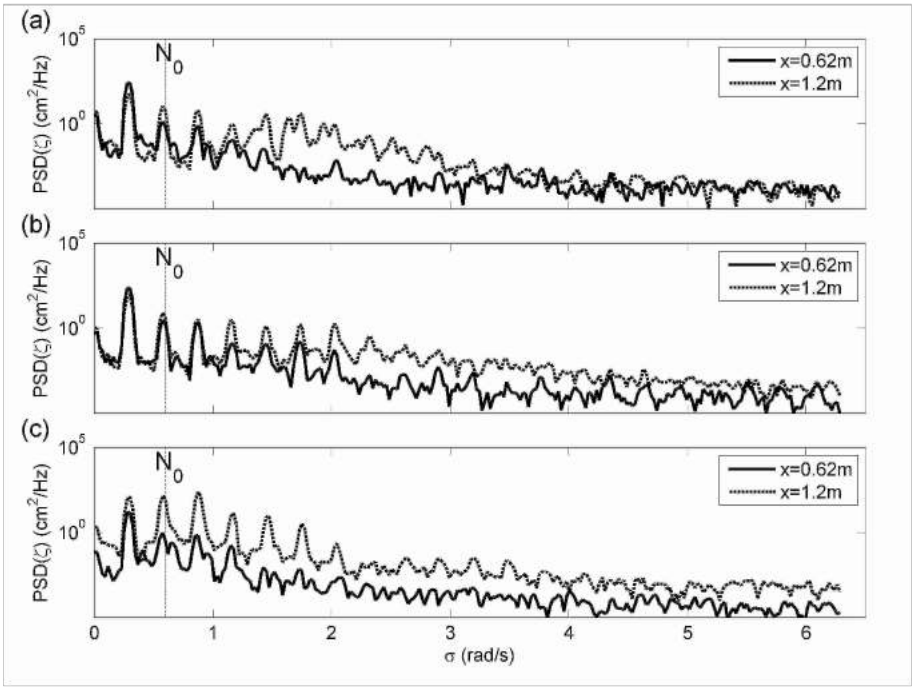

FIGURE 11. Power spectra of the steady-state pycnocline displacements at $x = 0.62$ m and $x = 1.20$ m in (a) EXP08 ($\gamma = 0.11$), (b) EXP22 ($\gamma = 0.17$) and (c) EXP16 ($\gamma = 0.19$), with all the three plots normalized by the same constant.

The two closely spaced probes at $x = 1.2$ m and $x = 1.254$ m were introduced only after EXP08 was performed. Analyzing the time series data from these two closely-spaced acoustic probes in EXP22 ($2\omega_f \approx N_0$ and $\gamma = 0.17$), we find that the higher-frequency peaks move with the same speed as the main depression (or the envelope) on which they sit. They move at 2.3 cm/s; the speed being larger than the mode-1 wave speed ($c_1 = 1.1$ cm/s) for $\omega \approx 2.5$ rad/s (frequency representative of the bulge observed in figure 11(b)). This suggests that the observed solitary waves were mode-1, with the solitons moving faster than the corresponding linear mode-1 wave because of nonlinear effects. Finally, the soliton speed is neither very close to the horizontal phase speed of the incident wave beam (1.83 cm/s, derived from the PIV data, again ruling out the phase speed matching mechanism in our experiments) nor close to that of the 2nd-mode

structure of the the 2nd harmonic discussed in section 3 (with observed $\lambda_2 = 35$ cm, we obtain 3.24 cm/s, suggesting the solitons are rather independent from the higher harmonics).

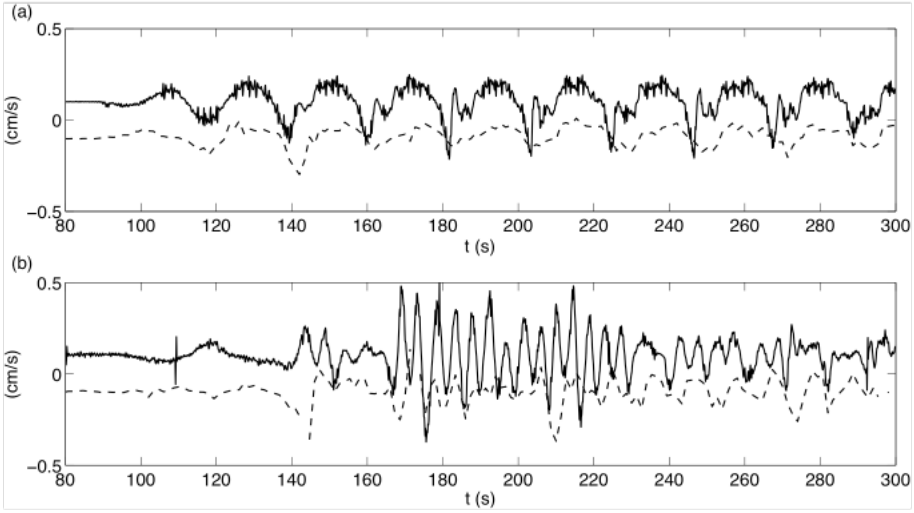

FIGURE 12. EXP 22, comparison of time series of the vertical velocity $d\zeta/dt$ extracted from the ultrasonic probes (continuous line) and from the PIV images at the closest location to the ultrasonic probes (dashed line), for probes located at (a) $x = 0.62$ m and (b) $x = 1.20$ m. The data do oscillate around 0 but are arbitrary shifted of ± 0.1 cm s^{-1} to make the comparison easier.

5. Discussion

In this paper, we have experimentally studied the effect of an internal wave beam impinging on a pycnocline, and the waves and flows this induces. Two different techniques were used to study these phenomena. PIV data from the lower layer of constant stratification provides velocity fields in a vertical plane, with a sampling frequency of 3 Hz. An array of ultrasonic probes, on the other hand, gives times series of local mean vertical displacements of the pycnocline at a much higher sampling frequency of 240 Hz. The two techniques are complementary since the PIV measurements offer a large field of view and the ultrasonic probes focus on the pycnocline where PIV cannot be used because of strong optical distortion and sparse particle seeding.

The results from the two independent measurement techniques can be compared to a certain extent and hence be used to further reaffirm the conclusions drawn from the

data. The first time derivative of the mean pycnocline displacements measured by the ultrasonic probes should qualitatively correspond to the vertical velocity obtained from PIV data from just below the pycnocline (The comparison can only be qualitative because the acoustic probes provide a vertical average of displacements within the pycnocline, not a value at a specific depth.). To illustrate this point, we present in figure 12 time series of the vertical velocity of the pycnocline obtained with the two techniques at $x = 0.62$ m and $x = 1.2$ m for EXP22. The continuous lines are obtained by taking the time derivative of the probe signals; the dashed lines represent the mean vertical velocities (over 5 mm^2) derived from the PIV data centered at these x-locations and at a depth $z = -5.25$ cm. It is clear that the low-frequency oscillations (of the order of the forcing frequency ω_f) are identical in both datasets, whereas the higher frequencies (larger than ω_f) are larger for the vertical velocity from the ultrasonic probes. This is mainly due to the fact that these high frequencies are localized in the pycnocline itself (for EXP22, $\omega_f \simeq N_0/2$) and have weak signatures below it. Finally, an important feature is the presence of out-of-phase oscillations of the vertical velocity of the pycnocline in between its base and its mean position (around $t = 170$ s or 220 s in figure 12 (b) for instance). These are evidence of mode-2 (or higher) internal waves in the pycnocline, in agreement with our findings in section 3.2.

Our experiments were inspired by oceanic observations (New & Pingree (1992); New & Da Silva (2002); Azevedo *et al.* (2006); Da Silva *et al.* (2007, 2009)), theoretical works (Gerkema (2001); Akylas *et al.* (2007)) and numerical studies (Maugé & Gerkema (2008); Grisouard *et al.* (2011)). Apart from the expected result of the generation of groups of solitary waves, the full picture that emerges turns out to be intricate, with the additional features of a mean current and higher harmonics.

We have found higher harmonics being generated at the junction of the incident and

reflected beams, as expected from theory by Tabaei & Akylas (2003). Moreover we found that these harmonics are trapped in the pycnocline when their frequency exceeds, or is close to that of the constantly stratified lower layer. These trapped harmonics are each uni-modal, with a well-defined wavelength. The wavelengths and vertical profiles of these modes are significantly affected by a residual current in the upper layer, which, too, finds its origin in the region where the main beam reflects. Theoretical studies on internal-wave reflection do predict residual currents (Tabaei *et al.* 2005, e.g.), but only in the very region of reflection. Our experiments, however, demonstrate that they can be much more extensive horizontally, in the direction of wave propagation. We are not aware of any theoretical work that may explain this phenomenon. Also, the apparently three-dimensional structure of the flow deserves a separate study.

We observe the generation of internal solitary waves only when the stratification is such that the parameter γ is close to 0.1, which is consistent with the theoretical criterion put forward by Gerkema (2001). Although weak in amplitude, we demonstrated that these waves are intrinsically nonlinear as they manifest themselves in spectra not as a superposition of harmonics but as a bulge. This interpretation of the spectra is suggested by looking at spectra from a KdV-type model.

Although our experiments clearly show the generation of trapped 2nd-mode higher harmonics in the pycnocline, the ISWs seem to be of 1st-mode, in line with most oceanic observations. Yet, exceptions may occur, as is clear from the numerical work by Grisouard *et al.* (2011) and also from oceanic observations such as the one shown in Figure 13. Here we see a SAR image from the Mozambique Channel with surface signatures of ISWs. While these signatures look like many other typical SAR signatures of ISWs, with larger amplitude waves leading the wave trains in their direction of propagation, close inspection of their bright and dark patterns reveals that they may be mode-2 solitary like waves.

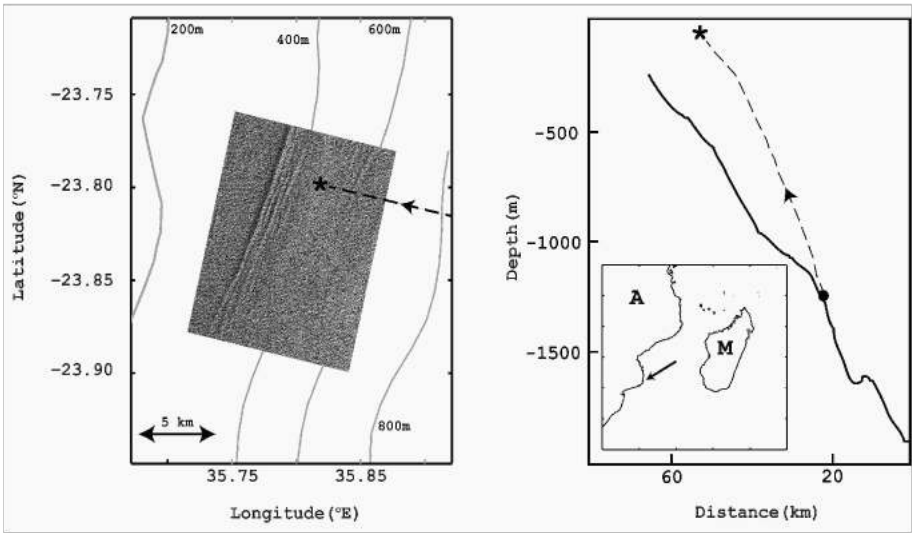

FIGURE 13. (a) SAR image of the Mozambique Channel dated 24 September 2001 at 7:39 UTC, showing a packet of ISWs consistent with mode-2 vertical structure. The star symbol on the image indicates the predicted position where an internal tide beam impinges the thermocline. (b) On the right hand side a vertical section (perpendicular to the ISW crests) is shown with a simulated beam trajectory based on local stratification (represented by the dashed line). Dark bold circle shows critical slopes from where the beam admittedly originates. The dark star symbol shows the location where the beam impacts the thermocline (as well as in part a), and the arrows indicate the direction of energy propagation. Inset shows geographic location of the observation; M stands for Madagascar and A for the African continent (the arrow in the inset denotes the location of the image).

Indeed, a dark band pattern preceding a bright band (in the propagation direction) reveals a surface current divergence preceding a convergence, which is consistent with a mode-2 solitary like wave (for more details on SAR signatures of mode-2 ISWs (Da Silva *et al.* 2011, see e.g.)). In addition, the ISWs in figure 13 are located close to (but ahead of) the surfacing of an internal (tidal) ray emanating from critical slopes off the Mozambique shelf break. The image in figure 13 provides evidence of mode-2 solitary like waves that are consistent with Local Generation after the impact of an internal (tide) wave beam on the pycnocline.

Finally, we are not aware of oceanic observations in which trapped higher harmonics were found in a pycnocline. In the context of internal tidal beams impinging on a seasonal thermocline, this phenomenon is in any case not be expected, for the semidiurnal tidal frequency (1.4×10^{-4} rad/s) is much lower than the typical value of N in the seasonal thermocline (1×10^{-2} rad/s); in other words, the harmonic would have to be of an extremely high multiple for it to be trapped. The mean flow, on the other hand, has not been observed either, as far as we are aware, but there seems to be no *a priori* reason why it should not occur. In any case, in oceanic observations, too, one would typically find a mixture of higher harmonics (not trapped) and internal solitary waves. The idea we have put forward here to distinguish them in internal-wave spectra, may provide a useful tool in the oceanographic context as well.

We thank Samuel Viboud and Henri Didelle for their help during the experiments, Marc Moulin for the cams design and acknowledge helpful discussions with Joel Sommeria. The experiments were supported by funds from the Hydralab III Transnational Access Program (6th FP) and ANR PIWO (contract number ANR-08-BLAN-0113). We also thank MIT-France for partially funding the travel expenses of Manikandan Mathur.

REFERENCES

Akylas, T. R., Grimshaw, R. H. J., Clarke, S. R. & Tabaei, A. 2007 Reflecting tidal wave beams and local generation of solitary waves in the ocean thermocline. *J. Fluid Mech.* **593**, 297–313.

Azevedo, A., Da Silva, J. C. B. & and, A. L. New 2006 On the generation and propagation of internal solitary waves in the Southern Bay of Biscay. *Deep-Sea Res. I* **53**, 927–941.

Da Silva, J. C. B., New, A. L. & Azevedo, A. 2007 On the role of SAR for observing "local generation" of internal solitary waves off the Iberian Peninsula. *Can. J. Remote Sensing* **33** (5), 388–403.

Da Silva, J. C. B., New, A. L. & Magalhaes, J. M. 2009 Internal solitary waves in the Mozambique Channel: observations and interpretation. *J. Geophys. Res.* **114** (C05001), doi:10.1029/2008JC005125.

Da Silva, J. C. B., New, A. L. & Magalhaes, J. M. 2011 On the structure and propagation of internal solitary waves generated at the Mascarene Plateau in the Indian Ocean. *Deep-Sea Res. I* **58** (3), 229–240.

Delisi, D. P. & Orlanski, I. 1975 On the role of density jumps in the reflexion and breaking of internal gravity beams. *J. Fluid Mech.* **69**, 445–464.

Fincham, A. & Delerce, G. 2000 Advanced optimization of correlation imaging velocimetry algorithms. *Experiments in Fluids* **29**, S1.

Gerkema, T. 1996 A unified model for the generation and fission of internal tides in a rotating ocean. *J. Mar. Res.* **54** (3), 421–450.

Gerkema, T. 2001 Internal and interfacial tides: beam scattering and local generation of solitary waves. *J. Mar. Res.* **59** (2), 227–255.

Gostiaux, L., Didelle, H., Mercier, S. & Dauxois, T. 2007 A novel internal waves generator. *Experiments in Fluids* **42**, 123–130.

Grisouard, N., Staquet, C. & Gerkema, T. 2011 Generation of internal solitary waves in a pycnocline by an internal wave beam: a numerical study. *J. Fluid Mech.* **676**, 491–513.

Horn, D. A., Imberger, J. & Ivey, G. N. 2001 The degeneration of large-scale interfacial gravity waves in lakes. *J. Fluid Mech.* **434**, 181–207.

Jackson, C. 2007 Internal wave detection using the moderate resolution imaging spectroradiometer (modis). *J. Geophys. Res.* **112**, C11012.

Jiang, C. H. & Marcus, P. S. 2009 Selection rules for the nonlinear interaction of internal gravity waves. *Phys. Rev. Letters* **102**, 124502.

Mathur, M. & Peacock, T. 2009 Internal wave beam propagation in nonuniform stratifications. *J. Fluid Mech.* **639**, 133–152.

Maugé, R. & Gerkema, T. 2008 Generation of weakly nonlinear nonhydrostatic internal tides over large topography: a multi-modal approach. *Nonlin. Process. Geophys.* **15**, 233–244.

Mercier, M. J., Martinand, D., Mathur, M., Gostiaux, L., Peacock, T. & Dauxois, T. 2010 New wave generation. *J. Fluid Mech.* **657**, 308–334.

Michallet, H. & Barthlemy, E. 1997 Ultrasonic probes and data processing to study interfacial solitary waves. *Exp. in Fluids* **22**, 380–386.

New, A. L. & Da Silva, J. C. B. 2002 Remote-sensing evidence for the local generation of internal soliton packets in the central Bay of Biscay. *Deep-Sea Res.* **49** (5), 915–934.

New, A. L. & Pingree, R. D. 1990 Large-amplitude internal soliton packets in the central Bay of Biscay. *Deep-Sea Res.* **37**, 513–524.

New, A. L. & Pingree, R. D. 1992 Local generation of internal soliton packets in the central Bay of Biscay. *Deep-Sea Res.* **39**, 1521–1534.

Tabaei, A. & Akylas, T. R. 2003 Nonlinear internal gravity wave beams. *J. Fluid Mech.* **482**, 141–161.

Tabaei, A., Akylas, T. R. & Lamb, K. G. 2005 Nonlinear effects in reflecting and colliding internal wave beams. *J. Fluid Mech.* **526**, 217–243.

Thorpe, S. A. 1998 Nonlinear reflection of internal waves at a density discontinuity at the base of the mixed layer. *J. Phys. Oceanogr.* **28**, 1853–1860.

Chapter 5

On the structure and propagation of internal solitary waves generated at the Mascarene Plateau in the Indian Ocean

Deep-Sea Research I 58 (2011) 229–240

Contents lists available at ScienceDirect

Deep-Sea Research I

journal homepage: www.elsevier.com/locate/dsri

On the structure and propagation of internal solitary waves generated at the Mascarene Plateau in the Indian Ocean

J.C.B. da Silva [a,*], A.L. New [b], J.M. Magalhaes [a]

[a] CIMAR/CIIMAR—Centro Interdisciplinar de Investigação Marinha e Ambiental and Departamento de Geociências, Ambiente e Ordenamento do Território, Universidade do Porto, Rua do Campo Alegre, 687, 4169-007 Porto, Portugal
[b] National Oceanography Center, Southampton, Ocean Modelling and Forecasting Group, European Way, Southampton SO14 3ZH, UK

ARTICLE INFO

Article history:
Received 12 August 2010
Received in revised form
30 November 2010
Accepted 6 December 2010
Available online 13 December 2010

Keywords:
Internal solitary waves
Synthetic Aperture Radar
Internal wave generation
Lee waves
Mode-2 solitary waves

ABSTRACT

Analysis of a comprehensive dataset of Synthetic Aperture Radar (SAR) images acquired over the sea area around the Mascarene Plateau in the western Indian Ocean reveals, for the first time, the full two-dimensional spatial structure of internal solitary waves in this region of the ocean. The satellite SAR images show that powerful internal waves radiate both to the west and east from a central sill near 12.5°S, 61°E between the Saya de Malha and Nazareth Banks. To first order, the waves appear in tidally generated packets on both sides of the sill, and those on the western side have crest lengths in excess of 350 km, amongst the longest yet recorded anywhere in the world's oceans. The propagation characteristics of these internal waves are well described by first mode linear waves interacting with background shear taken from the westward-flowing South Equatorial Current (SEC), a large part of which flows through the sill in question. Analysis of the timings and locations of the packets indicates that both the westward- and eastward-traveling waves are generated from the western side of the sill at the predicted time of maximum tidal flow to the west. The linear generation mechanism is therefore proposed as the splitting of a large lee wave that forms on the western side of the sill, in a similar manner to that already identified for the shelf break generation of internal waves in the northern Bay of Biscay. While lee waves should form on either side of the sill in an oscillatory tidal flow, that on the western side would be expected to be much larger than that on the eastern side because of a superposition of the tidal flow and the steady westward flow of SEC. The existence of a large lee wave at the right time in the tidal cycle is then finally confirmed by direct observations. Our study also confirms the existence of second mode internal waves that form on the western side of the sill and travel across the sill towards the east.

1. Introduction

Internal Solitary Waves (ISWs) are thought to play an important role for global mixing in the upper layers of the ocean, and are thus relevant to the setting of the near sea-surface temperature structure (Shroyer et al., 2010), air–sea exchange processes, and the evolution of the climate system. Large baroclinic or internal tides (ITs) are well known to result from the interaction of the surface (or barotropic) tide with steep seafloor or shelf break topography (New, 1988). Subsequently, these ITs steepen as they propagate away from the topography and shorter-period non-linear ISWs develop, usually phase locked to the IT troughs (Pingree et al., 1986; Gerkema, 1996; Shaw et al., 2009). The breaking of ISWs may then contribute significantly to turbulent mixing in the near-surface layers, through the continual triggering of instabilities as they propagate (Moum et al., 2003). The highly turbulent character of well-developed ISWs propagating near the pycnocline has also been demonstrated by Pinkel (2000) and Klymak et al. (2006).

In particular, isolated deep ocean ridges, such as the Mascarene Plateau in the Indian Ocean and the Hawaiian Ridge in the Pacific, are important sinks for surface-tide energy through conversion to ITs and ISWs (Egbert and Ray, 2003; Lozovatsky et al., 2003) and are consequently sites of elevated mixing. For instance, Lozovatsky et al. (2003) estimate diapycnal mixing from these processes to be of the order of $1–2 \times 10^{-4}\ m^2\ s^{-1}$ in the main pycnocline up to distances of 100 km to the east of the Mascarene Plateau, decaying to typical background values of $10^{-5}\ m^2\ s^{-1}$ at distances of 1000 km from the topography.

Mixing due to internal waves also plays a significant role for the evolution of biology in the near-surface layer. Pingree et al. (1986) have shown that the increased biomass (zooplankton and phytoplankton) in the northern Bay of Biscay is related to the cooling of the sea surface through mixing caused by internal waves, where the internal tidal amplitude is at a maximum. In addition, vertical redistribution of heat, biomass, and nutrients may be caused by shear-driven mixing associated with ISWs and their interaction with geostrophic flow, as has been speculated by Moum et al.

* Corresponding author. Tel.: +351 220402476; fax: +351 220402490.
E-mail address: jdasilva@fc.up.pt (J.C.B. da Silva).

0967-0637/$ - see front matter © 2010 Elsevier Ltd. All rights reserved.
doi:10.1016/j.dsr.2010.12.003

(2008). Enhancement of primary production can also occur simply by increasing the average light intensity (through vertical uplifting) experienced by phytoplankton near the base of the mixed layer (e.g. da Silva et al., 2002, who show that this mechanism may be operative in the central Bay of Biscay). Enhanced primary production also seems to be significantly affected by ISWs in other regions such as the west African shelf (Ostrowski et al., 2009).

Remote sensing techniques have now revealed the presence and structure of ITs on scales that cannot be realized from traditional *in situ* measurements. While altimetry has been extensively used to observe ITs (Ray and Mitchum, 1997) at a global scale, it is somewhat limited because of the resolution of the orbit track on the ground. Pingree and New (1995) used medium resolution satellite imaging sensors, which provided a synoptic description of the internal tides in the Bay of Biscay, revealing directionality, long-crestedness (spatial coherence), and spatial extent. They detected ITs in both visible and thermal infrared imagery, relying on mechanisms such as temperature variations associated with the crests of ITs (cooler water is uplifted to near the sea surface at the positions of IT crests, where wind mixing enhances surface cooling).

Although this mechanism is operative in the Bay of Biscay and effectively revealed the ITs there, it is the compilations from satellite SAR observations that provide the best evidence for the presence of the shorter period ISWs in the ocean (Elachi and Apel, 1976; Alpers and Salusti, 1983; Thompson and Gasparovic, 1986; Brandt et al., 1996; New and Da Silva, 2002; Azevedo et al., 2006; da Silva et al., 2007, 2009; da Silva and Helfrich, 2008). This is due to a mechanism whereby horizontally propagating internal waves, centered on the thermocline typically some tens of meters below the surface, can generate a signature in the surface roughness field because of the modulating effect of convergence and divergence in the near-surface currents associated with the internal waves. This modulation is most effective for short period (30 min or shorter) ISWs because the straining of short (Bragg) surface waves (or ripples) is strongest at these periods. It may also be possible to detect tidal period internal waves (with periods of 12.4 h) in the presence of surface films and/or when the surface currents associated with ITs induce alternating wind conditions relative to the surface with wind against tide exhibiting larger radar backscatter than wind with tide (Ermakov et al., 1998). Finally, SAR observations have also provided unprecedented insight into the generation mechanisms of ISWs and ITs (e.g. Brandt et al., 1997; Nash and Moum, 2005; da Silva and Helfrich, 2008; da Silva et al., 2009).

Although SARs provide details of the two-dimensional spatial structure of horizontally propagating internal waves in the upper thermocline, it is usually necessary to compile a sufficiently large dataset covering different phases of the complete (semi-diurnal) tidal cycle to gain insight about the generation process. It is indeed possible to investigate and reconstruct the propagation history of ISWs (and ITs) from a given source, although caution must be taken with tidal aliasing relative to the spring–neap tidal cycle (a sun-synchronous polar orbiter is phase locked with the fortnightly tidal cycle, and thus all images at spring tides correspond approximately to a certain (semi-diurnal) tidal phase, while all images at neap tides correspond to the opposite phase). In this paper we show for the first time a large SAR dataset over the Mascarene Plateau, revealing this as a major hot-spot of ISW and IT generation in the Indian Ocean. The area influenced by ISWs is larger in extent than other very energetic regions such as the Bay of Biscay, the Sulu Sea, and the Andaman Sea, and the ISWs are comparable to those in the south China Sea in terms of along-crest lengths and propagation distances.

Baines (1982) developed a linear analytical (two layer) model for the generation of interfacial and internal tidal waves forced by the interaction of the barotropic tide with steep shelf-break topography. The density structure consisted of two layers separated by an interface, the upper layer being uniform in density, the lower layer having a constant stratification. He showed that a semi-diurnal vertical perturbation of the interface over the upper slope region splits into two progressive interfacial IT waves, one propagating on-shelf and the other off-shelf during each complete tidal cycle. The troughs of the ITs are generated over the upper slope region at the time of maximum off-shelf flow. More recent and advanced numerical models (Gerkema, 1996; Vlasenko et al., 2005) result in qualitatively similar results. This trough-splitting mechanism was also reported by Pingree et al. (1986) from direct observations of IT troughs in the Bay of Biscay. Here, the two sets of IT troughs were also observed to be generated from the upper slopes at the time of maximum off-shelf tidal streaming. In addition, Maxworthy (1979) made a series of laboratory experiments to simulate flow over an underwater ridge (or sill) that showed the formation of a depression on the lee side of the ridge, which evolved in a similar way to those thermocline depressions observed by Pingree et al. (1986) and other observations described by Chereskin (1983) and Farmer and Smith (1980).

The Mascarene Plateau or Ridge is situated in the western portion of the south Indian Ocean, and extends for over 2000 km between Seychelles in the north (4°S, 56°E) and Mauritius in the south (20°S, 57°E) and consists of a series of ridges separated by shallow banks or "shoals" (see Fig. 1). In this study we concentrate on the rectangular area between 10°S and 15°S and 56–64°E that includes a passage between 12°S and 13°S between the Saya de Malha and Nazareth Banks. This passage is of the order of 70 km long and oriented in the NNE–SSW direction, comprising a sill that is 400 m deep on average, and a narrow deeper channel centered approximately at 12.5°S and 60.9°E (see also Fig. 6 for detailed

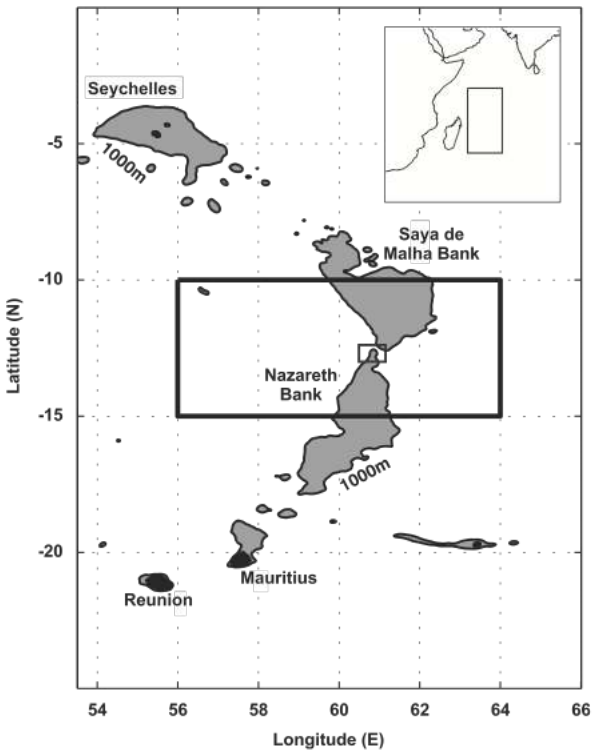

Fig. 1. Study area for the present work, in relation to the western Indian Ocean (see top-right inset). Shadow regions represent areas shallower than 1000 m and dark regions represent land (Seychelles, Mauritius, and Reunion as well as smaller islands). The outer dark rectangular frame shows the area surveyed with SAR, and is shown in detail in Fig. 4. The inner rectangular frame shows the area of detailed topography shown in Fig. 6.

bathymetry). The South Equatorial Current (SEC) dominates the mean surface currents in this area. On the east side of the banks (near 64°E) there is a strong westward mean flow, which extends between 10°S and 16°S with near-surface currents of 30–70 cm s^{-1}. Over the sill there is also a predominantly mean flow to the west with typical speeds of 50–70 cm s^{-1}, resulting from the flow being constrained between the two banks (Saya de Malha and Nazareth). On the western side of the plateau the SEC comprises two current cores centered near 12–13°S and 18–19°S with average speeds of 30–40 cm s^{-1} (New et al., 2007). The currents are more or less uniform in the upper well-mixed layer (depths of 50–100 m) but become weaker deeper down, extending to 500–1000 m in depth. Barotropic tidal currents over the sill (see above) are also significant. Both semi-diurnal and diurnal constituents can add to give amplitudes as high as 35 cm s^{-1} in the east–west direction during spring tides (Egbert and Erofeeva, 2002, see also http://www.oce.orst.edu/research/po/research/tide/index.html). The M_2 and S_2 tidal constituents individually have amplitudes of typically 15 cm s^{-1}, and so there is a strong spring–neap variability. Diurnal components such as K_1 and O_1 have amplitudes of 5 and 3 cm s^{-1}, respectively.

The present study is motivated by an observational campaign that was undertaken by R.R.S. Charles Darwin (cruise 141, New, 2003; New et al., 2005, 2007) between 1 June and 11 July 2002. One of the objectives of the cruise was to make an assessment of the energy fluxes and mixing produced by internal waves in the vicinity of the Mascarene Plateau. This paper amplifies this objective by reporting ISW characteristics observed in SAR images of the study region. Large amplitude ITs and ISWs have indeed been observed *in situ* by Morozov and Vlasenko (1996) and Konyaev et al. (1995) to the east of the Mascarene Plateau, but the full two-dimensional spatial structure of these waves was not made clear.

In ship-based transects across the plateau near 12–13°S, Konyaev et al. (1995) reported broad solitary depressions of the thermocline appearing with semi-diurnal period at the eastern edge of the sill, which propagated to the east and evolved into ISW trains. These ISWs were mode-1 (with vertical oscillations in phase between 50 and 300 m), had amplitudes of about 90 m, and their surface manifestations were observed as some 3 km wide rip bands stretching from horizon to horizon with 1 m high surface waves and white caps (similar to the observations in the Andaman Sea reported by Osborne and Burch, 1980). Konyaev et al. (1995) offered two possible interpretations for the generation mechanism of these waves. According to the first interpretation, the observed ISW trains were simply the result of a gradual nonlinear evolution of the internal tidal trough. The second interpretation was concerned with the "local generation" hypothesis, in which ISWs are generated through the interaction of internal tidal beams with the upper ocean thermocline structure (see New and Pingree, 1990, 1992; Gerkema, 2001; New and da Silva, 2002; Azevedo et al., 2006; Akylas et al., 2007; da Silva et al., 2007, 2009). Konyaev et al. (1995) also observed the formation of a depression of the thermocline with high-frequency oscillations on the western side of the sill when the combined flow (tidal plus steady westward current) reached a maximum ($\sim$1.5 m s^{-1}). A particular feature reported by these authors was the presence of second mode short-period oscillations on the western/lee side of the sill that resulted in an elevation/depression of the upper/lower part of the thermocline, respectively. Some of the short-period waves found above the sill were also of second mode, and, according to Konyaev et al. (1995), were relatively short-lived and did not always survive crossing the sill (about 15 km wide).

In the present paper, while we do indeed report SAR signatures consistent with the mode-2 internal waves observed by Konyaev et al. (1995), the main focus is on the long-lived ISWs (mode 1) that propagate over several hundreds of km to both sides of the sill. The main aims of the paper are to describe for the first time the complete two-dimensional (near-surface) structure of the ISW packets on both sides of the plateau, and to propose a simple generation mechanism for them (splitting of a large internal lee wave that forms on the western side of the sill).

The paper is organized as follows. In Section 2 we present the results of analysis of a comprehensive dataset of SAR imagery on both sides of the sill between Saya de Malha and Nazareth Banks, and reveal in the form of a composite map the along-crest coherence and propagation extent of ISWs generated near the sill. Some of the crests of these ISWs exceed 300 km in length and propagate for more than 400 km to the west, and for some 300 km to the east. We then analyze in Section 3 the propagation characteristics of these ISWs based on a travel-time graph obtained from the SAR imagery at different tidal phases, and support this with an analysis of linear internal wave phase speeds resulting from the local stratification and shear currents. Section 4 then proposes a generation mechanism and source for the waves and presents direct observational evidence of the development of a large lee wave or internal tidal thermocline depression on the western side of the sill that supports our generation mechanism. In Section 5 we then discuss evidence for the mode 2 ISWs, which are found only relatively close to the sill and do not propagate for large distances into the open ocean. Finally, Section 6 summarizes and discusses our results.

2. SAR observations

In all, over 100 ENVISAT ASAR images (in Wide Swath, WS, mode with a viewing area of 400×400 km^2) were requested from the European Space Agency (ESA). The period of the images spanned from November 2008 to January 2010. No images were available from the period of the field work on R.R.S. Charles Darwin (1 June–11 July 2002) because at that time there was no satellite antenna collecting ENVISAT ASAR images in this remote region of the Indian Ocean. In addition, 22 ENVISAT ASAR images were acquired in Image Mode (IM) and revealed the morphology of radar signatures of ISWs in high spatial detail, although these were not used in the present study because the swath width (100 km) was not large enough to gain insight into the generation source and propagation extent of the ISWs (for detailed discussion see da Silva et al., 2007).

Fig. 2a and b shows two typical ASAR WS images covering an area of about 400×400 km^2 each, which illustrate the two-dimensional horizontal coherence of ISWs observed to either side of the plateau (Fig. 2a acquired on 11 February 2009 at 18:31 UTC covers the western side and Fig. 2b acquired on 25 May 2009 at 05:27 UTC covers the eastern side). Mode-1 internal waves will be revealed in SAR images by a bright band preceding (in the direction of travel) a dark band (see Alpers, 1985), as opposed to a mode-2 wave, in which a dark band precedes a bright band. This is because for a mode-2 ISW the surface convergence and divergence patterns are reversed in relation to those corresponding to a mode 1 wave. This causes a SAR signature similar to that resulting from an ISW of elevation, as has been explained by Liu et al. (1998). Inspection of these and other similar images shows ISW signatures consistent with mode 1 deep water ISW trains of depression with crest lengths in excess of 350 km, slightly more developed (in terms of crest length) to the west of the sill in comparison to the ISWs observed to the east. These are amongst the longest-crested ISWs that have been observed anywhere in the world, exceeding those observed in the Sulu Sea and similar to those in the south China Sea. Since the thermocline depth is shallow compared to the total water depth we can assume that the ISWs are waves of depression, and the direction of propagation can be confirmed by considering hydrodynamic modulation theory (Alpers, 1985). According to this theory the bright bands associated with the ISW crests should

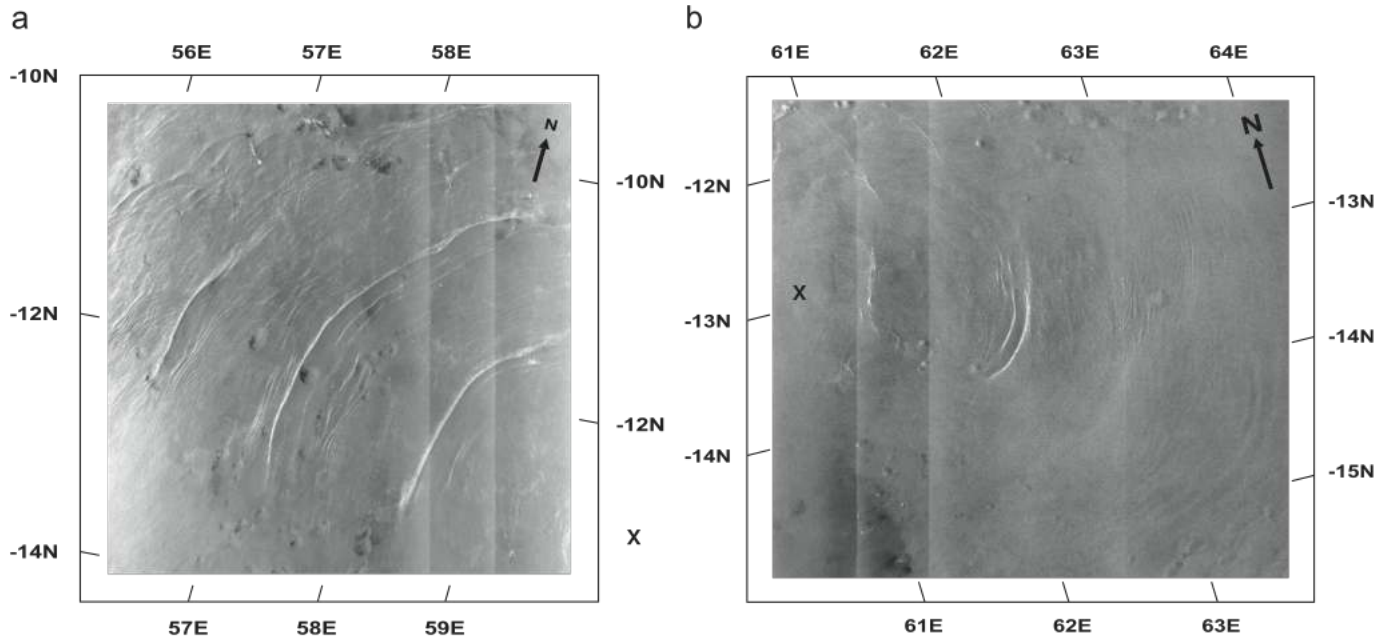

Fig. 2. (a) ENVISAT ASAR image in WS mode for 11 February 2009 acquired at 18:31 UTC. The image is approximately 400 × 400 km^2 and shows long-crested ISWs exceeding crest lengths of 350 km. Mark "X" denotes a reference location in connection with a proposed generation source for the observed ISWs. (b) ENVISAT ASAR image in WS mode for 25 May 2009 acquired at 05:27 UTC. The image is approximately 400 × 400 km^2. Mark "X" denotes a reference location in connection with a proposed generation source for the observed ISWs.

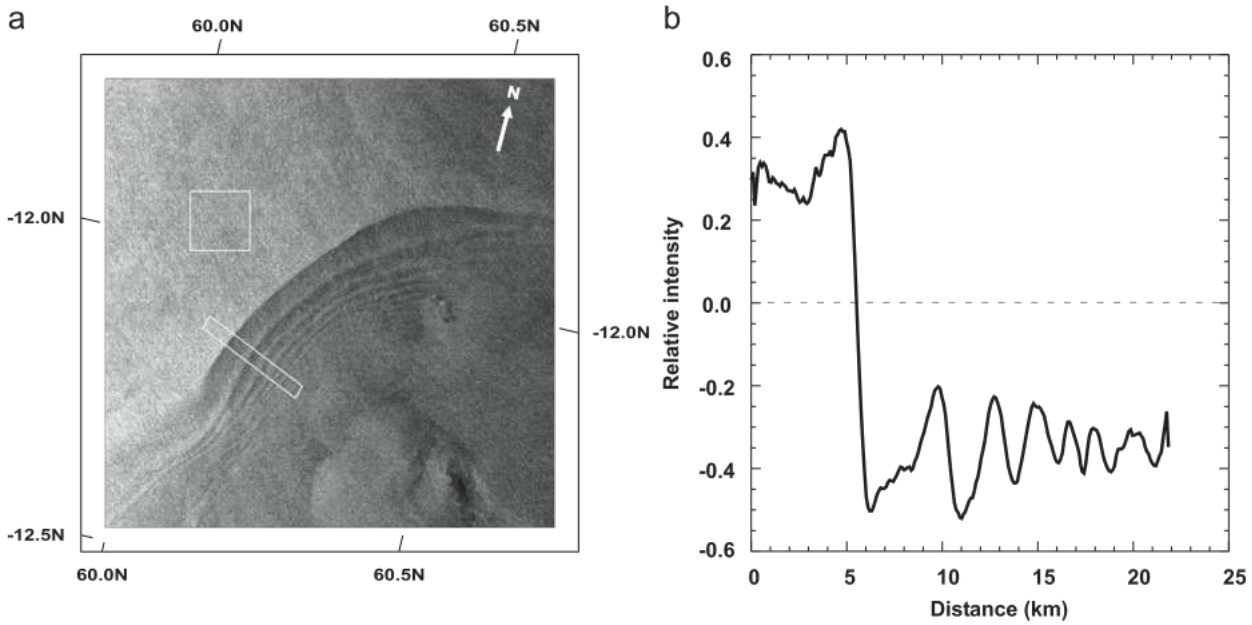

Fig. 3. (a) Full resolution extract of ENVISAT image showing a typical ISW train (dated 13 December 2008 at 18:17 UTC) to the west of the Mascarene Ridge. The narrow rectangle shows the area for the radar backscatter transect shown in (b), and the squared box was chosen as an image background level. (b) Normalized radar cross section profile along the transect shown in (a), normalized by the average radar backscatter of the squared box also shown in (a). Note the initial positive backscatter variation of the first (and largest) soliton in the packet, and the significant transition to lower (and negative) backscatter values of the following waves in the packet. This is a typical feature of an undular internal bore.

appear ahead of (in the direction of wave propagation) the darker bands, in particular for the first wave of the packet. That this is the case is easy to identify in Fig. 2a (see also Fig. 3). The general appearance of ISWs is that they are radiating from a source with a possible location somewhere near position "X" (defined below) in Fig. 2a and b.

In individual SAR images on the western side (Fig. 2a) the ISW wave packets along the propagation path are often spaced at about 100–140 km, which, assuming a semi-diurnal generation periodicity, translates to an average propagation speed of up to 3.1 m s^{-1}. On the eastern side (Fig. 2b) the inter-packet separation is somewhat shorter and varies between 95 and 125 km (equivalent to an average propagation speed up to 2.8 m s^{-1}).

Fig. 3a shows a typical ISW train (acquired on 13 December 2008 at 18:17 UTC) in a stage of early development, propagating to the west of the sill and centered at approximately 12°S, 60.5°E. A radar

backscatter profile across the ISW train is presented in Fig. 3b, normalized to the image intensity at the background level taken as the average normalized radar cross section of the square marked in Fig. 3a (ahead of the wave train and thus unperturbed by the waves). Wavelengths decrease towards the rear of the packet as is usually the case for ISW trains in the ocean, from 5 km in the leading wave to about 1 km towards the rear. Note the sharp (step-like) decay of average radar backscatter from the first to the following waves in the train. This suggests a bore-like waveform similar to those found in other regions (Wesson and Gregg, 1988; da Silva at al., 2000; Jeans and Sherwin, 2001). The wave train is observed over deep water and since the leading wave has a brighter backscatter signature to the west, this confirms that this is a train of mode-1 waves of depression propagating to the west.

We also note that in many images only bright bands (with no associated dark bands) are observed in the SAR images, as in for example Fig. 2b. These SAR signatures have a similar morphology to those in other regions such as the Andaman Sea, the Sulu Sea, and the south China Sea (Zhao et al., 2004a). In these cases, bands of breaking meter-scale surface waves occur in the region of strong convergence over the descending branch of each ISW, causing enhanced radar backscatter (see e.g. Thompson, 1988; Kudryavtsev and Johannessen, 2004). This is due to the high phase speeds of the ISWs, which cause internal wave–surface wave interaction in the meter-scale portion of the surface wave spectrum (Phillips, 1973).

Fig. 4 presents a composite constructed by mapping the locations of the ISWs (only leading crests for each individual packet are marked, for simplicity) in a selection of 34 ENVISAT ASAR WS and one TerraSAR-X overpasses, in relation to the bathymetry of the region. This clearly shows a high level of organized ISW activity to both sides of the Mascarene Plateau. Analysis of all SAR images revealed that ISWs are found throughout the year (in all seasons) and that the wave activity is more pronounced near spring tides. In fact, all wave packets in Fig. 4 correspond to spring tides or are from a period of a few days after springs. In Fig. 4 the long dashed line represents the mean axis of propagation of the observed ISWs and the shorter dashed line is perpendicular to the propagation axis and is marked for reference. On the west side of the ridge, ISWs travel towards about 300°T and on the east side towards about 120°T. From Fig. 4 it can be seen that there is a radial spreading (increasing crest lengths with distance from the sill) both to the west and east, and the long-crested ISWs are typically coherent for 400 km to the west and 250 km to the east. The ISW wavelengths typically exceed 5 km for the leading waves on both sides of the sill. The point marked "X" at the intersection of the proposed propagation path with the line perpendicular to it (the two dashed lines in Fig. 4) is a reference location to measure distances of propagation from a plausible internal wave generation source (see below). Note that this location is also marked in Fig. 2a and b for reference (and also in Figs. 6 and 8a).

In addition to the ENVISAT ASAR images, we have analyzed 7 TerraSAR-X ScanSAR images (for which the swath is approximately 100×100 km^2) focusing on the expected generation region (centered at point "X" in Fig. 4). These are not shown, but are discussed further below. They reveal that there is a "dead zone" to the west of "X" at least 35 km wide where no SAR signatures of the initial stages of internal wave formation are observed. This is likely to be due to the necessary time taken for the ISWs to form from the internal tidal thermocline depression that forms in the lee of the

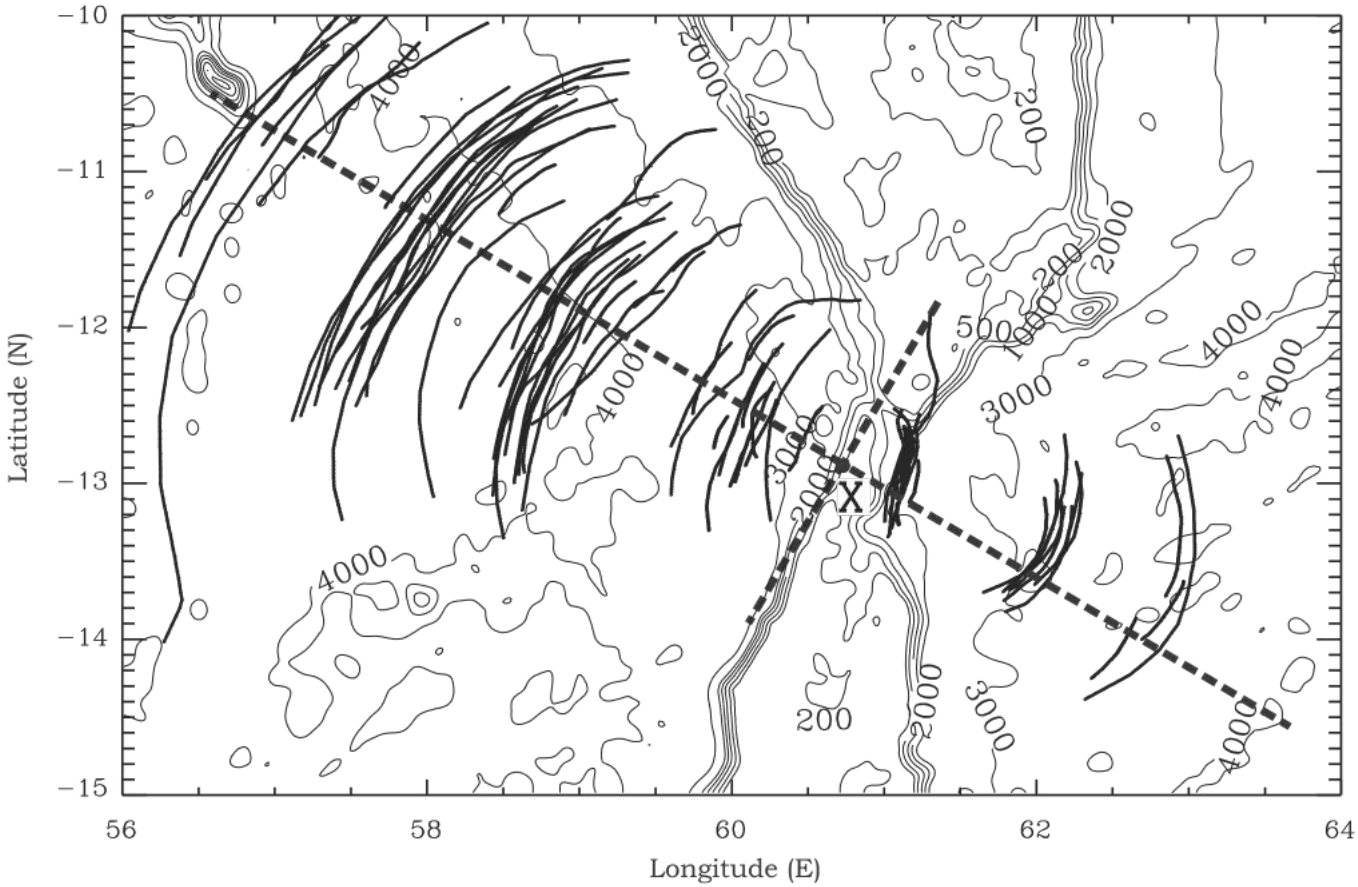

Fig. 4. Composite map of ISW observations based on ENVISAT ASAR images for the study region (only leading waves for each packet are marked for clarity). The longer dashed line represents an approximate propagation axis of the ISWs and the smaller dashed line is perpendicular to it and intersects it at position "X" (see text for details). Contours mark isobaths in meters at 200, 500, 1000, 2000, 3000, and 4000 m.

sill. We also note that the crest extent and SAR signature amplitudes are less developed on the eastern side of the plateau as compared to those on the western side, and the ISWs penetrate more extensively to the west of the Mascarene Plateau (more than 400 km to the west as compared to about 250–300 km to the east).

3. Internal solitary wave propagation

Analysis of the dataset described in Section 2 suggests a generation source of the internal waves somewhere near the sill between the Saya de Malha and Nazareth Banks (and possibly on the western side of the sill), in that both sets of wave patterns appear to be radiating or propagating from this location (i.e. somewhere near position X). This would certainly be consistent with Konyaev et al. (1995), who reported that a hydraulic jump is generated only on the western side of the sill, when the combined flow (tidal and steady South Equatorial Current) reaches its maximum. To begin to locate the generation position and time more accurately, and to assess the propagation speeds of the waves, Fig. 5 presents a travel-time graph relating position (distance from point "X", whose geographic coordinates are 12°53′S and 60°44′E) and time (with respect to maximum eastward barotropic tidal flow) of each leading ISW packet detected in the SAR images. Note that the times after maximum eastward tidal flow for each SAR image were obtained by comparison with the tides predicted by the tidal model OTIS (Egbert and Erofeeva, 2002; see also http://www.oce.orst.edu/research/po/research/tide/index.html), which employed the M_2, S_2, and K_1 tidal constituents in a (1/4)° resolution model. The distance scale in Fig. 5 is defined as distance from point X (positive to the east) along the long dashed line in Fig. 4, and the data points are marked in green to the east of the plateau and red to the west. Since an individual SAR image usually has signatures of several of these packets, corresponding to generation on different semi-diurnal tidal cycles, each image may contribute several points to the figure. For these occurrences, the positions of the wave packets are displaced by multiples of the tidal cycle (12.42 h) to align them along a plausible propagation pathway.

To these data points in Fig. 5 we have applied best fit lines. The slopes of these lines indicate an average propagation speed of 2.38 m s^{-1} for the eastward traveling waves and 2.99 m s^{-1} for the westward traveling waves. Here, we are making the assumption that the ISW packets are trapped in the troughs of near-surface internal tides, which are generated with a semi-diurnal frequency (as is the case elsewhere, for example in the Bay of Biscay, New and da Silva, 2002). The speeds derived from Fig. 5 are therefore considered to represent the phase speeds both of the internal tides and the (leading) ISWs in each packet. The scatter of the points about the idealized lines is to be expected as the waves may be refracted by varying stratification, propagate through variable currents and vertical shears, and originate at slightly different phases of the tide due to interference with diurnal constituents. We also note that the satellite (ENVISAT) orbit allows images to be captured only at certain times of the semi-diurnal tidal cycle. The grouping of the data points in Fig. 5 is related to this fact. Since the orbit is phase locked with the fortnightly spring–neaps cycle, sampling within the flood–ebb cycle is aliased so that near spring tides the images always correspond to a similar flood–ebb phase of the semi-diurnal tide. However, the "first" (corresponding to the minimum time) red point in Fig. 5 is that of a single TerraSAR-X image, and is slightly separated from the next group of points because the overpasses of TerraSAR-X and ENVISAT are separated in time by about 4 h.

We now compare the internal tidal phase velocities inferred from the travel-time graph in Fig. 5 with two-layer linear theory (which can support mode-1 waves only). New et al. (2007) measured and discussed the stratification and currents in the upper ocean with a CTD and shipboard and lowered ADCPs over the sill and to a distance to the east and west of the sill, and these observations are now used to estimate theoretical phase speeds. There is considerable shear in the upper ocean, and here we will use as a first approximation a two-layer model with the assumption

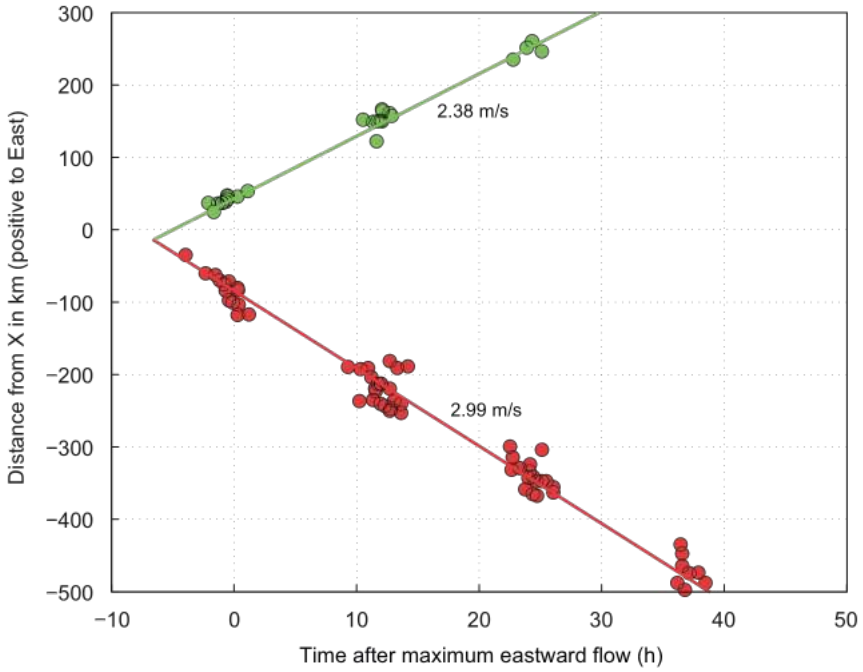

Fig. 5. Travel-time graph based on available SAR images (those of Fig. 4). The vertical axis represents the distance of leading ISWs in each packet measured from position "X" along the propagation axis. Times are referred to maximum eastward tidal flow according to the OTIS tidal model (see text for details). Red points represent western-propagating waves (negative distances) and green points show eastern-propagating waves (positive distances). Note the larger propagation speeds to the west (c=2.99 m s^{-1}) compared to lower speeds to the east (c=2.38 m s^{-1}). The intersection of the fitted lines gives insight into the generation time and position (about 7 h before maximum eastward flow, and 15 km to the west of X).

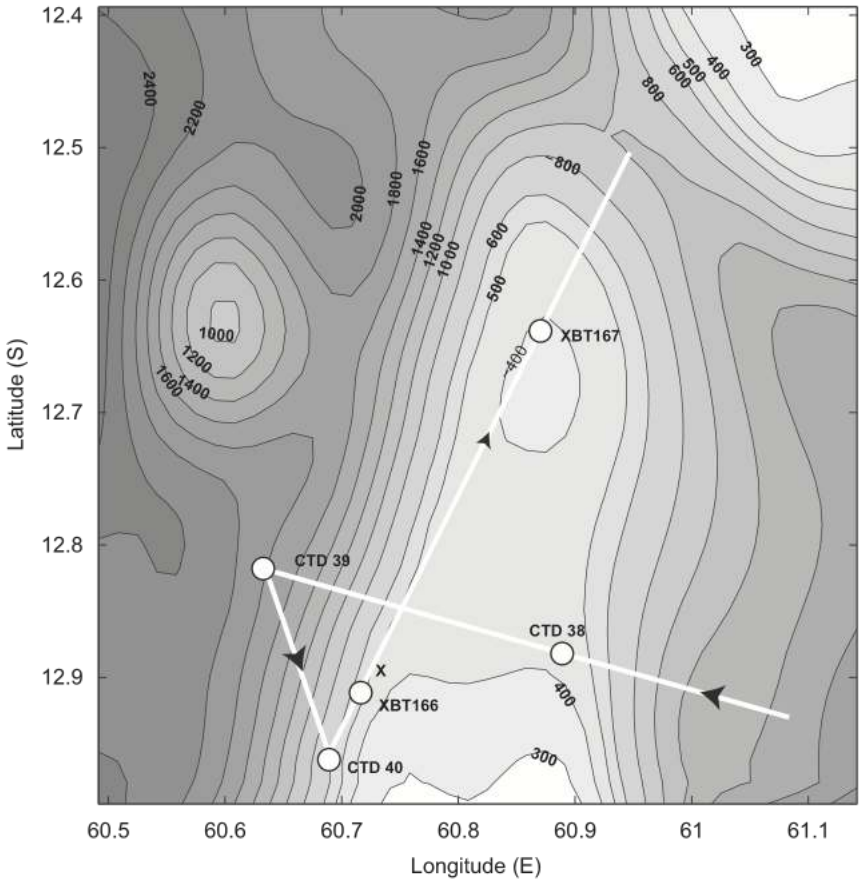

Fig. 6. Seafloor topography (m) over the sill between the Saya de Malha and Nazareth Banks obtained from composite measurements of the Smith and Sandwell (1997) dataset and New et al. (2007). The area of this figure is represented by the inner black rectangle in the map of Fig. 1. Contour interval is from 100 down to 600 m, and every 200 m thereafter. The ship track on 28–29 June 2002 is marked by the white line and CTD and XBT stations are shown. Dark arrows indicate the direction of ship. The position "X" is also shown.

Table 1
Deep water linear phase speeds on the western and eastern sides of the sill at 12.5°S in the Mascarene Plateau. See text for details of the calculation methods.

West		East	
Observed C_p=2.99 m s^{-1}		Observed C_p=2.38 m s^{-1}	
Two-layer phase speeds	Modal phase speeds	Two-layer phase speeds	Modal phase speeds
C_p=2.93 m s^{-1}	With shear:	C_p=2.14 m s^{-1}	With shear:
h_1=50 m;	2.67 m s^{-1}	h_1=50 m;	2.09 m s^{-1}
h_2=3750 m	Mode-1	h_2=2950 m	Mode-1
u_1=0.4 m s^{-1};	1.64 m s^{-1}	u_1=0.4 m s^{-1};	1.23 m s^{-1}
	Mode-2		Mode-2
u_2=0.05 m s^{-1}	1.05 m s^{-1}	u_2=0.05 m s^{-1}	0.77 m s^{-1}
	Mode-3		Mode-3
$\Delta\rho/\rho$=4.9 × 10^{-3}		$\Delta\rho/\rho$=4.9 × 10^{-3}	

that the waves are long compared with the depth of the ocean (see e.g. Baines, 1995). In this case the phase speed is given by

$$c_{\pm} = \frac{u_1 d_2 + u_2 d_1}{d_1 + d_2} \pm \left(\frac{g' d_1 d_2}{d_1 + d_2}\right)^{1/2} \left(1 - \frac{(u_2 - u_1)^2}{g'(d_1 + d_2)}\right)^{1/2} \quad (1)$$

where d_i, u_i, and ρ_i are the depth, speed, and density of the upper (i=1) and lower (i=2) layers, respectively, and $g' = g(\rho_2 - \rho_1)/\rho_2$. Note that the Mascarene Plateau is close enough to the equator for rotational effects to be neglected in Eq. (1). Taking the parameters for the two-layer model based on the local stratification (derived from CTD station 39, see Fig. 6) and on a representative mean current structure for the SEC derived from the ADCP data (see Table 1), very good agreement with the observations is obtained on both sides of the sill: 2.14 and 2.93 m s^{-1} to the east and west, respectively (see Table 1). This indicates that the IT waves propagate with a speed commensurate with their behaving as linear (mode 1) long waves on the interface, and that the difference between the phase speeds observed on the east and west side of the sill is primarily due to the presence of the background steady current (the southern Equatorial Current). In other words, the propagation speeds of the waves are enhanced when traveling with the mean current, and retarded when traveling against it.

To reinforce these conclusions, we now also derive the linear phase speeds from a model in which the stratification and current structure changes continuously in the vertical in a more realistic manner. The Taylor–Goldstein equation including a background shear flow was therefore solved numerically to investigate the propagation speeds for internal tidal modes (see Smyth et al., 2010) and we assumed a semi-diurnal frequency. Here we again used mean current and density profiles from the observational data. The current profile was taken from average ADCP measurements near the sill (see Fig. 4c of New et al., 2007, near 13°S), and the density structure used was again that of CTD station 39. We also took the ocean depth as 3800 m to the west of the sill and 3000 m to the east. Table 1 then presents the modal phase speeds for the first three modes using this continuous model. It is readily seen that the first baroclinic mode gives the most realistic phase speeds, with predicted speeds of 2.09 and 2.67 m s^{-1} to the east and west, respectively. Again, these speeds are in reasonable agreement with the values estimated from the travel-time graph in Fig. 5. Note that

the observed phase speeds (derived from the SAR images) are, however, higher than the calculated ones (see Table 1, derived from linear theory). This is quite probably because of nonlinear effects, which are well known to increase the phase speed of linear waves.

4. Internal solitary wave generation

A consistent picture has been provided by Fig. 5 of essentially constant propagation speeds on both sides of the sill. Importantly, the two lines showing mean propagation on each side of the sill intersect at a suggested generation site and time. This strongly indicates that both sets of ISWs can be considered as being generated at 15 km to the west of the sill (position X), and at about 7 h before maximum eastward flow. In other words, the waves form just to the west of the sill at the time of maximum westward flow, which would be when the largest depression of the thermocline would be expected here. This condition would then exactly match the generation position and times found by Pingree et al. (1986) at the Celtic Sea shelf break in the northern Bay of Biscay: that a large thermocline depression forms just oceanwards of the shelf break at the time of maximum off-shelf streaming and that this depression or trough then splits into two and sends IT waves traveling both onto the shelf and into the deep ocean (i.e. in both directions). The ITs in the Bay of Biscay were then found to form ISWs through nonlinearity and dispersion after a time lag of about 3–6 h. Note that a shorter time lag would be expected for the Mascarene Plateau (and may indeed be derived from the SAR images) since the effects of the earth's rotation are reduced here, as discussed by e.g. Farmer et al. (2009) and Gerkema (1996). We therefore propose that a similar trough-splitting mechanism occurs in the present case, and now investigate whether there is evidence of the proposed large thermocline depression forming at the suggested time and position. For this we again utilize the *in situ* data collected during R.R.S. Charles Darwin cruise 141 and discussed by New et al. (2007).

Fig. 6 illustrates the ship track (white line) on 28–29 June 2002 when several CTD/LADCP and XBT stations were conducted as well as shipboard ADCP measurements. It should be noted that the bathymetry in Fig. 6 is a composite of the 1′ Smith and Sandwell

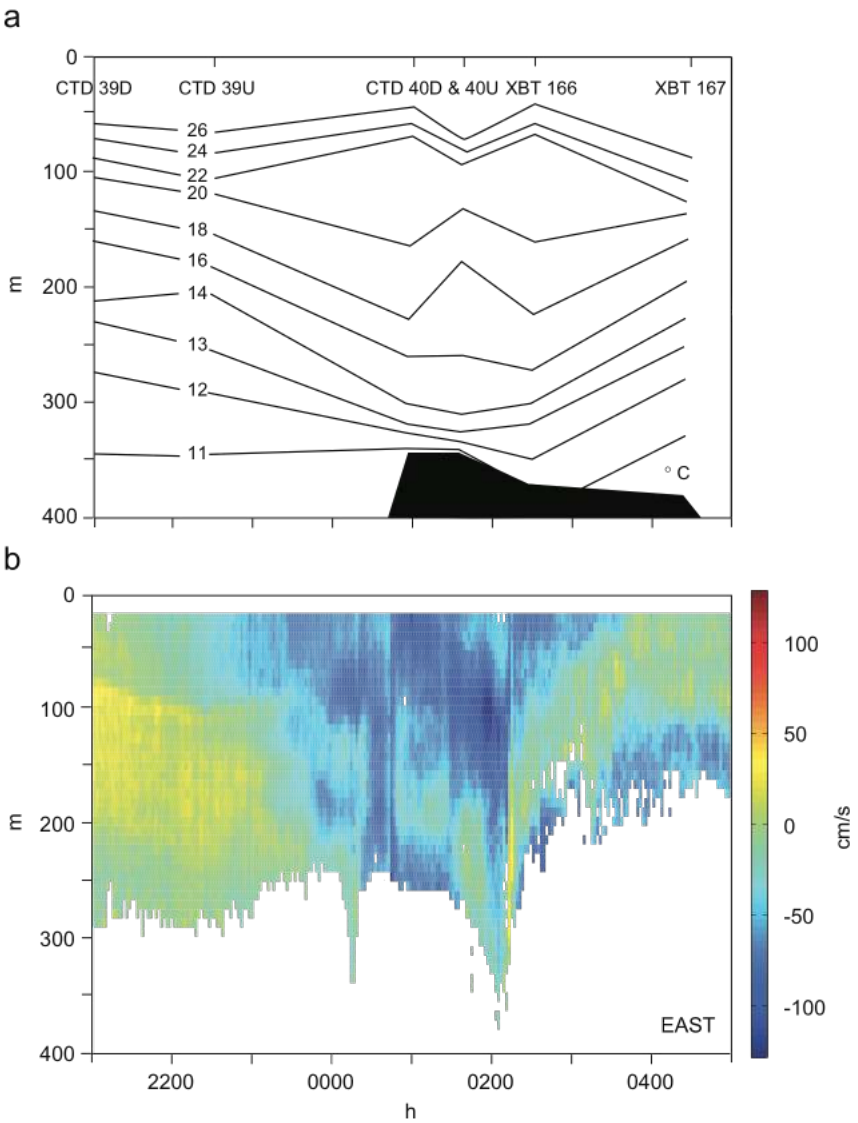

Fig. 7. (a) Section showing isotherms along ship track (see Fig. 6). The seafloor is shown as the filled contour. Vertical ticks on the top horizontal axis show the positions of CTD and XBT stations (and D and U indicate the downcasts and upcasts for the CTD stations). The vertical axis shows depth in meters. The horizontal axis shows time in UTC for 28–29 June 2002. (b) Corresponding section of eastward component of shipboard ADCP measurements along the same ship track as in (a). The horizontal and vertical axes are the same as for (a). The color scale is as indicated on the right-hand side of figure. Note the character of the horizontal currents between 00:00 and 03:00 UTC consistent with mode-2 internal waves.

(1997) global bathymetry (which New et al. (2007) concluded could often be significantly in error) and the bottom topography measured during the cruise using an EM12 swath bathymetry system (which shows accurate depths but only along the ship track). New et al. (2007), for instance, indicated that the ridge crest between the Nazareth and Saya de Malha Banks is, for most of its length, fairly uniform in depth and flat-topped, generally being about 400–450 m deep. This is about 800 m shallower than the bathymetry in Smith and Sandwell (1997). New et al. (2007) also showed that the deeper channel between the two banks (at 12.5°S) is in a location very similar to that predicted by Smith and Sandwell (1997), but is about 550 m shallower. Fig. 6 was therefore constructed by assuming the sill to be more or less flat-topped and some 15 km wide, with depths matching those observed along the ship track, and with overall shape and extent defined from the Smith and Sandwell (1997) dataset.

As illustrated in Fig. 6, the ship first made the transect from the southeast corner of the figure towards the west–northwest, passing over the top of the sill and completing CTD 38. After undertaking CTD 39 on the western side of the ridge and turning south-eastwards in deep water, the ship then found the sill crest again (undertaking CTD 40) before steaming north–northeastwards along the crest towards the Saya de Malha Bank. During this last passage XBTs 166 and 167 were undertaken. We also note that point "X" (defined in Fig. 4) is located on the western slopes of the ridge, at a depth of 500 m on the upper slopes of the sill. Therefore the suggested generation source (15 km to the west of X) lies over the deeper slopes of the ridge, at a depth of 2000–2200 m, and is actually very close to CTD station 39.

Fig. 7a shows isotherms along the ship track in Fig. 6 between CTD 39 and XBT 167, starting at 21:00 UTC on 28 June and finishing at 04:30 UTC on 29 June 2002. Fig. 7b reveals the corresponding shipboard ADCP currents (eastward component). We first note that, according to the OTIS tidal model (described above), the period of time corresponding to the measurements in Fig. 7 spans from approximately 2 h after the predicted maximum eastward tidal flow, passing through the maximum westward tidal flow at about 01:30 UTC and extending to slack water (for the tides) at 05:00 UTC. This is in excellent agreement with the ADCP measurements in Fig. 7b, since between 21:00 and 22:30 UTC the flow is indeed to the east (positive values) and then reverses to flow westwards until 03:00 UTC, with maximum westward flow near 01:30 UTC. In passing, we comment that since the OTIS currents agree in time with the ADCP measurements, this gives us confidence in the accuracy of the phases of the tidal model, and thus in our previous assumptions concerning the internal wave generation based on the SAR data in Fig. 5, namely that generation should occur at the time of maximum westward flow.

Between 23:00 UTC on 28 June and 01:00 UTC on 29 June the flow is westwards and coincides with a large depression of several isotherms in Fig. 7 (those at 20, 18, 16, 14, 13, and 12 °C). For instance, the 16 °C isotherm plunges down some 110 m in 2 h after 23:00 UTC, and the 14 °C isotherm falls 100 m in the same period. This is consistent with a large lee wave forming on the western side of the sill during the westward flow of the combined steady and tidal currents. The westward flow and downward-sloping of the isotherms commences from about the time the ship leaves CTD station 39 in deep water and commences passage up the shoaling slopes of the western side of the sill. The depression and westward flow are then most pronounced at CTD 40 and XBT 166, on the upper slopes of the western side of the sill. During the subsequent passage of the ship along the ridge crest the thermocline is then observed to rise, recovering mostly to its original position, at the same time the westward currents weaken and shift to flow eastwards again. This is therefore direct evidence for the proposed large lee wave or thermocline depression forming on the western side of the sill at exactly the right time of the tidal flow.

We postulate that this large depression then breaks into two progressive internal tidal waves, one traveling to the east and another to the west, in the manner of the splitting mechanism proposed by Baines (1982) and observed by Pingree et al. (1986). Subsequently, these internal tidal waves would be expected to evolve into nonlinear ISW trains as described by the models of Gerkema (1996) and Vlasenko et al. (2005).

5. Second mode internal waves

We now notice that Fig. 7 also shows clear evidence for mode 2 as well as mode 1 internal waves. Our view is that the large general depression of thermocline can be considered essentially as a mode 1 internal tide, which subsequently forms the mode-1 ISWs seen in the SAR images already presented. However, there are also mode 2 internal waves, which are evidenced by the simultaneous rising of the upper thermocline (near 50 m), and lowering of the mid-thermocline (150–200 m) at CTD 40D (the downcast of CTD 40), coupled with the small region of eastward flow near 150–200 m depth at 01:00 h. While the ship is on station at CTD 40 it appears that the upper and mid-thermoclines return to approximately the same vertical positions as they had at CTD 39U (the upcast of CTD 39), indicating that the mode-2 wave in the upper and mid-thermocline may have propagated away, possibly to the east, by the end of CTD 40. (The lower thermocline, however, is still at maximum depression throughout CTD 40.) Subsequently, as the ship transits along the ridge crest, it seems possible that the ship then crosses back into the mode-2 wave (at XBT 166) and then out of the feature again before XBT 167. This is consistent with a mode-2 wave oriented in the north–south direction that moves towards the east at these times. We also note that the *in situ* observations were conducted close to neap tides. Had these been near spring tides it is likely that the signatures of the mode-2 ISWs would have been even more pronounced, as would have been the over-arching mode 1 depression of the thermocline.

In our case study, over the sill between the Saya de Malha and Nazareth Banks, we know from previous work (Konyaev et al., 1995) that mode 2 waves have indeed been observed to propagate eastwards over the sill. This is also in agreement with SAR synergy observations (TerraSAR-X and ENVISAT ASAR). An example of these mode 2 wave trains is shown in Fig. 8a, in which it can be seen that a train of ISWs shows as a series of dark bands preceding bright bands (refer to the explanation of mode 2 ISW SAR signatures in Section 2) along their direction of propagation to the south-east (with a leading wave centered on 60.92°E and 12.90°S in the rectangular box at the left of the center of Fig. 8a). These waves give the appearance of traveling south-eastwards, and are located over the eastern side of the sill, as shown by the overlaid bathymetry. That these are indeed mode 2 waves is further illustrated in Fig. 8b, which shows the radar backscatter profile across the mode-2 wave train (with distance increasing from the west to the east). This reveals that a radar backscatter depression precedes positive variation for the leading wave in the packet. Note that the radar backscatter profile is normalized by the image background value (an average of the return value in the square box in Fig. 8a) since this is a well known methodology to study the SAR signatures of internal waves (da Silva et al., 1998). Comparison between Figs. 2 and 8 clearly illustrates the difference between SAR signatures of mode 1 and mode 2 waves. Also shown at the right-hand side of Fig. 8a (at 61.20°E and 12.81°S) is an example of the mode-1 ISWs that appear in the SAR images previously discussed. These mode-1 waves appear to have been generated by the previous tidal cycle, which generated the mode 2 waves at 60.92°E and 12.90°S. We

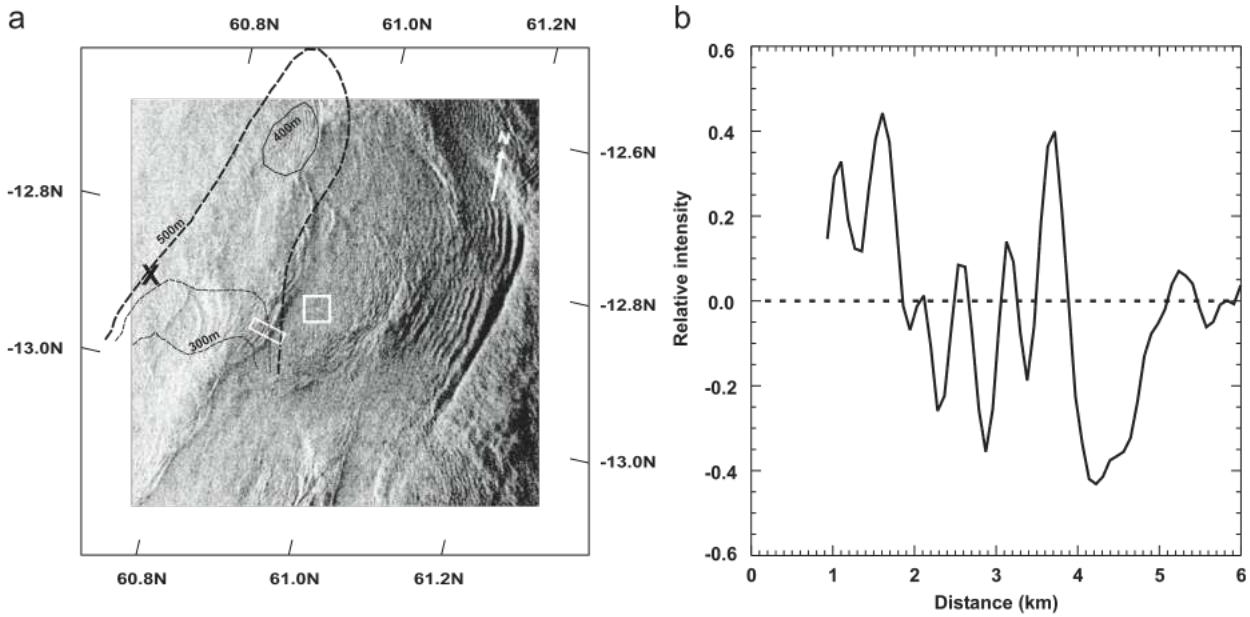

Fig. 8. (a) Full resolution extract of ENVISAT image dated 28 March 2009 at 18:17 UTC showing a typical signature of a mode-2 ISW. The image area is approximately 62×62 km^2. The narrow rectangle shows the area for the radar backscatter transect shown in (b), and the squared box was chosen as an image background level (see text for details). Position X is also marked for reference, and bathymetric contours are shown at depths of 300, 400, and 500 m. (b). Normalized radar cross section profile along the transect shown in (a), normalized by the average radar backscatter of the squared box also shown in (a). Note the initial negative backscatter variation of the first (and largest) soliton in the packet (on the right-hand side), which is typical of a mode-2 ISW SAR signature.

hypothesize that the mode-1 ISWs do not appear over the ridge because of the necessary time taken for them to form from the mode 1 tidal depression. We stress that in all 7 TerraSAR-X acquisitions (all near spring tides), as well as in many other ENVISAT ASAR images, it is common to observe mode 2 ISWs over the sill area. In fact, most of the observations of ISWs over the sill are consistent with mode 2 waves, in agreement with the observations of Konyaev et al. (1995).

During CTD station 38 on 28 June 2002 at 16:30 UTC a mode-2 ISW was recorded (not shown) when R.R.S. Charles Darwin was over the eastern side of the sill (at 12.885°S, 60.895°E). It may be possible to use this observation to estimate the propagation speed for the mode 2 ISWs over the sill by relating this to the mode 2 ISWs recorded at CTD station 40 on 29 June 2002 at 01:30 UTC, about 9 h later but some 16 km further west. Assuming that the mode 2 ISWs are traveling (south-)eastwards and appear at the position of CTD 38 at multiples of the semi-diurnal tidal cycle after 16:30 UTC on 28 June, we would expect mode 2 ISWs to reach CTD 38 at approximately, for instance, 05:00 UTC on 29 June (3.5 h after generation) or 17:30 UTC on 29 June (16 h after generation) and so on. Assuming that the waves from CTD 40 reach CTD 38 at the earlier time gives a phase speed of 1.27 m s^{-1}. This is comparable to the mode 2 phase speed estimated for deep water in Table 1 (1.23 m s^{-1} for the eastern side of the sill) but the waves are now traveling across the shallower water of the sill and would be expected to progress much more slowly. In fact, repeating the calculation with the Taylor–Goldstein equation (using the observed stratification and shear) but for the average sill depth of 400 m, shows that a mode-2 phase speed of 0.4 m s^{-1} would be expected. This agrees approximately with the phase speed estimated by assuming that the mode 2 waves generated at CTD 40 reach CTD 38 at 17:30 UTC on 29 June, which is 0.28 m s^{-1}.

This also implies that the mode 2 waves cross all or most of the sill (as far as CTD 38 at least). This, however, is consistent with Fig. 8a, which indeed shows the mode 2 ISWs at the eastern edge of the sill. We furthermore recall that Konyaev et al. (1995) found mode 2 waves over the sill several times during their measurements, and reported that some of these waves are sometimes arrested and even displaced backwards (in relation to their direction of propagation to the east) by the combined steady and tidal currents. They also estimated the mean speed of these mode 2 waves above the sill to be between 0.2 and 0.4 m s^{-1}, which is consistent with our estimates. These authors have reported, however, that the mode 2 waves do not survive the crossing of the sill.

6. Summary and discussion

In this paper we have investigated a comprehensive dataset of ENVISAT SAR and TerraSAR-X imagery of the central Mascarene Plateau in the Indian Ocean, and have shown the presence of packets of large ISWs propagating towards the west–northwest and the east–southeast from the sill between Saya de Malha and Nazareth Banks near 12.5°S. The waves propagate to at least 400 km to the west and 300 km to the east of the sill, with crest lengths as large as 350 km. This exceeds ISW crest lengths in other regions such as the Sulu Sea (crest lengths of up to 170 km), the Andaman Sea (150 km), and the Bay of Biscay (50 km) and is only comparable with those in the south China Sea with crest lengths in excess of 250 km (see e.g. Zhao et al., 2004b). The radar signatures correspond to large-amplitude backscatter modulations typical of surface rip bands associated with breaking meter-scale sea surface waves, which are modulated by strong surface currents associated with the ISWs (Konyaev et al. (1995) reported such surface roughness patterns on the eastern side of the sill). We therefore classify this region as a major hot-spot of ISW activity in the open ocean.

An investigation of the propagation characteristics of these ISWs on each side of the sill found that their phase speeds were in close agreement with those predicted from linear theory for either mode-1 or interfacial waves. A travel-time diagram inferred from the SAR image dataset indicated that the waves were generated from a location just westwards of the sill crest at the time of

maximum westward flow. We proposed that both sets of ISWs were formed from the splitting of a large tidally generated depression of the upper thermocline (or lee wave) that would form on the western side of the sill at this time. This "trough-splitting" would be consistent with the linear theoretical model of Baines (1982) and would generate internal tides traveling both eastwards and westwards. This mechanism has also been reported from direct observations in the ocean by Pingree et al. (1986) and is apparent in the model results of Gerkema (1996) and Vlasenko et al. (2005). The ISW formation would then result from the nonlinear disintegration of the internal tides, similar to the cases reported in the Sulu Sea (Apel et al., 1985) and in the Bay of Biscay (Pingree et al., 1986). Finally, direct evidence of this large lee wave on the western side of the sill was found at the right time in the tidal cycle in isotherm depressions and shipboard ADCP observations.

We consider that preferential generation of the internal tides and waves would be expected on the western side of the sill rather than on the eastern side, since the oscillatory tidal flow and steady westward background flow from the South Equatorial Current would combine to give an enhanced flow in the downslope direction (needed for the formation of the thermocline depression) only on this side of the sill. We also consider that a likely explanation of the observation that the wave packets are stronger (and propagate further) on the western side of the sill than those on the eastern side is that those traveling towards the east would need to pass over the sill itself. Since the sill is only 400–450 m deep, the internal tides or waves that pass over the sill would be long compared to the water depth and so would be expected to dissipate to some extent in their passage over the sill. In addition, the eastward-propagating waves travel against a "steady" shear flow in the South Equatorial Current, while the westward-propagating waves travel with the flow. It is possible that this may also lead to additional dissipation effects due to wave–current interactions for those waves traveling eastwards.

For the present sill on the Mascarene Plateau, Konyaev et al. (1995) reported that the vertical structure of the large (mode 1) lee wave at the sill included short-period waves above the sill with strong second mode components. We have also reported evidence for mode 2 ISWs near the sill, and we now briefly discuss a plausible mechanism for the formation of these waves. Over the sill (assuming 400 m as the average depth), phase speeds can be estimated for mode 1 and mode 2 waves in the presence of a steady background shear by solving the Taylor–Goldstein equation, as we have done above for the waves in deeper water. For the observed stratification and shear, these are 1.25 m s^{-1} for mode 1 and 0.4 m s^{-1} for mode 2 waves. Since the combined steady plus barotropic tidal currents may typically be 0.5–1.0 m s^{-1} during the maximum westward flow (even near neap tides, see Fig. 7b), the flow becomes supercritical with respect to the mode 2 waves. Stastna and Peltier (2005) showed that resonant generation of mode-2 solitary-like internal waves can be expected for such situations and we propose that this offers a likely explanation for the generation of the mode 2 ISWs in the present case. We also note that Farmer and Smith (1980) reported second mode hydraulic jumps and lee waves at Knight Inlet when the flow was supercritical with respect to mode 2 internal waves and near-critical for first mode internal waves. In addition, evidence of mode 2 baroclinic tides has also been found in the Strait of Gibraltar by Vázquez et al. (2006).

Acknowledgements

The SAR image data presented here were provided by the European Space Agency (ESA) under Project number AOPT-2423, and by the German Aerospace Center (DLR) under Project number OCE0056. One of us would like to thank the Portuguese Science and Technology Foundation (FCT) for a research grant (SFRH/BD/35898/2007). We thank both reviewers for their helpful comments, which we feel have helped to improve the paper significantly.

References

Akylas, T.R., Grimshaw, R.H.J., Clark, S.R., Tabaei, A., 2007. Reflecting tidal wave beams and local generation of solitary waves in the ocean thermocline. J. Fluid Mech. 593, 297–313. doi:10.1017/S0022112007008786.

Alpers, W., 1985. Theory of radar imaging of internal waves. Nature (London) 314, 245–247.

Alpers, W., Salusti, E., 1983. Scylla and Charybdis Observed From Space. J. Geophys. Res. 88 (C3), 1800–1808.

Apel, J.R., Holbrook, J.R., Liu, A.K., Tsai, J.J., 1985. The Sulu Sea internal soliton experiment. J. Phys. Oceanogr. 15, 1625–1651.

Azevedo, A., da-Silva, J.C.B., New, A.L., 2006. On the generation and propagation of internal solitary waves in the southern Bay of Biscay. Deep-Sea Res. I 53, 927941. doi:10.1016/j.dsr.2006.01.013.

Baines, P.G., 1982. On internal tides generation models. Deep-Sea Res. Part A 29, 307–338. doi:10.1016/0198-0149(82)90098-X.

Baines, P.G., 1995. Topographic Effects in Stratified Flows. Cambridge University Press, 482 pp.

Brandt, P., Alpers, W., Backhaus, J.O., 1996. Study of the generation and propagation of internal waves in the Strait of Gibraltar using a numerical model and synthetic aperture radar images of the European ERS-1 satellite. J. Geophys. Res. 101 (C6), 14237–14252.

Brandt, P., Rubino, A., Alpers, W., Backhaus, J.O., 1997. Internal waves in the Strait of Messina studied by a numerical model and synthetic aperture radar images from the ERS 1/2 satellites. J. Phys. Oceanogr. 27, 648–663.

Chereskin, T.K., 1983. Generation of internal waves in Massachusetts Bay. J. Geophys. Res. 88 (C4), 2649–2661.

da Silva, J.C.B., Ermakov, S.A., Robinson, I.S., Jeans, D.R.G., Kijashko, S.V., 1998. Role of surface films in ERS SAR signatures of internal waves on the shelf. 1. Short-period of internal waves. J. Geophys. Res. 103 (C4), 8009–8031. doi:10.1029/97JC02725.

da Silva, J.C.B., Ermakov, S.A., Robinson, I.S., 2000. Role of surface films in ERS SAR signatures of internal waves on the shelf. 3. Mode transitions. J. Geophys. Res. 105, 24089–24104. doi:10.1029/2000JC900053.

da Silva, J.C.B., New, A.L., Srokosz, M., Smyth, T., 2002. On the observability of internal tidal waves in remotely-sensed ocean color data. Gephys. Res. Lett. 29, 12. doi:10.1029/2001GL013888.

da Silva, J.C.B, New, A.L., Azevedo, A., 2007. On the role of SAR for observing "Local Generation" of internal solitary waves off the Iberian Peninsula. Can. J. Remote Sensing 33, 388–403.

da Silva, J.C.B., Helfrich, K.R., 2008. Synthetic Aperture Radar observations of resonantly generated internal solitary waves at Race Point Channel (Cape Cod). J. Geophys. Res. 113, C11016. doi:10.1029/2008JC005004.

da Silva, J.C.B., New, A.L., Magalhaes, J.M., 2009. Internal solitary waves in the Mozambique Channel: observations and interpretation. J. Geophys. Res. 114, C05001. doi:10.1029/2008JC005125.

Elachi, C., Apel, J.R., 1976. Internal wave observations made with an airborne Synthetic Aperture Radar. Geophys. Res. Lett. 3, 647–650.

Ermakov, S.A., da Silva, J.C.B., Robinson, I.S., 1998. Role of surface films in ERS SAR signatures of internal waves on the shelf. 2. Internal Tidal Waves. J. Geophys. Res. 103, 8032–8043. doi:10.1029/97JC02724.

Egbert, G.D., Ray, R.D, 2003. Semi-diurnal and diurnal tidal dissipation from TOPEX/POSEIDOM altimetry. Geophys. Res. Lett. 30 (17), 1907. doi:10.1029/2003GL017676.

Egbert, G.D., Erofeeva, S.Y., 2002. Efficient inverse modeling of barotropic ocean tides. J. Oceanic Atmos. Technol. 19, 183–204. doi:10.1175/1520-0426(2002)019 < 0183:EIMOBO > 2.0.CO;2.

Farmer, D.M., Smith, J.D., 1980. Tidal interaction of stratified flow with a sill in Knight Inlet. Deep-Sea Res. 27A, 239–254. doi:10.1016/0198-0149(80)90015-1.

Farmer, D., Li, Q., Park, J-H, 2009. Internal wave observations in the south china sea: the role of rotation and non-linearity. Atmosphere–Ocean 47 (4), 267–280. doi:10.3137/OC313.2009.

Gerkema, T., 1996. A unified model for the generation and fission of internal tides in a rotating ocean. J. Mar. Res. 54, 421–450. doi:10.1357/0022240963213574.

Gerkema, T., 2001. Internal and interfacial tides: beam scattering and local generation of solitary waves. J. Mar. Res. 59, 227–255. doi:10.1357/002224001762882646.

Jeans, D.R.G, Sherwin, T.J., 2001. The variability of strongly non-linear solitary internal waves observed during an upwelling season on the Portuguese shelf. Cont. Shelf Res. 21, 1855–1878. doi:10.1016/S0278-4343(01)00026-7.

Klymak, J.M., Pinkel, R., Liu, C.-T., Liu, A.K., David, L., 2006. Prototypical solitons in the south China Sea. Geophys. Res. Lett. 33, L11607. doi:10.1029/2006GL025932.

Konyaev, K.V., Sabinin, K.D., Serebryany, A.N., 1995. Large-amplitude internal waves at the Mascarene Ridge in the Indian Ocean. Deep-Sea Res. I 42, 2075–2091. doi:10.1016/0967-0637(95)00067-4.

Kudryavtsev, V., Johannessen, J., 2004. On effect of wave breaking on short wind waves. Geophys. Res. Lett. 31, L20310. doi:10.1029/2004GL020619.

Liu, A.K., Chang, Y.S., Hsu, M.-K., Liang, N.K., 1998. Evolution of nonlinear internal waves in the east and south China seas. J. Geophys. Res. 103 (C4), 7995–8008. doi:10.1029/97JC01918.

Lozovatsky, I.D., Morozov, E.G., Fernando, H.J.S., 2003. Spatial decay energy density of tidal internal waves. J. Geophys. Res. 108 (C6), 3201. doi:10.1029/2001JC001169.

Maxworthy, T., 1979. A note on internal solitary waves produced by tidal flow over a three-dimensional ridge. J. Geophys. Res. 84 (C1), 338–346.

Morozov, E.G., Vlasenko, V.I., 1996. Extreme tidal internal waves near the Mascarene Ridge. J. Mar. Syst. 9, 203–210. doi:10.1016/S0924-7963(95)00042-9.

Moum, J.N., Farmer, D.M., Smyth, W.D., Armi, L., Vagle, S., 2003. Structure and generation of turbulence at interfaces strained by internal solitary waves propagating shoreward over the continental shelf. J. Phys. Oceangr. 33, 2093–2112 10.1175/1520-0485(2003)033 < 2093:SAGOTA > 2.0.CO;2.

Moum, J., Nash, J.D., Klymak, J.M., 2008. Small scale processes in the coastal ocean. Oceanography 21 (4), 22–33.

Nash, J.D., Moum, J.N., 2005. River plumes as a source of large-amplitude internal waves in the costal ocean. Nature 437, 400–403. doi:10.1038/nature03936.

New, A.L., 1988. Internal tidal mixing in the Bay of Biscay. Deep-Sea Res. 35, 691–709. doi:10.1016/098-0149(88)90026-X.

New, A.L., Pingree, R.D., 1990. Large-amplitude internal soliton packets in the central Bay of Biscay. Deep-Sea Res. Part A 37, 513–524 doi:10.10116/0198-0149(90)90022-N.

New, A.L., Pingree, R.D., 1992. Local generation of internal soliton packets in the central Bay of Biscay. Deep-Sea Res. Part A 39, 1521–1534. doi:10.1016/0198-0149(92)90045-U.

New, A.L., da Silva, J.C.B., 2002. Remote-sensing evidence for the local generation of internal soliton packets in the central Bay of Biscay. Deep-Sea Res. I 49, 915–934. doi:10.1016/S0967-0637(01)00082-6.

New, A.L., 2003. R.R.S. Charles Darwin Cruise 141, 01 June—11 July 2002; satellite calibration and interior physics of the Indian Ocean: SCIPIO. Southampton Oceanography Centre Cruise Report No. 41, Southampton University, UK, 92 pp.

New, A.L., Stansfield, K., Smythe-Wright, D., Smeed, D.A., Evans, A.J., Alderson, S.G., 2005. Physical and biochemical aspects of the flow across the Mascarene Plateau in the Indian Ocean. Philos. Trans. R. Soc. A 363, 151–168. doi:10.1098/rsta.2004.1484.

New, A.L., Alderson, S.G., Smeed, D.A., Stansfield, K.L., 2007. On the circulation of water masses across the Mascarene Plateau in the south Indian Ocean. Deep-Sea Res. I 54, 42–74. doi:10.1016/j.dsr.2006.08.016.

Osborne, A.R., Burch, T.L., 1980. Internal solitons in the Andaman Sea. Science 208 (4443), 451–460 (New Series). doi:10.1126/science.208.4443.451.

Ostrowski, M., da Silva, J.C.B., Bazik-Sangolay, B., 2009. The response of sound scatterers to *El Niño*- and *La Niña*-like oceanographic regimes in the south-eastern Atlantic. ICES J. Mar. Sci. 66, 1063–1072. doi:10.1093/icesjms/fsp102.

Phillips, O.M., 1973. On the interactions between internal and surface waves. Izv. Atmos. Oceanic Phys. 9 (9), 954–961.

Pingree, R.D., Mardell, G.T., New, A.L., 1986. Propagation of internal tides from the upper slopes of the Bay of Biscay. Nature 312, 154–158. doi:10.1038/321154a.

Pingree, R.D., New, A.L., 1995. Structure, seasonal development and sunglint spatial coherence of the internal tide on the Celtic and Armorican shelves and in the Bay of Biscay. Deep-Sea Res. I 42, 245–284. doi:10.1016/0967-0637(94)00041-P.

Pinkel, R., 2000. Internal solitary waves in the warm pool of the western equatorial pacific. J. Phys. Oceanogr. 30, 2906–2926. doi:10.1175/1520-0485(2001)031 < 2906:ISWITW > 2.0.CO;2.

Ray, R.D., Mitchum, G.T., 1997. Surface manifestations of internal tides in the deep ocean: observations from altimetry and island gauges. Prog. Oceanogr. 40, 135–162. doi:10.1016/S0079-6611(97)00025-6.

Shaw, P.-T., Ko, D.S., Chao, S.-Y., 2009. Internal solitary waves induced by flow over a ridge: with applications to the northern south China Sea. J. Geophys Res. 114, C02019. doi:10.1029/2008JC005007.

Shroyer, E.L., Moum, J.N., Nash, J.D., 2010. Vertical heat flux and lateral mass transport in nonlinear internal waves. Geophys. Res. Lett. 37, L08601. doi:10.1029/2010GL042715.

Smith, W.H.F., Sandwell, D.T., 1997. Global sea floor topography from satellite altimetry and ship depth soundings. Science 277 (5334), 1956–1962. doi:10.1126/science.277.5334.1956.

Smyth, W.D., Moum, J.N., Nash, J.D., 2010. Narrowband, high-frequency oscillations at the equator. Part II: properties of shear instabilities. J. Phys. Oceanogr. doi:10.1175/2010JPO4451.1.

Stastna, M., Peltier, W.R., 2005. On the resonant generation of large-amplitude internal solitary and solitary-like waves. J. Fluid Mech. 543, 267–292. doi:10.1017/S002211200500652X.

Thompson, D.R., 1988. Calculation of radar backscatter modulations from internal waves. J. Geophys. Res. 93 (C10), 12,371–12,380. doi:10.1029/JC093iC10p12371.

Thompson, D.R., Gasparovic, R.F., 1986. Intensity modulation in SAR images of internal waves. Nature 320, 345–348. doi:10.1038/320345a0.

Vázquez, A., Stashchuk, N., Vlasenko, V., Bruno, M., Izquierdo, A., Gallacher, P.C., 2006. Evidence of multimodal structure of the baroclinic tide in the Strait of Gibraltar. Geophys. Res. Lett. 33, L17605. doi:10.1029/2006GL026806.

Vlasenko, V., Stashchuk, N., Hutter, K., 2005. Baroclinic Tides: Theoretical Modeling and Observational Evidence. Cambridge University Press, Cambridge, UK, 351 pp.

Wesson, J.C., Gregg, M.C., 1988. Turbulent dissipation in the Strait of Gibraltar and associated mixing. In: Nihoul, J.C.J., Jamart., B.M. (Eds.), Small-Scale Turbulence and Mixing in the Ocean. Elsevier Oceanography Series, Elsevier, Amsterdam, pp. 201–212.

Zhao, Z., Klemas, V., Zheng, Q., Yan, X., 2004a. Remote sensing evidence for the baroclinic tide origin of internal solitary waves in the northeastern south China Sea. Geophys. Res. Lett. 31, L06302. doi:10.1029/2003GL019077.

Zhao, Z., Klemas, V., Zheng, Q., Li, X., Yan, X., 2004b. Estimating parameters of a two-layer stratified ocean from polarity conversion of internal solitary waves observed in satellite SAR images. Remote Sensing Environ. 92, 276–287. doi:10.1016/j.rse.2004.05.014.

Chapter 6

Atmospheric gravity waves in the Red Sea: a new hotspot

Nonlin. Processes Geophys., 18, 71–79, 2011
www.nonlin-processes-geophys.net/18/71/2011/
doi:10.5194/npg-18-71-2011

Nonlinear Processes in Geophysics

Atmospheric gravity waves in the Red Sea: a new hotspot

J. M. Magalhaes[1], I. B. Araújo[2], J. C. B. da Silva[2,5], R. H. J. Grimshaw[3], K. Davis[4], and J. Pineda[4]

[1]Centro de Oceanografia and Departamento de Engenharia Geográfica, Geofísica e Energia (DEGGE), Faculdade de Ciências da Universidade de Lisboa, Campo Grande, 1749-016 Lisboa, Portugal
[2]CIMAR/CIIMAR – Centro Interdisciplinar de Investigação Marinha e Ambiental, Rua dos Bragas 289, 4050-123 Porto, Portugal
[3]Department of Mathematical Sciences, Loughborough University, Loughborough, LE11 3TU, UK
[4]Biology Department, MS 50, Woods Hole Oceanographic Institution, Woods Hole, Massachusetts 02543, USA
[5]Departamento de Geociências, Ambiente e Ordenamento do Território, Universidade do Porto, Rua do Campo Alegre, 687, 4169-007, Porto, Portugal

Received: 12 June 2010 – Revised: 5 January 2011 – Accepted: 18 January 2011 – Published: 3 February 2011

Abstract. The region of the Middle East around the Red Sea (between 32° E and 44° E longitude and 12° N and 28° N latitude) is a currently undocumented hotspot for atmospheric gravity waves (AGWs). Satellite imagery shows evidence that this region is prone to relatively high occurrence of AGWs compared to other areas in the world, and reveals the spatial characteristics of these waves. The favorable conditions for wave propagation in this region are illustrated with three typical cases of AGWs propagating in the lower troposphere over the sea. Using weakly nonlinear long wave theory and the observed characteristic wavelengths we obtain phase speeds which are consistent with those observed and typical for AGWs, with the Korteweg-de Vries theory performing slightly better than Benjamin-Davis-Acrivos-Ono theory as far as phase speeds are concerned. ERS-SAR and Envisat-ASAR satellite data analysis between 1993 and 2008 reveals signatures consistent with horizontally propagating large-scale internal waves. These signatures cover the entire Red Sea and are more frequently observed between April and September, although they also occur during the rest of the year. The region's (seasonal) propagation conditions for AGWs, based upon average vertical atmospheric stratification profiles suggest that many of the signatures identified in the satellite images are atmospheric internal waves.

Correspondence to: J. C. B. da Silva (jdasilva@fc.up.pt)

1 Introduction

Internal waves (IWs) are ubiquitous in the ocean and atmosphere, and their ability to play an important role in density-stratified fluid dynamics, make them an important topic of research, which contributes to several scientific areas ranging from biological mixing and exchange processes, to ocean and atmospheric forecasting (Grimshaw, 2002; Vlasenko et al., 2005; da Silva et al., 2009). Atmospheric IWs in particular constitute a potentially serious hazard to aircrafts operating at low altitudes (Christie and Muirhead, 1983; Bedard et al., 1986). There have been reports of air crashes on approach and take-off related to encounters with large-amplitude AGWs in Australia (Christie and Muirhead, 1983) that essentially occur due to unexpected clear air turbulence and low level wind shear. These are capable of causing insufficient lift at take-off or disturbances to the glide path that may lead to undershoot or overshoot of the runway.

Remote sensing image data has been increasing IW observations worldwide. In particular, satellite imagery have proved very useful, adding a significant number of observations to the meteorology and oceanography literature (Jackson and Apel, 2002; Jackson, 2004, 2007; da Silva et al., 2007, 2009; da Silva and Magalhaes, 2009).

Roughness patterns on the ocean surface can be produced both by oceanic and atmospheric IWs, and are easily detected in Synthetic Aperture Radar (SAR) images. In these images, oceanic IW patterns arise either as a result of hydrodynamic modulation of Bragg waves or wave damping due to surface films (Alpers, 1985; da Silva et al., 2000), while atmospheric imaging of IWs is a consequence of wind stress variability associated with wave propagation (Alpers and Stilke, 1996).

Published by Copernicus Publications on behalf of the European Geosciences Union and the American Geophysical Union.

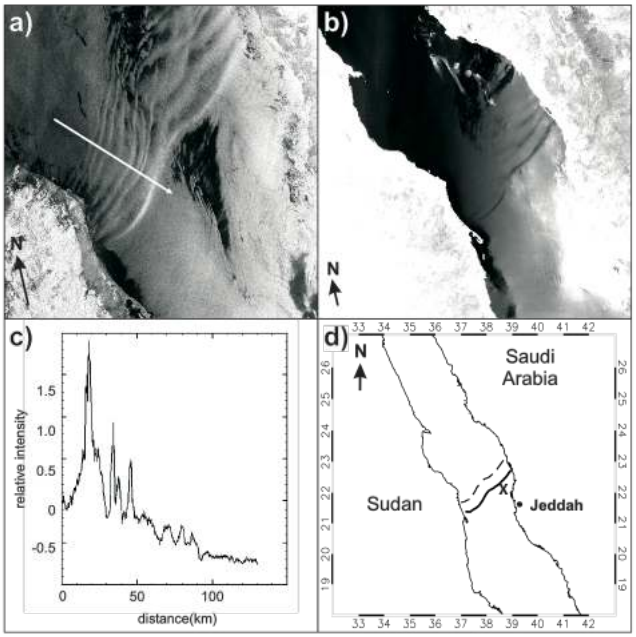

Fig. 1. Case study of an AGW occurrence in the Red Sea near Jeddah: **(a)** subset of an Envisat-ASAR image acquired at 07:26 (UTC) dated 11 May 2004. A transect profile is marked with a white arrow across the AGW packet (extending from NW to SE); **(b)** subset of a near-infrared MODIS-Terra image acquired at 08:12 (UTC) dated 11 May 2004; **(c)** relative intensity taken from the profile in the Envisat-ASAR image in **(a)**; **(d)** compiled feature map with the geographic locations of the leading waves in **(a)** (dashed line) and **(b)** (solid line), X marks the location where in situ measurements were made (22°04.509′ N, 38°46.181′ E) near Abu Madafi.

Furthermore, atmospheric IW condensation patterns in their ascending branches, and solar specular reflection (sunglint), may also be detected in near-infrared images (da Silva and Magalhaes, 2009).

Despite these different imaging mechanisms, in some cases discrimination between oceanic and atmospheric signatures in satellite imagery is difficult or even impossible and ambiguities often arise such as those exemplified by the discussions following the work of Kim et al. (2005a) (Zheng, 2005; Kim et al., 2005b; Gan et al., 2008). The global IW survey undertaken by Jackson (2007) (using MODIS imagery), showed that oceanic IWs are present in the Red Sea region (Fig. 1 in Jackson, 2007). Since we will clearly show here that AGWs are also present in the Red Sea, we alert for the possibility of misinterpretation in future studies. We stress that the problem of misclassification of IW satellite signatures is particularly severe in the Red Sea region because of the dry conditions and absence of roll clouds, and should therefore be taken under consideration especially when wavelengths approach values around 5–10 km.

AGW theories assume the existence of a waveguide, typically located in the lower layers of the troposphere, as a necessary condition for waves to propagate horizontally. These waveguides often take the earth's surface as their lower boundary, and rely on some suitable trapping mechanism in the upper layers to confine the wave energy (Rottman and Grimshaw, 2002). Several trapping mechanisms capable of preventing wave energy to radiate away in the vertical have been identified and presented in the literature (Scorer, 1949; Crook, 1986, 1988; Rottman and Grimshaw, 2002; da Silva and Magalhaes, 2009). These depend on the Scorer parameter (Scorer, 1949) which is related with the atmospheric stability and the wind speed vertical profile.

This paper presents satellite based evidence that the region of the Middle East around the Red Sea is a newly found hotspot for AGWs. It also aims to contribute to the issue of distinguishing between oceanic and atmospheric IW signatures in satellite images. Section 2 begins with a detailed case study of an AGW propagating over the Red Sea together with a comparison with weakly nonlinear long wave theory (using both the Korteweg-de Vries and Benjamin-Davis-Acrivos-Ono models). This analysis is extended to a brief description of two further case studies at the end of Sect. 2. In Sect. 3 the seasonal frequency of IW observations in the Red Sea is characterized and correlated with the region's seasonal average vertical stratification.

2 AGW case studies in the Red Sea

A case of an AGW propagating over the central section of the Red Sea on 11 May 2004 (near Jeddah, Saudi Arabia) is presented in Fig. 1. This wave packet was captured in an Envisat-ASAR image acquired at 07:26 UTC, and in a MODIS-Terra image acquired at 08:12 UTC (Fig. 1a and b, respectively). These are typical examples of AGW signatures that are seen in SAR and near-infrared (841–876 nm) imagery of the Red Sea. In this case, surface signatures of the wave packet extend across the Red Sea indicating that the along-crest length of the leading wave is at least 248 km (the wave crests may extend even further inland, but are not visible in this case).

In Fig. 1a the wave crests appear as alternating bright and dark bands (due to backscatter variations) as a result of fluctuating surface wind speed between the downdraft and updraft portions of the oscillations (Alpers and Stilke, 1996; Li et al., 2004). The propagation direction of the wave packet is approximately 130° (clockwise from North). The number of waves in the packet depends on the cross section chosen for the backscatter profile. At least 7 wave crests can be identified in the cross section in Fig. 1c, increasing to 9 waves in other sections. The distance between the leading and second wave of the packet is approximately 15 km. The characteristic length scale for an individual solitary wave is between 2–8 km (Fig. 1c) and there is clearly an amplitude-ordered backscatter profile, which suggests rank-ordered amplitude waves. This is a prominent feature of dispersive "solitary-like" wave trains (Christie, 1989). Fewer wave crests can

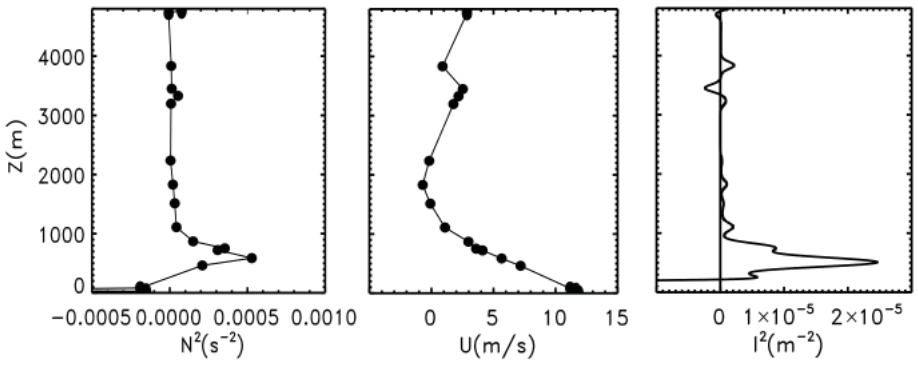

Fig. 2. Atmosphere's vertical structure and propagation conditions calculated using data from Jeddah weather station (11 May 2004 at 09:00 UTC). The buoyancy frequency is shown in **(a)**; horizontal wind velocity in the direction of wave propagation in **(b)**; and Scorer parameter in **(c)**. The solid circles in **(a)** and **(b)** represent real data whilst the solid curves represent smoothed fits to the data. The l^2 solid curve is calculated values using N^2 and U smoothed fits.

be identified in the near-infrared MODIS image (Fig. 1b) obtained 45 min later, where the surface expression of the waves appears as dark bands with no apparent cloud formations. The positions of the leading wave captured in both images are shown in Fig. 1d, from which an average propagation speed of 15.5 m s^{-1} was estimated (the phase speed actually varies along the wave front, from 17 m s^{-1} in the NE end, to 14 m s^{-1} in the opposite end). Assuming there is a background flow speed of 4.4 m s^{-1} along the propagation direction (suggested by the average U within the waveguide, see Fig. 2b) the estimated intrinsic average phase speed is 11.1 m s^{-1}. The characteristics of these waves make them comparable to the Australian Morning Glories (Smith, 1988; Christie, 1989; Rottman and Grimshaw, 2002), and to the AGWs in the Korean Peninsula (Gan et al., 2008) and in the Mozambique Channel (da Silva and Magalhaes, 2009).

AGWs, like their oceanic counterparts, are often modeled using weakly nonlinear long wave theories, even though the waves may be strongly nonlinear, see Smith (1988) and Rottman and Grimshaw (2002) for instance. The starting point is the Taylor-Goldstein equation based on linearized theory, given here in the Boussinesq approximation,

$$d^2w/dz^2 + (l^2 - k^2)w = 0, \quad (1)$$

where

$$l^2 = N^2/(U-c)^2 - U''/(U-c) \quad (2)$$

is the Scorer parameter, w is an eigenfunction for the vertical component of the velocity field (the actual vertical velocity is given by $\mathrm{Re}\{w(z)\exp(ik(x-ct))\}$), z is the vertical coordinate, N is the buoyancy frequency, U is the horizontal wind speed (in the wave propagation direction), c is the wave phase velocity, and k is the horizontal wavenumber, while U'' is the second derivative of $U(z)$. A vertical profile of the Scorer parameter was calculated using the phase speed estimated from the pair of satellite images in Fig. 1a and b, in which the wave packet was observed close to the Jeddah weather station (22°41′ N, 37°36′ E). This was then used to investigate pre-conditions supporting wave propagation. Since $l^2 - k^2$ in Eq. (1) can be interpreted as a vertical wavenumber then a layer where $l^2 > k^2$ will be capable of sustaining vertical wave propagation, while evanescent solutions and trapping occur when $l^2 < k^2$.

The vertical structure of the atmosphere for this case study is summarized in Fig. 2, and was calculated using data from the Jeddah weather station (at 09:00 UTC, 11 May 2004, which was acquired less than a hour after the MODIS satellite image in Fig. 1b). Figure 2a shows the vertical profile of the atmospheric stability, $N^2(z)$, Fig. 2b shows a profile of the horizontal wind velocity U in the direction of wave propagation, and Fig. 2c the Scorer parameter l^2. These results clearly show a layer (close to the ground) between approximately 200 m and 1000–1300 m, where N^2 develops a sharp increase, peaking around 500 m, and $l^2 > 0$, whereas above 1300 m $l^2 \approx 0$. Thus the vertical profile of the Scorer parameter in Fig. 2c is typical for a waveguide capable of sustaining horizontal wave propagation. This is a common mechanism to trap wave energy. Moreover, AGWs frequently occur when strong stratification occurs close to the earth's surface (Rottman and Grimshaw, 2002; da Silva and Magalhaes, 2009). Note that, in Eq. (2) N^2 tends to dominate over the other terms whenever sharp peaks in stability occur within the lower layers of the troposphere (in this case study U also varies linearly when $l^2 > 0$, implying that $U'' \approx 0$ and thus the second term is negligible compared to the first, see Fig. 2b). Note that here $l^2 \gg k^2$ in the boundary layer, enabling the use of weakly nonlinear long wave theory as follows.

As is well-known, there are two weakly nonlinear long wave models commonly used for AGWs, namely the Korteweg-de Vries (KdV) equation or the Benjamin-Davis-Acrivos-Ono (BDAO) equation. For the KdV case, the first step is to solve the Taylor-Goldstein Eq. (1) in the long wavelength limit ($k^2 = 0$) in a waveguide $h < z < H$ with

Table 1. List of values obtained by weakly nonlinear long wave analysis for the case study presented in Sect. 2, according to expressions (3, 4, 5 and 6). C_{linear} refers to the linear long wave phase speed solving Eq. (1) with the boundary condition indicated in the first line of the table. Φ refers to the modal function and the subscript indicates differentiation with respect to the vertical coordinate. See text for details.

	KdV	BDO
Upper boundary	$\phi = 0$ at $H = 3000$ m	$\phi_z = 0$ at $d = 1300$ m
C_{linear} (m s^{-1})	14.4	15.4
I	0.0476	0.0372
δ	3.9023×10^6	6.2365×10^3
μ	0.0164	0.0280
V (m s^{-1})	15.0	16.9
Amplitude (m)	114	178

the boundary conditions $w = 0$ at $z = h,\ H$. Here we set $h = 200$ m, but while it is clear that the waveguide is based on the strong stratification in the lower 1000 m, it is not so clear how to choose H. This is a common issue in modeling AGWs (see Noonan and Smith, 1985; Smith, 1988; Rottman and Einaudi; 1992; Rottman and Grimshaw; 2002, for a discussion of the issues involved). Here we choose $H = 3000$ m based on the observation that the Scorer parameter is close to zero from approximately 2300 m up to this level (see Fig. 2c) implying that waves are trapped below. This is a quite small value for H, and a larger value could well be more appropriate (e.g. another choice is $H = 3500$ m where l^2 becomes negative). Nevertheless, we shall proceed with $H = 3000$ m and find that then the linear long wave phase speed for a first mode wave is 14.4 m s^{-1}, which is slightly smaller than the observed propagation speed (approximately 15.5 m s^{-1}). This phase speed and the associated modal functions $w(z) = (c - U)\phi(z)$ can now be used to construct a weakly nonlinear model for these waves, based on the KdV equation. This leads to an expression for the vertical displacement of a solitary wave (see Grimshaw, 2002, for instance),

$$a\,\mathrm{sech}^2\kappa(x - Vt)\phi(z), \quad \text{where} \quad V - c = \frac{\mu a}{3} = 4\delta\kappa^2. \quad (3)$$

The coefficients μ and δ are determined from the integral expressions

$$I\mu = 3\int_h^H (c-U)^2\phi_z^3 dz, \quad I\delta = \int_h^H (c-U)^2\phi^2 dz,$$
$$I = 2\int_h^H (c-U)\phi_z^2 dz. \quad (4)$$

Here $\phi(z)$ is normalized so that $\phi(z = z_{\text{m}}) = 1$ where z_{m} is the height where $\phi(z)$ achieves its maximum value. In order to use these expressions, in the present case, we need to estimate the observed wavelength (defined as $1/\kappa$ from Eq. 3), corresponding to the width at an amplitude of $0.42a$ (measured from a reference level unperturbed by the solitary wave). From Fig. 1c, we estimate that $1/\kappa$ is approximately 5000 m, and using expressions (3), (4) for a mode 1 wave yields an amplitude $a = 114$ m and a nonlinear speed $V = 15.0$ m s^{-1} (see Table 1). Although this estimate of the phase speed is well within the observed range of values, the amplitude is somewhat smaller than we expected. However, we note that the expressions (3) are quite sensitive to the estimated value of $1/\kappa$. For instance, reducing the wavelength by a half increases the amplitude by a factor of four. Increasing the waveguide height H also leads to some improvement in these estimates, but brings the KdV model into a close similarity with the BDAO model discussed below. However, decreasing the waveguide height H leads to a curious anomaly, in that the predicted wave is one of depression, because the coefficient μ becomes negative. Examining the structure of the modal functions, and the formula (4) for μ, suggests that this unexpected effect is due to the wind shear in the bottom boundary layer. Since we expect AGWs riding on a bottom boundary layer to be waves of elevation, this reinforces the need to ensure that H is taken sufficiently large.

As a result of this anomalous behavior of the KdV model, we turned instead to the BDAO model. Here it is assumed that the atmosphere is essentially unbounded above the low-level waveguide (that is $H \to \infty$). Then the Taylor-Goldstein Eq. (1) is solved instead in the waveguide $h < z < d$, with the boundary conditions that $\phi = 0$ at $z = h$ as before, but with $\phi_z = 0$ at $z = d$. We set $h = 200$ m as before, and set $d = 1300$ m, since this is the level where l^2 first becomes very close to zero. This yields a linear long wave speed of 15.4 m s^{-1} which, while consistent with the linear long wave speed obtained from the KdV model (14.4 m s^{-1}), is also slightly closer to that observed (15.5 m s^{-1}) (see Table 1). In place of Eq. (3) the vertical displacement of a solitary wave is now given by

$$\frac{a\phi(z)}{1+\kappa^2(x-Vt)^2}, \quad \text{where} \quad V - c = \frac{\mu a}{4} = \delta\kappa. \quad (5)$$

$$I\mu = 3\int_h^d (c-U)^2\phi_z^3 dz, \quad I\delta = c^2\phi(z=d)^2,$$
$$I = 2\int_h^d (c-U)\phi_z^2 dz. \quad (6)$$

Here the modal function $\phi(z)$ is normalized so that $\phi(d) = 1$. Evaluating these expressions for a mode 1 wave, with a wavenumber $1/\kappa = 5000$ m yields a nonlinear speed $V = 16.9$ m s^{-1} (which overestimates the averaged value of 15.5 m s^{-1}) (see Table 1). The BDAO model predicts an amplitude $a = 178$ m, which is larger than that from the KdV

Table 2. Weakly nonlinear long wave analysis for the two case studies presented in the end of Sect. 2 (1 July 2007 and 17 May 2008). All times are in UTC. The upper boundaries are listed using "H" for KdV and "h" for BDO, and they represent the levels where $\Phi = 0$ and $\Phi_z = 0$, respectively. See text for more details.

	1 Jul 2007	17 May 2008
Satellite synergy	Terra 08:45 Aqua 10:20	Envisat 07:22 Aqua 11:00
Sounding	Jeddah 00:00 h	Jeddah 12:00h
C_{observed} (m s^{-1})	3.7–4.8	9.0–11.0
$\lambda_{\text{observed}}$ (m)	≈4000	≈3000
Upper boundary	$H = 1200$ m & $h = 800$ m	$H = 2100$ m & $h = 400$ m
Lower boundary	100 m	Surface
V (m s^{-1})	KdV = 4.8 & BDO = 8.7	KdV = 9.7 & BDO = 11.5
Amplitude (m)	KdV = 30 & BDO = 49	KdV = 315 & BDO = 420

model with $H = 3000$ m. Note that the BDAO solitary wave amplitude is less sensitive to the wavelength than KdV, as a decrease in the wavelength by a factor of two only doubles the amplitude.

Next, we extended the weakly nonlinear analysis to an additional two case studies, namely those of 1 July 2007, and 17 May 2008 (see Fig. 3). The results are summarized in Table 2 and suggest (similarly to the previous results) that the KdV phase speeds are well within the observed values, whereas the BDAO theory tends to overestimate the observed wave speeds. The amplitudes of both models (KdV and BDAO) are of the order of tens to hundreds of meters. However, they are generally smaller (although BDAO presents larger values than KdV) in comparison with other results obtained independently for other AGWs such as the ones discussed in Porter and Smyth (2002).

Finally, while these theoretical estimates of AGW phase speeds are within the general regime of the observations, we note that it is possible the observed waves are strongly nonlinear, as is often the case for AGWs (see the review by Rottman and Grimshaw, 2002).

3 SAR observations and seasonal average stratification

All available SAR images from ERS-SAR and Envisat-ASAR missions, between January 1993 and September 2008 (between 13°16′ N and 29°46′ N latitude and between 31°29′ E and 44°30′ E longitude), have been analyzed for the presence of wave-like signatures consistent with AGWs. These wave-like signatures were interpreted as AGWs based on spatial scales and patterns, for instance when their wavelengths were greater than 5 km, and/or when there were no signs of refraction patterns close to the coast of the Red Sea. The latter criterion is certainly a valid one when ambiguity between atmospheric and oceanic internal waves is an issue. We note in passing that, in the near shore region of the Red Sea, wavelengths exceeding 5 km would not be realistic for oceanic internal waves, since in shallow seas internal wave speeds (and thus their wavelengths) are typically small (less than 2 km). Internal wave-like signatures (believed to be of atmospheric nature) were distributed throughout most of the Red Sea, and were found in 92 radar images (23 ERS SAR and 69 ENVISAT ASAR). Such radar signatures can be observed throughout the year, with a clear increase in occurrence between April and September (Fig. 4a). A slight decrease is noticeable in August and no waves were found in November (monsoon period in this area). The dominant wave propagation directions (Fig. 5) vary approximately between 45° N and 110° N (NE and ESE), and between 245° N and 315° N (WSW and NW).

To support the atmospheric nature of most of the wave-like signatures and in order to study suitable trapping conditions in the atmosphere (and relate those results with the ones in Fig. 4a), pairs of satellite images (e.g. MODIS and SAR) are necessary to estimate phase speeds, and calculate the Scorer parameter (note that both phase speeds and U are required to calculate l^2, see Eq. 2). However, there are not enough radar images to cast image pairs and estimate phase speeds, needed to obtain a daily record of l^2 (note also that MODIS Terra/Aqua synergy is difficult to detect internal waves in the same day, because sunglint is usually not present in the same area in both images, and thus one of the images usually does not display clear signatures of AGWs). Therefore, at the present time, it is not possible to make a statistical analysis of l^2, and this investigation is restricted to the analysis of the atmospheric stability (N^2) as an important factor favoring the propagation of AGWs. We recall that N^2 plays a dominant role in determining waveguides capable of sustaining horizontal wave propagation near the sea surface (Eq. 2, and Sect. 2).

Upper air soundings were retrieved from the University of Wyoming website (http://weather.uwyo.edu/upperair/sounding.html) to obtain atmospheric vertical profiles and study the seasonal variability of stratification (monthly averages). A detailed analysis of the atmospheric stability was undertaken where a daily vertical profile of N^2 was

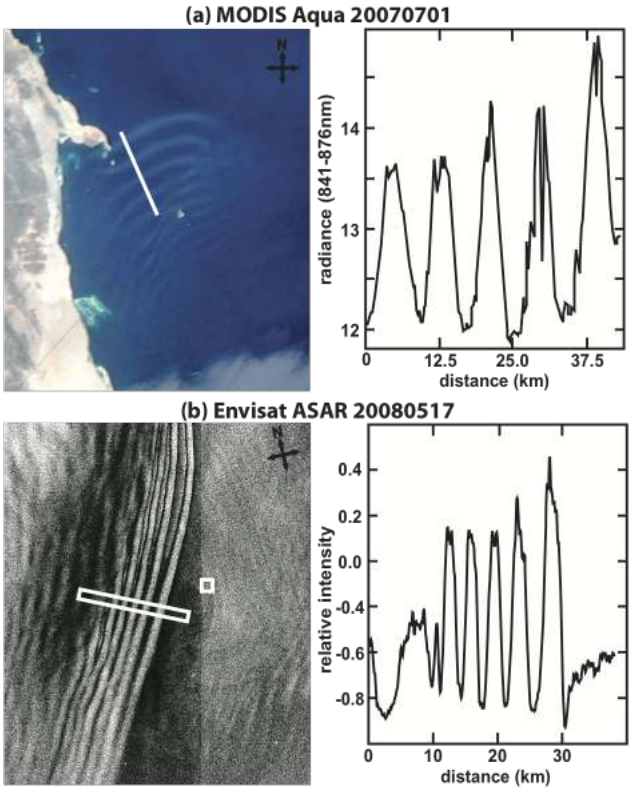

Fig. 3. Close-ups (subsets) for two case studies together with transect profiles represented by the white lines: **(a)** MODIS-Aqua image dated 1 July 2007 acquired at 10:20 UTC; **(b)** Envisat-ASAR image dated 17 May 2008 acquired at 07:22 UTC.

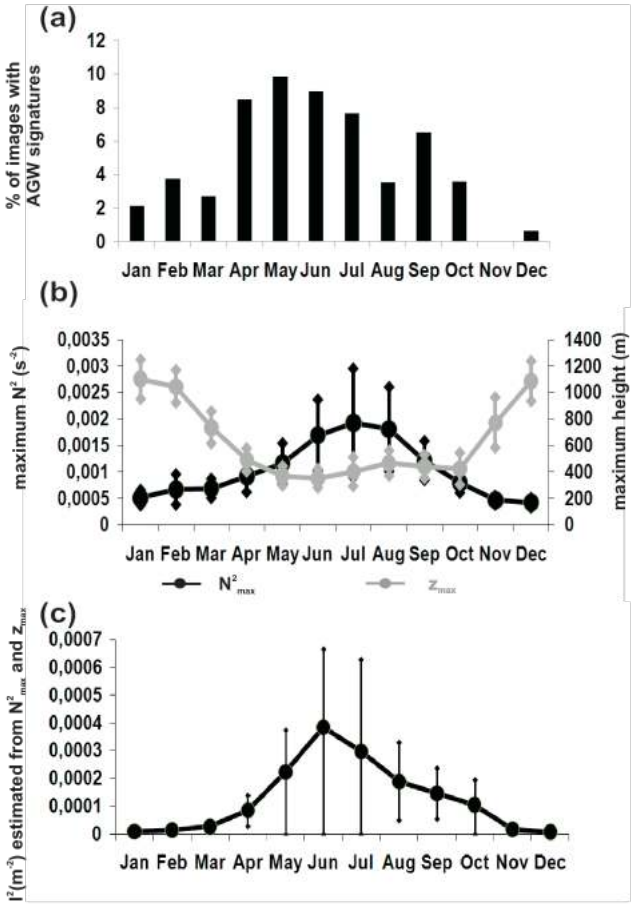

Fig. 4. **(a)** IW occurrences in Red Sea normalized by number of images per month, for the period between January 1993 and September 2008. **(b)** Monthly averages of stratification taken from Jeddah weather station, between 1993 and 2008, where $N^2_{\max}$ represents the averaged maximum values of N^2, and $z_{\max}$ represents the heights for which N^2 was at its maximum. Error bars show standard deviations. **(c)** Monthly averages of the maximum Scorer parameter estimated for the stratification given in **(b)** (error bars represent variability due to the standard deviations of $N_{\max}$ and $z_{\max}$).

calculated for Jeddah station (21.7° N, 39.2° E, located 17 m above Mean Sea Level), between 1993 and 2008. The maximum values of N^2 ($N^2_{\max}$), as well as the heights for which N^2 was at its maximum ($z_{\max}$), were estimated from each of those profiles. The monthly average distributions of $N^2_{\max}$ and $z_{\max}$ (for the period 1993 to 2008) are presented in Fig. 4b (standard deviations are shown in the form of error bars), which shows an increase in the stability maximum between April and September coincident with a decrease of $z_{\max}$ (when compared with the rest of the year). These variations are in close agreement with the period where IWs are more frequently observed in the SAR (see Fig. 4a).

This variability in the seasonal stratification affects the AGW propagation conditions as described by the curve of averaged l^2 as a function of month in year, shown in Fig. 4c. This curve represents the values of the Scorer parameter calculated from the monthly average distribution of $N^2_{\max}$ and $z_{\max}$, where each value is calculated using Eq. (2) at a level $z = z_{\max}$ and with stratification given by $N^2_{\max}$ (note the variability shown by error bars which represent the errors introduced by the standard deviations of $N_{\max}$ and $z_{\max}$). Here, U has been taken from the first case study (11 May 2004) as an average over the waveguide (in that case considered to be between 200 m and 1300 m, see Fig. 2b). In practice, this means that the second term on the right hand side of Eq. (2) is being neglected since $U'' \approx 0$, because we want to focus on the seasonal trends of the stratification and its dominant role in the pre-conditions for waves propagation. We note that the averaged U used to calculate the averaged l^2 is only a proxy that changes from case to case. However, a sensitivity analysis reveals that a representative value of U suffices since changing it moderately would not change the conclusions drawn from Fig. 4c. The phase speeds in Eq. (2) have been calculated using a two layer model for long waves $c = \sqrt{g'H}$, where the depth of the waveguide H was here set equal to $z_{\max}$. The reduced gravity $g' = g(\rho_2 - \rho_1)/\rho_1 = 0.12\,\mathrm{ms}^{-2}$ was calculated using densities from the case study (upper layer from 1300 m to 5000 m with $\rho_1 = 1.087\,\mathrm{kg\,m}^{-3}$; lower

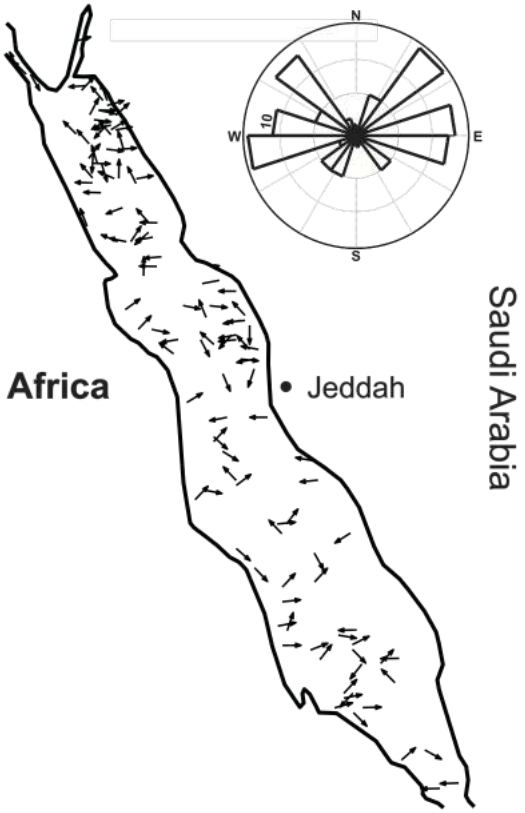

Fig. 5. Map with geographic locations and direction of propagation for all waves in Fig. 4a. At the top right corner an inset shows statistics of propagation directions of the observed AGWs.

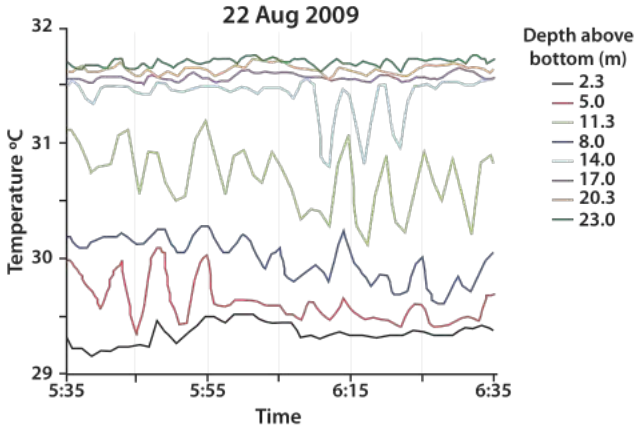

Fig. 6. Temperature measurements for 22 August 2009 near Abu Madafi (22°04.509′ N, 38°46.181′ E) using moored temperature loggers at 2.3, 5, 8, 11.3, 14, 17, 20.3 and 23 m above bottom (bottom depth ≈25.2 m).

layer from 200 m to 1300 m with $\rho_2 = 1.100\,\mathrm{kg\,m^{-3}}$) as a proxy for the densities in the two-layer model.

Figure 4c shows that the averaged l^2 rises substantially between April and September as a consequence of a double contribution from a stronger and shallower stratification (increase in $N^2_{\max}$ and decrease in $z_{\max}$). Indeed, increases in stratification and decreases in $z_{\max}$ contribute to the increase of the first term in Eq. (2), when considering that $c > U$. Note that according to the expression for the phase speed, c diminishes with H (and therefore with $z_{\max}$) decreasing the denominators in Eq. (2), whenever the phase speed approaches the values of U. We thus conclude that this seasonal variation in the atmospheric stratification contributes to an increase in the AGW favorable propagation conditions in the period where the wave-like signatures are more often observed (between April and September, see Fig. 4a).

The seasonal stratification of the water column has been analyzed to further investigate the nature of the wave-like signatures accounted in Fig. 4a. In situ temperature data were obtained from a mooring on the shelf edge near the exposed side of Abu Madafi coral reef (22°04.509′ N, 38°46.181′ E, see Fig. 1d) between May and October 2008, October 2008 and March 2009, and April 2009 and January 2010. The mooring included a sequence of temperature loggers positioned at 2.3, 5, 8, 11.3, 14, 17, 20.3 and 23 m above the sea floor (bottom depth ∼25.2 m). The inclusion of a subsurface buoy insured buoyancy reduced cable movement induced by currents. Overall, the water column was well mixed during the late fall and winter (November to February) and stratified in late spring and summer (May to August). High-frequency temperature oscillations were detected when the water column was stratified and appeared restricted to the lower part of the water column. Figure 6 shows a typical temperature section obtained in the study site (22 August 2009). No evidence of a strong oceanic internal wave field has been found from observations taken from the shelf edge. This result reinforces the idea that not only winter period observations (Fig. 4a) should be of atmospheric waves since there is no stratification in the ocean to sustain internal waves, but also summer large scale observations may be of atmospheric nature. We stress that the high-frequency oscillations in Fig. 6 have periods of the order of 5 min whilst the satellite observations of internal waves within this area typically have wavelengths (average distance from crest to crest) of 10 km. If these signatures were to be oceanic they would have phase speeds of the order of $30\,\mathrm{m\,s^{-1}}$, which is not a realistic value for oceanic internal waves.

These results, together with the analysis of the atmospheric stability show that the period between April and September is more favorable for AGW propagation, leading to the conclusion that the majority of the signatures observed in satellite imagery of the region are atmospheric.

4 Dicussions and summary

This study, combining images from ERS-SAR, Envisat-ASAR and MODIS sensors, and oceanic and atmospheric in situ data, shows the existence of suitable propagation

conditions for AGWs in the Red Sea region, revealing this area as a major hotspot of AGWs in the world. Although AGWs can be found year round, their occurrence is seasonal with a clear increase between April and September. The dominant propagation directions were between ESE and NE and between NW and WSW.

The atmospheric stability N^2 was used to investigate the existence of waveguides that can trap and prevent energy to radiate away in the vertical. The results show that the stratification plays a key role in determining favorable propagation conditions for AGWs, and that the first term of the Scorer parameter in Eq. (2) can be used as an indicator of these conditions.

The case studies presented in Sect. 2 show that weakly nonlinear long wave models predict phase speeds which are consistent with typical values of observed AGWs, with the KdV model performing slightly better than the BDAO model as far as estimated phase speeds are concerned. The amplitudes are relatively small compared to the waveguide height (e.g. $a/H \approx 0.04$ for KdV model in Table 1) thus being consistent with the use of weakly nonlinear theory. Note also that, in similar studies, Li et al. (2004) modeled nonlinear AGWs when this ratio was approximately 0.37 and obtained credible results. However, these amplitudes are generally smaller than those presented by Porter and Smyth (2002), who found amplitudes roughly half of the waveguide height. Nevertheless, they also used weakly nonlinear BDAO-type theory, and found reasonable agreement with Morning Glory observations.

The analysis above has also been undertaken for one case study in the Mozambique Channel (the case of a large AGW detected in satellite images dated 16 September 2004, and discussed in detail by da Silva and Magalhaes, 2009). Comparison with the Red Sea AGWs presented in this paper revealed similar characteristics. A similar bottom duct is found over water, and the same conclusions arise from applying KdV and BDO models, with both being in good agreement with the observed phase speed, and predicting small amplitudes compared to the waveguide height (e.g. $a/H \approx 0.04$ for KdV). Here also, weakly nonlinear theory seems appropriate to describe AGW observations.

Next we discuss briefly some possible generation mechanisms for the observed AGWs. The conjectures that follow are plausible explanations for wave generation based on our knowledge of the meteorology of the study region, whereas a more developed study is beyond the scope of the present paper. Mountain chains surrounding the Red Sea help constrain the average flow along its main axis (Patzert, 1974). Nevertheless, mesoscale atmospheric modeling (validated by in situ data) was used by Jiang et al. (2009) to add important results focusing on the cross-axis zonal winds within the Red Sea region. In fact, they found that the complex topography of the Red Sea contains several gaps along the coast, and that these direct numerous strong jet-like winds up to $15\,\mathrm{m\,s^{-1}}$ (with a significant zonal component) to flow frequently across the longitudinal axis of the Red Sea. This general frame of circulation is in agreement with the AGWs preferential directions of propagation presented in Fig. 5, where it is clearly seen that AGWs also have a strong zonal component. This encourages us to believe that several AGW wind driven generation mechanisms may be at work in the Red Sea, and that these are most likely related to the strong jet-like winds and variable topography. These wave generation mechanisms are commonly known as lee wave generation and upstream generation (see e.g. Vachon et al., 1994; Li et al., 2004). Particularly interesting is also the fact that some AGWs have phase lines (crests) almost parallel to the coastlines (see also the propagation directions in the map provided in Fig. 5). Since there are usually strong (daily) temperature contrasts along the Red Sea coasts (Pedgley, 1974) that could result in sea/land breezes, these could generate AGWs when they are sufficiently strong.

As these large-amplitude waves occur frequently near some airports, such as Jeddah International Airport in Saudi Arabia, knowledge of the pre-conditions for their propagation and near real time satellite observations can become useful for aircraft operation at low altitudes in the Red Sea and its coastal zone.

Finally, we believe that the distinction issue between oceanic and atmospheric internal waves in satellite images should not be neglected particularly in regions such as the Red Sea region (characterized by dry conditions and absence of roll clouds). Whilst many of the IWs in satellite observations in the Red Sea region can be interpreted as AGWs based solely on scale, refraction patterns and surface signatures (such as the case study in Fig. 1), there are oceanic IWs in the Red Sea (as shown by Jackson, 2007) that cannot be interpreted based on these criteria alone (especially when wavelengths approach values around 5–10 km).

Acknowledgements. This research was conducted with support from KAUST (King Abdullah University for Science and Technology) in collaboration with the Woods Hole Oceanographic Institution, Biology Department. The views expressed in this manuscript are those of the authors and do not necessarily represent the official opinion of KAUST. Some support was also provided by a Treaty of Windsor Grant awarded by the British Council (Portugal). SAR image data was provided by ESA under contract AOPT-2423. One of us would like to thank the Portuguese Science and Technology Foundation (FCT) for a research grant (SFRH/BD/35898/2007).

Edited by: K. Helfrich
Reviewed by: two anonymous referees

References

Alpers, W.: Theory of radar imaging of internal waves, Nature, 314, 245–247, 1985.

Alpers, W. and Stilke, G.: Observations of a nonlinear wave disturbance in marine atmosphere by synthetic aperture radar aboard the ERS 1 satellite, J. Geophys. Res., 101, 6512–6525, 1996.

Bedard, A. J., Canavero, F., and Einaudi, F.: Atmospheric gravity waves and aircraft turbulence encounters, J. Atmos. Sci., 43(23), 2838–2844, 1986.

Christie, D. R.: Long nonlinear waves in the lower atmosphere, J. Atmos. Sci., 46(11), 1462–1491, 1989.

Christie, D. R. and Muirhead, K. J.: Solitary waves: a hazard to aircraft operating at low altitudes, Aust. Met. Mag., 31, 97–109, 1983.

Crook, A. N.: The effect of ambient stratification and moisture on the motion of atmospheric undular bores, J. Atmos. Sci., 43(2), 171–181, 1986.

Crook, A. N.: Trapping of low-level internal gravity waves, J. Atmos. Sci., 45(10), 1533–1541, doi:10.1175/1520-0469(1988)045, 1988.

Da Silva, J. C. B. and Magalhaes, J. M.: Satellites observations of large atmospheric gravity waves in the Mozambique Channel, Int. J. Rem. Sens., 30(5), 1161–1182, 2009.

Da Silva, J. C. B., Ermakov, S. A., and Robinson, I. S.: Role of surface films in ERS SAR signatures of internal waves on the shelf. III. Mode transitions, J. Geophys. Res., 105(C10), 24089–24104, doi:10.1029/2000JC900053, 2000.

Da Silva, J. C. B., New, A. L., and Azevedo, A.: On the role of SAR for observing "local generation" of internal solitary waves off the Iberian Peninsula, Canad. J. Rem. Sens., 33(5), 388–403, 2007.

Da Silva, J. C. B., New, A. L., and Magalhaes, J. M.: Internal Solitary waves in the Mozambique Channel: Observations and interpretation, J. Geophys. Res.-Oceans, 114, C05001, doi:10.1029/2008JC005125, 2009.

Gan, X. L., Huang, W. G., Li, X. F., Chen, X. J., Lou, X. L., Zhao, Z. X., Yang, J. S., and Shi, A. Q.: Coastally trapped atmospheric waves on SAR, AVHRR and MODIS images, Inter. J. Rem. Sens., 29(6), 1621–1634, doi:10.1080/01431160701395260, 2008.

Grimshaw. R. H. J. (Ed.): Environmental Stratified Flows, Topics in Environmental Fluid Mechanics, 282 pp., Kluwer Academic Publishers, Boston, 2002.

Jackson, C. R. (Ed.): An Atlas of internal solitary-like waves and their properties, 2nd ed., 559 pp., http://www.internalwaveatlas.com, Global Ocean Associates, Alexandria, VA, 2004.

Jackson, C.: Internal wave detection using the moderate resolution imaging spectroradiometer (MODIS), J. Geophys. Res., 112, C11012, doi:10.1029/2007JC004220, 2007.

Jackson, C. R. and Apel, J. R. (Eds.): An Atlas of internal solitary-like waves and their properties, 1st ed., 559 pp., http://www.internalwaveatlas.com, Global Ocean Associates, Alexandria, VA, 2002.

Jiang, H., Farrar, J. T., Beardsley, R. C., Chen, R., and Chen, C.: Zonal surface wind jets across the Red Sea due to mountain gap forcing along both sides of the Red Sea, Geophys. Res. Lett., 36, L19605, doi:10.1029/2009GL040008, 2009.

Kim, D. J., Nam, S., Kim, H. R., Moon, W. M., and Kim, K.: Can near-inertial internal waves in the East Sea be observed by synthetic aperture radar?, Geophys. Res. Lett., 32, L02606, doi:10.1029/2004GL021532, 2005a.

Kim, H. R., Nam, S. H., Kim, D. J., Kim, K., and Moon, W. M.: Reply to comment by Q. Zheng on 'Can near-inertial internal waves in the East Sea be observed by synthetic aperture radar?', Geophys.Res. Lett., 32(20), L20607, doi:10.1029/2005GL024351, 2005b.

Li, X. F., Dong, C., C-Colón, P., Pichel, W. G., and Friedman, K. S.: Synthetic aperture radar observation of the sea surface imprints of upstream atmospheric solitons generated by flow impeded by an island, J. Geophys. Res., 109, C02016, doi:10.1029/2003JC002168, 2004.

Noonan, J. A. and Smith, R. K.: Linear and weakly nonlinear internal wave theories applied to 'morning glory' waves, Geophys. Astro. Fluid Dyn., 33, 123–143, 1985.

Patzert, W. C.: Wind-induced reversal in Red Sea circulation, Deep Sea Res., 21, 109–121, 1974.

Pedgley, D. E.: An outline of the weather and climate of the Red Sea, in: L'Oceanographie Physique de la Mer Rouge, pp. 9–27, U. N. Ed. Sci. and Cult. Org., Paris, 1974.

Porter, A. and Smyth, N. F.: Modelling the morning glory of the Gulf of Carpentaria, J. Fluid Mech., 454, 1–20, doi:10.1017/S0022112001007455, 2002.

Rottman, J. W. and Einaudi, F.: Solitary waves in the atmosphere, J. Atmos. Sci., 50, 2116–2136, 1992.

Rottman, J. W. and Grimshaw, R.: Atmospheric internal solitary waves, Environmental Stratified Flows, edited by: Grimshaw, R., 61–88, Kluwer Academic Publishers, Boston, 2002.

Scorer, R. S.: Theory of waves in the lee of mountains, Q. J. Roy. Meteorol. Soc., 75(323), 41–56, doi:10.1002/qj.49707532308, 1949.

Smith, R. K.: Travelling waves and bores in the lower atmosphere: the 'Morning Glory' and related phenomena, Earth-Sci. Rev., 25, 267–290, 1988.

Vachon, P. W., Johannessen, O. M., and Johannessen, J. A.: An ERS-1 synthetic aperture radar image of atmospheric lee waves, J. Geophys. Res., 99(22), 483–490, 1994.

Vlasenko, V., Stashchuk, N., and Hutter, K. (Eds.): Baroclinic Tides: Theoretical Modeling and Observational Evidence, 351 pp., Cambridge University Press, New York, 2005.

Zheng, Q.: Comment on "Can near-inertial internal waves in the East Sea be observed by synthetic aperture radar?" by D. J. Kim et al., Geophys. Res. Lett., 32, L20606, doi:10.1029/2005GL023770, 2005.

Chapter 7

SAR observations of internal solitary waves generated at the Estremadura Promontory off the west Iberian Coast

Magalhaes, J.M., da Silva, J.C.B., 2011. SAR observations of internal solitary waves generated at the Estremadura Promontory off the west Iberian Coast. Deep-Sea Res. I. Submitted.

SAR Observations of Internal Solitary Waves Generated at the Estremadura Promontory off the West Iberian Coast

J. M. Magalhaes[†] and J. C. B. da Silva[†]

[†]CIIMAR, Universidade do Porto, Rua dos Bragas 289, 4050-123 Porto, Portugal.

&

Department of Geosciences, Environment and Spatial Planning (DGAOT), Rua do Campo Alegre 687, 4169-007 Porto, Portugal.

To be submitted to Deep-Sea Research I

Corresponding author: J.M. Magalhaes (jmagalhaes@fc.ul.pt)

Abstract

A comprehensive dataset of Synthetic Aperture Radar (SAR) images from the west Iberian coast is used to identify the Estremadura Promontory as an oceanic hotspot for internal solitary waves. The full two-dimensional structure and the main physical properties of these waves are revealed for the first time. Composite maps and a statistical analysis show that these waves have two main propagation paths coming from the northern and southern slopes of the promontory, and that on average they have horizontal scales of the order of 400 m and crestlengths around 9 km. The overall propagation of the internal solitary wave field observed in the SAR images is evaluated, using a proxy measure for energy based on observed wavelengths, crestlengths and radar backscatter intensities. A refraction pattern is found to divert the meridionally propagating waves to the east, where they eventually dissipate in the inner-shelf regions close to shore. The barotropic body force is calculated and the most likely generation locations are identified. It is found that there is more 'energy' emanating from the south while the tidal forcing seems to be equally divided between both flanks of the promontory. Calculations using the vertical excursion inverse Froude number (defined by Legg and Klymak, 2008) indicate that this is probably related to the steeper slopes located in the northern side. This pronounced bathymetry is more likely to generate internal hydraulic jumps and overturning, which may inhibit the disintegration of the internal tide into solitary waves.

Keywords: Iberia coast; Portugal; Estremadura Promontory; Internal tides; Internal solitary waves; SAR; Refraction.

1. Introduction

Oceanic internal waves (IWs) owe their existence to the vertical density stratification that characterizes the oceans. Strong tidal flow over irregular bottom topography induces vertical motions at the tidal frequency, which can generate internal waves of tidal period that propagate along the thermocline (internal tides, ITs). These can then steepen and generate internal waves of shorter period that are usually termed internal solitary waves (ISWs), since they tend to occur in individual packets (frequently trapped in the troughs of the internal tide), and have often been identified with the soliton solutions of nonlinear wave theory.

The first observations and (*in situ*) measurements of oceanic IWs can be traced back for more than a century (Hansen and Nansen, 1909). However, the number of IW observations has been increasing significantly only over the last few decades, owing to the development of satellite technology and remote sensing techniques. These new measuring capabilities boosted the number of observations, which led to several studies that indicated that the phenomenon was in fact much more common than previously thought (Jackson and Apel, 2002; Jackson, 2004; Jackson, 2007). Indeed, recent studies have added to this conclusion by revealing that ISWs are not limited to shelf-break regions, but rather that their effects can extend far into open ocean areas at considerable distances from any generation sites (New and da Silva, 2002; Zhao et al., 2004; Azevedo et al., 2006; da Silva et al., 2007; da Silva et al., 2009; da Silva et al., 2011; Klymak et al., 2011). In particular, SAR satellites are very useful in revealing the two dimensional horizontal structure of oceanic ISWs, as well as their spatial and temporal distributions. This is because oceanic ISWs can be easily detected in SAR imagery as a result of the sea surface roughness patterns that they produce either from hydrodynamic modulation of Bragg waves by surface current gradients, or wave damping due to

surface films (Alpers, 1985; da Silva et al., 1998). SAR imagery has also been playing a key role in identifying and characterizing several ISW hotspots as well as in providing valuable insights into their generation mechanisms (*e.g.* New and da Silva, 2002; Vlasenko and Alpers, 2005; Nash and Moum, 2005; Azevedo et al., 2006; da Silva et al., 2007; da Silva and Helfrich, 2008; da Silva et al., 2009; and da Silva et al., 2011). (See da Silva et al., 2007 and da Silva et al., 2011 for a more detailed description on the role of SAR for observing ISWs and their corresponding generation mechanisms).

Satellite altimetry has also been extensively used to observe and study the IT on a global scale (see e.g. Ray and Mitchum, 1997), and to address tidal energy dissipation issues related with IW activity. For instance, important tidal energy sinks were found to be located in the open ocean far from any continental borders. Egbert and Ray (2003) found that one third of the total tidal energy dissipation was actually occuring over rough topography, in deep ocean areas such as the Hawaiian Ridge and the Mascarene plateau (Egbert and Ray, 2003). Numerical modelling and field data collected in the Mascarene Ridge also indicated similar conclusions (Lozovatsky et al., 2003). In fact, energy sinks in those locations were found to be related with energy from the surface-tide being lost in large amounts through conversion to ITs and to ISWs.

Considering that ISWs can hold a sizeable amount of energy (with the most energetic waves containing up to 0.1 Jm^{-1} in the Andaman Sea and 1.8×10^{9} Jm^{-1} in the South China Sea; see Osborne and Burch, 1980 and Klymak et al., 2006, respectively) and that they can propagate along considerable distances (of the order of hundreds km), some attention has also been devoted to understand the ultimate fate of IWs. Despite the fact that most of the energy is expected to be dissipated during breaking processes near shallow and coastal areas, it was found that IWs may have a highly turbulent character

as they propagate along the pycnocline, and that they are in fact continually triggering instabilities (Pinkel, 2000; Moum et al., 2003; Haren et al., 2005; Lamb and Farmer, 2011). Shroyer et al. (2010a, 2010b) in a comprehensive experimental set over the New Jersey's shelf have shown that IWs start to lose energy to turbulent mixing shortly after crossing the shelf-break, and that they contribute considerably to shelf dynamics in terms of vertical heat fluxes and ocean-shelf mass transports. ITs and IWs have also been shown to interact with other oceanographic phenomena such as upwelling jets, and drive intensified turbulence and dissipation in the water column (Avicola et al., 2007; Kurapov et al., 2010; Schafstall et al., 2010).

Klymak et al. (2006) and Legg and Klymak (2008) have also reported that a substantial amount of overturning can occur in the open ocean, in the presence of tidal flow over tall steep ridges. Legg and Klymak (2008) used numerical simulations to explore the influence of topographic slopes, tidal velocities and frequencies, and stratification in episodes of overturning and strong dissipation observed in the Hawaiian Ridge. They were able to identify two different regimes based on a vertical excursion inverse Froude number that was defined as $Fr_{Z\omega}^{-1} = \frac{\partial h}{\partial x}\frac{N}{\omega}$, where $\partial h/\partial x$ represents the bathymetric slope, ω is the tidal frequency evaluated, and N is the Brunt-Väissälä frequency found at the bottom. In particular, for large values of $Fr_{Z\omega}^{-1}$ (approximately above 3, see their Fig. 11) highly nonlinear jump-like lee waves were found to propagate upslope with overturning and enhanced dissipation, whereas small values of this quantity were only associated with linear responses and no overturning.

Mixing due to IWs is also important from a biological point of view. Sandstrom and Elliott (1984) have shown that in some regions, such as the Scotian shelf-break, the

dissipation of ISWs may constitute the primary mixing mechanism, and that it may be sufficient to induce strong upward fluxes of nutrients across the thermocline and produce bursts of primary production. Pingree et al. (1986) have reported increases in biomass and nutrient rich surface waters in the Celtic Sea shelf-break, which they concluded to be related with IW mixing, particularly when the tidal amplitude was at its maximum. Da Silva et al. (2002) showed that ISWs could furthermore influence primary production by a different mechanism. They suggested that enhanced primary production could simply occur due to the increase and decrease in available light experienced by phytoplankton during upward and downward advection induced by ISWs. More recently, Moum et al. (2008) have also conjectured that ISWs may interact with the geostrophic flow and cause shear-driven mixing responsible for vertical redistributions of heat and nutrients.

The Estremadura Promontory (labeled EP in Fig. 1b) region is located in the west coast of Portugal, to the west of Lisbon (see Fig. 1a). It is a large feature that broadens from the open ocean towards the coast for more than 150 km, and extends in the along-shore direction for more than 100 km. It is a complex region from a topographic point of view, with a series of smaller features like small-scale canyons and ridges, and where large canyons can also be found on either side of the promontory. The north boundary is dominated by the Nazareth canyon (labeled NC), one of the largest in the world, with its axis in an almost east-west direction, while to the south the Setubal Canyon (labeled SC in Fig. 1b) and the Lisbon Canyon (labeled LC) delineate the boundaries of EP. In this particular study we concentrate on the rectangular area outlined in Fig. 1a (shown in detail in Fig. 1b), which extends approximately between 8.5–11.5°W and 38–40°N, and over which the barotropic tidal flow is forced in a near-

perpendicular direction to the isobaths in the northern and southern slopes (in the western slopes the tide is mainly aligned with the isobaths).

ISWs have previously been reported to emanate from the southern edge of the promontory and propagate south by da Silva et al. (2007), in a process that is consistent with the local generation mechanism (New and Pingree, 1992; Gerkema, 2001; New and da Silva, 2002; Akylas et al., 2007; da Silva et al., 2009; Grisouard et al., 2011). In addition, both ITs and ISWs have been measured farther south (near Cape Sines, see Fig. 1a) using SAR imagery and *in situ* measurements (Small, 2002). Quaresma et al. (2007) have also used SAR together with *in situ* measurements to study the importance of large ISWs (generated at the Nazare canyon, see Fig. 1b for location) in sediment dynamics above the northern boundary of EP, but propagating northwards.

Of further relevance to this study is the oceanographic campaign undertaken as part of the MORENA project (EU MAST II Multidisciplinary Oceanographic Research in the Eastern Northern Atlantic) in the summer of 1994 (during the upwelling season) off the northern Portuguese coast, where large ITs and large amplitude ISWs (with thermocline displacements of more than 45 m and phase speeds in the order of 0.6 ms^{-1}) were observed to propagate towards the shelf (near the 41°N parallel). The ISWs evolution, energy and variability are discussed in Jeans and Sherwin (2001a, 2001b), and it was found that their periodicity was closely related with the semi-diurnal tidal cycle, but strong upwelling favorable winds could delay their arrival near coastal areas for more than 5 hours. It was also found that there was little variation in the waves' amplitudes between spring and neap-tides, and therefore that these waves constituted an important source of vertical mixing during the entire summer period within the inner-shelf regions (with individual waves associated with a total energy of the order of

3×10^6 Jm^{-1}). The underlying generation process for these ISWs was addressed subsequently by Sherwin et al. (2002). According to these authors the explanation for these unusually large waves was related to an along-slope generation mechanism that took place in a major westward projection of the shelf-edge located farther south (about 50 km long near 40.4°N). From there the ITs would propagate in the off-shelf direction, and subsequent refraction would bring them back onto the shelf. Only then steepening would occur to form ISW packets so that the refraction hypothesis could explain the orientation and location of ISW signatures observed in SAR imagery (see their Fig. 3).

The present study was initially motivated by a large number of satellite observations of oceanic ISWs identified off the west coast of Portugal. In fact, the authors have been collecting images from this study region for more than a decade, and a preliminary survey had readily shown that EP is a major hotspot for oceanic ISWs in the west Iberian margin. (Considerable ISW activity has also been detected farther north and south, although the largest numbers of observations were located within the promontory region). This was not surprising since this region exhibits the largest tidal currents over the entire west Iberian coast, and also because these tend to be aligned in the north-south direction, and therefore perpendicular to the isobaths (see Fig. 1b for detailed bathymetry). However, our analysis revealed that the majority of the ISW signatures were observed to have a strong eastern component in their direction of propagation, which increased as the waves approached the coast. This was somewhat unexpected given that the tidal forcing was mainly oriented in an orthogonal direction to the ISWs general propagation direction.

This paper focuses on characterizing the full two-dimensional spatial structure of the ISW field in the EP study region. Section 2 begins by presenting two typical case

studies of ISWs propagating in this study region, together with a comprehensive SAR image dataset. The corresponding statistical analysis and the main properties of the observed waves follow in Section 3, together with a quantitative analysis of their energetics. In Section 4 the most likely generation sites are examined using the Baines (1982) barotropic body forcing together with satellite observations. Discussions and a summary of our findings are presented in Section 5.

2. SAR Observations

The dataset that was used in the present study is composed of a selection of 29 satellite images (17 ENVISAT-ASAR images – 4 of which in Wide Swath mode and 13 in Image Mode, 8 images from the ERS-1&2, and 4 TerraSAR-X ScanSAR images). These were selected from a wider collection as being representative of the ISW field in EP. The complete dataset spans a time period that ranges from July 1992 to September 2010, all acquired during the summer period (from late June to late September), when stratification conditions are known to be favorable for oceanic ISWs to propagate. Note that to avoid tidal aliasing the dataset was selected such that the images could be fairly spread (in time) over both the semi-diurnal and the fortnightly tidal cycles. (Sun-synchronous polar-orbit satellites, such as ENVISAT and ERS-1&2, are phase locked with the fortnightly tidal cycle so that all spring/neap-tides always correspond approximately to the same semi-diurnal tidal phase).

Fig. 2 shows two typical SAR images observed in EP that exemplify the two-dimensional spatial coherence of the ISWs. The image in Fig. 2a was acquired from the ERS-2 on 14 July 1999 at 11h21m UTC and covers an area of approximately 80×70 km^2, and the image in Fig. 2b was acquired from the ERS-2 on 30 July 2010 at 22h55m UTC and covers an area of approximately 80×60 km^2.

A significant amount of ISWs travelling in different directions can be seen in both images, which are organized in rank-ordered packets of individual waves, and where the most prominent packets appear to be one or more tidal periods apart (as is usually found over the shelf). Nonetheless, both images seem to have different preferential directions of propagation (mainly towards the northeast and southeast in Fig. 2a and 2b, respectively), and the general appearance of the ISWs is that they are

radiating from different sources located somewhere along the southern and northern slopes of the promontory (in Fig. 2a and 2b, respectively). Examination of these and other similar images shows that they are consistent with mode 1 deep-water ISWs of depression that are usually trapped in the ITs troughs. Note that mode 1 internal waves will appear in SAR images as bright bands ahead of dark bands in the direction of propagation (see e.g. Alpers, 1985).

Further inspection of Fig. 2a reveals that the most prominent packets are separated along their apparent propagation path by distances roughly from 10 to 30 km (see labels from 'A' to 'D'). These distances can be translated into average propagation speeds (if a semi-diurnal period is assumed for their generation, at the same position and tidal phase) that decreases from 0.7 ms^{-1} in the deeper parts of the promontory to 0.2 ms^{-1} in the shallower areas. The same order of packet separation distances can be found in Fig. 2b, although identifying packets that are one tidal period apart is not as easy to identify as in Fig. 2a. Here inter-packet separations are approximately of the order of 20 km and the corresponding propagations speeds are around 0.4 ms^{-1}. These values are also confirmed using satellite (SAR/SAR) synergies such as the ones between ENVISAT-ASAR and TerraSAR-X (namely the images acquired on 12 September 2010 at 18h32m UTC and 22h14m UTC, respectively – not shown), where the average propagation speeds of several packets located in the centre regions of the promontory are estimated to be around 0.4 ms^{-1}. Finally, we note that similar propagation speeds for the IT have also been reported farther north (near parallel 41°N with 0.57 ms^{-1}) by Jeans and Sherwin (2001a), as well as farther south (off Cape Sines between 0.35 and 0.45 ms^{-1}) by Small (2002).

Figure 3 presents a composite map showing the interpretation of all ISW packets of significance that could be identified in a subset of 10 images selected from the initial dataset, and where the two images presented in Fig. 2 are included (a smaller set was preferred for clarity since mapping the entire dataset would result in an excessive overlap of ISW crests). We stress that the smaller collection of images was selected to still include examples from several different stages of the semi-diurnal and fortnightly tidal cycles. This in turn indicates that ISWs are observed throughout the entire spring-neap tidal cycle (take for example the two images in Fig. 2a and 2b, which were obtained during spring and neap-tides, respectively). This also means that the EP region is similar to the one surveyed farther north by Jeans and Sherwin (2001a, 2001b) where waves were also found during neap-tides with similar amplitudes to spring-tide waves. This is not the case in other regions such as the Bay of Biscay (New and da Silva, 2002) and the Mascarene Ridge (da Silva et al., 2011), where waves are more frequent and strongest during spring-tides.

For clarity, the overall result of merging all the available observations has been divided into different maps, each representing a different propagation path: one from the south and another from the north flanks of EP. It can be seen that all the waves that have been identified fall (to some extent) into one of two major directions of propagation (waves with a northeastern and southeastern propagation are depicted in Fig. 3a, 3b, respectively). Also note that there is no propagation to the west, and that the majority of the waves seem to radiate from point sources located somewhere along the outside borders of the promontory (one can take for instance the regions around 1000 m). Furthermore, the general directions of propagation appear to converge towards an east component, which strengthens as the waves approach the shallower near-shore regions.

In fact, the majority of the wavecrests that are located east of 9.6°W (meaning already in the inner-shelf) are strongly aligned in the north-south direction, and propagate directly towards the coast. These variations in direction along the waves' propagation paths can also be distinguished in the examples shown in Fig. 2. For instance, in Fig. 2a the labeled packets (from 'A' to 'D') begin with an initially north/northeast propagation and then start to align meridionally as they reach the inner-shelf. This refraction pattern is less evident but still noticeable in Fig. 2b where the waves develop from the north in a general south/southeast direction of propagation. Note that there are weaker signatures in this case that tend to fade away into the background backscatter as the waves approach the coast.

Also noteworthy, is the fact that many of the observations in Fig. 3b (showing southeast propagating waves) seem to be radiating from a localized region partially coincident with a smaller topographic feature of interest (a canyon-like structure just south of 39.4°N, oriented in the north-south direction along 10ºW approximately) located in the northwestern boundary of the promontory (see area corresponding to section II in Fig. 3b), and whose influence will be further discussed in Section 4 of this paper.

Finally, we also note in passing that some ISW signatures that were seen in the satellite images appear to reach very close to shore (sometimes less than 3 km away from the shore line, e.g. in Fig. 2a), and that the nature of these near-shore signatures seems to change in comparison with the ones observed farther out (e.g. packects 'A' and 'D' in Fig. 2a). Namely, the packet-like structure that is usually observed tends to fade and degenerate into a (lower frequency) blurred gray backscatter signature on top of a lighter background. Similar observations have also been reported by Small (2002)

farther south (off Cape Sines) with large amplitude internal waves (40 m in amplitude) propagating in areas with less than 100 m water depth.

3. Quantitative Analysis

We now present a quantitative analysis of the selected dataset. First we recall that 29 satellite images were analyzed for the presence of ISWs, and that from these a total of 759 different wave packets and 2056 individual ISWs were accounted for.

Fig. 4 presents some basic statistics concerning the waves' main properties. Fig. 4a shows the distribution of the along-crest coherence lengths (or crestlengths), and it can be seen that it is strongly skewed towards the lower end, with values ranging from a few km up to more than 40 km. However, the majority of the observations are characterized by crestlengths below 15 km, and the mean value for all the waves is around 9 km. Fig. 4b refers to the distribution of the wavelengths (L), which are considered here to be the separation between individual waves within a given packet (see also Fig. 5). These values range from a few hundred meters to more than 1 km and their distribution is also biased towards low values, but not to the same extent as for the crestlengths. More than 90% of the observations have horizontal length scales between 200 m and 600 m, and the dataset has a mean value of approximately 400 m. As a comparison, we note that Small (2002) encountered similar values off Cape Sines. Da Silva et al. (1998) and da Silva et al. (2000) also found that the observations near Oporto (parallel 41°N) had horizontal length scales of approximately 500 m (see our Fig. 1 for locations).

We now attempt (in a similar fashion to New and da Silva, 2002) to quantify and characterize the energy distribution associated with the ISW field in the study region. This is done by analyzing satellite profiles of backscatter SAR intensity (I) that are taken perpendicularly to the wavecrests and go through the (approximate) centre of the packets. Such an example is shown in Fig. 5 with respect to the profile illustrated in Fig.

2b by a line that extends approximately from the east-northeast to the west-southwest, and crosses the centre of the packet located in the upper centre of the image (which appears to be travelling east-northeast). Only three ISWs are shown here for clarity, and for ease of interpretation the distances in the horizontal axis are measured from the southwest end of the profile. From this profile it is then possible to define a measure for the waves' wavelengths and a proxy for their backscatter 'amplitudes' (see 'L' and 'a' in Fig. 5, respectively) – we stress that here 'L' is the distance between solitons (not the characteristic length of the solitary wave), and that 'a' is not to be taken as a real amplitude but rather a measure of the waves' 'strength' (note that large amplitudes are expected to have stronger signals in radar backscatter images and vice-versa).

We recall that the bright and dark bands typical of ISWs in SAR images can differ in appearance, depending on several parameters such as the wind speed and direction relative to wave propagation, and presence of organic surface films (see Alpers, 1985; da Silva et al., 1998; Brandt et al., 1999; Araújo et al., 2002 for a detailed discussion). In these cases the relative intensity variations, which are usually symmetrically distributed about a mean value close to zero (such as in Fig. 5), can be shifted towards more positive or negative values depending if the waves are seen as bright bands in a darker background or vice-versa. In such cases the appropriate definitions have been taken to correctly evaluate wavelengths and amplitudes.

As part of the usual SAR processing, the influence of the slant range effect (responsible for the along-range decrease in brightness observed for instance in Fig. 2b) is removed by taking the normalized backscatter intensity, which allows for wave amplitudes at different ranges to be compared within a given packet. The normalized backscatter intensity (or relative intensity) is given by $K=(I-I_0)/I_0$, where the reference

background value for intensity (I_0) is calculated by averaging I over an area typically larger than 25×25 pixels (about 6 km^2 for a spatial resolution of 30 m) that is usually ahead, and not disturbed by, the ISW packet (see da Silva et al., 1998, for details).

SAR profiles were therefore calculated to retrieve wavelengths and amplitude equivalents for the entire dataset, which were then used together with the crestlengths to define an 'energy' proxy for each ISW packet. The 'energy' proxy was defined according to the methodology of New and da Silva (2002) by using an analogous expression to surface waves, which defines the total 'energy' in a wave packet as

$$E = \Sigma_{i=1}^{n} a_i^2 L_i l_i \tag{1}$$

where n is the number of individual waves in the packet, a and L are the amplitude and wavelength (as defined above), l is the crestlength, and the indexation variable (i) refers to the ith wave in the packet. Note that this quantity (E) should not be identified with the physical (mechanical) energy contained in a wave packet; it is only a proxy of that energy, meant for comparison between different packets.

The methodology described above can now be used to assess the energy spatial distribution in the ISW field, but to do so the overall contribution from every ISW packet needs to be accounted for. This means that different energies from different images will have to be taken into account. However, the SAR intensity amplitudes can differ simply due to variations in the wind speed, as discussed by Brandt et al. (1999) and Araújo et al. (2002). ISW profiles of different images need to be taken into account if a meaningful 'energy' spatial distribution is to be made. This problem can be solved if the contributions from the different packets in each image are considered individually (each with its own 'energy'), but summed together over the entire dataset (meaning all

packets from all images) to reach an overall assessment of the energy distribution. By doing so the bias in the distribution of *E* throughout the different images will disappear since there will be no direct comparison between images, and only the overall contribution will prevail. The only assumption that needs to be made is that the wind field must be fairly constant over each individual image, which seems reasonable since the area of the promontory over which the observations are being measured is too small (less than 100×100 km^2) for significant variations in winds to occur. Note that during the selection process of the SAR images used in this study, we only considered images where the backscatter was reasonably uniform.

To see how *E* varies over the promontory region, the whole area has been divided into four meridional sections, each covering different longitude intervals that are labeled in Fig. 3 (separated by dashed lines and identified on top of each panel with 'I', 'II', 'III' and 'IV'). The preferred choice for this division was such that the promontory region could be divided into a main area covering the centre (sections II and III), located between two adjacent areas representative of the borders towards the open ocean and the inner-shelf (sections I and IV, respectively). This separation enables the longitudinal variations in the 'energy' field to be evaluated, while also allowing to track the waves' propagation paths (which were already seen to suggest refraction with a strong east component).

For the reason explained above, the corresponding 'energy' distributions were normalized by the corresponding area of the ISWs observation inside each of the meridional sections (just the area with ISW observations and not the entire section), and it is this quantity *E** that is shown in Fig. 6 (with matching longitude intervals annotated on top of the figure). To take into account how *E** is distributed among the different

directions of propagation, circular diagrams are used with intervals of 30 degrees that represent the ISW propagation directions. Therefore, each slice in these circular charts represents the overall contribution for E^* (summed continually over the entire 759 wave packets) for all ISWs inside the corresponding longitude interval that were identified as having a direction of propagation between the two matching limits of that particular slice. For reference, we also note that the outer dashed circular line corresponds to the value marked on top of each diagram in bold, while the smaller white circle in the centre is one order of magnitude less.

A close inspection of Fig. 6 reveals that there is an order of magnitude difference between the two middle sections and sections I and IV (see the summed contribution of 'energy' at the bottom of each section diagram), and that there is a local maximum of E^* in the centre of the promontory. This is closely related to how the different longitude intervals were selected, and means that regions II and III (in the centre) have more 'energy' per unit area than the adjacent regions. In fact, Fig. 3 adds to this remark since it shows that the majority of the ISWs and the largest crestlengths are more frequently observed in the centre regions (meaning that the waves are more developed there, to the east of EP western flanks and to the west of the inner-shelf). Furthermore, the distribution of the ISW crests in Fig. 2 reinforces this idea. It can be seen that the waves located farther offshore (see for instance packet A) have smaller crestlengths, which then develop towards the centre region (packet B), before starting to dissipate in the near-shore areas (*e.g.* D in Fig. 2a).

One other observation that can be drawn from Fig. 6 is that there is a clear sign of refraction along the waves' propagation paths. This can be seen by examining how E^* is distributed along the directions of propagation, and how these distributions vary as

the waves propagate towards shallower areas near the shore. Farther offshore (in region I) the waves' crests are mainly propagating in the north-south direction, which is not surprising since the tidal forcing has the same direction. In the centre regions (II and III) the waves reach a fully developed state (and hence there is more 'energy' in total) and it can be seen that refraction starts to increase the amount of 'energy' in the east propagation direction, while other waves must still be forming since there is also some 'energy' associated with meridionally oriented waves. After crossing the inner-shelf (in region IV) the waves start to dissipate (and so the total 'energy' per unit area decreases) and refraction has driven nearly all the 'energy' to focus in the east direction.

As already mentioned above, it is not surprising that the waves in the offshore regions tend to align with the tidal forcing, which is oriented perpendicularly to the main axis of the promontory. However, there is a clear asymmetry between the amount of wave energy that propagates towards the north and south. This asymmetry is best seen in the circular diagram of Fig. 7, which shows the total distribution of 'energy' for the entire domain along the propagation directions. In this diagram, all the sections (I to IV) were merged together and considered as a single area. The distribution in Fig. 7 clearly shows that more energy is flowing to the north than to the south (43% of the total normalized 'energy' is going north and only 16% is going south), but it also shows that the flow energy is directed mainly to the east (41% in total, which is also a clear sign of refraction). These issues will be further discussed in the following sections.

4. Analysis of Wave Generation

The analysis made on the composite maps (in Fig. 3) suggests that the general appearance of the ISWs is that they seem to be radiating from several point sources, with distinct locations in the northern and southern slopes of the promontory. Therefore, we now turn our investigation to identify possible candidates for the generation of the observed ISWs using the barotropic tidal forcing of Baines (1982).

This methodology has often been used to search and identify hotspot regions for IT generation. Azevedo et al. (2006) have used this method to investigate ISWs in the southern Bay of Biscay (near Cape Finisterre, Iberia Peninsula). In some independent studies, Pichon and Correard (2006) and Pichon et al. (2011) have also calculated the barotropic tidal forcing, and similar sources for the waves discussed in Azevedo et al. (2006) were found. Da Silva et al. (2007) have used similar methods to study other ISW observations in the same region studied by Azevedo et al. (2006), but propagating in a different direction, as well as in the southern slopes of EP, but propagating to the South. More recently, Baines (1982) barotropic body force has been used to identify ISWs hotspots (observed in SAR imagery) along the Mozambique shelf-edge of the Mozambique Channel (da Silva et al., 2009). Of further importance to the present paper is the body force analysis undertaken by Sherwin et al. (2002) to explain the large ISWs found to propagate in the inner-shelf off Oporto (see Fig. 1a for location). Many other authors have also used this technique during the last decade, as a valuable indicator of where large ITs may be generated (e.g. Colosi et al., 2001; Merrifield and Holloway, 2002; Niwa and Hibiya, 2004).

According to Baines (1982) the method of finding the solutions for the linearized equations of motion (assumed in a rotating, stratified, inviscid ocean), which

represent IT generation resulting from the interaction between surface tides and bottom topography, can be divided in two different problems: the first problem is to find the solution in an 'equivalent' non-stratified ocean; while the second is concerned with determining the additional motion resulting from the vertical stratification in density. This means that the equations of motion need to be divided into the barotropic and baroclinic components (corresponding to the non-stratified ocean and the internal waves, respectively). The equations that involve the body force (F), which drives IW motion can then by written as

$$\frac{\partial u_i}{\partial t} + f \hat{z} \times u_i + \frac{1}{\overline{\rho_0}} \nabla P_I + \frac{\rho_I g \hat{z}}{\overline{\rho_0}} = F = -\frac{g \rho_B}{\overline{\rho_0}} \hat{z} \qquad (2)$$

where u_i are the velocity components of the internal wave motion, $\rho_0(z)$ is the vertical density profile in static equilibrium (from which the vertical average $\overline{\rho_0}$ is calculated), ρ_B and ρ_I are the density perturbations relative to ρ_0 due to the barotropic and internal wave motions, respectively (which means that the total density perturbation is given by $\rho = \rho_B + \rho_I$), and P_I is the internal wave pressure perturbation. The notations for time, Coriolis parameter, gravity, and unit vector for upward direction, follow their standard representations (t, f, g and $\hat{z}$, respectively).

From the continuity equation, it can be written that $\partial\rho_B/\partial t = -w_B \, \partial\rho_0/\partial z$, which means that the vertical velocity of the barotropic flow w_B (resulting from the barotropic flow over submarine topography) will introduce perturbations in the density field ρ_B (since the mean density field will be displaced vertically). If the barotropic tide can be considered to be in the hydrostatic regime (which strictly speaking can only be a valid assumption if the baroclinic tide is also hydrostatic, see Garrett and Gerkema, 2007),

then w_B can be expressed in terms of a volume flux vector given by $Q = (Q_x, Q_y) = (u_B h, v_B h)$. In this case the vertical velocity of the barotropic flow can be rewritten as

$$w_B = \frac{z}{h^2}\left(Q_x(t)\frac{\partial h}{\partial x} + Q_y(t)\frac{\partial h}{\partial y} \right) \tag{3}$$

where u_B and v_B are the zonal and meridional components of the barotropic flow (respectively), and h is the ocean depth.

In equation (2) the last term, which represents the body force F, can then be changed to include the above definitions, and be rewritten as

$$F(z) = -\frac{zN^2(z)}{h^2}\left[\left(\int Q_x dt\right)\frac{\partial h}{\partial x} + \left(\int Q_y dt\right)\frac{\partial h}{\partial y} \right] \tag{4}$$

where the Brunt-Väisällä frequency is again given by N, and the integration in time is made with respect to some interval within the tidal period. This expression thus represents the barotropic tidal forcing that arises from the oscillating surface tide going back and forth over submarine topography, and which drives the internal motions such as the internal tide.

In our calculations, the tidal velocities were taken from the 1/12° resolution OTIS model (Oregon state university Tidal Inversion Software, developed by Egbert and Erofeeva, 2002), the bathymetry data is part of the one minute global bathymetry (available online at http://topex.ucsd.edu/www_html/srtm30_plus.html) from Smith and Sandwell (1997), and N (assumed to be horizontally constant) was calculated by smoothing in the vertical a typical summer stratification of the study region (taken from the World Ocean Circulation Experiment – WOCE, 3rd of September 1992 located approximately at 38.90°N 10.23°W and thus close to the southwestern flanks of the

promontory). To compute the body force, the M_2 and S_2 tidal constituents were assumed, since these are the most representative for EP (see also da Silva et al., 2007). We note that similar calculations were performed with the eleven constituents (4 diurnal, 4 semi-diurnal, and 4 from the fortnightly tidal cycle) available in the OTIS model, and that *F* remains nearly the same. The tidal current ellipses needed to calculate *Q* were then derived using least-squares fits to the data in each grid point, since the original outputs do not form perfectly closed ellipses due to the slowly varying nature of the tide. The resulting tidal ellipses were interpolated to a 1' spatial resolution grid using a bilinear scheme, which enabled *F* to be calculated in the finer bathymetry grid. Lastly, the resulting body force was integrated over the vertical coordinate (to include the contribution from the entire water column at each grid point), and the maximum value for the tidal cycle under consideration was used to create a two dimensional map that enables *F* to be evaluated in a concise manner (see Fig. 9a).

The data needed to compute the body force was taken from the same date as the image presented in Fig. 2a, which was selected as being representative of *F* over the study region. We note that this image was acquired during spring-tides and that the forcing maps remain qualitatively the same in neap-tides (although the magnitudes decrease roughly by a factor of two). The corresponding tidal ellipses and the absolute maximum of the depth-integrated body force over a complete (semi-diurnal) tidal cycle are thus shown in Figs. 8 and 9, respectively.

On the one hand, it can be readily seen that the tidal currents achieve their largest values over EP (aligned mainly in the meridional direction and reaching values above 10 cms^{-1}, see reference ellipse on the right side of Fig. 8). We reiterate that the major axis of the tidal ellipses are nearly aligned with the bathymetric gradient on the

northern and southern flanks, but are roughly parallel to the isobaths over the western slopes of EP. However, there is a rapid decrease in the tidal currents towards the open ocean areas that is noticed immediately after crossing the promontory region in the north-south direction. We note in passing that the tidal current velocities over EP are in fact among the largest anywhere along the west Iberian margin, including the Gulf of Cadiz (Quaresma and Pichon, 2011).

On the other hand, a closer inspection of the body force in Fig. 9a shows that there are localized small regions of maximum forcing coincident with steep slopes (with depths approximately between 200 and 1500 m, except for region 4) that are located around the northern, southern, and western boundaries of the promontory (see Table 1 for a list of the major localized forcing regions). The tidal forcing is (in general) very weak everywhere else so that the body force decays rapidly to zero in the shallower areas above the 500 m depth contour, and in the deep ocean basins that surround the promontory. A total of four main regions with particularly elevated forcing can be identified, all within the steep slopes of the promontory. There is one large region to the north that immediately stands out since it covers a wide area that extends in the east-west direction (region 1 in Table 1) and is partially coincident with the canyon-like structure near 39.4°N (already identified in Fig. 3b) and the southern slopes of the Nazare canyon. There are several smaller potential sources with local maxima of F located farther to the west that are nearly aligned with the western flank of the promontory, the strongest of which is located near 39.1°N (Table 1, region 3). Finally, there are several more maxima in the southern slopes (see regions 4 to 6 in Table 1). The majority of these seems to be associated with the horseshoe-like elevation located at 38.8°N that extends offshore. The remaining maxima are scattered farther inshore,

but still located along the steep slopes in the south flank. These sites of elevated forcing are to be discussed in the next section.

5. Summary and Discussion

A selection of 29 SAR images acquired during the summer season between 1992 and 2010 in the EP region has been investigated in this paper. The presence of significant ISW activity in this area has been revealed by satellite imagery and it has been confirmed that EP is a hotspot for the occurrence of oceanic ISWs. This investigation adds to previous studies made farther north (Jeans and Sherwin, 2001a, 2001b; Sherwin et al., 2002) and farther south (Small, 2002; da Silva et al., 2007), which had previously identified other hotspot regions, and confirms that the west Iberian coast is an important region where oceanic ISWs can be frequently and continuously observed during the summer season.

A statistical analysis based on the initial dataset of 29 SAR images has shown that these ISWs have average crestlengths and horizontal scales of about 9 km and 400 m, respectively. Additionally, composite maps based on a subset of 10 images strongly suggested that there are two major paths of propagation emanating from the northern and southern flanks of the promontory. This idea is also supported by the 'energy' results presented in Figs. 6 and 7. The increasing concentration of 'energy' into east propagating ISWs suggests that the bathymetric structure of the promontory refracts the waves generated to the north and south such that wavecrests become basically aligned with the meridional direction. This can also be seen in Fig. 3, where the majority of the waves in section IV are travelling parallel to the isobaths and essentially aligned with the coastline. Fig. 2a also shows clear signs of refraction along the several tidally separated packets that go from 'A' to 'D'. The overall impression then is that the promontory seems to have some sort of a 'lens-like' effect that causes meridionally

propagating waves to refract to the east and diverts the waves towards the inner-shelf regions.

The ‘energy’ analysis has also shown that there is an increase followed by a decrease in the total normalized ‘energy’ E^* from the deeper areas (offshore) towards the coastline (that is from section I to section IV). A possible interpretation for the local maximum in the centre of the promontory is that sections II and III have ISWs in larger number and in more developed stages (longer crestlengths), while sections I and IV are associated with generation and dissipation/breaking processes, respectively. This is indeed the idea born out of the composite maps (Fig. 3a and 3b) as well as from the images like the one in Fig. 2a, where the signatures in SAR clearly indicate that there is a chronological sequence between early stages offshore, fully developed packets in the centre of EP, and dissipation processes near the shore.

Baines (1982) depth integrated body force has been calculated and used to determine the most likely generation regions in the study area. Four regions of particularly elevated values have been found, all of which within the steep slopes that surround the promontory area (generally between 200 and 1500 m – see Table 1 for a complete list). These regions are identified as the main candidates for the generation of the ISWs observed to propagate in EP. Moreover, the majority of the observations are characterized by crestlengths below 15 km (see Fig. 4a), and the mean value is only 9 km. These crestlengths are small compared with other fully developed ISWs in nearby regions farther north and south, suggesting localized sources for the generation of ISWs on the flanking areas of EP. We also note in passing that the maximum labelled N1 in Fig. 9b is coincident with the small-scale canyon-like feature, which is anticipated here to be one of the most important generation regions on the northern flank of EP

(confirming the overall impression already discussed when we analyzed the composite maps of Fig. 3).

We now comment on the pertinent asymmetry between the body force and the 'energy' distribution of the ISWs. While Fig. 3 shows the majority of waves within the deeper areas of EP propagating with north and south components (which then refract towards the coast), Fig. 7 clearly indicates that there is an asymmetry between the amount of 'energy' with north and south components (43% and 16%, respectively). In principle this should translate into more generation sources (and hence more tidal forcing) available in the southern flanks rather than in the north side of the promontory. However, this does not seem to be the case, since Fig. 9a indicates that the area where the body force is more significant is equally distributed between the northern and southern flanks. This is even clearer in Fig. 9b which shows the body force integrated in the longitudinal direction along EP, which will be further discussed in the following paragraphs.

This apparent inconsistency may be related to the significant difference of bottom slopes between the northern and southern flanks. According to Legg and Klymak (2008) this could have a major influence in the processes by which the internal tide develops, since the steepness of the bathymetry together with stratification can dictate the existence of internal hydraulic jumps with overturning rather than the usual steepening and disintegration into solitary waves.

These two different regimes can be parameterized using the vertical excursion inverse Froude number $Fr_{Z\omega}^{-1}$ already defined in the Introduction. To see how the previous analysis of the generation regions based on F changes in light of these new arguments a longitude integrated plot of the maximum body force was calculated in Fig.

9b with and without the restriction of elevated regions of $Fr_{Z\omega}^{-1}$ (which are characteristic of overturning events). We first notice that there is a clear increase in the longitude integrated forcing that matches the outer borders of the promontory area. Within this elevated widespread region of *F* there are several local maxima that can be identified (see dashed line in Fig. 9b): one in the north (N1, which is also the overall maximum), one in the centre (C1) and two in the south (S1 and S2). However, this distribution of *F* changes significantly when a restriction is added to eliminate the contribution of *F* whenever $Fr_{Z\omega}^{-1}$ is greater than 3.5 (solid line). This value was set based on the two regimes identified for the Hawaiian Ridge by Legg and Klymak (2008), and above which internal hydraulic jumps and overturning may be found (see the Introduction section).

The solid line (where the restriction has been applied) shows that N1 is significantly reduced, whereas C1, S1 and S2 remain practically unchanged. In fact, while the overall contribution represented by the dashed line (where no restrictions are applied) is divided roughly in two equal parts between the northern and southern EP, the solid line (where $Fr_{Z\omega}^{-1}$ is limited) shows quite different values of forcing, with the south part overtaking 60% of the overall forcing. We thus suggest that the steeper slopes on the northern flanks may cause the internal tide to enter a regime with internal hydraulic jumps and strong overturning (similar to the Hawaiian Ridge case described in Legg and Klymak, 2008), and that this may contribute (at least partially) to the different amounts in 'energy' propagation evident from Fig. 7.

Moreover, according to Legg and Klymak (2008), the isopycnical vertical displacements in this overturning regime are scaled by U_0/N rather than by the vertical

tidal excursion ($\frac{U_0}{\omega}\frac{\partial h}{\partial x}$). Using typical values for the study region this means that isopycnal displacements generated over the northern slopes would be roughly an order of magnitude lower than the isopycnal displacements in the south before overturning occurs. This means that steep slopes (like those in the northern flanks of EP) prevent the IT to grow beyond a certain limit, and therefore over those steep slopes the IT would be more unstable than over the more gentle southern slopes. We anticipate this to be a plausible reason why there is less 'energy' and fewer waves generated at the northern flanks of EP propagating to the south, as well as a possible explanation for the ISW radar signatures being systematically weaker over the northern slopes when compared with the south. In fact, we underline that this result is evident in the overall dataset of SAR profiles: on average backscatter intensities for waves with northerly components are 0.53, compared to 0.39 for waves with southerly components.

Finally, we stress that the 'lens-like' effect identified in EP may be important in terms of near-surface mixing. On the one hand, the results presented by Legg and Klymak (2008) indicate that the internal hydraulic jumps with overturning may constitute an important source for local tidally generated mixing when in the presence of tall steep topography. We suggest that the northern flanks would produce more mixing since $Fr_{Z\omega}^{-1}$ is higher there (and above the critical value for overturning to occur) than over the southern flanks. On the other hand, the SAR images (and also Fig. 6, last panel) suggest that a significant amount of energy may be reaching very close to shore due to refraction. Consequently, the cross-shelf energy budgets may be reaching farther into the inner-shelf than previously thought, and a significant amount of energy may be available to mixing in near-shore areas very close to the coast.

We thus conclude that the elevated ISW activity over the large-scale EP (one of the largest promontories in the world's oceans) reported in this paper reveal evidence that a significant amount of barotropic tidal energy is being converted to ITs and ISWs during the summer. Furthermore, such barotropic to baroclinic conversion of tidal energy is largely focused along the major axis of EP through refraction of ISWs. Other parts of the ocean with similar promontories and bathymetry features may also be responsible for significant barotropic to baroclinic tidal conversion and mixing, through ISWs propagating and breaking over the shelf.

Acknowledgements. SAR image data was provided by ESA under contract AOPT-2423, and DLR project OCE0056. One of us would like to thank the Portuguese Science and Technology Foundation (FCT) for a research grant (SFRH/BD/35898/2007). The authors would also like to thank Dr. Adrian New from the National Oceanographic Centre Southampton for discussions on several important ideas.

6. References:

Akylas, T.R., Grimshaw, R.H.J., Clark, S.R., Tabaei, A., 2007. Reflecting tidal wave beams and local generation of solitary waves in the ocean thermocline. J. Fluid Mech. 593, 297-313. doi:10.1017/S0022112007008786.

Alpers, W., 1985. Theory of radar imaging of internal waves. Nature (London) 314, 245-247. doi:10.1038/413245a0.

Araújo, I.B., da Silva, J.C.B., Ermakov, S.A., Robinson, I.S., 2002. On the role of wind direction in ERS SAR signatures of internal waves on the Iberian Shelf. Global Atmos. Ocean Syst. 8 (4), 269-281.

Avicola, G.S., Moum, J.N., Perlin, A., Levine, M.D., 2007. Enhanced turbulence due to the superposition of internal gravity waves and a coastal upwelling jet. J. Geophys. Res. 112, C06024. doi:10.1029/2006JC003831.

Azevedo, A., da Silva, J.C.B., New, A.L., 2006. On the generation and propagation of internal waves in the southern Bay of Biscay. Deep-Sea Res. I 53, 927941. doi:10.1016/j.dsr.2006.01.013.

Baines, P.G., 1982. On internal tides generation models. Deep-Sea Res. Part A 29, 307-338. doi:10.1016/0198-0149(82)90098-X.

Brandt, P., Romeiser, R., Rubino, A., 1999. On the determination of characteristics of the interior ocean dynamics from radar signatures of internal solitary waves. J. Geophys. Res. 103, 8009-8031. doi:10.1029/1999JC900092.

Colosi, J.A., Beardsley, R.C., Lynch, J.F., Gawarkiewicz, G., Chiu, C.-S., Scotti, A., 2001. Observations of nonlinear internal waves on the outer New England continental shelf during the summer Shelfbreak Primer study. J. Geophys. Res. 106 (C5), 9587-9601. doi:10.1029/2000JC900124.

da Silva, J.C.B., Ermakov, S.A., Robinson, I.S., Jeans, D.R.G., Kijashko, S.V., 1998. Role of surface films in ERS SAR signatures of internal waves on the shelf. 1. Short-period of internal waves. J. Geophys. Res. 103 (C4), 8009-8031. doi:10.1029/97JC02725.

da Silva, J.C.B., Ermakov, S.A., Robinson, I.S., 2000. Role of surface films in ERS SAR signatures of internal waves on the shelf. 3. Mode transitions. J. Geophys. Res. 105, 24089-24104. doi:10.1029/2000JC900053.

da Silva, J.C.B., New, A.L., Srokosz, M., Smyth, T., 2002. On the observability of internal tidal waves in remotely-sensed ocean color data. Geophys. Res. Lett. 29, 12. doi:10.1029/2001GL013888.

da Silva, J.C.B., New, A.L., Azevedo, A., 2007. On the role of SAR for observing "Local Generation" of internal solitary waves off the Iberian Peninsula. Can. J. Remote Sensing 33, 388-403. doi:10.5589/m07-041.

da Silva, J.C.B., Helfrich, K.R., 2008. Synthetic Aperture Radar observations of resonantly generated internal solitary waves at Race Point Channel (Cape Cod). J. Geophys. Res. 113, C11016. doi:10.1029/2008JC005004.

da Silva, J.C.B., New, A.L., Magalhaes, J.M., 2009. Internal solitary waves in the Mozambique Channel: observations and interpretation. J. Geophys. Res. 114, C05001. doi:10.1029/2008JC005125.

da Silva, J.C.B., New, A.L., Magalhaes, J.M., 2011. On the structure and propagation of internal solitary waves generated at the Mascarene Plateau in the Indian Ocean. Deep-Sea Res. I 58, 229-240. doi:10.1016/j.dsr.2010.12.003.

Egbert, G.D., Ray, R.D., 2003. Semi-diurnal and diurnal tidal dissipation from TOPEX/POSEIDOM altimetry. Geophys. Res. Lett. 30 (17), 1907. doi:10.1029/2003GL017676.

Egbert, G.D., Erofeeva, S.Y., 2002. Efficient inverse modeling of barotropic ocean tides. J. Oceanic Atmos. Technol. 19, 183-204. doi:10.1175/1520-0426(2002)019<0183:EIMOBO>2.0.CO;2.

Garrett, C., Gerkema, T., 2007. On the body-force term in internal-tide generation. J. Phys. Oceanogr. 37 (8), 2172-2175. doi:10.1175/JPO3165.1.

Gerkema, T., 2001. Internal and interfacial tides: beam scattering and local generation of solitary waves. J. Mar. Res. 59, 227-255. doi:10.1357/002224001762882646.

Grisouard, N., Staquet, C., Gerkema, T., 2011. Generation of internal solitary waves in a pycnocline by an internal wave beam: a numerical study. J. Fluid Mech. 676, 491-513. doi:10.1017/jfm.2011.61.

Helland-Hansen, B., Nansen, F., 1909. The Norwegian Sea – its Physical Oceanography based upon the Norwegian researches 1900-1904. (Report on Norwegian Fishery and Marine Investigations, Vol. II, No. 2). Det Mallingske Bogtrykkeri, Kristiania.

van Haren, H., Groenewegen, R., Laan, M., Koster, B., 2005. High sampling rate thermistor string observations at the slope of Great Meteor Seamount. Ocean Sci. 1, 17-28. doi:10.5194/os-1-17-2005.

Jackson, C.R., 2004. An atlas of internal solitary-like waves and their properties. Second edition. Available online at: www.internalwaveatlas.com (accessed 07 January 2010).

Jackson, C., 2007. Internal wave detection using the moderate resolution imaging spectroradiometer (MODIS). J. Geophys. Res. 112, C11012. doi:10.1029/2007JC004220.

Jackson, C.R., Apel, J.R., 2002. An atlas of internal solitary-like waves and their properties. First edition. Available online at: www.internalwaveatlas.com (accessed 07 January 2010).

Jeans, D.R.G., Sherwin, T.J., 2001a. The variability of strongly non-linear solitary internal waves observed during an upwelling season on the Portuguese shelf. Cont. Shelf Res. 21, 1855–1878. doi:10.1016/S0278-4343(01)00026-7.

Jeans, D.R.G., Sherwin, T.J., 2001b. The evolution and energetics of large amplitude nonlinear internal waves on the Portuguese shelf. J. Mar. Res. 59, 327-353. doi:10.1016/S0278-4343(01)00026-7.

Klymak, J. M., Pinkel, R., Liu, C.-T., Liu, A. K., David, L., 2006. Prototypical solitons in the South China Sea. Geophys. Res. Lett. 33, L11607. doi:10.1029/2006GL025932.

Klymak, J.M., Alford, M.H., Pinkel, R., Lien, R.-C., Yang, Y.J., Tang, T.-Y., 2011. The breaking and scattering of the internal tide on a continental slope. J. Phys. Oceanogr. 41, 926-945. doi:10.1175/2010JPO4500.1.

Kurapov, A.L., Allen, J.S., Egbert, G.D., 2010. Combined effects of wind-driven upwelling and internal tide on the continental shelf. J. Phys. Oceanogr. 40, 737-756. doi:10.1175/2009JPO4183.1.

Lamb, K.G., Farmer, D., 2011. Instabilities in an Internal Solitary-like Wave on the Oregon Shelf. J. Phys. Oceanogr. 41, 67-87. doi:10.1175/2010JPO4308.1.

Legg, S., Klymak, J., 2008. Internal hydraulic jumps and overturning generated by tidal flow over a tall steep ridge. J. Phys. Oceanogr. 38, 1949-1964. doi:10.1175/2008JPO3777.1.

Lozovatsky, I.D., Morozov, E.G., Fernando, H.J.S., 2003. Spatial decay energy density of tidal internal waves. J. Geophys. Res. 108 (C6), 3201. doi:10.1029/2001JC001169.

Merrifield, M.A., Holloway, P.E., 2002. Model estimates of M2 internal tide energetics at the Hawaiian Ridge. J. Geophys. Res. 107 (C8), 3179. doi:10.1029/2001JC00996.

Moum, J.N., Farmer, D.M., Smyth, W.D., Armi, L., Vagle, S., 2003. Structure and generation of turbulence at interfaces strained by internal solitary waves propagating shoreward over the continental shelf. J. Phys. Oceanogr. 33, 2093-2112. doi:10.1175/1520-0485(2003)033<2093:SAGOTA>2.0.CO;2.

Moum, J., Nash, J.D., Klymak, J.M., 2008. Small scale processes in the coastal ocean. Oceanography 21 (4), 22-33.

Nash, J.D., Moum, J.N., 2005. River plums as a source of large-amplitude internal waves in the coastal ocean. Nature 437, 400-403. doi:10.1038/nature03936.

New, A.L., Pingree, R.D., 1992. Local generation of internal soliton packets in the central Bay of Biscay. Deep-Sea Res. Part A 39, 1521-1534. doi:10.1016/0198-0149(92)90045-U.

New A.L., da Silva, J.C.B., 2002. Remote-sensing evidence for the local generation of internal soliton packets in the central Bay of Biscay. Deep-Sea Res. I 49, 915-934. doi:10.1016/S0967-0637(01)00082-6.

Niwa, Y., Hibiya, T., 2004. Three-dimensional numerical simulation of M_2 internal tides in the East China Sea. J. Geophys. Res. 109 (C4), C04027. doi:10.1029/2003JC001923.

Osborne, A.R., Burch, T.L., 1980. Internal solitons in the Andaman Sea. Science 208 (4443), 451-460 (New Series). doi:10.1126/science.208.4443.451.

Pichon, A., Correard, S., 2006. Internal tides modelling in the Bay of Biscay. Comparisons with observations. Scientia Marina 70 (S1), 65-88. doi:10.3989/scimar.2006.70s165.

Pichon, A., Morel, Y., Baraille, R., Quaresma, L.S., 2011. Internal tide interactions in the Bay of Biscay: observations and modelling. J. Mar. Syst. doi:10.1016/j.jmarsys.2011.07.003. In Press.

Pingree, R.D., Mardell, G.T., New, A.L., 1986. Propagation of internal tides from the upper slopes of the Bay of Biscay. Nature 312, 154-158. doi:10.1038/321154a.

Pinkel, R., 2000. Internal solitary waves in the warm pool of the western equatorial pacific. J. Phys. Oceanogr. 30, 2906-2926. doi:10.1175/1520-0485(2001)031<2906:ISWITW>2.0.CO;2.

Quaresma, L.S., Vitorino, J., Oliveira, A., da Silva, J., 2007. Evidence of sediment resuspension by nonlinear internal waves on the western Portuguese mid-shelf. Marine Geology 246, 123-143. doi:10.1016/j.margeo.2007.04.019.

Quaresma, L.S., Pichon, A., 2011. Modelling the barotropic tide along the West-Iberian margin, J. Mar. Syst. doi:10.1016/j.jmarsys.2011.09.016.

Ray, R.D., Mitchum, G.T., 1997. Surface manifestations of internal tides in the deep ocean: observations from altimetry and island gauges. Prog. Oceanogr. 40, 135-162. doi:10.1016/S0079-6611(97)00025-6.

Sandstrom, H., Elliott, J.A., 1984. Internal tide and solitons on the Scotian Shelf: a nutrient pump at work. J. Geophys. Res. 89 (C4), 6415-6426. doi:10.1029/JC089iC04p06415.

Schafstall, J., Dengler, M., Brandt, P., Bange, H., 2010. Tidal-induced mixing and diapycnal nutrient fluxes in the Mauritanian upwelling region. J. Geophys. Res. 115, C10014. doi: 10.1029/2009JC005940.

Sherwin, T.J., Vlasenko, V.I., Stashchuk, N., Jeans, D.R.G., Jones, B., 2002. Along-slope generation as an explanation for some unusually large internal tides. Deep-Sea Res. I 49, 1787-1799. doi:10.1016/S0967-0637(02)00096-1.

Shroyer E.L., Moum, J.N., Nash, J.D., 2010a. Vertical heat flux and lateral mass transport in nonlinear internal waves. Geophys. Res. Lett. 37, L08601. doi:10.1029/2010GL042715.

Shroyer, E.L., Moum, J.N., Nash, J.D., 2010b. Energy transformations and dissipation of nonlinear internal waves over New Jersey's continental shelf. Nonlinear Processes Geophys. 17, 345-360. doi:10.5194/npg-17-345-2010.

Small, J., 2002. Internal tide transformation across a continental slope off Cape Sines, Portugal. J. Mar. Syst. 32, 43-69. doi:10.1016/S0924-7963(02)00029-5.

Smith, W.H.F., Sandwell, D.T., 1997. Global sea floor topography from satellite altimetry and ship depth soundings. Science 277 (5334), 1956-1962. doi:10.1126/science.277.5334.1956.

Vlasenko, V., Alpers, W., 2005. Generation of secondary internal waves by the interaction of an internal solitary wave with an underwater bank. J. Geophys. Res. 110, C02019. doi:10.1029/2004JC002467.

Zhao, Z., Klemas, V., Zheng, Q., Yan, X.-H., 2004. Remote sensing evidence for the baroclinic tide origin of internal solitary waves in the northeastern South China Sea. Geophys. Res. Lett. 31, L06302. doi:10.1029/2003GL019077.

Figures and Tables

#	Latitudes (°N)	Longitudes (°W)	Depths (m)	Local Maxima (m^2s^{-2})
1	39.3 – 39.5	10.1 – 9.7	500 – 1500	1.0
2	39.3	10.2 – 10.1	500 – 1000	0.3
3	39.0 – 39.1	10.3 – 10.2	400 – 1000	0.6
4	38.7 – 39.0	10.3 – 10.1	500 – 2000	1.0
5	38.7 – 38.9	10.1 – 10.0	200 – 1500	0.9
6	38.7	9.9 – 9.8	200 – 1000	0.4

Table 1. Main hotspots and local maxima of Baines (1982) depth-integrated body force *F* identified in Fig. 9a, in the region surrounding the Estremadura Promontory.

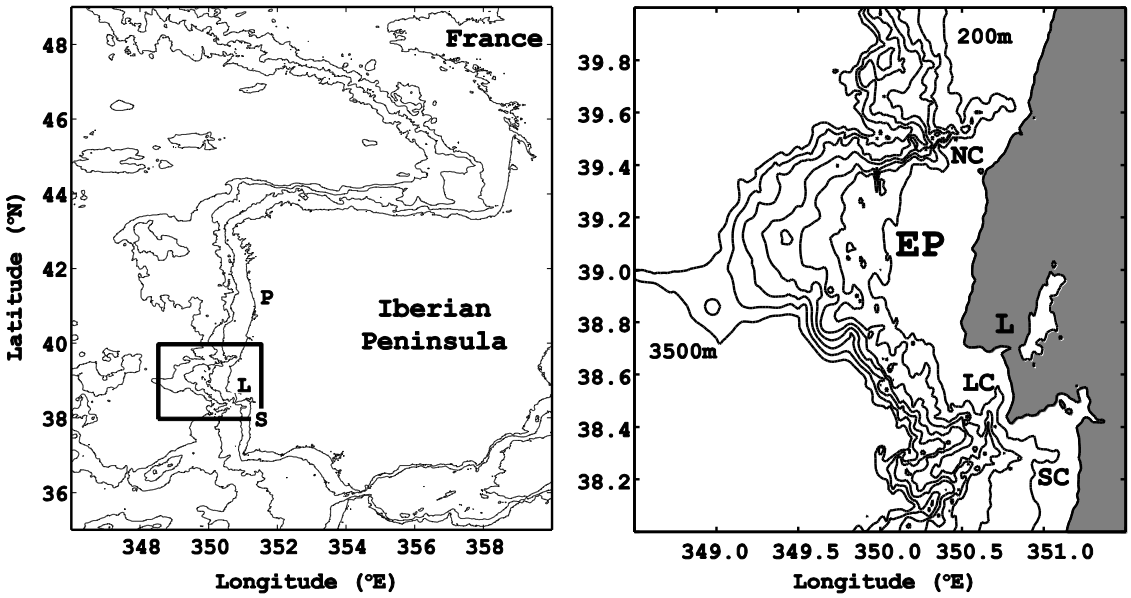

Fig. 1. (a-left) Study area for the present work in relation to the western Iberian Peninsula. The contours mark isobaths in meters (0, 200, 2000 and 4000 m). The dark rectangular frame shows the study area surveyed with SAR, which is shown in detail in Fig. 1b. The labels P, L and S stand for locations of Oporto, Lisbon and Sines, respectively. (b-right) Detailed bathymetry of the study area. Gray areas represent land and the isobaths for 200 m, 1000 m, and then every 500 m until 3500 m are shown in black contours. The reference location for the Estremadura Promontory is labeled EP, and L marks the city of Lisbon. Three major canyons enclose the promontory: Nazare canyon (NC), Lisbon canyon (LC) and Setubal canyon (SC).

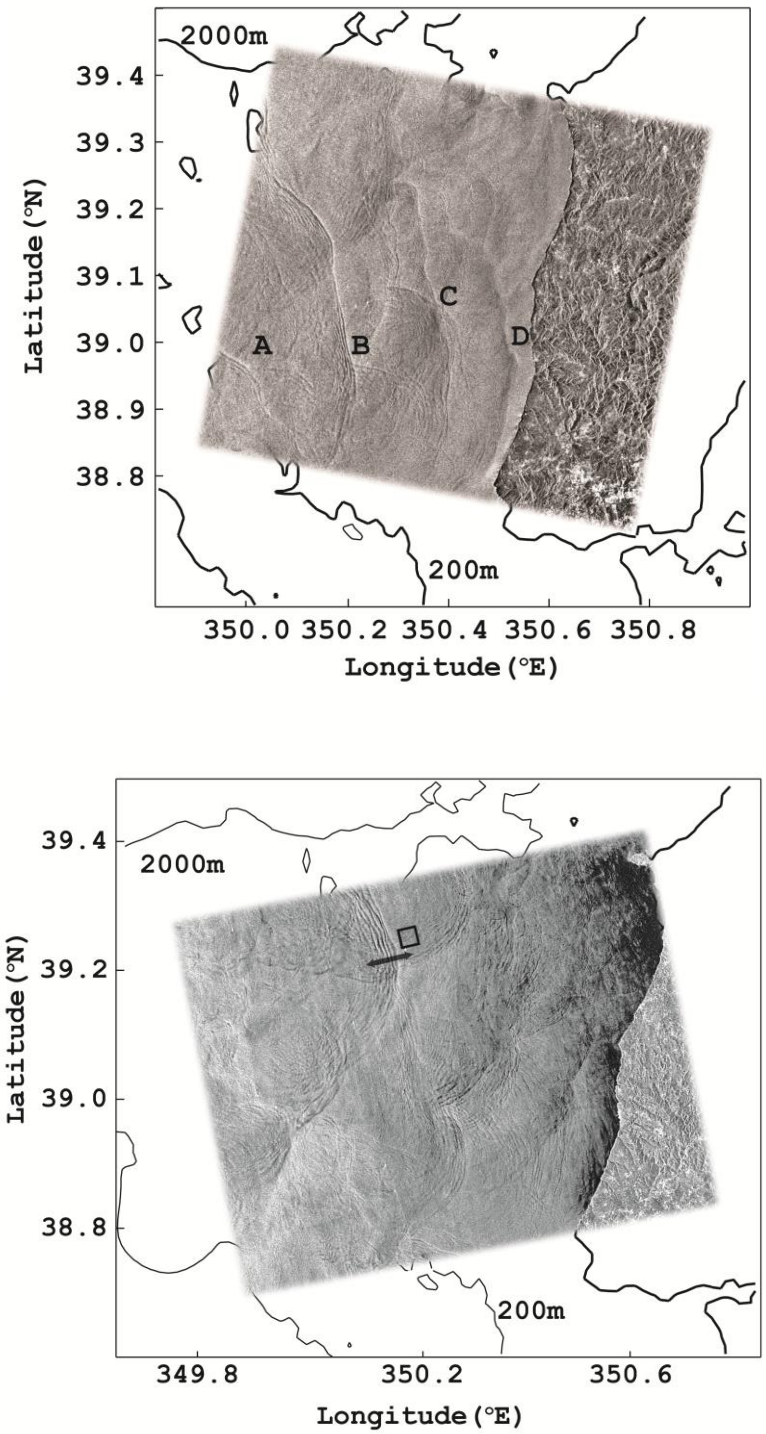

Fig. 2. (a-top) Subset of an ERS2-SAR image dated 14 July 1999 acquired at 11h21m UTC showing an area to the northwest of Lisbon with approximately 80×70 km^2. (b-bottom) Subset of an ERS2-SAR image dated 30 July 2010 acquired at 22h55m UTC showing an area to the southwest of Lisbon with approximately 80×60 km^2. The black transect shows the position from where the radar backscatter profile in Fig. 5 is taken, and the square box was chosen as an adequate image background unperturbed by the ISWs. Both images show ISWs propagating in rank-ordered packets which are propagating with an east velocity component, probably generated over the northern and southern flanks of the promontory, respectively. Depth contours for the 200 m and 2000 m levels are also shown.

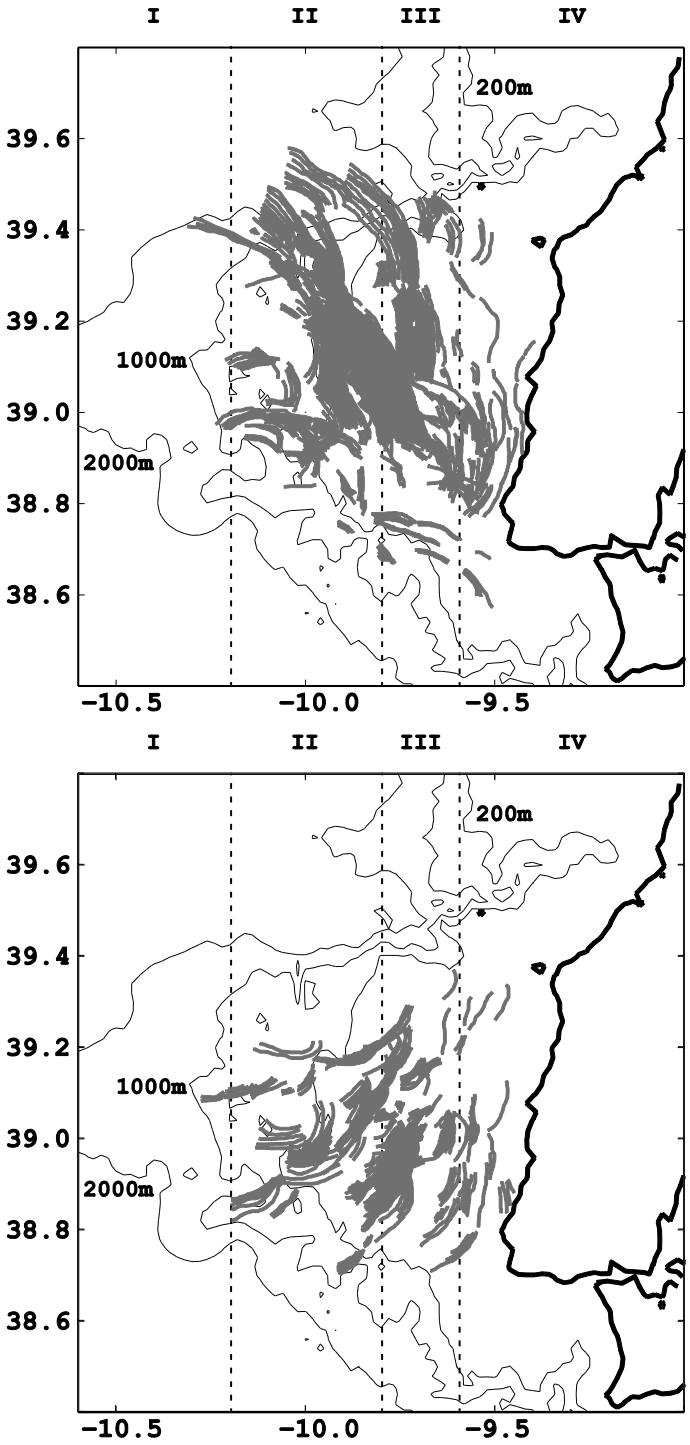

Fig. 3. (a-top) Composite map of ISW observations propagating from the southern flanks based on a subset of 10 images for the study region. Contours mark isobaths in meters at 200 m, 1000 m and 2000 m. For reference four meridional sections are labelled from I to IV and delineated by dashed vertical lines (see text for details). (b-bottom) same as Fig. 3a but for ISWs coming from the northern flanks of the Estremadura Promontory.

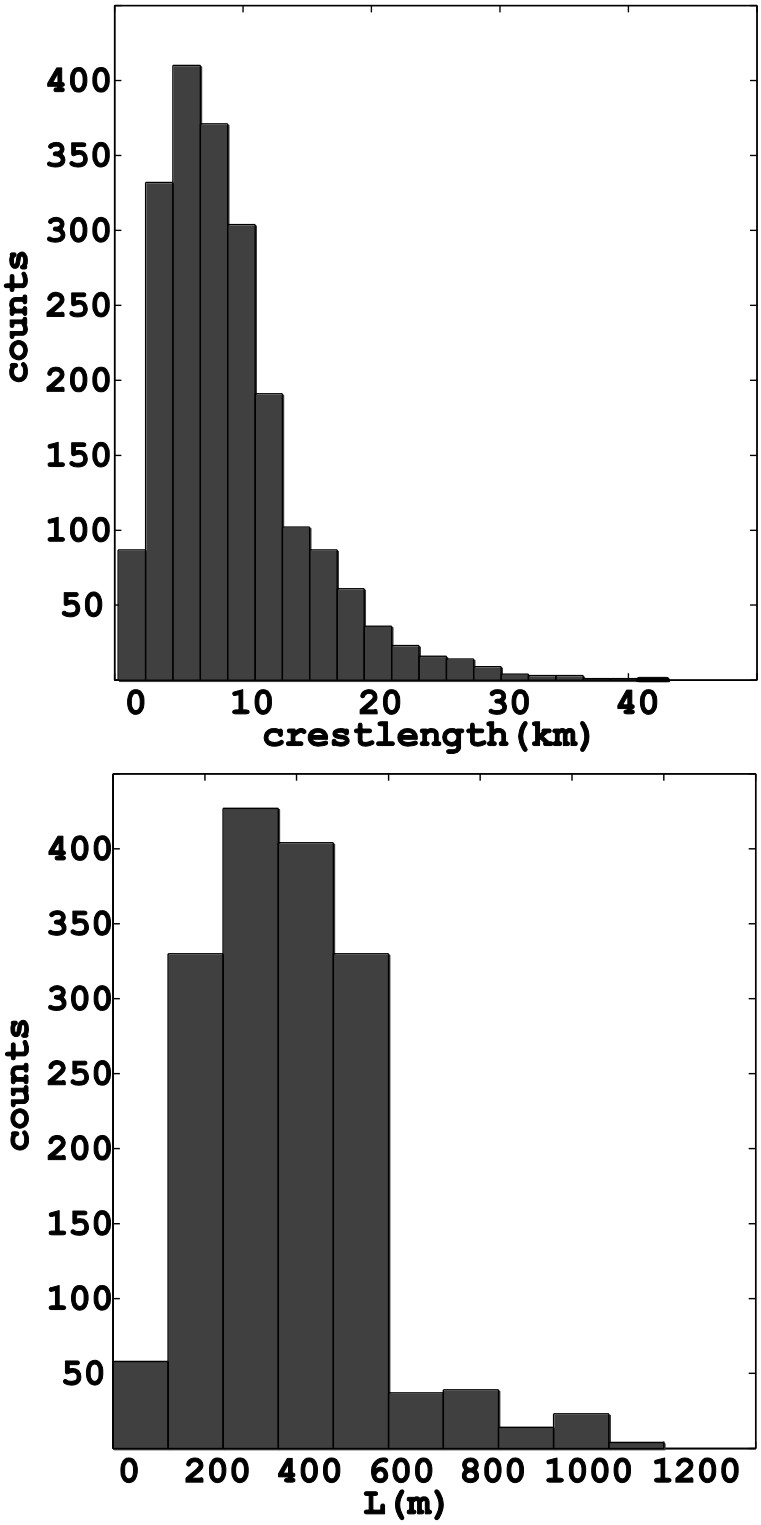

Fig. 4. Distribution of ISW main properties in the Estremadura Promontory accumulated over the entire dataset of 29 SAR images. (a-top) Crestlength (km). (b-bottom) Wavelength (m).

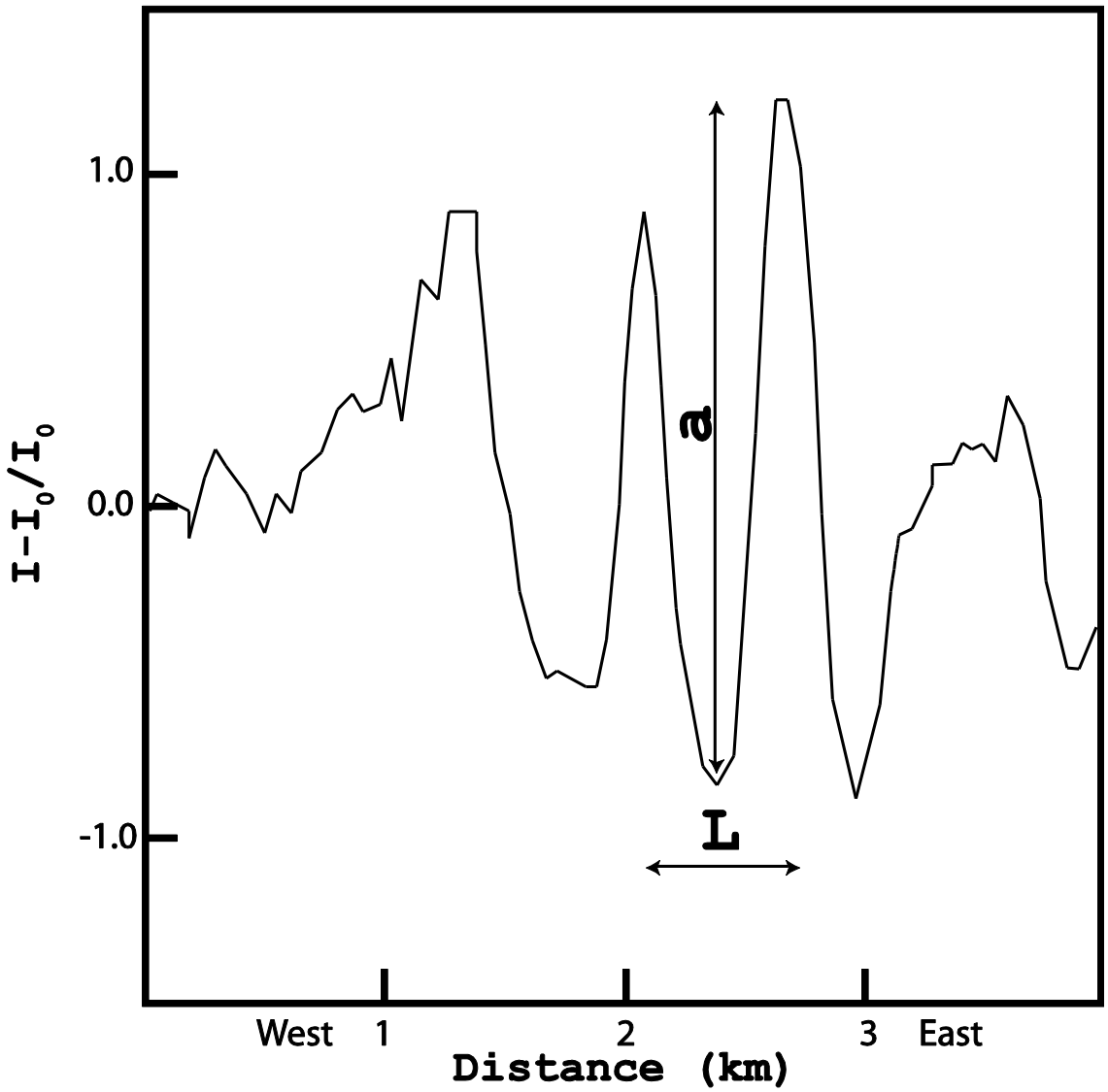

Fig. 5. Example of a normalized radar cross section profile along the transect shown in Fig. 2a (small dark line). The values are normalized by the average radar backscatter of the squared box also shown in Fig. 2a (small dark square). The parameters a and L used to calculate E are also shown.

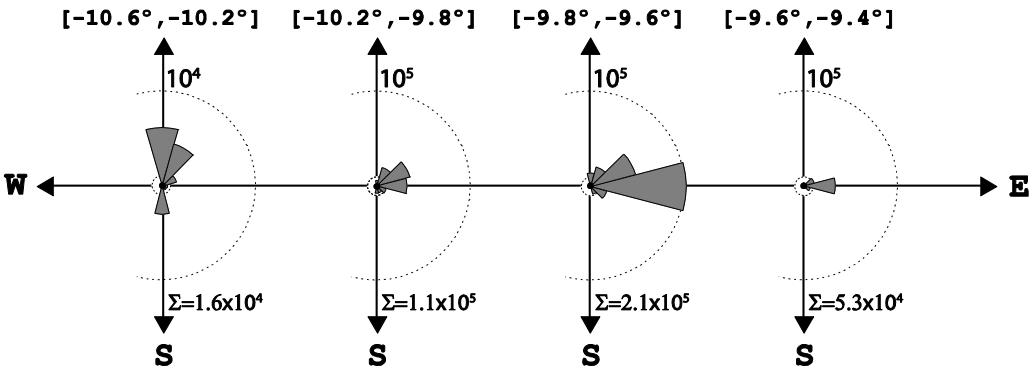

Fig. 6. Normalized energy E* circular diagrams (divided in 30° intervals) for the entire dataset and for each of the meridional sections in Fig. 3 (corresponding longitude interval annotated on top of each diagram). The outer dashed line represents the value for the wave energy marked on top and the smaller dashed circle is an order of magnitude less. The total energy normalized by the area of observation (Σ) is shown for each section at the bottom of each panel.

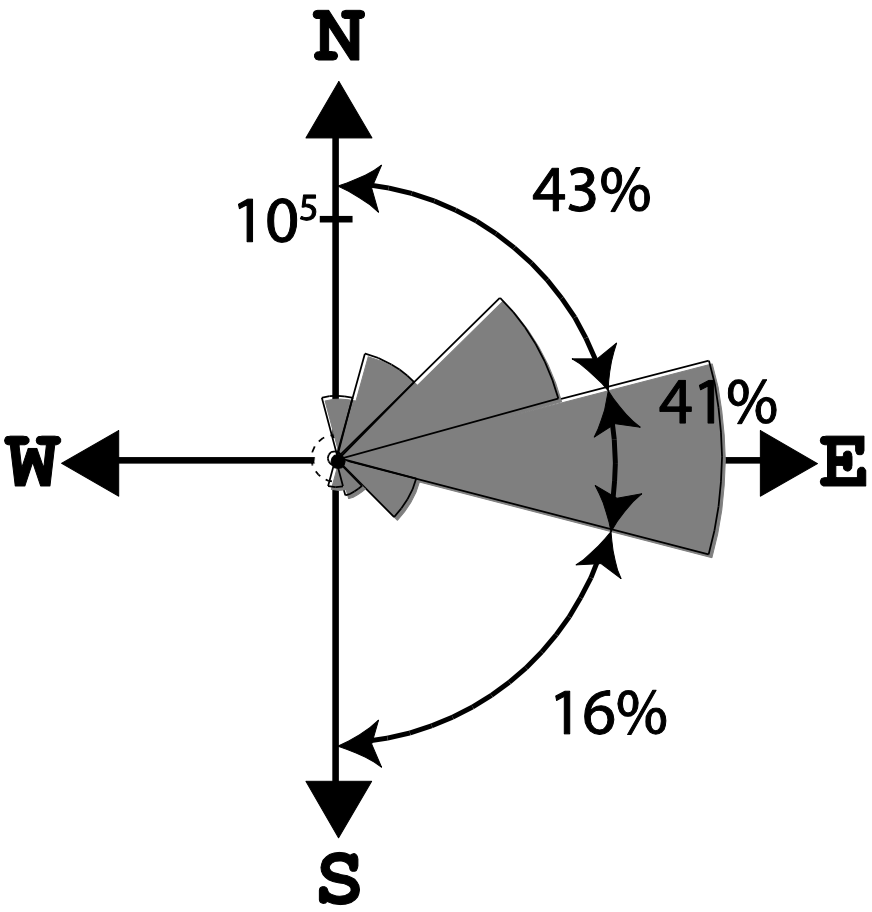

Fig. 7. Same as Fig. 6 but for all the sections (I, II, III and IV) merged together, that is the energy budget for the whole study region.

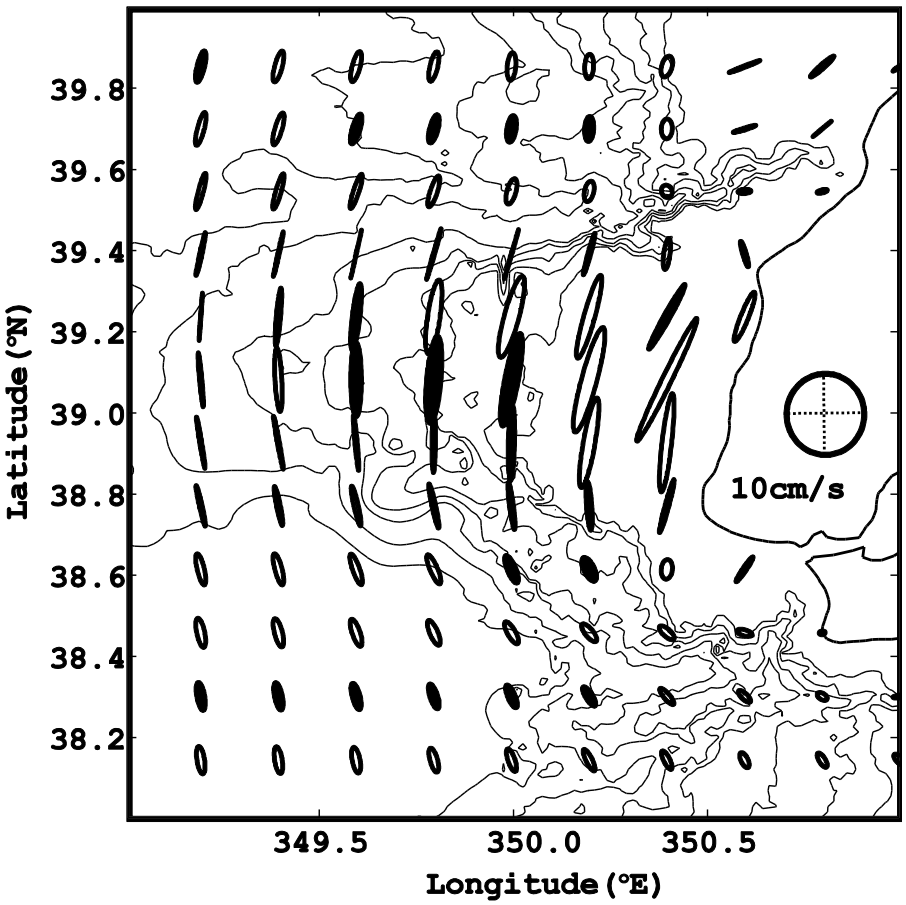

Fig. 8. Tidal current ellipses for 14 July 1999 (see text for details). A reference ellipse is shown on the right-hand side (with both axes representing a speed of 10 cms^{-1}). Depth contours are also shown in m (starting at 200m, 500m, 1000m, 1500m, 2000m 3000m, and 4000m).

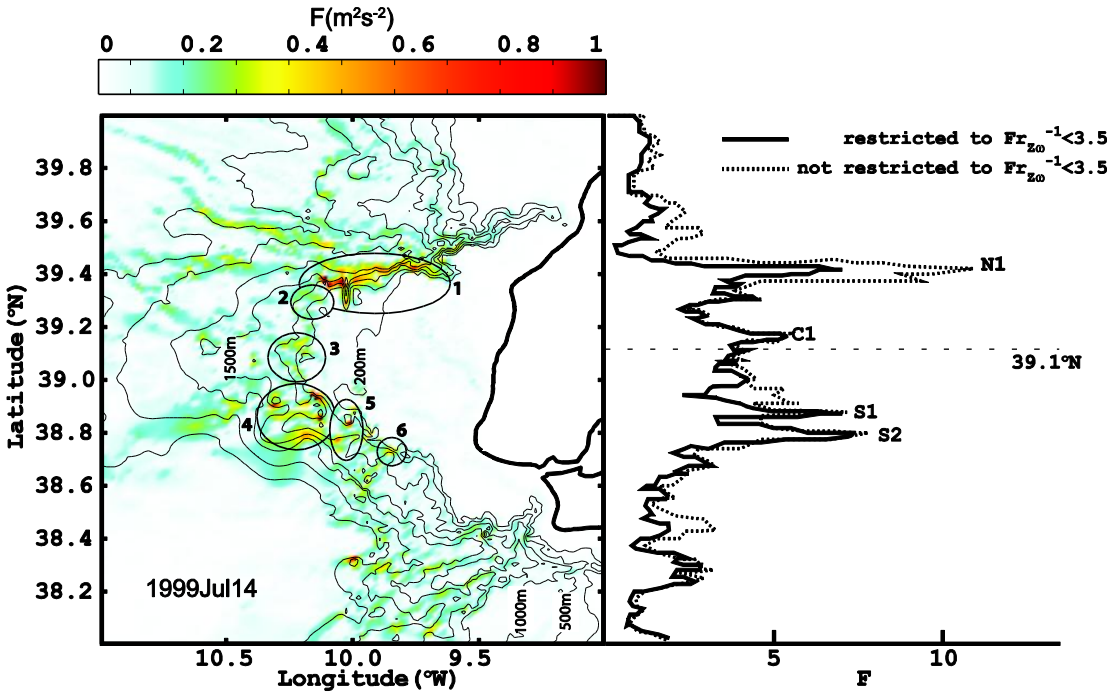

Fig. 9. (a) Maxima of Baines (1982) depth-integrated body force F over a complete tidal cycle (calculated using Eq. (4)) for 14 July 1999. The regions in Table 1 are highlighted in black circles, with the corresponding number placed next to them. Depth contours are the same as in Fig. 8. (b) Same as Fig. 9a but integrated along longitude (dashed line) and restricting values of F to areas where $Fr_{Z\omega}^{-1}$ is less than 3.5 (solid line). Regions of elevated forcing are labeled in the north part of the promontory (N1), centre (C1) and south (S1 and S2).

Chapter 8

Concluding Remarks

This thesis describes how satellite remote sensing data (mainly SAR and MODIS) are used to identify IW hotspots in several regions of the world's oceans, and how satellite imagery can be combined with other data sources to study and characterize IW fields. The main achievements and conclusions can be summarized into four different study regions as follows:

1 – Mozambique Channel

It is shown that MC is a hotspot for observing ISWs in the ocean and in the atmosphere. SAR imagery clearly identifies the Sofala shelf (between 20° and 21°S) as a hotspot for the generation of ISWs and Internal Tides (ITs), which travel oceanwards away from the shelf-break. This location is characterized by strong barotropic tidal forcing and large tidal transports, coupled with critical topography at the shelf-break. Farther north and south, the forcing is reduced and insufficient to generate ISWs. It is suggested that the ISW packets observed in satellite result from both direct generation at the shelf-break and from local generation at about 80 km oceanwards from the break, where the surfacing of IT rays reach the thermocline. Some seasonal differences in the wave patterns are investigated, where waves seem to penetrate more extensively into the channel during the southern summer, and appear slightly farther to the south during the southern winter. We also conclude that the local generation process is more likely to occur during the winter when the stratification is reduced. SAR imagery reveals that the MC is a preferential region for observing mode 2 solitary-like IWs and refraction patterns. The data suggests that these waves can also be generated by tidal beams – similarly to some of the mode 1 waves. This confirms some conclusions drawn from other independent studies using modelling and laboratory experiments (Grisouard et al., 2011; Mercier et al., 2012, respectively) about the origin of mode 2 solitary-like waves by tidal beams. Synergies between SAR images and altimetry data revealed that ISWs in MC frequently interact with oceanic features such as eddy-like structures, causing significant IW refraction. These eddies, which propagate year-round through MC, affect the local vertical structure of the ocean (both dynamically and in terms of stratification), being capable of 180° changes in the ISWs propagation directions. Finally, large-scale AGWs are also found to be a ubiquitous feature in MC, especially from July to October (see da Silva and Magalhaes, 2009), and care should be taken to avoid miss-interpretations of the oceanic/atmospheric nature of these waves in SAR images.

2 – Mascarene Ridge

A large dataset of Envisat-ASAR and TerraSAR-X images shows the presence of packets of large ISWs propagating from a submarine sill between Saya de Malha and Nazareth Banks, near 12.5°S in the Mascarene Ridge of the Indian Ocean. The waves propagate for at least 400 km to the west and 300 km to the east of the sill, with crest lengths as large as 350 km. This exceeds ISW crest lengths in other regions such as the Sulu Sea (crest lengths of up to 170 km), the Andaman Sea (150 km) and in the Bay of

Biscay (50 km), and is only comparable with those in the south China Sea with crest lengths in excess of 250 km (see e.g. Zhao et al., 2004). The Mascarene Ridge is therefore classified as a major hotspot of ISW activity in the open ocean. The propagation characteristics of these ISWs in terms of phase speeds are in close agreement with those predicted from linear theory for mode 1 long interfacial waves. A travel-time diagram inferred from the SAR image dataset indicated that the waves were generated from a location just westwards of the sill crest at the time of maximum westward flow. Therefore, it is proposed that both sets of ISWs are formed from the splitting of a large tidally-generated depression of the upper thermocline (or lee wave) which forms on the western side of the sill at that time. ISWs are expected to be stronger on the western side of the sill, since the tidal flow and steady westward background flow (that of the south Equatorial Current) combine to give an enhanced flow in the downslope direction (to the west). We also consider that a likely explanation of the stronger wave packets to the west (which also propagate further) of the sill is that those travelling towards the east would need to pass over the sill itself. Since the sill is only 400-450 m deep, the ITs or ISWs which pass over the sill would be long compared to the water depth and so would be expected to dissipate to some extent. In addition, the eastward-propagating waves travel against a "steady" shear flow in the south Equatorial Current, while the westward-propagating waves travel with the flow. It is possible that this may also lead to additional dissipation effects due to wave-current interactions for those waves travelling eastwards. Satellite evidence is also found for mode 2 ISWs near the sill where the flow becomes supercritical, and where resonant generation of mode 2 solitary-like IWs can be expected to occur.

3 – Red Sea region

In this study region satellite images are combined with *in situ* data to reveal a major hotspot for the observation of AGWs. Although these waves can be found year round, their occurrence is seasonal with a clear increase between April and September. The dominant propagation directions are between east-southeast and northeast, and between northwest and west-southwest. The atmospheric buoyancy frequency was used to investigate the existence of waveguides that can trap and prevent energy to radiate away in the vertical. The results show that the stratification plays a key role in determining favourable propagation conditions for AGWs. A weakly nonlinear long wave analysis is presented for some case studies, and the models predict phase speeds which are consistent with typical values of observed AGWs, with the KdV model performing slightly better than the Benjamin-Davis-Acrivos-Ono model as far as estimated phase speeds are concerned. The amplitudes found with both models are relatively small compared to the waveguide height, thus being consistent with the use of weakly nonlinear theory. However, these amplitudes are generally smaller than those presented by other studies (e.g. Porter and Smyth, 2002), where amplitudes can have half of the waveguide height (like in the Australian Morning Glories). Nevertheless, in these cases weakly nonlinear theory also found reasonable agreement with the observations. Some possible generation mechanisms are briefly discussed for the observed AGWs, whereas a more developed study is beyond the scope of this thesis. Mountain chains surrounding the Red Sea help constrain the average flow along its main axis (Patzert, 1974). However, mesoscale atmospheric modelling (validated by *in situ* data) was used by Jiang et al. (2009) to add important results focusing on the cross-axis zonal winds within the Red Sea region. In

fact, they found that the complex topography of the Red Sea contains several gaps along the coast, and that these direct numerous strong jet-like winds up to 15 ms^{-1} to flow frequently across the longitudinal axis of the Red Sea. This general frame of circulation is in agreement with the AGWs preferential directions of propagation. This suggests that several AGW wind driven generation mechanisms may be at work in the Red Sea, and that these are most likely related to the strong jet-like winds and variable topography. Particularly interesting is also the fact that some AGWs have phase lines (crests) almost parallel to the coastlines. Since there are usually strong (daily) temperature contrasts along the Red Sea coasts (Pedgley, 1974) that could result in sea/land breezes, these could generate AGWs when they are sufficiently strong. Finally, distinction issues between oceanic and atmospheric IWs in satellite images should be taken into consideration in regions such as the Red Sea (characterized by dry conditions and absence of roll clouds). Whilst many of the IWs in satellite observations in the Red Sea region can be interpreted as AGWs based solely on scale, refraction patterns and surface signatures (such as the case study in Figure 4, see the Introduction Section), there are oceanic IWs in the Red Sea (as shown by Jackson, 2007) that cannot be interpreted based on these criteria alone (especially when wavelengths approach values around 5-10 km).

4 – Estremadura Promontory (Portugal)

A selection of SAR images acquired during the summer seasons between 1992 and 2010 shows the presence of significant ISW activity over the Estremadura Promontory (a headland projection extending for some 150 km towards the west off Lisbon). This investigation adds to previous studies made farther north (Jeans and Sherwin, 2001a, 2001b; Sherwin et al., 2002; Quaresma et al., 2007) and farther south (Small, 2002; da Silva et al., 2007), which had previously identified other hotspot regions, and confirms that the west Iberian Coast is an important region where oceanic ISWs can be frequently and continuously observed during the summer season. A statistical analysis shows that these ISWs have average crestlengths and horizontal scales of about 9 km and 400 m, respectively. Composite maps suggested that they propagate within two major propagation paths coming from the northern and southern flanks of the promontory. The overall impression is that the promontory seems to have some sort of a 'lens-like' effect that causes meridionally propagating waves to refract to the east and diverts the waves towards the inner-shelf regions. The 'lens-like' effect identified in the Estremadura Promontory may be important in terms of mixing, since SAR images suggest that a significant amount of energy may be reaching very close to shore due to refraction. Consequently, the cross-shelf energy budgets may be extending farther into the inner-shelf than previously thought, and a significant amount of energy may be available to mixing in near-shore areas very close to the coast. Baines (1982) depth integrated body force has been used to determine the most likely generation regions in the study area. Four regions of particularly elevated values have been found, all of which within the steep slopes that surround the promontory area (generally between 200 and 1500 m). An energy analysis of the ISWs observed in the SAR shows an asymmetry between the amount of energy with north and south components, which should translate into more generation sources (and hence more tidal forcing) available in the southern flanks rather than in the north side of the promontory. However, this does not seem to be the case, since the areas where the body force is more significant are equally distributed between the northern and southern flanks. We suggest that this apparent inconsistency is related to

the significant difference of bottom slopes between the northern and southern flanks. According to Legg and Klymak (2008) this could have a major influence in the processes by which the IT develops, since the steepness of the bathymetry together with stratification (at the bottom) can dictate the existence of internal hydraulic jumps with overturning rather than the usual steepening and disintegration of the IT into ISWs. Finally, it is concluded that a significant amount of barotropic tidal energy is converted to interfacial ITs and ISWs during the summer over the slopes of the Estremadura Promontory (one of the largest promontories in the world's oceans). Furthermore, such barotropic to baroclinic conversion of tidal energy is largely focused along the zonal axis of the promontory through refraction of ISWs. Other parts of the ocean with similar promontories and bathymetry features may also be responsible for significant barotropic to baroclinic tidal conversion and mixing, through ISWs propagating and breaking over the shelf.

One of the most important conclusions that can be drawn from the ensemble of these studies is that satellite remote sensing greatly contributes to the discovery of new IW hotspots, as well as in providing valuable data to describe the waves' main properties and characteristics. It has also been shown that satellite imagery can be added to *in situ* data and modeling results to provide unprecedented insights into the waves' generation and propagation mechanisms. For future work, it is clear that satellite remote sensing continues to have much to offer, particularly since so little is known about IWs on a global scale. In this framework, at least two major trends can be identified as promising grounds for future research. The first is related with satellite data synergies using multiple satellite missions and different sensors (or satellite constellations). The use of different satellites (capturing the same IW event at different times) would allow insights into the evolution phases of the waves' two-dimensional (horizontal) structures. This would certainly contribute to answer some pertinent questions concerning ISW generation mechanisms and propagation patterns (like discrimination of tidal phases in IW generation and provide detailed refraction effects). Additionally, the use of different sensors is also important, mainly to study the interaction of IWs with other oceanographic phenomena such as upwelling filaments, which can be seen in thermal infrared data. The second possibility is related with the use of very high resolution satellite data. This would certainly bring major advances in the study of IW breaking, turbulence, and mixing issues, since these are often small-scale processes taking place in near-shore areas. Satellite images with very high spatial resolutions could also be used to obtain data concerning the initial stages of ISW formation, which would also help to determine more accurately some of the aspects of their early formation.

References

(for chapters 1 and 8)

Alpers, W., Huang, W., 2011. On the Discrimination of Radar Signatures of Atmospheric Gravity Waves and Oceanic Internal Waves on Synthetic Aperture Radar Images of the Sea Surface. IEEE Trans. Geosci. Remote Sens. 49 (3), 1114-1126. doi:10.1109/TGRS.2010.2072930.

Baines, P.G., 1982. On internal tides generation models. Deep-Sea Res. Part A 29, 307-338. doi:10.1016/0198-0149(82)90098-X.

Benjamin, T.B., 1966. Internal waves of finite amplitude and permanent form. J. Fluid Mech. 25, 241-270. doi:10.1017/S0022112066001630.

Bedard, A.J., Canavero, F., Einaudi, F., 1986. Atmospheric gravity waves and aircraft turbulence encounters. J. Atmos. Sci. 43 (23), 2838-2844. doi:10.1175/1520-0469(1986)043<2838:AGWAAT>2.0.CO;2.

Bogucki, D., Dickey, T., Redekopp, L.G., 1997. Sediment resuspension and mixing by resonantly generated internal solitary waves. J. Phys. Oceanogr. 27, 1181-1196.

Cacchione, D.A., Pratson, L.F., Ogston, A.S., 2002. The shaping of continental slopes by internal tides. Science 296, 724-727. doi:10.1126/science.1069803.

Christie, D.R., Muirhead, K.J., 1983. Solitary waves: a hazard to aircraft operating at low altitudes. Aust. Met. Mag. 31, 97-109.

d'Alembert, J.R., 1747. Recherches sur la courbe que forme une corde tenduë mise en vibration. Histoire de l'académie royale des sciences et belles lettres de Berlin Hist. Acad. R. Sci. Belles Lett. Berl. 3, 214-219.

da Silva, J.C.B., Magalhaes, J.M., 2009. Satellite observations of large atmospheric gravity waves in the Mozambique Channel. Int. J. Remote Sens. 30 (5), 1161-1182. doi:10.1080/01431160802448943.

da Silva, J.C.B., New, A.L., Azevedo, A., 2007. On the role of SAR for observing "Local Generation" of internal solitary waves off the Iberian Peninsula. Can. J. Remote Sens. 33, 388-403. doi:10.5589/m07-041.

da Silva, J.C.B., New, A.L., Magalhaes, J.M., 2009. Internal solitary waves in the Mozambique Channel: observations and interpretation. J. Geophys. Res. 114, C05001. doi:10.1029/2008JC005125.

da Silva, J.C.B., New, A.L., Magalhaes, J.M., 2011. On the structure and propagation of internal solitary waves generated at the Mascarene Plateau in the Indian Ocean. Deep-Sea Res. I 58, 229-240. doi:10.1016/j.dsr.2010.12.003.

Drazin, P., 1991. The life of a solitary wave. New Scientist 132 (1797), 34-37.

Dushaw, B.D., 2006. Mode-1 internal tides in the western North Atlantic Ocean. Deep-Sea Res. I 53 (3), 449-473. doi:10.1016/j.dsr.2005.12.009.

Garrett, G., Munk, W., 1979. Internal waves in the ocean. Annu. Rev. Fluid Mech. 11, 339-369. doi:10.1146/annurev.fl.11.010179.002011.

Gerkema, T., 2001. Internal and interfacial tides: beam scattering and local generation of solitary waves. J. Mar. Res. 59, 227-255. doi:10.1357/002224001762882646.

Gerkema, T., Zimmerman, J.T.F., 2008. An Introduction to Internal Waves. Lectures notes, Royal NIOZ, Texel, 207 pp.

Grisouard, N., Staquet, C., Gerkema, T., 2011. Generation of internal solitary waves in a pycnocline by an internal wave beam: a numerical study. J. Fluid Mech. 676, 491-513. doi:10.1017/jfm.2011.61.

Helland-Hansen, B., Nansen, F., 1909. The Norwegian Sea – its Physical Oceanography based upon the Norwegian researches 1900-1904. (Report on Norwegian Fishery and Marine Investigations, Vol. II, No. 2). Det Mallingske Bogtrykkeri, Kristiania.

Jackson, C.R., 2004. An atlas of internal solitary-like waves and their properties. Second edition. Available online at: www.internalwaveatlas.com (accessed 01 December 2011).

Jackson, C., 2007. Internal wave detection using the moderate resolution imaging spectroradiometer (MODIS). J. Geophys. Res. 112, C11012. doi:10.1029/2007JC004220.

Jackson, C.R., Apel, J.R., 2002. An atlas of internal solitary-like waves and their properties. First edition. Available online at: www.internalwaveatlas.com (accessed 01 December 2011).

Jeans, D.R.G., 1995. Solitary internal waves in the ocean. A literature review completed as part of the internal waves contribution to MORENA, UCES Rep U95-1 Unit for Coastal and Estuarine Studies, Marine Science Laboratories, Menai Bridge, Anglesey, UK.

Jeans, D.R.G., Sherwin, T.J., 2001a. The variability of strongly non-linear solitary internal waves observed during an upwelling season on the Portuguese shelf. Cont. Shelf Res. 21, 1855-1878. doi:10.1016/S0278-4343(01)00026-7.

Jeans, D.R.G., Sherwin, T.J., 2001b. The evolution and energetics of large amplitude nonlinear internal waves on the Portuguese shelf. J. Mar. Res. 59, 327-353. doi:10.1016/S0278-4343(01)00026-7.

Jiang, H., Farrar, J.T., Beardsley, R.C., Chen, R., Chen, C., 2009. Zonal surface wind jets across the Red Sea due to mountain gap forcing along both sides of the Red Sea. Geophys. Res. Lett. 36, L19605. doi:10.1029/2009GL040008.

Joseph, R.J., 1977. Solitary waves in a finite depth fluid. J. Phys. A: Math. Gen. 10 (12), L225-L227. doi:10.1088/0305-4470/10/12/002.

Krauss, W., 1966. Methoden und Ergebnisse der theoretischen Ozeanographie II: Interne Wellen. GebrÄuder BorntrÄager, Berlin, 248 pp.

Legg, S., Klymak, J., 2008. Internal hydraulic jumps and overturning generated by tidal flow over a tall steep ridge. J. Phys. Oceanogr. 38, 1949-1964. doi:10.1175/2008JPO3777.1.

McPhee-Shaw, E., 2006. Boundary-interior exchange. Reviewing the idea that internal-wave mixing enhances lateral dispersal near continental margins. Deep-Sea Res. II 53 (1-2), 42-59. doi: 10.1016/j.dsr2.2005.10.018.

Magalhaes, J.M., Araújo, I.B., da Silva, J.C.B., Grimshaw, R.H.J., Davis, K., Pineda, J., 2011. Atmospheric gravity waves in the Red Sea: a new hotspot. Nonlinear Process. Geophys. 18, 71-79. doi:10.5194/npg-18-71-2011.

Mercier, M.J., Mathur, M., Gostiaux, L., Gerkema, T., Magalhaes, J.M., da Silva, J.C.B., Dauxois, T., 2012. Soliton generation by internal tidal beams impinging on a pycnocline: laboratory experiments. J. Fluid Mech. Accepted.

New, A.L., 2003. R.R.S. Charles Darwin Cruise 141, 01 June-11 July 2002; satellite calibration and interior physics of the Indian Ocean: SCIPIO. Southampton Oceanography Centre Cruise Report No. 41, Southampton University, UK, 92 pp.

New, A.L., Pingree, R.D., 1992. Local generation of internal soliton packets in the central Bay of Biscay. Deep-Sea Res. Part A 39, 1521-1534. doi:10.1016/0198-0149(92)90045-U.

New, A.L., da Silva, J.C.B., 2002. Remote-sensing evidence for the local generation of internal soliton packets in the central Bay of Biscay. Deep-Sea Res. I 49, 915-934. doi:10.1016/S0967-0637(01)00082-6.

New, A.L., Stansfield, K., Smythe-Wright, D., Smeed, D.A., Evans, A.J., Alderson, S.G., 2005. Physical and biochemical aspects of the flow across the Mascarene Plateau in the Indian Ocean. Philos. Trans. R. Soc. A 363, 151-168. doi:10.1098/rsta.2004.1484.

New, A.L., Alderson, S.G., Smeed, D.A., Stansfield, K.L., 2007. On the circulation of water masses across the Mascarene Plateau in the south Indian Ocean. Deep-Sea Res. I 54, 42-74. doi:10.1016/j.dsr.2006.08.016.

Ono, H., 1975. Algebraic solitary waves in stratified fluids. J. Phys. Soc. Jpn. 39 (4), 1082-1091. doi:10.1143/JPSJ.39.1082.

Osborne, A.R., Burch, T.L., 1980. Internal solitons in the Andaman Sea. Science 208 (4443), 451-460 (New Series). doi:10.1126/science.208.4443.451.

Patzert, W.C., 1974. Wind-induced reversal in Red Sea circulation. Deep Sea Res. Oceanogr. Abstr. 21 (2), 109-121. doi:10.1016/0011-7471(74)90068-0.

Pedgley, D.E., 1974. An outline of the weather and climate of the Red Sea. In: L'Oceanographie Physique de la Mer Rouge. U. N. Ed. Sci. and Cult. Org., Paris, 312 pp.

Porter, A., Smyth, N.F., 2002. Modelling the morning glory of the Gulf of Carpentaria. J. Fluid Mech. 454, 1-20. doi:10.1017/S0022112001007455.

Potter, R., 2001. Internal waves in the Andaman Sea. PhD dissertation, University of Southampton.

Quaresma, L.S., Vitorino, J., Oliveira, A., da Silva, J., 2007. Evidence of sediment resuspension by nonlinear internal waves on the western Portuguese mid-shelf. Mar. Geol. 246, 123-143. doi:10.1016/j.margeo.2007.04.019.

Reeder, M.J., Christie, D.R., Smith, R.K., Grimshaw, R.H.J., 1995. Interacting “Morning Glories” over Northern Australia. Bull. Am. Meteorol. Soc. 76 (7), 1165-1172. doi:10.1175/1520-0477(1995)076<1165:IGONA>2.0.CO;2.

Sandstrom, H., Elliott, J.A., 1984. Internal tide and solitons on the Scotian Shelf: a nutrient pump at work. J. Geophys. Res. 89 (C4), 6415-6426. doi:10.1029/JC089iC04p06415.
Sherwin, T.J., Vlasenko, V.I., Stashchuk, N., Jeans, D.R.G., Jones, B., 2002. Along-slope generation as an explanation for some unusually large internal tides. Deep-Sea Res. I 49, 1787-1799. doi:10.1016/S0967-0637(02)00096-1.

Small, J., 2002. Internal tide transformation across a continental slope off Cape Sines, Portugal. J. Mar. Syst. 32, 43-69. doi:10.1016/S0924-7963(02)00029-5.

Swart, N.C., Lutjeharms, J.R.E., Ridderinkhof, H., de Ruijter, W.P.M., 2010. Observed characteristics of Mozambique Channel eddies. J. Geophys. Res. 115, C09006. doi:10.1029/2009JC005875.

Zabusky, N.J., Kruskal, M.D., 1965. Interaction of "Solitons" in a Collisionless Plasma and the Recurrence of Initial States. Phys. Rev. Lett. 15 (6), 240-243. doi:10.1103/PhysRevLett.15.240.

Zhao, Z., Klemas, V., Zheng, Q., Yan, X., 2004. Remote sensing evidence for the baroclinic tide origin of internal solitary waves in the northeastern south China Sea. Geophys. Res. Lett. 31, L06302. doi:10.1029/2003GL019077.